Advances in Colloid and Interface Science 283 (2020) 102215

Contents lists available at ScienceDirect

Advances in Colloid and Interface Science

journal homepage: www.elsevier.com/locate/cis

Historical Perspective

Surface chemistry of graphene and graphene oxide: A versatile route for their dispersion and tribological applications

Ajay Chouhan [a,b,1], Harshal P. Mungse [a,1,2], Om P. Khatri [a,b,*]

[a] Chemical and Material Sciences Division, CSIR-Indian Institute of Petroleum, Dehradun 248005, India
[b] Academy of Scientific and Innovative Research, Ghaziabad 201002, India

ARTICLE INFO

Article history:
15 June 2020
Available online 30 July 2020

Keywords:
Graphene
Materials chemistry
Surfaces and interfaces
Dispersion
Lubrication

ABSTRACT

Graphene, the most promising material of the decade, has attracted immense interest in a diversified range of applications. The weak van der Waals interaction between adjacent atomic-thick lamellae, excellent mechanical strength, remarkable thermal conductivity, and high surface area, make graphene a potential candidate for tribological applications. However, the use of graphene as an additive to liquid lubricants has been a major challenge because of poor dispersibility. Herein, a thorough review is presented on preparation, structural models, chemical functionalization, and dispersibility of graphene, graphene oxide, chemically-functionalized graphene, and graphene-derived nanocomposites. The graphene-based materials as additives to water and lubricating oils improved the lubrication properties by reducing the friction, protecting the contact interfaces against the wear, dissipating the heat from tribo-interfaces, and mitigating the corrosion by forming the protecting thin film. The dispersion stability, structural features, and dosage of graphene-based dispersoids, along with contact geometry, play important roles and govern the tribological properties. The chemistry of lubricated surfaces is critically reviewed by emphasizing the graphene-based thin film formation under the tribo-stress, which minimizes the wear. The comprehensive review provides variable approaches for the development of high-performance lubricant systems and accentuates the lubrication mechanisms by highlighting the role of graphene-based materials for enhancement of tribological properties.

Contents

* Corresponding author at: Chemical and Material Sciences Division, CSIR-Indian Institute of Petroleum, Dehradun 248005, India.
E-mail address: opkhatri@iip.res.in (O.P. Khatri).
[1]Equally contributed.
[2]Present address: Department of Chemistry, Adarsha Science, J. B. Arts & Birla Commerce College, Dhamangaon - 444709, India.

https://doi.org/10.1016/j.cis.2020.102215
0001-8686/

1. Introduction

Graphene, the atomic-thick two-dimensional honeycomb lattice structure of carbon material, has attracted immense interest due to remarkable mechanical, electrical, thermal, and optical properties [1,2]. The large surface area (2630 m^2g^{-1}), excellent mechanical strength (Young's modulus: 1 TPa; fracture strength: 130 GPa), and superior thermal conductivity (5000 WmK^{-1}) make graphene an ideal material for lubricant applications [3–5]. The graphene as a solid thin film for micro-devices, additive to various liquid lubricants, and filler to composite materials have shown remarkable improvement in friction and wear characteristics [6–10]. Graphene, as a thinnest solid lubricant film, effectively reduced the adhesion and friction forces when coated on various substrates [11]. The weak van der Waals interaction between the atomic-thick lamellae of graphene provides low-resistance to shear and lowers the friction. Therefore, a single sheet of graphene shows higher friction than multilayer-graphene. Lee et al. have explicitly revealed that friction monotonically increased as the number of layers decreased [6]. The significantly high mechanical strength of graphene protects the contact interfaces under the tribo-stress and subsidizes the wear. Recently, Sumant et al. demonstrated that a single layer of graphene on steel substrate could last for 6400 sliding cycles under the contact stress of ~0.5 GPa and provides excellent wear-resistance [12]. Graphene is impermeable to liquids and gases viz. water and oxygen, and it reduces the corrosive and oxidative events of rubbing surfaces [13]. These findings revealed that graphene could be an excellent candidate for liquid lubricants to reduce the friction and wear of interacting surfaces [14,15]. However, the long-term dispersion stability of graphene in lubricating oils has been a major challenge for the lubricant industries. The graphene shows incompatibility with most of solvents/lubricants and tends to agglomerate driven by high cohesive interaction.

Use of environment-friendly and energy-efficient technologies is gaining immense interest to curb environmental pollution and channelize the energy resources in proficient ways for sustainable growth. The transport sector consumes ~20% of the global energy and accounts for ~18% of the total anthropogenic greenhouse gas emissions [16]. The road transportation is identified as one of the prime sources for rising CO_2 in the environment [17]. The ~33% of fuel energy in a passenger car is consumed to overcome the friction in the engine, transmission, tires, and breaks [18]. The implementation of advanced tribological solutions and lubricant technologies can conserve as much as 17.5% of the energy being utilized in road transportation [19]. The dynamic changes in engine design and materials of engine parts/tools along with stringent environmental policies and emission regulations are posing several challenges to the lubricant industries. The use of good lubricants conserves the energy by lowering the friction, increase the life of engine components/machinery parts by protecting the surfaces against the wear, and decrease the CO_2 emission by the smooth operation of the engine.

Lubricants are composed of lube base oil and a diversified range of additives. The composition of lubricants governs by their targeted applications. Primarily, they lubricate the engineering surfaces by decreasing the friction and wear, dissipating the heat from contact interfaces, inhibiting the corrosion, subsidizing the oxidative events, and dispersing the foreign particles and oxidized products. Therefore, the lubricant additives include friction-modifier, antiwear, and extreme-pressure additive, corrosion-inhibitor, viscosity-modifier, oxidation-inhibitor, and so on are used to impart performance characteristics to the lubricants [20]. The surface-active antiwear and friction modifier additives play important roles, particularly in the boundary and mixed lubrication regimes, and decrease wear and friction by forming the lubricious tribo thin film. The zinc dialkyldithiophosphates (ZnDDPs)-based compounds are widely used to subsidize the wear and improve the lubrication properties. Over the recent past, the use of sulfur, phosphorus, halogen, and metal constituted conventional additives, including the ZnDDPs, are gaining significant concerns because of their adverse effects on the environment and poisoning effects to exhaust emission catalysts [21,22]. Thus, a lot of efforts have been directed to replace the conventional additive like ZnDDPs. Over the last few years, nanostructural layered materials (viz. graphene, *h*-BN, MoS_2, WS_2) have shown significant progress in the fundamental studies signifying their potential for lubricant applications [6,11,23]. In this context, graphene has emerged as one of the most promising candidates because of intriguing low-frictional and antiwear properties to replace the conventional ZnDDPs-based additive.

The intriguing and favourable properties of graphene, *h*-BN, MoS_2, and WS_2 nanosheets (Table 1), viz. remarkably high mechanical strength, excellent thermal conductivity, low shear strength, and large surface area protect the tribo-interfaces against the wear, dissipate the heat from contact interfaces, reduce the friction by facilitating the sliding under tribo-stress, and furnish a high coverage on contact interfaces. Fig. 1 shows the atomic structure of graphene, *h*-BN, MoS_2, and WS_2 nanosheets. The *h*-BN nanosheets are made of atomic-thick lamellae, where the boron and nitrogen are alternatively placed and linked with each other by covalent linkages in a hexagonal lattice structure. These atomic-thick lamellae are held together by weak van der Waals interaction. The MoS_2 and WS_2 exhibit molecular layered structure, where each Mo/W atom is sandwiched between two sulfur atoms in a trigonal prismatic arrangement. These molecular lamellae are stacked with each other by weak van der Waals interaction. Under the tribo-stress, the weak interaction between atomic/molecular lamellae in graphene, *h*-BN, MoS_2, and WS_2 nanosheets eases the shearing along the sliding direction because of interplanar slip and reduces the friction. The strong inter-atomic covalent bonding within each lamella in these 2D materials provides remarkably high mechanical strength and improves the antiwear properties [28–31]. The graphene, *h*-BN, MoS_2, and WS_2 form a tribo-induced thin film on contact surfaces, which facilitates the sliding and avoids the direct contact between the tribo-pair. Therefore, the 2D layered materials are gaining significant interest in lubricant applications.

Graphene oxide (GO), an oxidized form of graphene has been a well-established precursor to prepare the reduced graphene oxide (rGO), graphene-based composites, and chemically-functionalized graphene. The oxygen functionalities in the GO facilitate the interaction with various chemical species via covalent linkages. The other interactive forces, such as the van der Waals linkages, π-π interactions, hydrogen bonding, and ionic interactions, assist for the non-covalent functionalization of graphene, GO, and rGO [32–34].

Table 1
Mechanical and thermal properties of 2D layered materials [24–27].

2D Materials	Young modulus, GPa	Breaking/fracture strength, GPa	Thermal conductivity, W/mK
Graphene	990–1060	130	3000–5000
h-BN	792–942	65–76	751
MoS_2	246–282	16–30	–
WS_2	254–290	–	–

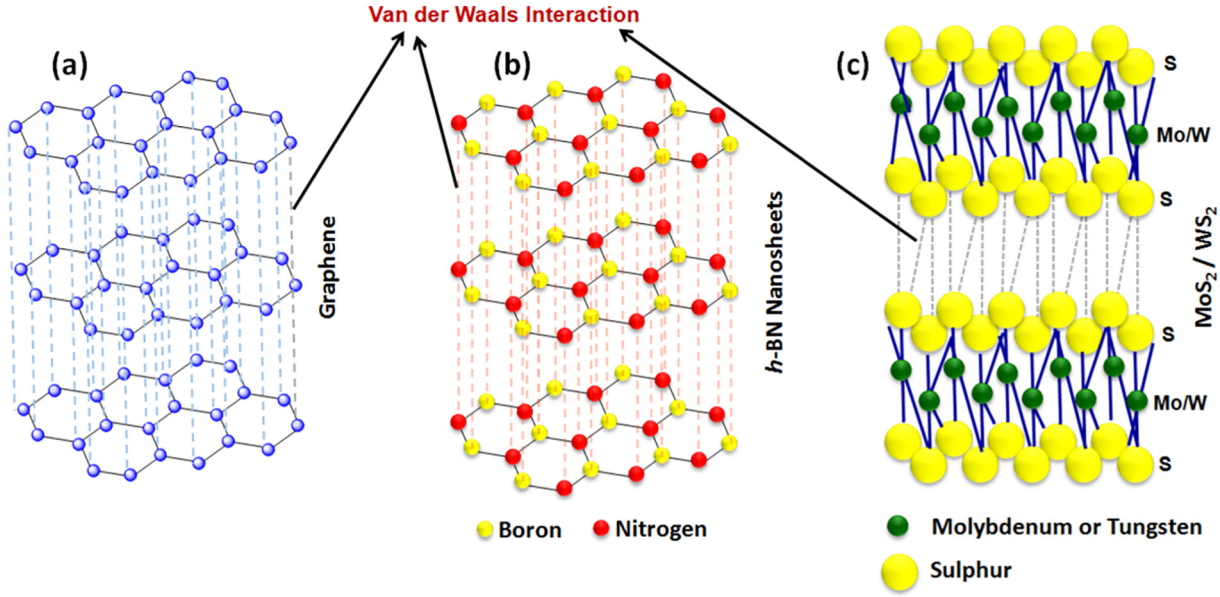

Fig. 1. Representative atomic structure of (a) graphene, (b) *h*-BN, (c) MoS_2 and WS_2 nanosheets along with illustration of van der Waals interaction between their atomic/molecular lamellae.

The GO exhibits plenty of oxygen functionalities such as hydroxyl, epoxide, carbonyl, ether, phenolic, and carboxylic groups. Among them, most of the epoxide, hydroxyl, and ether functionalities are located in the basal plane, whereas the carboxylic groups are placed along the edges of GO sheets [35–37]. The chemical reactivity of GO enables it's potential for various applications, including lubrication. Herein, chemical and structural features of GO and rGO, their chemical functionalization by different chemical approaches, and their dispersion in aqueous, organic solvents, and a wide range of lubricating oils are critically reviewed. The graphene-based materials are subsequently applied as additives for liquid lubricant applications and discussed their roles in the reduction of friction and wear by emphasizing the lubrication mechanism based on microscopic and spectroscopic analyses of lubricated surfaces.

2. Synthesis and chemical structure of graphite oxide/graphene oxide

2.1. Synthesis of graphite oxide/graphene oxide

Harsh oxidation of graphite powder leads to the formation of graphite oxide. The extended interlamellar spacing in the graphite oxide because of basal plane oxygen functionalities and trapped water molecules facilitates their lateral splitting by the aid of sonication and forms the GO. The graphite oxide was discovered much earlier (in 1859) than the graphene (in 2004). A very first report by the British chemist B. C. Brodie has described the preparation of graphite oxide by oxidation of graphite in the presence of fuming nitric acid and potassium chlorate as oxidizing agents [38]. The C:H:O ratio of synthesized graphite oxide was reported to be 61.04:1.85:37.11. Staudenmaier has addressed an improved oxidation method by addition of potassium chlorate in a small amount, and further oxidation was carried out by acidifying the mixture with concentrated sulphuric acid [39]. These methods were considered as hazardous and time-consuming processes. In 1958, Hummers and Offeman developed a rapid and relatively safer approach for preparing the graphite oxide by treating graphite with an anhydrous mixture of sulphuric acid, sodium nitrate, and potassium permanganate [40]. The Hummers' method avoids the use of highly corrosive fuming nitric acid. The use of potassium permanganate and sodium nitrate mixture resulted in an oxygenated-rich form of graphite oxide. Recently, Tour et al. have improved the Hummers' method to increase the efficiency of the oxidation process. In the improved approach, sodium nitrate was eliminated, the amount of potassium permanganate was raised, and oxidation reaction was carried out in a mixture of sulphuric acid/phosphoric acid (9:1 ratio) to afford a higher amount of oxidized graphite compared to Hummers' method [41]. Improvements over the various synthesis methods of graphite oxide have been pursued continuously to yield effective alternatives. The graphite oxide is a non-stoichiometric material, and its chemical structure and composition are primarily governed by the synthesis approach, use of oxidizing reagents, reaction conditions, and graphite precursor.

Fundamentally, there is no considerable chemical difference in the graphite oxide and the GO. The graphite oxide is the platform material for the preparation of GO by exfoliation. Structurally, the GO consists of a limited number of lamellae (maximum 10), whereas the graphite oxide possesses an unlimited number of layers with expanded interlamellar spacing, driven by ample oxygen functionalities in the basal plane and the trapped water molecules via hydrogen bonding network. The graphite oxide prepared by variable oxidation routes (Fig. 2) is exfoliated in the water or polar solvents by the aid of sonication and afforded the GO [42,43]. The sonication (bath sonication or probe sonication) is well established and widely used approach for exfoliation of graphite oxide. However, it leads to some structural damages in the GO lamellae. The degree of oxygen functionalities in the graphite oxide, sonication medium and time, ultrasonic frequency, and intensity govern the exfoliation and quality of resultant GO.

2.2. Chemical structure of graphite oxide/graphene oxide

Unlike the graphene, GO is a structurally distorted sheet of sp^2 carbons in the honeycomb lattice structure with the infusion of numerous sp^3 carbons due to oxygen functionalities. The atomic-thick lamellae of GO are linked with each other by the interlamellar spacing of 6 to 9 Å. The presence of oxygen functionalities in the basal plane and trapped water molecules by hydrogen interaction expand the interlamellar spacing. Thus the interlamellar spacing in GO (6–9 Å) is noted to be significantly higher than for the graphene (3.34 Å). The chemical structure of GO has been a subject of considerable debate and remains a challenge because of a large-degree of structural disorder, non-stoichiometric composition, variation in oxygen functionalities, and lack of consistency

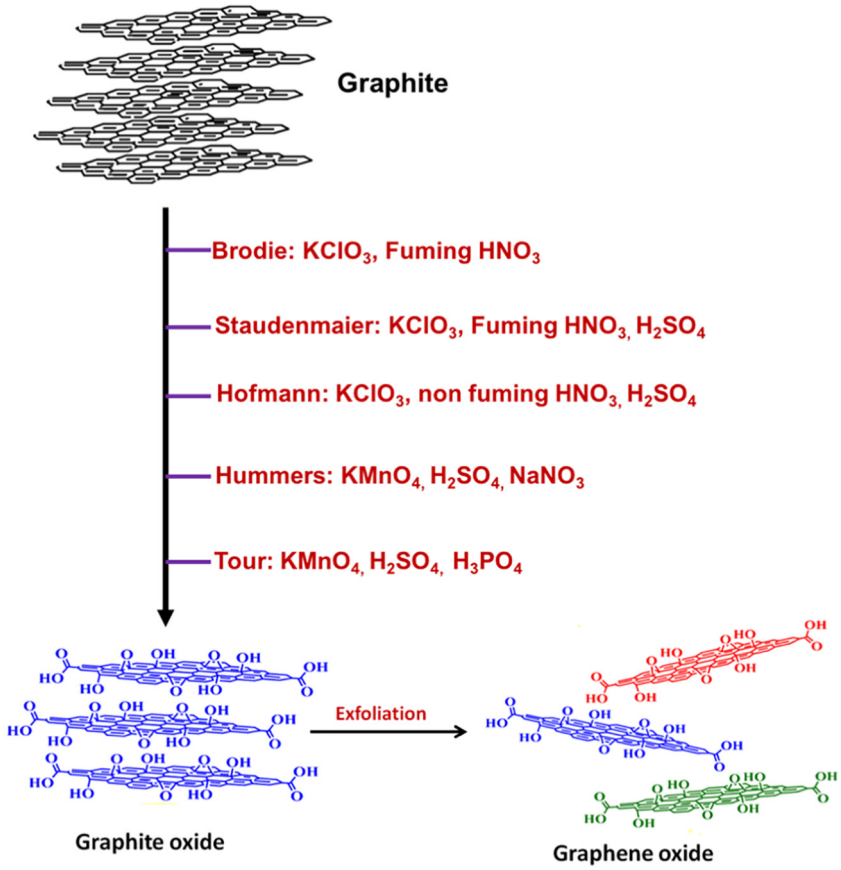

Fig. 2. Variable chemical approaches for the synthesis of graphite oxide from graphite and then exfoliation into GO. Chemical synthesis routes govern the C to O ratio in graphite oxide.

in the production cycles. Several structural models of graphite oxide and GO have been proposed over the last 80 years. The Hofmann, Ruess, Scholz-Boehm, Nakajima-Matsuo, Lerf-Klinowski, Dekany, and Ajayan models are well-debated structural models (Fig. 3).

A very first model of graphite oxide having repetitive units of 1,2-epoxides was proposed by Hofmann and Holst [44]. G. Ruess has demonstrated a modified structural model containing hydroxyl groups located at the sp^3 hybridized carbon in the basal plane [45]. Scholz and Boehm have proposed the hydroxyl and carbonyl groups at different positions along with C═C units within the corrugated layers, whereas the ether-based oxygen groups were ruled out [46]. A new structure model of graphite oxide was proposed by Nakajima and Matsuo consisting of interlinked carbon layers by sp^3 bonds perpendicular to the carbon network. They emphasized the presence of hydroxyl and carbonyl groups below and above the carbon layers [47]. The Lerf and Klinowski model was proposed based on ^{13}C and ^{1}H NMR. They have demonstrated that graphite oxide is composed of the aromatic region with non-oxidized benzene rings and aliphatic six-membered rings. The presence of the hydroxyl group distorted the configuration and developed the wrinkles in the layers. Furthermore, the oxygen functionalities like 1,2-epoxide and hydroxyl groups are mainly present at the basal plane, while edges carry carboxyl groups [48]. It was further supported by nanostructural studies of the GO based on high-resolution transmission electron microscopic analyses [49]. Chemical and microstructural analysis results support the Lerf and Klinowski model. Therefore, it has gained wide acceptance [36,50]. Dekany et al. have proposed

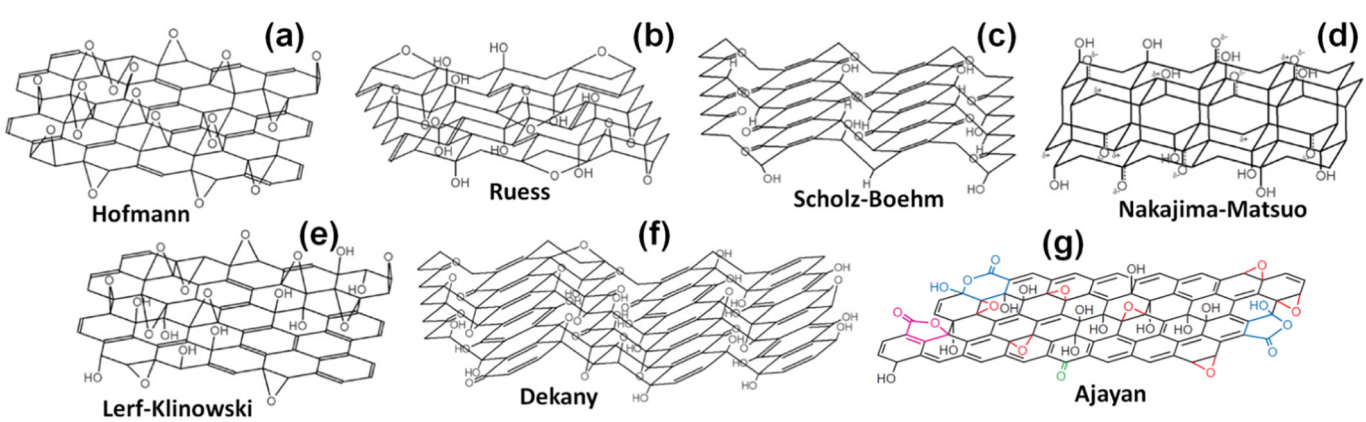

Fig. 3. Structural models of graphite oxide; (a) Hofmann model, (b) Ruess model, (c) Scholz-Boehm model, (d) Nakajima-Mastsuo model, (e) Lerf-Klinowski model, (f) Dekany model, and (g) Ajayan model.

the structural model based on elemental analysis, XRD, ^{13}C MAS-NMR, FTIR, XPS, and ESR analyses [35]. The proposed structural model suggests that graphite oxide is comprised of two distinct domains of trans-linked cyclohexane chairs and flat hexagon ribbons with C═C linkages (Fig. 3f). The phenolic groups were introduced to explain the acidity of the graphite oxide. Recently, Ajayan and co-workers have suggested the presence of five- and six-membered-ring lactols based on ^{13}C NMR of graphite oxide [51]. The ratio of different functional groups in the graphite oxide is proposed to be 115:3:63:10:9 for hydroxyl and epoxide; lactol O–C–O; graphitic sp^2 carbon; lactol, ester, and acid carbonyl; and ketone carbonyl, respectively.

The structural models of graphite oxide based on experimental results were further compared with density functional calculations. It predicted that partial oxidation is thermodynamically favourable over the complete oxidation [50]. The oxidation conditions primarily govern the distribution and abundance of oxygen functional groups in the graphite oxide. The graphite oxide and GO exhibits excellent dispersibility in water and it is attributed to high polarity and formation of hydrogen bonding by oxygen functionalities with water. The high polarity further extends the compatibility of GO with polar solvents [52]. A wide range of oxygen functionalities in GO facilitates its interaction with organic molecules, polymers, nanomaterials, etc. As a result, GO has been an excellent precursor to prepare the rGO, chemically-functionalized graphene, graphene-based composites, and their derivatives.

3. Synthesis and chemical structure of graphene/rGO

3.1. Synthesis of graphene/rGO

A breakthrough invention of atomically thin carbon films by Geim and Novoselov has exponentially propelled the potential of graphene for fundamental studies to application perspective [55]. Over the last 15 years, a lot of efforts have been directed to synthesize the graphene (Fig. 4). The mechanical exfoliation of highly oriented pyrolytic graphite (HOPG) using the scotch tape yielded a high-quality graphene. However, it has very low throughput and limits its scope for large-scale production. The epitaxial growth is an attractive alternative to prepare good-quality graphene for electronic applications [56,57]. The high temperature, vacuum, cost, and low throughput are few concerns which limit the production of graphene at mass-scale, particularly for industrial applications. The chemical vapor deposition (CVD) of graphene on a variety of polycrystalline metal substrates has been addressed using the hydrocarbons viz. methane, ethylene, benzene, and acetylene as carbon sources [58]. The transfer and removal of graphene from the metal substrates, low yield, and reproducible growth at low temperature are few of the drawbacks which need to be defeated for the mass-scale industrial applications. The mechanical exfoliation of graphite is one of the promising approaches to produce large-scale graphene at low cost. The mechanical exfoliation by sonication, ball-milling, and recently emerged fluid dynamics approaches are gaining increasing attention for graphene production [53]. The solvents and exfoliating agents govern the quality and quantity of graphene produced by liquid-phase exfoliation. The addition of pre-designed exfoliating reagents in the given solvent improves the exfoliation yield and avoids the aggregation of graphene [59]. The solvents with the surface tension of ~40 $mJ.m^{-2}$ are considered to be a suitable medium for liquid-phase exfoliation of graphite and then dispersion of resultant graphene. The *N*-methyl-2-pyrrolidone (NMP) has been recognized as one of the most efficient solvents for exfoliation of graphite [60]. The liquid-phase exfoliation is a highly versatile approach to produce good-quality graphene. Nevertheless, liquid-phase exfoliation has some disadvantages such as the requirement of a large quantity solvents, low yield, toxicity and irritant nature of most of the solvents, etc.

Chemical reduction of GO has been a most versatile, scalable, and economical approach to produce the rGO. Although the rGO carries some residual oxygen functionalities yet it exhibits a reasonable extent of graphene features. Therefore, rGO produced by chemical reduction is gaining considerable interest for industrial applications. The density functional calculations revealed that the complete reduction of graphene oxide into pure graphene is a difficult process [50]. Over the last decade, several reducing and dehydrating agents like hydrazine hydrate, sodium borohydride, $LiAlH_4$, hydroquinone, thiourea, alcohols, etc. have been addressed to produce the rGO [62–64]. The residual oxygen functionalities and structural features of the rGO are collectively governed by the reducing agents and the reduction parameters. The hydrazine hydrate has been a most established reducing agent and exhibits excellent reduction efficiency to eliminate a significant degree of oxygen functionalities from the GO. Hence, it has been widely accepted for laboratory work to industrial production of the rGO at a mass-scale.

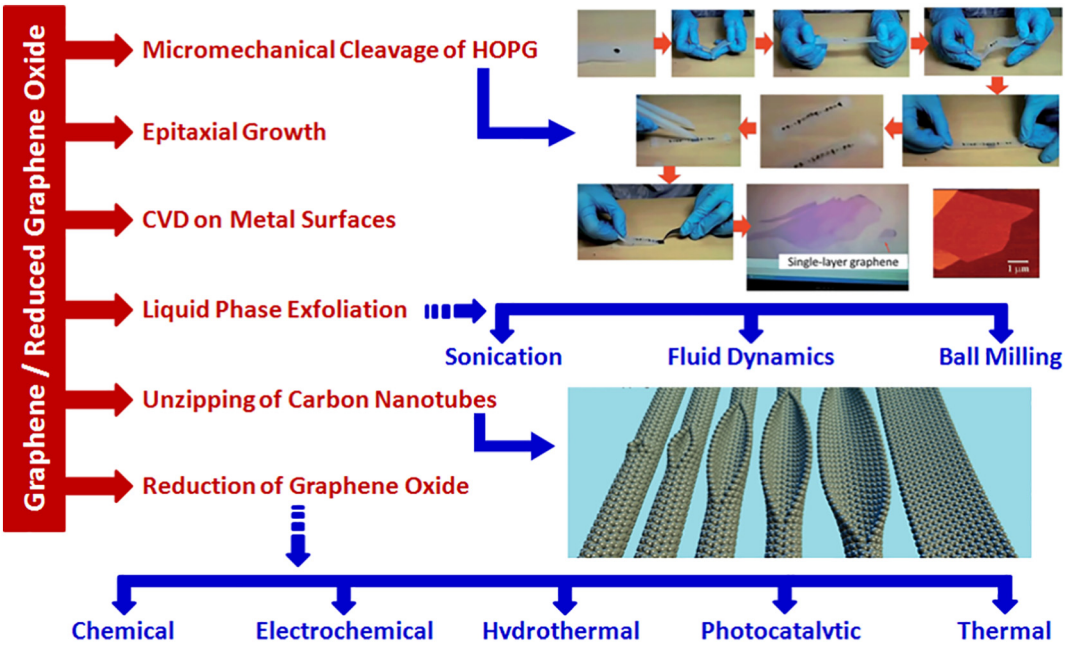

Fig. 4. Overview of variable approaches to prepare graphene and rGO. Reproduced with permission [53,54].

The hazardous, corrosiveness, and toxicity of most of chemical reducing agents are gaining significant concerns. As a result, green approaches are showing immense interest. Over the recent past, various environmentally-friendly reducing reagents viz. ascorbic acid, amino acids and plant extracts have been demonstrated to prepare the rGO [65–68]. Alternatively, the photocatalytic, electrochemical, and thermal reduction approaches have been developed to produce the rGO by avoiding the heteroatom contamination [69–71]. Ganguly et al. have monitored the deoxygenation events at different stages of thermal reduction process and suggested the formation of phenolic groups via *a* reaction between the epoxide groups and adjacent hydroxyl groups at ~400 °C. The high-temperature reduction generates several structural defects and compromises the quality of the rGO. The sub- and supercritical hydrothermal reduction of GO facilitated the elimination of hydroxyl, carboxylic, epoxide, and carbonyl functionalities and recovered the π-conjugated network at a significant extent (Fig. 5). The hydrothermal reduction of GO is considered as a green and clean approach for regulating the deoxygenation events as a function of temperature [37,61]. The oxidative chemical processing of carbon nanotubes successfully produced the graphene. Tour et al. have developed a simple solution-based oxidative process to yield graphene nanoribbons by longitudinal unzipping of carbon nanotubes. The subsequent chemical reduction restored the chemical conductivity [54].

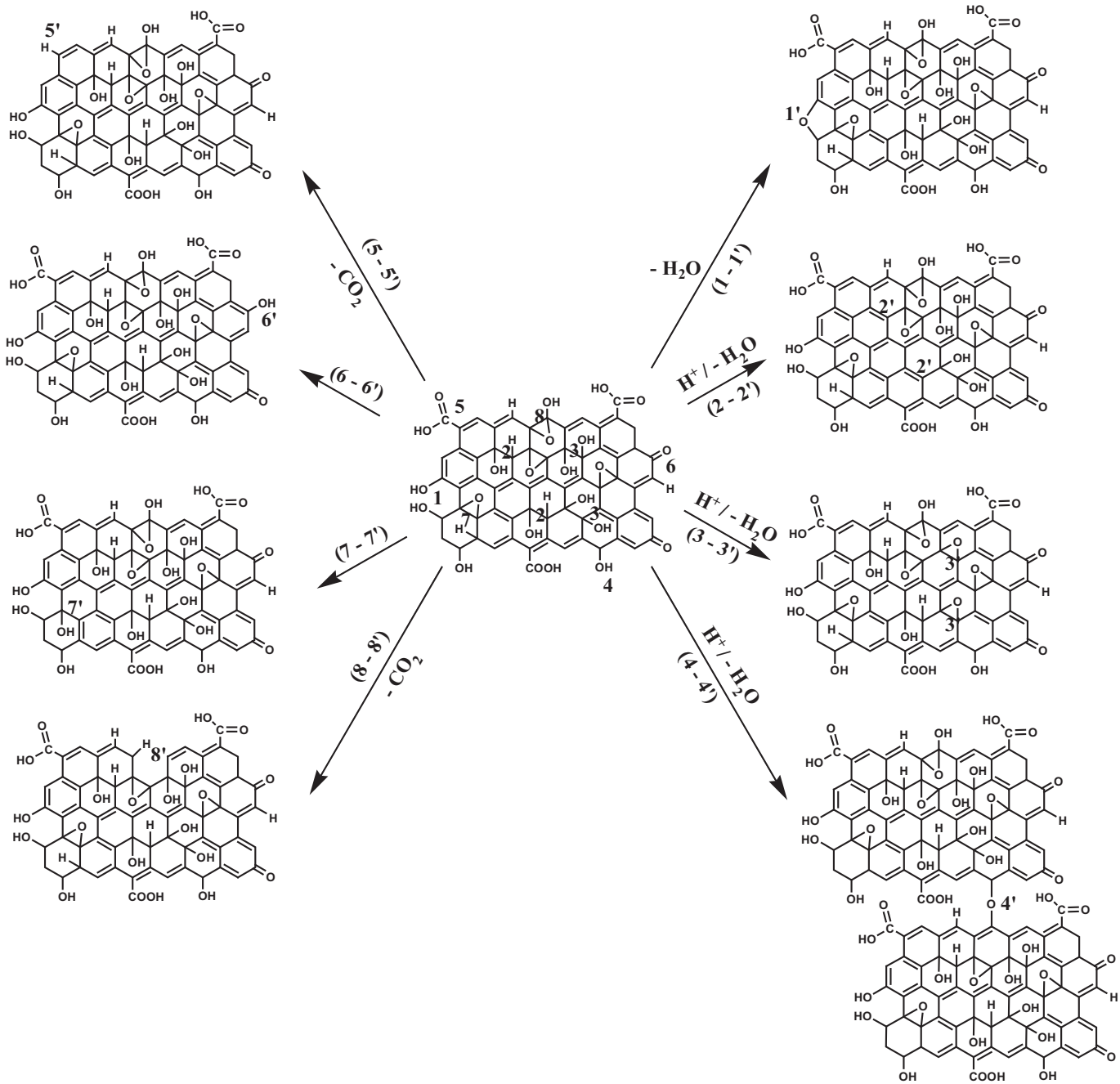

Fig. 5. Deoxygenation of GO by the elimination of hydroxyl, carboxylic, epoxide, and carbonyl groups during hydrothermal treatment using sub- and supercritical water. Chemical changes are indicated by numbering the respective carbons in the GO. The carbon associated with position numbers 1, 2, 3, 4, 5, 6, 7, and 8 represent dehydration to cyclic ether, dehydration to olefinic bond, dehydration to epoxide, intermolecular dehydration to ether, decarboxylation, reduction of carbonyl group into hydroxyl group, epoxide-to-hydroxyl conversion, and decarboxylation by consuming carbon from GO skeleton, respectively. Reproduced with permission [61].

3.2. Chemical structure of graphene/rGO

Recently, the Carbon Journal's editorial board has recommended the nomenclature of two-dimensional carbon materials and explicitly defined the graphene (monolayer vs. multilayer) and the rGO [72]. Fundamentally, graphene is a single-atom-thick sheet of hexagonally arranged, sp^2-bonded carbon atoms. The lateral dimension of graphene can vary from a few nanometers to the micron range. It is mostly prepared by chemical vapor deposition on the metal substrate [58]. The stacking of atomic-thick lamellae of graphene via van der Waals interaction yielded multilayer graphene, and the number of lamellae in multilayer graphene varies from 2 to 10 [72]. In most studies, the term graphene includes the multilayer graphene as well. The rGO is made by chemical, thermal (hydrothermal/solvothermal), photochemical, microwave, or microbial processing of GO by reducing the oxygen content. The rGO exhibits structural defects, residual oxygen functionalities, and a little fraction of sp^3 carbon; as a result, it carries structural distortion in the 2D structure. The ratio of C/O in rGO varies by the oxidation process. Yet, the rGO carries the most of the fundamental properties of graphene, to a significant extent. Furthermore, ease of scalability and low cost make rGO favourable for several applications [73].

Graphene exhibits strong intraplanar bonding between the sp^2 hybrid carbons placed in the honeycomb lattice structure, whereas the weak interplanar interaction connects graphene lamellae in the (002) plane. The two-dimensional structure, along with an extended π-electron network of graphene renders remarkable electronic properties. The interactions between electrons and honeycomb lattice structure yield the quasiparticles, which are also known as massless Dirac fermions and offer exceptional electronic phenomena such as anomalous room-temperature quantum hall effect (QHE) and extraordinary high carrier mobility [1]. Graphene shows weak affinity and interaction for chemical transformation. However, the atomic hydrogen can react with graphene and convert the highly conductive metallic state of graphene into an insulator, also known as graphane [74]. The intercalation of atoms and molecules in the basal plane of graphene acted as nanoreactors and enhanced the surface reactions. The small spacing in the graphene leads to new chemistry viz. “catalysis” and “electrochemistry” under the cover [75]. The graphene has been established as a versatile platform for grafting of various catalytic sites for heterogenization of homogeneous catalysts [76,77]. The doping of heteroatoms, chemical grafting, loading of nanomaterials, introduction of structural defects, and chemical functionalization have expanded the potential of graphene and rGO for a wide range of chemical, electrocatalytic and photocatalytic reactions [78–83]. The N-doped graphene exhibits high photocatalytic activity for reduction of CO_2 and electrocatalytic activity for the oxygen reduction reactions. The nitrogen-doped sites viz. pyridinic N, graphitic N, and pyrrolic N in the graphene generate the catalytic centres for the electrocatalysis and photocatalysis [84,85]. The graphene deposited on a solid surface revealed significant differences in their properties, which includes morphological features, surface chemistry, and surface/interface properties. The deposition and interaction of graphene with semiconductors, ceramics, polymers, biomaterials, and metals also influence the properties of graphene. Therefore, the surface/interfacial properties are gaining significant attention for several applications such as catalysis, optoelectronics, lubrication, corrosion, coatings, composites, and, so on [86]. The covalent functionalization in the basal plane of graphene can be obtained by breaking the sp^2 linkages and the formation of sp^3 carbons. The oxidation of graphite into graphite oxide and then exfoliation into GO is one of the simplest examples to generate the oxygen functionalities in the basal plane of graphene. The unpaired electrons which are produced at the adjoining sites to the point of covalent bonding increase the chemical reactivity, leading to a chain reaction from the point of the initial attack [87]. The surface properties of graphene controlled by their preparation routes, have been applied to fabricate the superhydrophobic thin film to bring new opportunities for high-performance coating and multifunctional devices [88]. In the recent past, several efforts have been made towards covalent and non-covalent functionalization of graphene to meet the requirement for a wide range of applications and expand their potential for industrial utilization.

4. Dispersion of GO, graphene, rGO and chemically-functionalized graphene

The GO has been an ideal candidate for production of solution-processable rGO at a large scale for various applications. The presence of ample oxygen functionalities makes GO a highly polar and hydrophilic material, which facilitate long-term dispersibility of GO in water. The dispersion of GO in organic solvents has been gaining significant importance for expanding their potential for a diversified range of applications. The stability of GO dispersion prepared by exfoliation of graphite oxide in different organic solvents via bath sonication was explored to understand the interactive forces [89]. As shown in Fig. 6, the GO could be dispersed in several organic solvents, except in methanol, dichloromethane (DCM), *n*-hexane, *o*-xylene. The poor compatibility of GO with acetone,

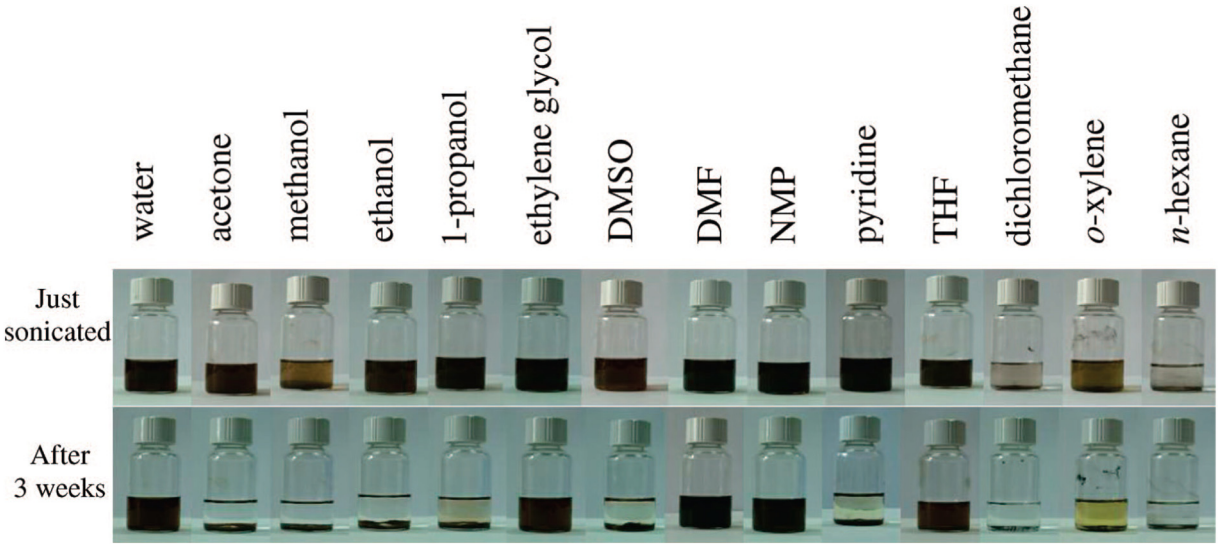

Fig. 6. Digital photographs of GO dispersion prepared via bath sonication in water and organic solvents. Top-line vials show dispersions immediately after sonication, whereas bottom line vials display dispersions after three weeks in different solvents. Reproduced with permission [89].

ethanol, 1-propanol, dimethyl sulfoxide (DMSO), and pyridine allow GO lamellae to gradually aggregate and settle-down in the solvent. The GO dispersion in *N, N*-dimethylformamide (DMF), NMP, tetrahydrofuran (THF), and ethylene glycol exhibits long-term dispersibility. The high electrical dipole moment of water (1.82 D), DMF (3.24 D), NMP (4.09 D), THF (1.75 D), and ethylene glycol (2.31 D) favours the dispersibility of polar GO in these solvents. However, the poor dispersibility of GO in the DMSO (high electrical dipole moment; 4.09D) signified that besides the polarity of the solvents other parameters are also important for determining the dispersibility [89]. Kymakis et al. demonstrated that the dispersion of GO and rGO is governed by surface tension, solvent polarity, and the Hansen solubility parameters [90]. The dispersion cohesion (δ_D), hydrogen bonding cohesion (δ_h), and polarity cohesion (δ_p) collectively represent the Hansen solubility parameters [91]. The dispersion of GO and rGO in highly polar solvents like DMF, NMP, etc. via sonication is considered as an energy-extensive approach, and it furnishes low yield. The homogeneous dispersion of rGO in organic solvents prepared by a chemical approach using GO dispersion in the synergistic ratio of water and applicable organic solvents like NMP, DMF, DMSO, THF, ethanol, acetone, acetonitrile, etc. promises good potential for a wide range of chemically-processable applications. The reduction of GO in these solvents using hydrazine hydrate as a reducing agent furnished the homogeneous dispersion of rGO. The NMP, DMF, DMSO, THF, and ethanol having the sum of $\delta_h + \delta_p$ in the range of 13–29 exhibited a good dispersion of rGO. The solvent with $\delta_h + \delta_p$ lesser than 10 and higher than 30 couldn't disperse the rGO [91]. The surface energies of GO (62 mN/m) and rGO (46 mN/m) also govern their dispersibility. The polar and hydrogen bonding components are significantly higher in the GO compared to rGO. Therefore, GO exhibited good dispersibility in most polar solvents. The equal values of the Hildebrand solubility parameter (δ_T) of solvents and solute (GO/rGO) favours the dispersion. The higher dispersibility of rGO ($\delta_T = 22$) in dichloromethane ($\delta_T = 20.2$; 1.6 μg/mL), chlorobenzene ($\delta_T = 19.6$; 3.4 μg/mL), *o*-dichlorobenzene ($\delta_T = 20.5$; 8.94 μg/mL), 1-chloronaphthalene ($\delta_T = 20.6$; 8.1 μg/mL) was explained based on compatibility of their Hildebrand solubility parameter [90].

The production of dispersible rGO by chemical reduction routes carries not only residual oxygen functionalities but also exhibits several structural defects, which compromise their electronic, mechanical, and structural properties. Alternatively, liquid-phase exfoliation of graphite in various organic solvents via sonication or intercalation approaches has gained attention for the production of defect-free large-size graphene sheets [53,59]. The liquid-phase exfoliation is one of the simple methods to produce large quantities of graphene, which can be useful for both electronic and biomedical applications. The energy required to exfoliate graphene should be balanced by interaction energy between the graphene and the solvent. Coleman et al. have revealed that solvents with surface tension in a range of 40–50 mJ/m^2 favour the exfoliation of graphite and dispersion of graphene [60]. The *o*-dichlorobenzene (DCB) exhibits excellent capability to produce the graphene by exfoliation of graphitic materials. The higher surface tension of DCB (36.6 mJ/m^2) favoured the exfoliation of graphite and furnished the high yield of graphene. Furthermore, the π-π interaction between the aromatic rings of DCB and graphene facilitates dispersion stability [92]. Several studies have been carried out demonstrating the exfoliation and dispersion of graphene in NMP. However, the low dispersion concentration limits their potential for several applications. A multi-step process of exfoliation could yield a significantly high concentration of graphene in the NMP. The centrifugation of exfoliated graphite in NMP, then filtration to obtain the exfoliated powder, followed by re-dispersion in the NMP via sonication significantly improved the dispersion concentration having an average of 3–4 layers in each sheet of graphene. Even after some sedimentation, the 26–28 mg.mL^{-1} concentration of dispersed graphene was found with indefinite stability [93].

The chemical stabilizers viz. surfactants, functionalized polymers, aromatic-rich molecules, and ionic liquids exfoliate the graphite via sonication by overcoming the van der Waals interactions between the graphene lamellae. Simultaneously, the stabilizers are adsorbed on the exfoliated graphene lamellae through non-covalent interactive forces viz. π-π, cation-π, and hydrophobic interactions, which avoid the re-stacking to make their stable dispersion [94–98]. The exfoliation of graphite in organic solvents of low boiling points with the presence of stabilizers has been gaining increasing interest. The hyperbranched polyethylene (HBPE) assisted exfoliation of graphite in low boiling points solvents viz. chloroform and THF yielded the stable dispersion, whereas the HBPE provides steric stabilization against restacking of graphene lamellae [98]. The chemical reduction of GO in the controlled reaction media and the presence of stabilizer facilitates the dispersion of rGO in the targeted solvents. The green tea, rich in polyphenols, not only reduced the GO but also made them dispersible in most organic solvents and water (Fig. 7). The π-π interaction between the aromatic rings of polyphenols and rGO furnished the stable dispersibility in NMP, DMSO, DMF, ethanol, and acetone [67]. The surfactants play a critical role to disperse the hydrophobic graphene in water. The polyethylene nonylphenylether (Igepal CO890) a non-ionic surfactant (200–300 ppm) furnished the stable dispersion of graphene in water [99].

The chemistry of surfactants governs their interaction with targeted nanomaterials. The molecular strategy to design the surfactants by introducing the ionic groups to an electron-deficient π-conjugated unit along with flexible alkyl spacers significantly enhanced the stability of graphene in the water. The electron-deficient aromatic units of surfactants show good affinity with graphene via π-π interaction and simultaneously ionic groups facilitate the dispersibility of surfactant-stabilized graphene lamellae in the water. The resultant dispersion of graphene was found to be stable for more than four months [101]. The presence of zwitterionic polymeric dispersant such as succinic anhydride-functionalized polyethylenimine (PEI-SA) facilitated the exfoliation of graphene and simultaneously stabilized the dispersion in water. The cation-π interaction between the protonated amines in dispersant and π-electron-rich structure in graphite along with the steric hindrance of PEI-SA stabilized the graphene dispersion in the water for more than six months [102]. The presence of negatively charged carboxylic group (COO^-) in the GO and rGO facilitate their dispersion in aqueous and organic solvents based on ionic interaction with surfactants. The hydrophilic end of surfactant-like didoceyldimethylammonium cation showed ionic interaction with negatively charged carboxylic groups of GO and rGO, whereas hydrophobic tail showed affinity towards organic solvents. A shaking of such mixture transferred the surfactant-stabilized GO and rGO in the chloroform, as demonstrated in Fig. 8 [100]. A simple approach to prepare the graphene by Li^+-OH^- assisted exfoliation

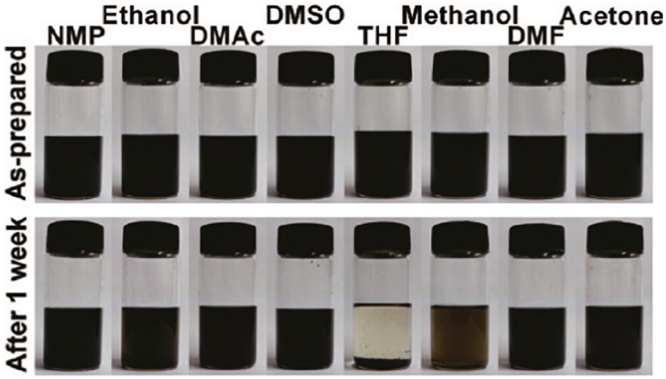

Fig. 7. Dispersion of rGO prepared via reduction of GO using the green tea. Concentration of graphene in organic solvents: 0.2 mg.mL^{-1}. Reproduced with permission [67]. (For interpretation of the references to colour in this figure legend, the reader is referred to the web version of this article.)

showed stable dispersion of graphene in water without sonication or surfactants. The positive charge introduced due to intercalation of Li^+ to graphene attracted the negatively charged hydroxyl groups and made them hydrophilic for stable dispersion in water [103].

Ionic liquids (ILs) are established as an excellent exfoliating and dispersing medium for graphene. The interactions between the π-electron clouds of graphene and positive charge of cationic moieties in ionic liquids facilitate the dispersion. Importantly, most of the ILs have surface tensions in the range of surface energy of graphite, which is the prime requirement for any dispersing media/solvent to exfoliate the graphite [112,113]. The graphite was efficiently exfoliated using the 1-hexyl-3-methylimidazolium hexafluorophosphate (HMIM-PF_6) ionic liquid, and resultant dispersion exhibited stability more than three weeks with maximum graphene concentration of 5.33 $mg.mL^{-1}$ [112]. The molecular dynamics study and experimental kinetic analysis revealed that collective van der Waals forces between graphene and ILs express the long-range dispersion interaction and short-range cation-π interaction [119]. The low-viscosity ionic liquid-like 1-ethyl-3-methylimidazolium dicyanamide (EMIM-DCA) IL yielded stable dispersion of 1 wt% graphene via mechanical mixing and sonication, and it exhibited stability for more than two months [114]. The poly(1-vinyl-3-butylimidazolium chloride), a polymeric ionic liquid stabilized-graphene sheets furnished stable dispersion in the 1-butyl-3-methylimidazolium hexafluorophosphate (BMI-PF_6) ionic liquid driven by π-π interaction between the imidazolium rings of the polymeric ionic liquid and the graphene lamellae [115]. The ionic liquid-based polyether, poly(1-glycidyl-3-methylimidazolium chloride) as stabilizers furnished the stable dispersion of graphene in the aqueous medium [120]. Table 2 summarizes the dispersion stability of GO, rGO, and graphene in a wide range of organic solvents and water.

Solvothermal reduction of GO in organic solvents is the most emergent chemical reduction to produce the stable dispersion of rGO in the processable solvents without the use of any stabilizer or surfactant [97,121,122]. The solvothermal reduction of GO in DMF yielded the $[NH_2(CH_3)_2]^+$-stabilized graphene (STG), which is dispersible in the DMF. The dispersion of STG (0.3 $mg.mL^{-1}$) in DMF was found to be stable for more than one year [97]. The STG could be re-dispersed (Fig. 9) in those organic solvents (NMP, DMSO, DMAC, and acetonitrile), which have a product of polarity and hydrogen bonding cohesive parameters in the range of 13–29. The solvothermal reduction of GO in NMP functionalized the rGO (STRG) by peroxy radicals being generated by solvothermal processing of NMP in the presence of air. The steric effect of functionalized groups on the surface of STRG sheets facilitates their dispersion in organic solvents viz. DMF, NMP, propylene carbonate, ethanol, and THF [121]. Karner et al. revealed that the combination of thermal and chemical deoxygenation events by NMP under the solvothermal processing produced the rGO (SRGO). The NMP molecules are grafted via hydrogen linkages with residual oxygen functionalities of SRGO. The resultant SRGO exhibited good dispersibility in organic solvents like DMSO, ethyl acetate, THF, acetonitrile, DMF, and $CHCl_3$ with minimal precipitation even after six weeks [122]. Table 3 summarizes the dispersion stability of chemically functionalized rGO, polymeric-stabilized rGO/graphene, and dispersant-assisted rGO/graphene in a wide range of organic solvents and water.

The γ-ray irradiation to GO has been established as an environmentally benign and cost-effective approach for preparing the rGO at a large-scale. Zhang et al. demonstrated a simple method to produce a stable dispersion of rGO by γ-ray irradiation of GO in DMF [142]. The electrons being formed by the interaction of high-energy γ-ray irradiation with DMF facilitate the reduction of GO. Furthermore, the formation of $N(CH_3)_2^+$ by radiolysis of DMF deposited on the surface of rGO sheets. As a result, rGO prepared by γ-ray irradiation could be re-dispersed in DMF, THF, Isopropanol, Glycol, NMP, as shown in Fig. 10. These dispersions are noted to be stable for two weeks. The γ-ray-based radiolysis also functionalized the rGO with poly(ethylene)glycol (PEG-200) via hydrogen bonding network between the residual oxygen functionalities of rGO and the oxygen atom of PEG molecules. The PEG-functionalized rGO exhibited stable dispersibility [143].

Dispersibility of graphene-based materials in lube oils is one of the major prerequisites for furnishing intriguing low-fictional and antiwear properties. The high cohesive interaction driven by large surface area, structural defects, and π-π interaction between the graphene sheets leads to the formation of agglomerates. The larger size agglomerates of graphene adversely influenced the uninterrupted supply of graphene to contact interfaces. The highly disorganized arrangement of graphene sheets in such agglomerates damages the interplanar low shearing properties of graphene. Therefore, the intriguing low-frictional and antiwear properties of graphene-based materials can be achieved efficiently; when they are thoroughly dispersed, and their fascinating tribological properties are not compromised.

The use of dispersants/surfactants and the chemical functionalization of graphene are recognized as simple and economic approaches to improve the dispersibility of graphene in lube-base oils. The use of dispersants and grafting of surface-active molecules over the graphene sheets are selected based on the nature of lube oils being used for dispersion of graphene-based materials. The grafting of long alkyl chains on GO and rGO increase the compatibility of resultant graphene-based materials with mineral and synthetic lube base oils, driven by the van der Waals interaction between the long alkyl chains of surface-active molecules grafted on graphene-based materials and the hydrocarbon content of lube base oil [144]. Furthermore, the chain length of grafted molecules also governs the degree of dispersibility. The dispersion stability of alkylated graphene in hydrocarbon solvents increased with increasing the chain length of alkyl groups grafted over the graphene's surface. The grafting of 3,5-di-tert-butyl-4-hydroxybenzaldehyde over

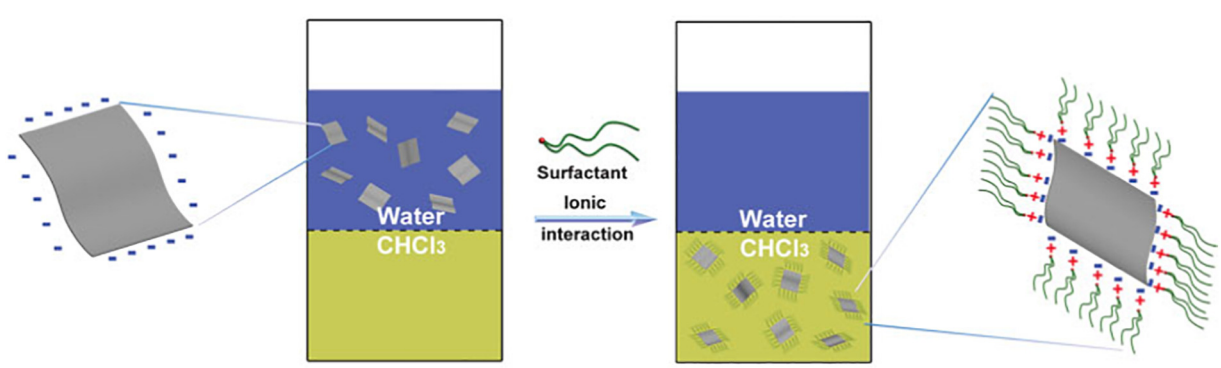

Fig. 8. Schematic illustration representing the transfer of graphene sheets from water to chloroform with the aid of surfactant based on ionic interactions. Reproduced with permission [100].

Table 2
Dispersion stability of GO, rGO, and graphene in a wide range of organic solvents and water.

No.	Sample description	Medium of dispersion	Dose	Dispersion stability	Reference
1	GO prepared by Hummers' method	NMP, DMF, THF, ethylene glycol	0.5 $mg.mL^{-1}$	>3 Weeks	[89]
2	Ultrasound-assisted GO dispersion	NMP, DMF, THF, Water, ethylene glycol	0.5 $mg.mL^{-1}$	>24 Hours	[90]
3	rGO prepared by hydrazine reduction of GO	1-Chloronaphthalene, NMP, *o*-chlorobenzene	0.5 $mg.mL^{-1}$	>24 Hours	[90]
4	rGO dispersion by reduction of GO in DMF and then top-up with targeted organic solvents	DMF, DMSO, THF, NMP, acetone, ethanol, acetonitrile	0.03 $mg.mL^{-1}$	Stable dispersion	[91]
5	Graphene prepared by liquid-phase exfoliation of graphite	NMP	0.01 $mg.mL^{-1}$	5 Months	[60]
6	Graphene prepared by liquid-phase exfoliation of graphite	*o*-DCB	0.01 $mg.mL^{-1}$	–	[92]
7	Liquid-phase exfoliated graphene via multistep approach	NMP	26–28 $mg.mL^{-1}$	Indefinitely	[93]
8	Liquid-phase exfoliated graphene in low boiling point solvents	Chloroform, ethanol	0.5 $mg.mL^{-1}$	80% content stable	[94]
9	Pristine graphene	THF	–	Stable dispersion	[95]
10	rGO prepared in organic media via chemical reduction of GO	NMP, DMF	–	2 Months	[96]
11	Graphene prepared by solvothermal reduction of GO	DMF	0.3 $mg.mL^{-1}$	1 Year	[97]
12	Graphene prepared by liquid-phase exfoliation assisted by hyperbranched polyethylene stabilizer	THF $CHCl_3$	0.045 $mg.mL^{-1}$ 0.18 $mg.mL^{-1}$	–	[98]
13	Graphene prepared via reduction of GO in green tea (polyphenols-based stabilizers)	NMP, DMSO, DMF, ethanol, acetone	0.2 $mg.mL^{-1}$	1 Week	[67]
14	Surfactants-stabilized graphene sheets	Water	0.75 $mg.mL^{-1}$	4 Months	[101]
15	Graphene prepared by cation-π interaction induced exfoliation of graphite using polymeric dispersant	Water	0.56 $mg.mL^{-1}$	6 Months	[102]
16	Graphene prepared by Li-OH driven exfoliation of graphite without sonication and surfactant	Water	0.09 $mg.mL^{-1}$	–	[103]
17	Solution-processed exfoliated graphene nanoplatelets with the aid of 15% polycarboxylate-based surfactant	Water	1%	6 Hours	[104]
18	Graphene platelets prepared by fluorinated surfactant-assisted ultrasonic exfoliation of graphite	Water	–	3 Weeks	[105]
19	Graphene prepared by sodium cholate surfactant-assisted exfoliation of graphite	Water	0.41 $mg.mL^{-1}$	Stable dispersion	[106]
20	Graphene prepared by sodium deoxycholate surfactant-assisted exfoliation of graphite	Water	2.58 $mg.mL^{-1}$	Stable dispersion	[106]
21	Graphene prepared by sodium cholate surfactant-assisted exfoliation of graphite	Water	0.3 $mg.mL^{-1}$	Stable dispersion	[107]
22	Graphene prepared by sodium taurodeoxycholate surfactant-assisted exfoliation of graphite	Water	7.1 $mg.mL^{-1}$	–	[108]
23	Graphene prepared by hexahydroxytriphenylene (as exfoliant and dispersant)-assisted exfoliation of graphite	Water	0.28 $mg.mL^{-1}$	2 Months	[109]
24	Solution-processed exfoliated graphene with the aid of vinylimidazole-based polymer as a high-performance stabilizer	Water	3.25 $mg.mL^{-1}$		[110]
25	Liquid phase production of graphene by sodium dodecylbenzene sulfonate surfactant assisted exfoliation of graphite	Water	–	>6 Weeks	[111]
26	Liquid-phase exfoliated graphene in Ionic Liquid	HMIM-PF_6 ionic liquid	5.33 $mg.mL^{-1}$	3 Weeks	[112]
27	Liquid-phase exfoliated graphene in Ionic Liquid	BMIM-Tf_2N ionic liquid	0.95 $mg.mL^{-1}$	Small sedimentation	[113]
28	Graphene dispersion via mechanical mixing and sonication	EMIM-DCA ionic liquid	1 wt%	2 Months	[114]
29	Polymeric ionic liquid-stabilized graphene	BMI-PF_6 ionic liquid	0.8 $mg.mL^{-1}$	2 Months	[115]
30	Liquid-phase exfoliated graphene in Levulinic acid	Levulinic acid	0.065 $mg.mL^{-1}$	–	[116]
31	Sonication-free dispersion of GO using internal pressure from released of intercalated CO_2	Ethanol, THF, DMF, NMP	1.0 $mg.mL^{-1}$	Stable dispersion	[117]
32	Sulfonated graphene	Water	2.0 $mg.mL^{-1}$	–	[118]

the rGO sheets facilitates its dispersion in SN-150 mineral lube oil. The tertiary butyl groups over the surface of chemically-functionalized rGO exhibit cohesive interaction with hydrocarbon chains of SN-150 oil driven by van der Waals interaction, resulting in good dispersion for enhancement of lubrication properties [126]. The graphene shows immiscibility with synthetic polyol lube base oil. The covalent grafting of octadecyl chains by using the organosilanes improved the dispersion stability. Furthermore, the grafting patterns of organosilanes over the surface of GO and rGO govern their dispersibility [145]. The modification of GO and rGO sheets with imidazolium ionic liquids (ILs) by simple mixing or covalent grafting improved their compatibility with various lube base oil viz. multialkylated cyclopentane and PEG 200 [146,147]. The variable strategies for synthesizing and functionalization of graphene, GO, rGO are designed considering the chemical nature and physicochemical properties of lube base oil.

5. Tribological applications of graphene-based materials

5.1. Graphene, GO and rGO as lubricant additive

Water-based lubricants are widely used for several engineering applications such as oil extraction, cutting fluids, metal finishing, hydraulic fluids, metal forming processes, and so on. The low cost, abundant availability, good thermal conductivity, and environmental compatibility make water an excellent lubricating media. The natural systems use water as a lubricating fluid. In the biological systems, the presence of proteins, especially glycol-proteins, modify the interactive surfaces to make them lubricated in the presence of water-based fluids. The water without additives is a poor lubricant in most of the man-made engineering systems. The high adhesion, formation of oxides/hydroxides, and corrosion-induced degradation limits its potential for metal surfaces. Therefore, water-miscible additives, which can protect the metal

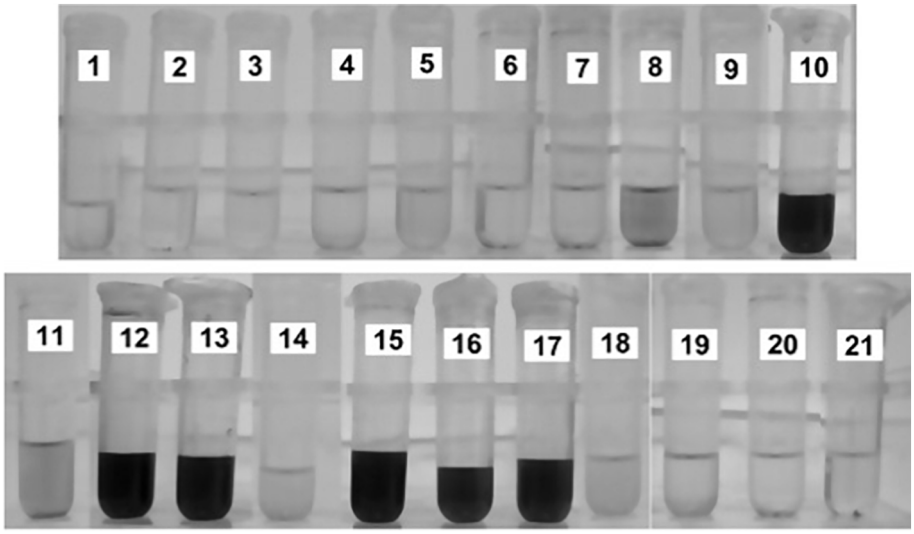

Fig. 9. Dispersion of $[NH_2(CH_3)_2]^+$-stabilized graphene (STG) in variable organic solvents and water. The number on each sample represents the solvents; (1) hexane, (2) triethylamine, (3) toluene, (4) dimethyl ether, (5) diethylamide, (6) DCM, (7) chloroform, (8) ethyl acetate, (9) THF, (10) pyridine, (11) acetone, (12) NMP, (13) *N*,*N*-dimethylacetamide (DMAC), (14) 2-isopropanol, (15) acetonitrile, (16) DMF, (17) DMSO, (18) ethanol, (19) ethylene glycol, (20) water, and (21) methanol. Reproduced with permission [97].

surfaces and dissipate the heat, are gaining significant attention for aqueous-based lubricating systems.

The tribological system generates heat because of friction. The dissipation of heat from contact interfaces is the prime requirement for a good lubricant system [148]. The conductivity of graphene-blended lubricants is governed by intrinsic thermal property of graphene along with the interfacial thermal resistance between the graphene-based materials and the lube oil. The 2D planar structure, along with significantly high surface area, makes graphene-based materials highly promising candidates to take away the heat from contact zones when they are nicely dispersed in the lubricating medium. The higher degree of interfacial contacts between the GO/chemically-functionalized rGO and water, driven by excellent dispersibility, notably reduced the contact resistance and furnished the excellent thermal conductivity to water [149,150]. The inherently high thermal conductivity in the chemically-functionalized rGO provided excellent heat dissipation properties to lubricant system.

The aqueous dispersion of GO has been an excellent lubricating fluid to reduce friction and wear. The stable dispersion of single-layered GO in water (1 wt%) significantly improved the lubrication between the steel plate and tungsten carbide (WC) ball (Fig. 11). The average coefficient of friction was reduced to ~0.05 from 0.4 (for purified water) and showed no apparent wear even after 60,000 cyclic contacts. The elemental mapping results suggested the adsorption of GO sheets on the contact interfaces for the enhanced lubrication performance [151]. The aqueous dispersion of GO as a lubricating medium between the diamond-like carbon-coated steel disc and stainless steel ball decreased the coefficient of friction by 57% compared to water. The presence of GO inhibited the oxidative corrosion of contact interfaces. The lowering of friction was attributed to the formation of GO-based tribo-layer by the embedding of GO sheets on the contact interface and binding of water molecules on GO-based tribo-layer, which facilities the lubrication [152].

The pH of GO dispersion influenced the chemical structure and nature of the charge. The increasing pH from acidic to alkaline not only breaks-down the sheets but also reduced them; consequently, significant changes were observed in the tribo-performance. The coefficient of friction and wear were increased at higher pH. The variable lubrication mechanisms at different pH were attributed to the physicochemical and morphological features of GO. The larger size of GO sheets at acidic pH tended to cover the contact interfaces by forming a protective tribo-film, which reduced the wear and friction, effectively. The relatively smaller sheets of GO at alkaline pH couldn't form a good quality tribo-thin film, whereas they entered the contact area and caused the high density to scratch the sliding pairs. Consequently, high wear with alkaline dispersion of GO [153]. The efficacy of lubrication by GO-based dispersion can be improved using the chemically-functionalized engineering surfaces. The 3-aminopropyltriethoxysilane (APS) coated albronze facilitates the deposition of GO sheets driven by the interaction between the oxygen functionalities of GO and amino groups of APS thin film, which results in the formation of durable and good quality tribo-film on the contact interface. The tribo-results revealed the significant reduction of friction (44%) and wear rate (80%) compared to the deionised water, and it was attributed to the synergistic effect of the amino-terminated surface of albronze and GO additive [154]. The fluorination of GO enhances lubrication performance. The fluorination of GO at variable reaction conditions (temperature: 40 and 180 °C; F_2 concentration: 1 and 6%) yielded the oxygen-enriched GO (OFG) and fluorine-enriched GO (FGO). The difference in chemical composition, structural features, and dispersibility of GO, OFG, and FGO in water govern their tribo-performance. The aqueous dispersion of OFG (0.5 mg. mL^{-1}) decreased the wear rate between the steel tribo-pair by 47% and 31% compared to that of water and GO dispersion, respectively. However, FGO with poor-dispersibility with water couldn't improve the tribo-performance of water. The ample oxygen functionalities make the OFG highly dispersible in the water, whereas the presence of fluorine in the OFG decreased the interlamellar-spacing, which facilitates the interplanar slips under the tribo-stress. The collective effects of good dispersibility and self-lubricating properties of OFG offered excellent tribo-performance for aqueous-based lubricant system [155].

The GO as an additive to water showed significantly improved friction-reducing and antiwear capability than the graphene. The superior tribological performance of GO nanofluids is attributed to highly hydrophilic oxygen-enriched functionalized groups (hydroxide, carboxylic, carbonyl, and so on) over the surface of GO. The high polarity of GO, driven by oxygen functionalities, facilitates the deposition on metal-based tribo-surfaces. The improved adhesion between the GO and the metal surface furnish long-term stability and load-bearing capacity to GO-based tribo thin film compared to the graphene [156]. Furthermore, the excellent dispersibility GO in the water ensures its uninterrupted supply to the contact area and form the protective layer on the interacting surfaces. Table 4 summarizes the various approaches for the preparation of GO dispersion in water and then their lubrication

Table 3
Dispersion stability of chemically functionalized rGO, polymeric-stabilized rGO/graphene, and dispersant-assisted rGO/graphene in a wide range of organic solvents and water.

No.	Sample description	Medium of dispersion	Dose	Dispersion stability	Reference
1	Graphene dispersion via solvothermal reduction of graphene oxide in DMF	DMF NMP, DMSO, DMAC, acetonitrile	0.3 $mg.mL^{-1}$ –	1 Year –	[97]
2	Solvothermally-reduced and functionalized GO by NMP	NMP DMF, ethanol, THF, propylene carbonate,	1.4 $mg.mL^{-1}$ –	1 Month –	[121]
3	Solvothermally reduced graphene oxide (SRGO) by NMP	DMSO, ethyl acetate, THF, acetonitrile, DMF, ethanol, $CHCl_3$	1 $mg.mL^{-1}$	6 Weeks	[122]
4	Chemically functionalized graphene by 1,3 dipolar cycloaddition of azomethineylide	Ethanol	0.5 $mg.mL^{-1}$	> 30 Days	[123]
5	Hydrazinium ion-stabilized graphene	Water	–	Few months	[124]
6	Ethylenediamine triacetic acid-functionalized rGO by silylation and then reduction	Water	1 $mg.mL^{-1}$	3 Months	[125]
7	3,5-di-tert-butyl-4-hydroxybenzaldehyde grafted-graphene (Gr-DtBHBA)	SN-150 Mineral Lube Oil	0.8 $mg.mL^{-1}$		[126]
8	Fluorinated graphene prepared by direct fluorination of graphene utilizing F_2	Liquid Paraffin	0.3 $mg.mL^{-1}$	Stable	[127]
9	Nano-fibrillated cellulose (NFC) stabilized rGO	Water	0.3 $mg.mL^{-1}$	Stable	[128]
10	Graphene nanosheets prepared by chemical reduction in DMF using ethylenediamine as a reducing agent	DMF	–	–	[129]
11	Octadecylamine-functionalized Graphene	Hexadecane	0.1 $mg.mL^{-1}$	2 Days	[10]
12	Bio-functionalized graphene produced by ultrasound-assisted exfoliation of graphite by self-assembling of fungal hydrophobin Vmh2 protein	Ethanol-Water (6:4 ratio)	–	6 Months	[130]
13	Poly(N-vinyl-2-pyrrolidone) stabilized rGO prepared by reducing GO in the presence of poly(N-vinyl-2-pyrrolidone)	Water	4 $mg.mL^{-1}$	Several months	[131]
14	rGO prepared by ultrasound-assisted reduction of GO using hydrazine reducing agent	Water	1 $mg.mL^{-1}$	40 Days	[132]
15	Graphene prepared by silk fibroin (protein) nanofibers-assisted exfoliation of graphite in water	Water	1.92 $mg.mL^{-1}$	30 Days	[133]
16	Poly(acrylic acid) brushes-functionalized thermally rGO	Water	0.05 wt%	4 Days	[134]
17	Surfactant ($TSiPD^{\cdot+}$) stabilized graphene prepared by sonication of graphene in $TSiPD^{\cdot+}$ solution	Water	10 $mg.mL^{-1}$	1 Month	[135]
18	Polymeric dispersant-stabilized rGO prepared by reduction of GO in the presence of poly(3,4-ethylene dioxythiophene): poly(styrene sulfonate) dispersant	Water	1 $mg.mL^{-1}$	6 Months	[136]
19	Electrostatically-stabilized rGO prepared by reduction of GO using the excess of hydrazine and NH_3 solution	Water	0.5 $mg.mL^{-1}$	2 Days	[137]
20	Graphene-polyaniline composite prepared by in-situ polymerization of aniline on the surface of polystyrene sulfonic acid-grafted graphene	Water	0.25 $mg.mL^{-1}$	3 Weeks	[138]
21	Chemically modified graphene produced by hydrazine reduction of KOH-stabilized GO dispersion in water	Water	–	4 Months	[139]
22	Graphene produced by ultrasound-assisted exfoliation of graphite in the presence of vinylimidazole-based polymeric stabilizers in water	Water	3.25 $mg.mL^{-1}$	–	[110]
23	Gelatin-assisted fabrication of graphene by exfoliation of graphite in water	Water	0.3 $mg.mL^{-1}$	4 Weeks	[140]
24	Graphene prepared by chemical reduction of GO in the presence of nonionic Pluronic copolymer (poly(ethylene oxide)-*block*-poly(propylene oxide)-*block*-poly-(ethylene oxide) triblock copolymer	Water	1 $mg.mL^{-1}$	–	[141]
25	rGO prepared by γ-ray induced reduction of GO in DMF at room temperature	DMF, THF, isopropanol, glycol, NMP	1 $mg.mL^{-1}$	2 Weeks	[142]

performance under variable conditions viz. applied load, speed, contact geometry, and frictional pair.

The incompatibility between the highly polar GO nanosheets and the non-polar mineral lube oil leads to poor dispersion. It has been a great challenge for their utilization in industrial lubricant applications. Recently, Wu et al. revealed that GO could be dispersed in the aviation lubricant with the aid of sonication. However, such dispersion showed poor stability for a long time. Nonetheless, GO as an additive (0.5 wt%) to aviation lubricant could improve the load-carrying capacity, friction, and wear-resistant by 18%, 15%, and 34%, respectively, between the Si_3N_4 and steel tribopair. The detailed studies of worn surfaces based on EDX and Raman spectroscopic measurements suggested that GO can easily enter the contact interfaces and formed a protective thin film, which reduced the friction and protected the contact interfaces against the wear [166]. The GO dispersion stabilized by polyisobutylsuccinic acid-polyamine ester dispersant in mineral oil has been investigated under the boundary and elastohydrodynamic regimes and showed significant improvement in lubrication performance between the steel tribo-pair. The formation of protective thin film by GO was accountable for the reduction in friction and wear [167].

The GO and graphene have been explored as potential additives for a diversified range of lubricating fluids to enhance the tribo-performance by reducing the friction and protecting the contact interfaces [159,168]. The chemically-exfoliated graphene suspended in the ethanol decreased the coefficient of friction and wear by factors of 6 and 4, respectively, between the steel tribopair. The Raman spectroscopic analyses of the graphene-lubricated worn track showed the suppressed signature of iron oxide, revealing the passivation of contact interfaces by a conformal protective coating of graphene layers. The tribo-induced deposition of graphene layers not only reduced the tribo-corrosion and wear but also facilitated the shearing; which results in a significant reduction of friction between the steel tribo-pair [168]. The dispersion of exfoliated graphene stabilized by Triton X-100 surfactant has been demonstrated as aqueous-based lubricants for the steel tribopair. An aqueous dispersion of graphene (110 $\mu g.mL^{-1}$) decreased the friction by 81% and wear volume by two orders of magnitude owing to the formation of graphene-based tribo-layer on the sliding contact interfaces. Furthermore, the stabilized dispersion of graphene outperformed the GO dispersion under identical experimental conditions. The lubrication mechanism emphasized the role of surfactant, which facilitates the graphene deposition process on the contact interfaces by adjusting the

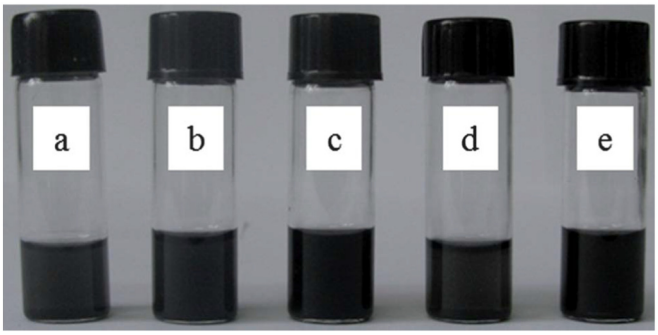

Fig. 10. Dispersion of rGO prepared by γ-ray irradiation-based reduction of GO in the DMF. The dispersion of rGO in (a) isopropanol, (b) glycol, (c) DMF, (d) THF, and (e) NMP solvents are shown after two weeks to demonstrate dispersion stability. Reproduced with permission [142].

dispersion wettability of the mating surfaces for superior tribo-performance [160]. The dispersion of Span-80 surfactant-stabilized graphene in the polyalphaolefin (PAO4) lube oil exhibited significantly improved lubrication properties for textured alloy cast iron surface. The 0.01 wt% dose of graphene in PAO4 could reduce the wear rate of flat and textured surfaces by 50% and 90%, respectively. The enhanced tribo-performance was attributed to the combined effect of micro-dimples on the textured surface and graphene nano-additive. The sheared graphene layers under the sliding contact stress formed a protective thin film of low shear strength. Furthermore, storing of graphene dispersion in the dimple accelerates thin film formation under the tribo-stress, consequently significantly enhanced tribo-performance by graphene dispersion for textured surfaces [169].

Graphene tends to form aggregates driven by cohesive interaction and settle down in the lubricants, which compromised the tribo-performance of graphene-based lubricants. The crumpled graphene balls prepared by rapidly evaporating of aerosol droplets of GO sheets exhibited excellent dispersibility in the PAO4 lube oil; whereas the agglomerations were seen in the dispersion of rGO, carbon black, and graphite particles in the PAO4 lube oil. The dispersion of crumpled graphene balls reduced the friction (20%) and wear coefficient (85%) of lube oil and outperformed the dispersions of rGO, carbon black, graphite particles, and fully formulated 5W30 lubricant (Fig. 12). The self-dispersion, high mechanical strength, and nanoscale ball bearing-function collectively enhanced the lubrication performance of crumpled graphene balls-based lubricant [170]. The high mechanical strength and inertness of fluorinated graphene promise its potential for tribological applications. The fluorinated graphene prepared by liquid-phase exfoliation of fluorinated graphite as lubricant additive to PAO40 significantly improved the anti-wear property and exhibited better friction stability along with durability of lube oil [171]. The graphene quantum dots (GQDs) as an additive to PAO lube oil showed notably enhanced tribo-performance between the steel tribopair under the boundary lubrication by reducing the friction (60%) and wear (91%). The improved lubrication performance was attributed to the synergistic effect of a densely packed protective tribo thin film formed on the contact interfaces and presence of friction-induced graphene-like debris in the contact area [172]. Table 5 summarizes the various approaches for the preparation of GO, graphene, and rGO along with their application as additives to various lubricating media for enhancement of tribological properties.

The rGO prepared by chemical, thermal, radiation-induced reduction of GO showed excellent potential as a lubricant additive to improve the tribological properties between the engineering surfaces. The synthesis approaches influence the chemical and structural features of rGO. Ramaprabhu et al. have synthesized graphene by solar light-induced exfoliation of graphite oxide. The prepared graphene nanosheets showed good hydrophobicity and excellent dispersibility in the engine oil. The graphene-based engine oil (0.025 mg.mL^{-1}) decreased the friction and wear scar diameter by 80% and 33%, respectively, whereas extreme pressure properties increased by 40% compared to the engine oil. The enhancement of tribo-performance was attributed to topological structure, high mechanical strength of graphene, excellent dispersibility, and the formation of nano-bearing between the steel balls [175]. The direct thermal reduction of GO yielded a lot of wrinkles, folds, holes, and structural defects, which alter the intrinsic features of graphene, including shearing properties under the tribo-stress. The thermal reduction of GO in sulphuric acid produced the rGO (SA-trGO) lamellar structure without folds and wrinkles. The SA-trGO as an additive to PAO6 exhibited outstanding tribo-performance and decreased the coefficient of friction and wear rate by 30% and 75%, respectively [176]. The thermal reduction of graphite oxide in the presence of KOH yielded the highly exfoliated rGO (herGO), and the

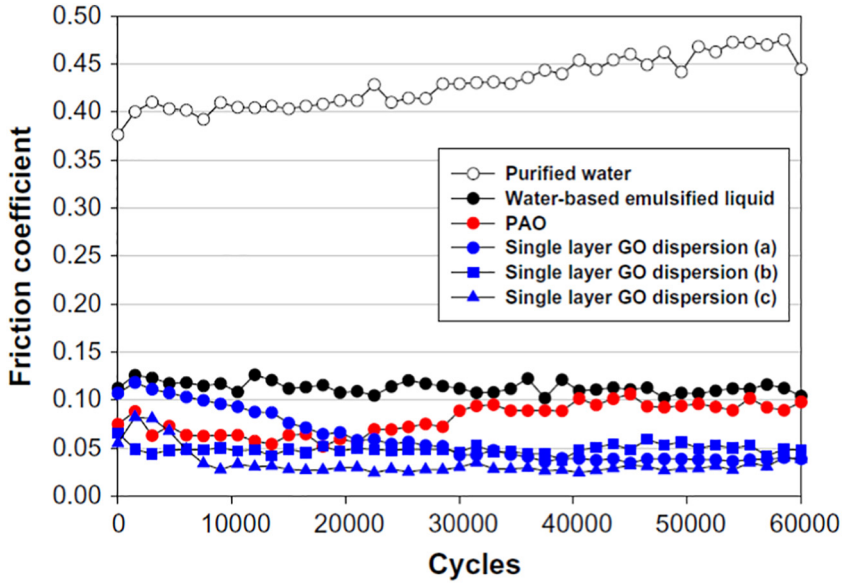

Fig. 11. Variation in the coefficient of friction between the WC ball and stainless steel plate in the presence of water-based lubricating fluids, including dispersion of GO. The friction measurements are carried out using purified water, water-based emulsified liquid, PAO, and three different samples of GO dispersion (a) (b) and (c) as lubricating medium. Applied load: 1.88 N. Reproduced with permission [151].

Table 4
Preparation of GO dispersion by various approaches and their lubrication performance under variable working conditions viz. applied load, speed, contact geometry, and frictional pair.

No.	Preparation method/brief description	Lube medium	Frictional pair	Load	Contact geometry	Friction reduction	Wear reduction	Reference
1	GO Prepared by modified Hummers' method and microwave irradiation	Water	Steel/WC Ball	1.88 N	Ball-on-disk	87.5%	–	[157]
2	GO Prepared by modified Hummers' method	Water	DLC/Steel	10 N	Ball-on-disk	57%	–	[158]
3	Commercially procured GO; accessed the effect of pH (3.1–9.7)	Water	Steel/Steel	20 N	Ball-on-three-plates	44.4%	17.1% (wear scar radius)	[153]
4	Commercially procured GO; used for amino-terminated self-assembled thin-film on albronze	Water	Steel/Albronze	2 N	Ball-on-disk	43.6%	79.7% (wear rate)	[154]
5	Selective fluorination of GO; having a variable degree of oxygen functionalities and fluorine	Water	Steel/Steel	20 N	Ball-on-plate	~22%	47% (wear rate)	[155]
6	GO Prepared by Hummers' method	Water	Steel/Steel	10 N	Ball-on-plate	~74%	64% (wear scar diameter)	[159]
7	Exfoliation of graphite in water with aid of Triton X-100 (non-ionic surfactant)	Water	Steel/Steel	2–15 N	Ball-on-plate	81.3%	61.8% (wear scar diameter)	[160]
8	Graphene-oxide nanosheets with an ionic liquid	Water	Si_3N_4/Sapphire	2–4 N	Ball-on-disk	Superlubricity	–	[161]
9	Graphene-oxide nanoflakes and ethanediol in aqueous medium	Water	Si_3N_4/SiO_2	2–4 N	Ball-on-disk	Superlubricity	–	[162]
10	Pristine graphene, fluorinated graphene and graphene oxide nanoflakes were deposited on SiO_2 substrates to form graphene coatings	Water & glycerol	Si_3N_4/SiO_2	1.5–4 N	Ball-on-disk	Superlubricity	–	[163]
11	Graphene oxide and onion-like carbon nano additive	Water	Steel/Steel	2–10 N	Ball-on-disk	~29%	–	[164]
12	Tribological performances of SiO_2/graphene combinations as water-based lubricant additives	Water	Steel/Mg alloy	3 N	Ball-on-disk	48.5%	79% Wear volume	[165]

microstructure of herGO is controlled by the ratio of graphite oxide and KOH. The herGO as an additive to PAO6 (0.5 wt%) decreased the wear scar depth and coefficient of friction by 90% and 44%. The enhanced tribo-performance was attributed to shearing by the book-like layered microstructure of herGO [177].

Besides the chemical structure, the microstructure of rGO sheets also monitors the lubrication properties. The rGO with regular edges as an additive to the hydraulic oil favoured the lubrication by reducing the coefficient of friction (28%) and wear-scar depth (14%), whereas the rGO with irregular edges and wrinkles showed no significant changes in tribo-performance of hydraulic oil. The graphene sheets with regular edges formed the thick and consistent tribo-film under the sliding stress, which avoided the asperities contacts and enhanced the lubrication properties (Fig. 13). The graphene with irregular edges and wrinkles formed the thin film of discrete patches, leading to direct contact between the asperities of mating surfaces and provides high resistance to shear under the sliding stress; consequently, relatively higher friction and wear [178]. The rGO has been demonstrated as an additive to lubricants for improving the tribological properties by (a) reducing the frictional energy losses, (b) enhancing the lubricant drain time, (c) increasing the wear-resistivity of machinery parts, (d) improving the conductivity to take away the heat from contact interfaces, and (e) decreasing the carbon footprints by fuel conservation. Furthermore, the rGO exhibited no signatures of acute toxicity during in-vitro studies using prokaryotic and eukaryotic cells. These results suggest the safe use of rGO as a lubricant additive not only enhances the tribo-performance

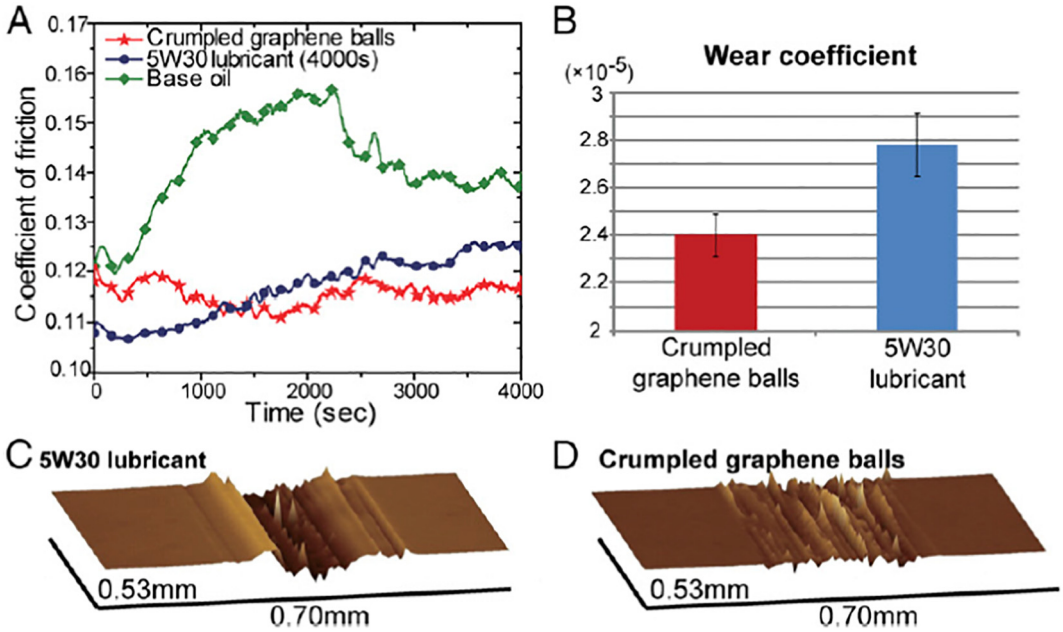

Fig. 12. Comparison of lubrication between fully formulated 5W30 lubricant and crumpled graphene balls in PAO4 base oil. The 0.1 wt% dose of crumpled graphene balls in the PAO4 base oil outperformed the fully formulated 5W30 lubricant. (A) Coefficient of friction, (B) wear coefficient, and (C and D) 3D profile images of the wear tracks using the 5W30 lubricant and crumpled graphene balls in PAO4 base oil. Reproduced with permission [170].

Table 5
Lubrication enhancement by dispersion of GO, graphene, and rGO as additives to lubricating media. The contact geometry, dosage of graphene-based materials, and lubricating media are presented to understand their roles for enhancement of tribological properties.

No.	Preparation method/brief description	Additive	Lube medium	Additive dosage	Contact geometry	Friction reduction	Wear reduction	Reference
1	Commercially procured GO nanoplates	GO	4010 Aviation lubricant	0.25–1.0 wt%	Four-ball	14.7%	34% (wear scar diameter)	[166]
2	Modified Hummers' method; polyisobutylsuccinic acid-polyamine ester was used to prepare the GO dispersion in the oil	GO	SN-150	0.01 wt%	Ball-on-disk	14–18%	12–30% (wear scar diameter)	[167]
3	Chemical exfoliation of highly oriented pyrolytic graphite	Graphene	Ethanol	1.0 $mg.L^{-1}$	Ball-on-disk	84%	83% (wear volume)	[168]
4	Commercially procured graphene; dispersed in the PAO 4 lubricant with the assistance of Span-80 dispersing agent	Graphene	PAO4 + 1 wt% Span-80	0.01 wt%	Ball-plate (flat and textured)	~51%	52% (wear rate)	[169]
5	Crumpled graphene balls prepared by capillary compression in rapidly evaporating aerosol droplets of GO sheets	Crumpled graphene balls	PAO4	0.01–0.1 wt%	Ball-on-disk	20%	85% (wear rate)	[170]
6	Fluorinated-graphene prepared by ultrasound-assisted exfoliation of fluorinated graphite in NMP using EDA as an intercalation agent	Fluorinated-graphene	PAO40	0.1–0.4 mg. mL^{-1}	Ball-on-disk	–	~79% (wear rate)	[171]
7	Graphene quantum dots were prepared by acid treatment and chemical exfoliation of conventional pitch-based carbon fibers	GQDs	Multialkylatedcyclopentanes	2.0 wt%	Ball-on-disk	60%	91% (wear volume)	[172]
8	Graphene sheets were wrapped to form horn-shaped cones with a half-fullerene cap (30–50 nm length and 2–5 nm diameter)	Graphene-based nano-horns	Poly-alkylene glycol	0.04–1.0 wt%	Ball-on-disk	18%	70% (wear volume)	[173]
9	Commercially procured graphene	Graphene	Esterified bio-oil	0.5 wt%	Four-ball	~35%	~27% (wear scar diameter)	[174]
10	Graphene was prepared by exfoliation of graphite oxide using focused solar light radiation	Graphene	Engine oil	0.012–0.062 mg. mL^{-1}	Four-ball	80%	33% (wear scar diameter)	[175]
11	Thermal reduction of GO at 160 °C in sulphuric acid to prepare a lamellar structure of rGO without folds and wrinkles	SA-tRGO	PAO6	0.0–1.0 wt%	Ball-on-disk	30%	75% (wear rate)	[176]
12	Thermal reduction of graphite oxide with a variable mole ratio of KOH at 700 °C	hrGO	PAO6	0.5 wt%	Ball-on-disk	44%	90% (wear scar depth)	[177]
13	Reduced graphene oxide of different micro-morphologies having regular edges (RG), irregular edges (ir-RG), and both irregular edges and wrinkles (ir-RWG) prepared by ball-milling of commercially procured rGO	RG, ir-RG, ir-RWG	Hydraulic oil	0.1–5.0 wt%	Ball-on-disk	27.9%	14.1% (wear depth)	[178]
14	Commercially procured rGO	rGO	Base oil	–	Ball-on-disk	40%	–	[179]
15	Reduced graphene oxide with variable interlamellar spacing prepared by chemical (FLG-Ls) and thermal (FLG-Ms) reduction of GO; Commercially procured highly oriented multilayer graphene (MLG-Ss)	FLG-Ls, FLG-Ms, MLG-Ss	PAO6	0.1–2.0 wt%	Ball-on-disk	~50%	~93% (wear depth)	[180]
16	Mild thermal reduction of GO at 700 °C	MrGO	PAO6	0.25–2.0 wt%	Ball-on-disk	30%	73.5% (wear depth)	[181]

but also reduces the environmental impact of transportation for sustainable growth of automotive sector [179].

The state near to vanish the friction is known as superlubricity. It is the most efficient way to reduce the losses of frictional energy and has attracted significant attention over the recent past. The origin of ultra-low friction lies in the incommensurability between the rotating graphite layers. The presence of graphite flake between the substrate and the tip elucidated the contact orientation-dependence friction. The two contact orientations governed by rotational angle furnished the high friction, where the graphite flake and the substrate lattices might have perfectly aligned and achieved the commensurate contact, whereas the rest of contact orientations in the intermediate rotational angle established the incommensurate contact and furnished superlubricity [182]. The superlubricity can be achieved when the graphene is synergistically used with nanodiamond particles and diamond-like carbon. The graphene sheets at a sliding interface wrapped the nanodiamonds under the sliding tribo-stress and yielded the nanoscrolls of the reduced contact area. The slid of such nanoscrolls against the diamond-like carbon surface, achieved the incommensurate contact, and remarkably reduced the coefficient of friction to ~0.004, signifying the macroscopic superlubricity [183]. The graphene nanoflakes over the graphite surface showed translational and rotational motions between commensurate initial and final states, as deduced from a scanning tunneling microscope. A tip-induced transition of graphene nanoflakes with underlying

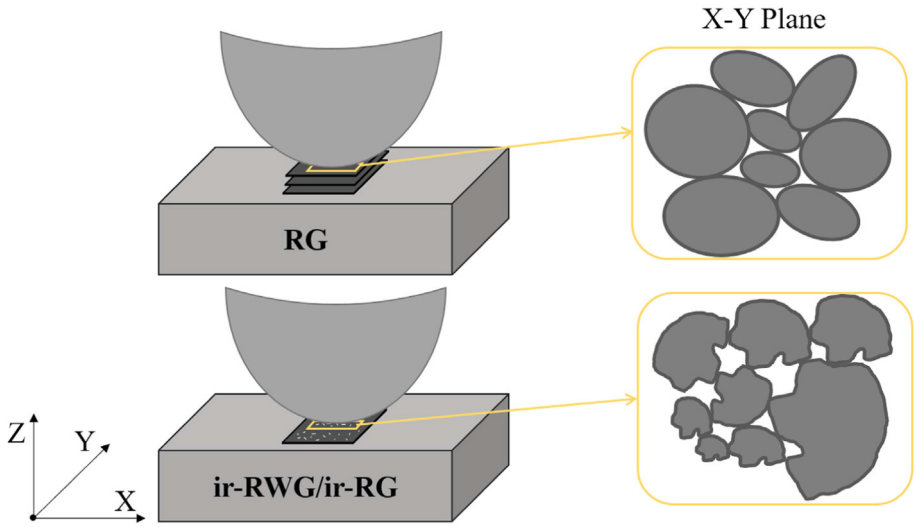

Fig. 13. Lubricating mechanism emphasizing the role of micromorphological features of graphene sheets (having regular or irregular edges) in the formation of a protective thin film on contact interfaces. RG: regular edges graphene; ir-RG: irregular edges graphene; ir-RWG: irregular edges and wrinkles graphene. Reproduced with permission [178].

graphite surface formed a commensurate to an incommensurate (the superlubric state) contact orientation, followed by rapid sliding until another commensurate position is reached [184]. The superlative state of graphene for remarkably low friction is further explored by molecular dynamics and new force field techniques. The unusual sliding mechanisms and temperature dependence of graphene in different contact orientations furnished the superlative state [185].

Recently, Luo group presented a novel method to achieve the liquid-superlubricity under extreme contact pressure by the synergistic effect of 2D materials and liquid molecules [161]. A robust macroscale liquid-superlubricity ($\mu \approx 0.005$) under extreme pressure of 600 MPa was recorded by a combination of GO sheets with ionic liquid ([Li(EGO]PF_6) for Si_3N_4/sapphire tribo-pair. Ionic liquid helps to form a boundary layer at the tribo-interfaces, while the GO sheets showed extremely low shear properties, and the combined effect led to liquid-superlubricity under extreme pressure. The macroscale superlubricity ($\mu \approx 0.0037$) is also achieved by a combination of GO nanoflakes with ethylene glycol at the Si_3N_4/SiO_2 interface [162]. Most recently, the graphene coating on SiO_2 substrates was made by using pristine graphene (PG), fluorinated graphene (FG), and GO materials for determination of superlubricity characteristics in the presence of an aqueous solution of glycerol [163]. It was noted that PG coating exhibited better tribological properties as compare to FG and GO coatings. Superlubricity ($\mu = 0.004$) was achieved by a combination of glycerol with PG coating was attributed to the formation of graphene nanoflakes tribofilm at the contact zone.

5.2. Chemically functionalized graphene, GO and rGO as lubricant additive

Graphene and rGO as additives to lubricants perform well when they are thoroughly dispersed in the lube oil and exhibited long-term dispersion stability. In the recent past, several approaches have been made to functionalize the GO and rGO to make them dispersible in lubricating oils. The GO, a non-stoichiometric material with ample oxygen functionalities, offers a platform for rich chemistry to occur within the interplanar gallery (basal plane) and along the edges of sheets [33,156,157]. The selective chemical functionalization targeting the specific type of oxygen functionality or reactions with multiple oxygen functionalities make the GO a potential material for several applications [186,187]. In the recent past, numerous types of functionalization based on covalent and non-covalent interactions driven by oxygen functionalities, π-electron-rich structure, and structural defects of GO have been demonstrated. The primary purpose of chemical functionalization of GO and rGO is to furnish their long-term dispersibility in liquid media or solvents for expanding their potential for various applications, particularly for those domains, where the solution-processed graphene is needed [32,188–190]. Herein, functionalization of GO, rGO, and graphene is critically reviewed emphasizing their dispersion in the lubricating fluids and enhancement of tribological properties by graphene-based additives.

The carboxylic groups in GO were selectively targeted for grafting of alkylamines via amide linkage using the thionyl chloride as a coupling reagent. The long alkyl chains of octadecylamine-functionalized GO (GO-ODA) furnished cohesive interaction with hexadecane; consequently, the GO-ODA is nicely dispersed in hexadecane. The minute dose of GO-ODA (0.06 $mg.mL^{-1}$) decreased the coefficient of friction and wear scar diameter of hexadecane by 26% and 9%, respectively. The enhanced tribo-performance was attributed to uninterrupted supply of GO-ODA to contact interfaces of steel tribopair [10]. The presence of oxygen functionalities viz. hydroxyl, ether, epoxy, etc., particularly in the basal plane of alkylated GO decreased the modulus and mechanical strength [32,161]. Thus, the GO-ODA as an additive couldn't show significant improvement in the wear (9% only).

The rGO prepared by chemical reduction exhibits the residual oxygen functionalities. The structural defects distributed across the sheet of rGO and the edges are prone to be oxidized into the carboxylic acid using mild nitric acid. The carboxylic groups in partially oxidized rGO were targeted for covalent coupling with ODA via an amide linkage to yield the alkylated-rGO (Fig. 14). The stable dispersion of rGO-ODA in the 10W40 engine oil significantly reduced the coefficient of friction (36%) and wear scar diameter (35%) between the steel balls. Furthermore, the tribo-performance of rGO-ODA was found to be better than the corresponding GO-ODA. The presence of oxygen functionalities in the GO-ODA diminished the shearing under the tribo-stress; consequently, poor performance compared to rGO-ODA [144]. The atomic force microscopic studies further revealed that the presence of oxygen functionalities in graphene oxide compromised the mechanical properties and the effective Young's modulus is estimated to be lower than the graphene [191]. Sahoo et al. have demonstrated simultaneous reduction of GO and grafting of ODA without using any reducing and coupling agent [192]. The surface functionalization of GO with ODA was facilitated by nucleophilic addition reaction between the amino group of ODA and epoxy group of GO [193]. The long alkyl chain of ODA grafted on the GO generates hydrophobicity and showed excellent compatibility with heavy paraffin oil. The 1 wt% dose of highly dispersible GO-ODA significantly decreased the coefficient of friction (~81%) compared to

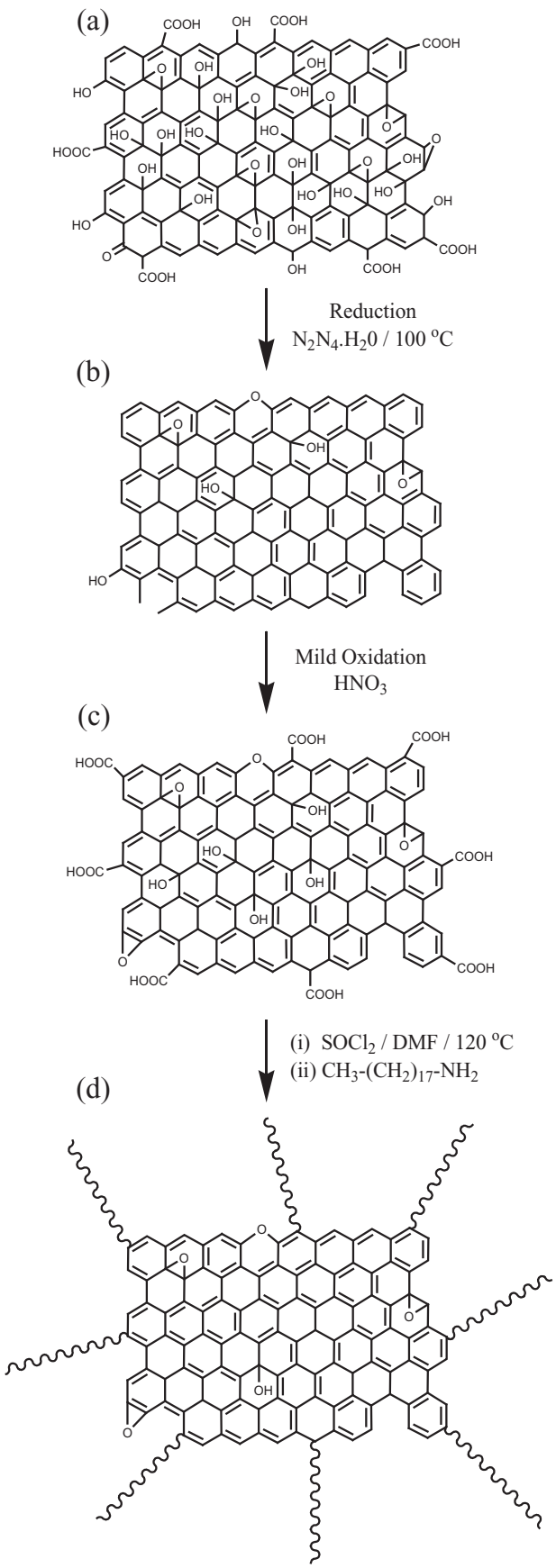

Fig. 14. Schematic models of (a) GO and (b) rGO, illustrating the distribution of various oxygen functionalities in their basal plane and along the edges. (c) The mild oxidation of rGO selectively introduced carboxylic groups at the edges and defects sites of rGO sheets. (d) ODA-functionalized rGO, prepared through amide linkage between the carboxylic sites of rGO and ODA. Reproduced with permission [144].

that of graphene in the heavy paraffin oil under the mean Hertzian contact pressure of 0.9 MPa [192].

Recently, Khatri et al. revealed the participation of phenolic, carboxylic, epoxy, and other oxygen functionalities for interactions with alkylamines. The refluxing of aqueous dispersion of GO with ethanolic solution of alkylamine proficiently grafts the alkylamines via nucleophilic addition interaction with basal plane epoxy groups, hydrogen linkages with the oxygen functionalities, and columbic interactions with weak acidic sites like carboxylic and phenolic groups as demonstrated in Fig. 15 [194]. The facile approach for grafting of ODA in the basal plane and simultaneous reduction of oxygen functionalities in GO not only restore the graphitic characteristics but also make the GO-ODA nicely dispersible in the 10W40 lube oil (Fig. 16). The minute dosage (0.02 $mg.mL^{-1}$) of GO-ODA notably decreased the friction and wear of fully formulated 10W40 engine oil. The analysis of worn surfaces, particularly the Raman spectroscopic results suggested the deposition of sheared graphene lamellae on the contact interfaces under the sliding stress. The deposited graphene-based thin-film not only protects the tribo-pairs against the undesirable events of wear but also facilitates the shearing to reduce the friction [195]. The carboxylic groups in GO show immense potential for the covalent functionalization with variable organic moieties to convert water-miscible GO to oil-compatible graphene-based materials for liquid lubricant applications. The oleic diethanolamide borate (ODAB) has been selectively grafted on GO via an amide linkage. The resultant GO-ODAB exhibited excellent dispersibility in the SN 500 lube base oil. The coefficient of friction and wear scar diameter were decreased by 38.4% and 42%, respectively, using the 0.02 wt% dosage of GO-ODAB between the steel tribo-pair [196]. The dodecyl chains were introduced on the surface of GO via click chemistry-based multi-step covalent functionalization, which includes the preparation of alkyne-functionalized GO via amide linkage with carboxylic groups of GO and then click coupling between alkyne-grafted GO and azidodecane. The resultant material (GO-CuAAC) as an additive to petroleum lube oil enhanced the tribological properties by reducing the friction (16%) and wear (30%) [197].

The non-covalent functionalization of rGO with poly(ethylene glycol) via γ-radiolysis enhanced the dispersion of resultant material (rGO-PEG) in the PEG. The high energy γ-radiation exposure formed the PEG radicals, which are reacted with rGO through hydrogen bonding between the oxygen atoms of PEG molecules and residual hydroxyl groups of rGO [142]. The γ-radiolysis-based functionalization of rGO expanded the interlamellar spacing by intercalation of PEG molecules. The stable dispersion of rGO-PEG reduced the coefficient of friction and wear rate by 38% and 55%, respectively compared to the un-irradiated rGO sample in the PEG lubricating media. The rGO-PEG with expanded interlamellar spacing easily sheared under the sliding tribo-stress between the contact interfaces and reduced the friction [Fig. 17]. Furthermore, rGO nanosheets are adsorbed on the contact interfaces driven by mechano-chemical energy and formed the graphene-based tribo-film, which not only protected the contact interfaces but also acted as a solid lamellar lubricant to ease the sliding of contact interfaces under the tribo-stress [143]. The PEGylated graphene (Gr-PEG) having amino-terminal group has been explored as nano-additive for enhancement of tribological properties of aqueous-based lubricants. The amino-containing PEG molecules were grafted on carboxylic groups-enriched graphene via amidation process. The Gr-PEG exhibited good dispersibility in water and notably decreased the friction (39%) and wear rate (81%) compared to the pure water. The enhanced lubrication performance of Gr-PEG-based aqueous lubricant was attributed to the formation of fluid adhesive film and graphene-based protective tribo-

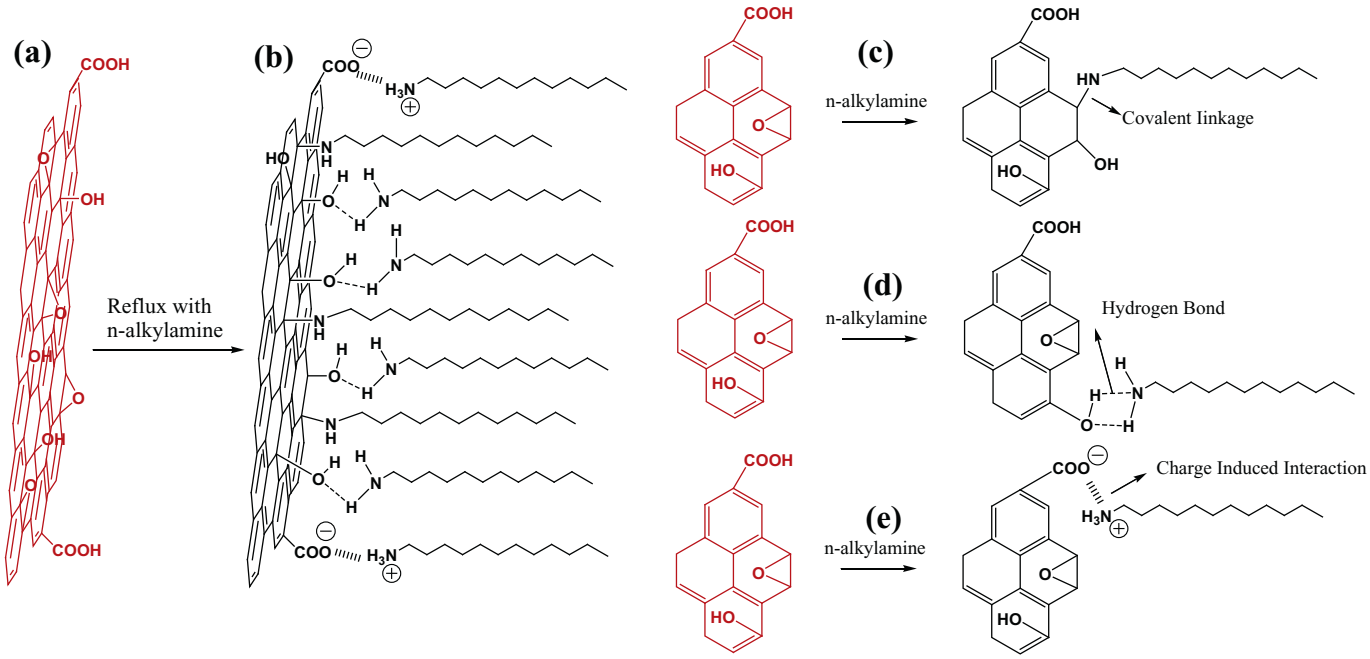

Fig. 15. (a) Schematic model of GO, (b) *n*-alkylamine grafted on the GO via multiple interaction pathways with basal plane oxygen functionalities. (c) Covalent linkage of *n*-alkylamine via a nucleophilic addition reaction by unzipping of an epoxy ring, (d) hydrogen bonding between the hydroxyl groups of GO and the amino groups of *n*-alkylamines, and (e) charge-induced interaction between weakly acidic sites (carboxylic and phenolic) of GO and *n*-alkylamines. Reproduced with permission [194].

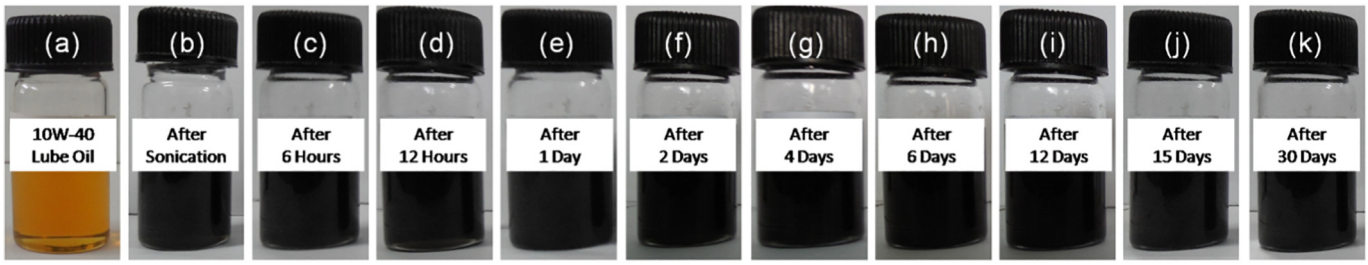

Fig. 16. Digital images of (a) 10W40 lube oil and (b–k) dispersion of GO-ODA in 10W40 lube oil (0.04 mg.mL^{-1}) as a function of time. Time for each image is noted on the respective dispersion sample bottle. Reproduced with permission [195].

film, which prevented direct contact between the friction pairs [198]. The scope of graphene as an additive to water-based lubricant was further expanded by covalent functionalization of GO with amino-terminated block copolymer using the 3-(trihydroxysilyl)-1-propane sulfonic acid linker. The resultant liquid-like graphene showed excellent dispersibility in the water and as an additive it decreased the friction and wear rate by 53% and 91%, respectively compared to the water. The remarkable lubrication properties of functionalized graphene dispersion in the water were attributed to the formation of graphene-based tribo-film on the contact interfaces driven by electrostatic adsorption under the tribo-stress and molecular rearrangement of liquid-like graphene [199].

The increasing importance of environment-friendly green lubricants has attracted great attention towards novel additives based on green chemistry. In this context, ionic liquids have been identified as promising candidates as lubricants and additives to reduce the friction and wear efficiently, while keeping the environment clean and green [200–203]. The wide range of cations and anions makes ionic liquids highly designable molecules for targeted engineering surfaces and lubricants. In the recent past, the hybrids of graphene and ionic liquids have shown great potential as lubricant additives for enhancement of tribological properties [175–177]. The commercially procured graphene was sonicated and then stirred with 1-butyl-3-methylimidazolium iodide (BMIM-I) ionic liquid to obtain the graphene-ionic liquid (Gr-IL) hybrid. The resultant Gr-IL hybrid served as an effective lubricant for aluminum-steel tribo pair and substantially reduced the friction and the wear [204]. The simultaneous reduction by KOH and functionalized of GO with imidazolium-based ionic liquids yielded the MGO-ILs *via* reaction of epoxy group of GO with imidazolium ionic liquids and the non–covalent linkages viz. π–π stacking, cation–π, and van der Waals interactions [146]. The MGO-ILs exhibited good dispersibility in alkylated cyclopentane lube base oil and significantly enhanced the tribo-performance by reducing the friction (27%) and wear volume (74%). The worn surface analysis revealed the formation of ionic liquids-containing graphene-rich tribo-film, which prevented the direct contact between the sliding surfaces and improved the friction and wear properties [146].

Graphene-ionic liquids hybrid nanomaterials prepared by chemical grafting of imidazolium ring on the graphene nanosheets using organosilane as a bifunctional chemical linker has been a promising approach to prepare stable dispersion of graphene in PEG-200 synthetic lube base oil. Furthermore, this approach has a merit to replace the associated anion via metathesis reaction using bis(salicylato)borate (BScB), oleate (OL), and hexafluorophosphate (PF_6) anions. The Gr-BScB, Gr-OL, and Gr-PF_6 hybrid nanomaterials (Fig. 18) as additives to synthetic lube base oil remarkably improved the lubrication properties

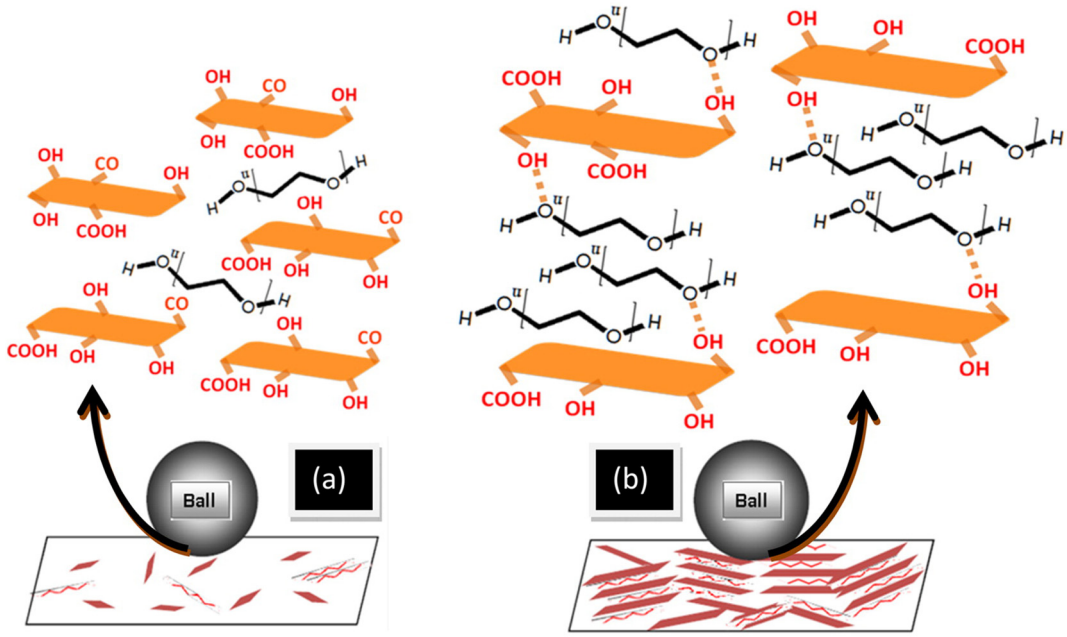

Fig. 17. Lubrication mechanism using (a) un-irradiated rGO with PEG, and (b) γ-irradiated rGO-PEG samples. Intercalated PEG molecules in rGO driven by hydrogen linkages facilitate the sliding between steel tribopair under tribo-stress. Reproduced with permission [143].

by reducing the friction and wear between steel tribo-pair. Besides the graphene, the anionic structure of ionic liquids also played a significant role and governed the lubrication properties. A tribo-induced thin film composed of Gr-ionic liquids and its tribo-chemical products with contact interfaces lubricated the sliding interfaces. The BScB anion-based Gr-ionic liquid hybrid exhibited the lowest friction, whereas oleate analogous showed the smallest wear [147]. Table 6 summarizes the preparation of chemically functionalized GO, rGO, and graphene along with their application as additives to various lubricating media for enhancement of tribological properties.

The intriguing properties of graphene-based materials, particularly high surface area, good thermal conductivity, low shear, and excellent mechanical strength, which are governed by their chemical and structural features, make them lubricious additives to liquid lubricants. The ultralow thickness of graphene-based materials, along with their good dispersibility, facilitates their uninterrupted supply to tribo-interfaces and forms the graphene-based thin film, which reduced the friction and wear. The high surface area of graphene covers the larger contact area of tribo-interfaces by stress-induced thin film formation. The graphene thin film prevents the direct contact of the sliding surfaces and eases the sliding because of interplanar low shear strength [211]. The graphene lamellae are surface-active, particularly under the tribo-stress, and deposited on the contact interfaces of tribopair [212]. The deposited graphene sheets not only facilitate the sliding along the basal plane of the graphene but also the deposited sheets furnish the slip with graphene lamellae in the liquid dispersion; as a result, it reduced the friction and protected the tribopair against the wear. The structural defects, wrinkles, surface functionalization, number of lamellae in graphene, roughness, and mechanical properties of tribo-interfaces, and interlamellar spacing in graphene-based materials influence the frictional properties [144,213–215]. Graphene effectively offers excellent anti-friction and antiwear properties. However, graphene is prone to agglomerate in lube oils because of cohesive interaction between their sheets, which adversely influences the frictional properties. The use of dispersant or chemical functionalization of graphene makes them nicely dispersed in variable lube base oil and effectively offers the inherent low frictional properties between the tribopair. The uninterrupted supply of chemically functionalized graphene to contact interfaces and formation of tribo-induced thin film facilitates the sliding because of low shear strength and avoiding direct contact between the tribo-interfaces, which result in significant improvement in lubrication properties.

The formation of graphene-based tribo thin-film governs by several factors viz. affinity of graphene with tribo-interfaces, applied load, the dosage of graphene in the lubricating fluid, dispersion stability, effect of other surface-active additives in the lube, structure and chemical composition of graphene, and so on. The wearing of materials under the tribo-stress forms the pristine surface of the metal, which is considered to attract the graphene nanosheets. The delaminated graphene sheets under the sheared contact are gradually deposited on the sliding interfaces. As the tribo-sliding goes on, the graphene nanosheets in the lubricants enter the contact interfaces and easily sheared with deposited graphene-based tribo thin-film and reduced the friction [195]. Biswas et al. have revealed that deposition and removal of molecular lamellae of such nanostructural layered materials-based tribo thin film on the sliding interfaces are continuous processes [216].

The microscopic mapping of contact interfaces by Raman spectroscopy suggested the heterogeneous nature of graphene-based tribo thin film on the contact interfaces. Fig. 19 explicitly revealed the discrete patches of the graphene-based thin film on the contact interfaces and also suggested the heterogeneity of graphene thin film within the individual patches, and it was attributed to the roughness of the tribo-interfaces and load distribution [126].

5.3. Graphene-based nanocomposites and hybrid materials as lubricant additive

Graphene-based nanocomposites and hybrid materials show rapid progress for their applications as a lubricant additive for enhancement of tribological properties. The synergistic effect among two or more components in the nanocomposites and hybrid materials along with their compatibility with lubricating media make them promising materials for lubricant applications. Chen et al. synthesized the supercritical CO_2-assisted metal nanoparticles (Au, Ni, Cu)-decorated-GO nanocomposites (Sc-M/GO) with regular size distribution (Au and Cu: 5–10 nm; Ni: <5 nm) of metal nanoparticles [217–219]. The Sc-Au/GO nanocomposite (0.1 wt%) as an additive to PAO lube base oil reduced the coefficient

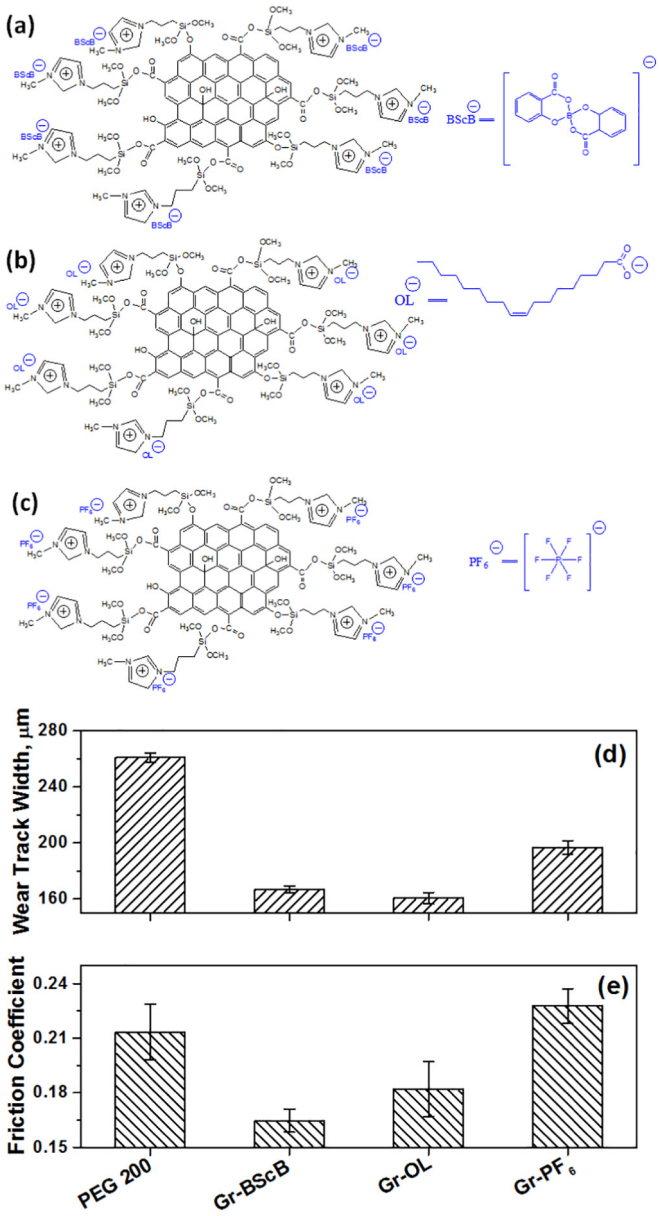

Fig. 18. Representative chemical structures of (a) Gr-BScB, (b) Gr-OL, and (c) Gr-PF_6 hybrid nanomaterials. (d) Wear track width and (e) average coefficient of friction of steel disc lubricated with PEG 200 and Gr-ILs hybrid nanomaterials (Gr-BScB, Gr-OL and Gr-PF_6) blend in the PEG 200 (Dose: 0.02 $mg.mL^{-1}$). Reproduced with permission [147].

of friction (33.6%) and wear rate (73%) between steel tribopair. The Sc-Au/GO nanocomposite in lubricating oil is believed to enter the contact interfaces and could eventually accumulate in pits/grooves; consequently, the contact surfaces became smooth and flat. The deposited Sc-Au/GO nanocomposite gradually covered the mating surfaces (Fig. 20) and avoided the direct contact between the friction pair, which is attributed for a significant reduction in friction and enhanced anti-wear ability. The GO nanosheets are exfoliated by Au nanoparticles under the tribo-stress and ease the interlamellar sliding, which can effectively reduce the friction in the boundary lubrication regime [217].

Recently, graphene-based composites with metal and metal oxide nanomaterials have attracted considerable attention because of their improved tribological properties, particularly under the boundary lubrication regime. The Cu and CuO as spherical nanoparticles and nanorods of variable aspect ratio, respectively, act as nano-bearings between the mating surfaces and furnish rolling-based mechanism to enhance the tribological properties [220,221]. The rGO-Cu nanocomposite with well-distributed Cu nanoparticles of 20 nm size as an additive to paraffin oil showed low friction and improved the load-bearing and antiwear properties compared to oil mixed with a blend of individuals Cu nanoparticles and rGO nanosheets [222]. The microscopic results based on worn surface analysis revealed the formation of a composite thin film which could prevent not only the direct contact between the mating surfaces but also bear the load. Moreover, the formation of nano-bearings between the contact interfaces contributes a significant role in the reduction of friction and wear. The oleic acid capped Cu/rGO nanocomposites as an additive (0.5 wt%) to PAO oil decreased the friction (45%) and wear (53%) between steel tribo-pair. The EDX results of lubricated surfaces revealed the formation of Cu/rGO nanocomposites-based tribo film, which improved the tribological properties [223]. The α-Fe_2O_3/GO nanocomposite could easily enter the contact zone between the mating surfaces and yielded a physical tribo thin film, which could bear the load and improve the antiwear property [224]. Therefore, α-Fe_2O_3/GO nanocomposite having α-Fe_2O_3 nanorods of 3–5 nm diameter and 15–30 nm length as an additive to paraffin oil exhibited a remarkable reduction in friction (64%) and improved the antiwear properties (76%). The enhanced tribological features were attributed to the combination of rolling effects and the formation of tribo thin films on the mating surfaces by α-Fe_2O_3/GO nanocomposite. The graphene decorated with ceria nanoparticles (CeO_2/Gr) as an additive to paraffin oil offers considerably improved antiwear properties under a high load condition [225]. The improved tribological properties by CeO_2/Gr nanocomposite were attributed to synergistic antiwear effect and friction reduction by CeO_2 nanoparticles and graphene sheets. The CeO_2 nanoparticles not only prevented the tribo-interfaces against the wear but also inhibited the restacking of graphene. Simultaneously graphene provides an ideal carrier to load the CeO_2 nanoparticles without aggregation. The LaF_3-GO hybrid as a lubricant additive to water enhanced the tribological properties by forming the protective tribochemical thin film over the contact interfaces of steel tribopair [226]. Table 7 summaries various types of graphene-based nanocomposites and hybrid materials as additives to lubricating media for enhancement of tribological properties. The contact geometry, the dosage of graphene-based nanocomposites, and lubricating media are outlined to understand their roles for improvement of tribological properties.

The MX_2 (M = Mo, W; X = S, Se), the dichalcogenides exhibit molecular lamellar structure, where the weak van der Waals interaction connects the MX_2 lamellae and furnish the intracrystalline slip under the sliding stress. As a result, MX_2 nanostructured layered materials are gaining increasing attention as lubricating materials for tribological applications [31,244,245]. The synergistic effects between MoS_2/$MoSe_2$ and graphene in their nanocomposites significantly improved the lubrication properties under boundary lubrication [231–233]. The nano-sized MoS_2 deposited on graphene could enter the contact zone of mating surfaces and formed the stable and durable boundary thin film, which reduced the friction and wear. The XPS of worn surfaces revealed the formation of tribo-induced thin film based on MoS_2/G nanocomposites [233]. The FeS_2(pyrite)/rGO nanocomposite prepared by hydrothermal method increased the load-bearing capacity of tribopair. The FeS_2/rGO as an additive to paraffin oil decreased the friction by ~67%. The improved tribological properties were attributed to the synergistic effects of rGO and FeS_2 layers (Fig. 21). The FeS_2/rGO composites not only filled the micro-gaps of mating surfaces but also formed a homogenous lubricating film under the high sliding contact pressure, which bears the high load, reduces the friction, and prevents the direct contacts between tribo-interfaces. Moreover, the delaminated FeS_2 sheets under the tribo-stress facilitate the sliding because of the planner structure of rGO sheets between the mating surfaces [234]. The grafting of polyacrylamide, polyacrylates, and polyaniline on GO not only improved the dispersibility in lubricating media but also enhanced the tribological properties [237–239]. Polyacrylamide-functionalized GO (FGO-PAM) prepared by microwave-assisted surface-initiated redox polymerization

Table 6
Lubrication enhancement by dispersion of chemically functionalized GO, rGO, and graphene as additives to various lubricating media. Contact geometry, dosage of graphene-based materials, and lubricating media are presented to understand their roles for enhancement of tribological properties.

No.	Preparation method/brief description	Additive	Lube medium	Additive dosage	Contact geometry	Friction reduction	Wear reduction	Reference
1	Selective grafting of alkylamines ($C_n = 8, 12, 18$) targeting carboxylic groups of GO via amide linkage using thionyl chloride as a coupling agent	Gr-ODA	Hexadecane	0.04–0.08 mg. mL^{-1}	Four-ball	26%	9% (wear scar diameter)	[10]
2	Functionalization of carboxylic groups-enriched rGO with octadecylamine via amide linkage using thionyl chloride as a coupling agent	rGO-ODA	10W40 oil	0.01–0.05 mg. mL^{-1}	Four-ball	36%	35% (wear scar diameter)	[144]
3	Simultaneous chemical reduction and surface functionalization of GO with octadecylamine targeting basal plane epoxide functionalities	GO-ODA	Paraffin oil	1 wt%	Pin/Ball-on-disk	~81%	–	[192]
4	Functionalization of basal plane functionalities (epoxide, hydroxyl) of GO surface with ODA	GO-ODA	10W40 oil	0.01–0.06 mg. mL^{-1}	Ball-on-disk	25%	25% (wear track width)	[195]
5	Selective grafting of oleic diethanolamide borate on carboxylic groups of GO surface using thionyl chloride as a coupling agent	GO-ODAB	SN-500 oil	0.01–0.04 wt%	Four-ball	38.4%	42.0% (wear scar diameter)	[196]
6	Surface functionalization of carboxylic groups with azidodecane via click chemistry using thionyl chloride as a coupling agent	GO-CuAAC	500 N oil	0.005–0.015 wt %	Four-ball	16%	30% (wear scar diameter)	[197]
7	γ-Radiolysis-based functionalization of rGO with poly (ethylene glycol)	rGO-PEG	PEG-200	0.02–2.0 mg. mL^{-1}	Ball-on-disk	38%	55% (wear scar)	[143]
8	Covalent grafting of amino-containing PEG onto the surface of carboxylated graphene using a toluene-2,4-diisocyanate bridging agent	Gr-PEG	Water	0.005–0.1 wt%	Ball-on-disk	58.2%	81.2% (wear rate)	[198]
9	The sulfonation of GO surface using 3-(trihydroxysilyl)-1-propane sulfonic acid followed by grafting of amino-terminated block copolymer	GO-F	Water	10–100 mg. mL^{-1}	Ball-on-disk	53%	91% (wear rate)	[199]
10	Graphene-ionic liquid-based hybrid prepared by sonication and stirring of graphene with ionic liquid	Gr-ILs	Ionic liquid	–	Ball-on-disk	~67%	–	[204]
11	Modified GO obtained by simultaneous reduction and functionalization of GO with imidazolium ionic liquids in presence of KOH	MGO-ILs	Multiple alkylated cyclopentane	0.1 wt%	Ball-on-disk	27%	74% (wear volume)	[146]
12	Commercially procured graphene was thoroughly blended with ionic liquid (octyl-3-methylimidazolium tetrafluoroborate)	Gr-IL	10W40 oil	0.005 wt%	Ball-on-disk	73%	–	[205]
13	Carboxylated rGO prepared by mild oxidation of rGO was used for selective grafting of ionic liquids based on covalent interaction	Gr-ILs	PEG-200	0.01–0.05 mg. mL^{-1}	Ball-on-disk	23%	38.5% (wear track width)	[147]
14	GO simultaneously reduced and functionalized with 3,5-di-tert-butyl-4-hydroxybenzaldehyde using (3-aminopropyl)trimethoxysilane as a chemical linker	Gr-DtBHBA	SN-150	0.2–0.8 mg. mL^{-1}	Four-ball	40%	17% (wear scar diameter)	[126]
15	Chemically rGO functionalized with oleic acid via heating the blend of rGO and oleic acid	rGO-OA	PAO 9	0.01–0.1.0 wt%	Four-ball	17%	14% (wear scar diameter)	[206]
16	Graphene refluxed with a mixture of stearic and oleic acids (mass ratio 3:5)	Gr-OA/SA	SN-350 oil	0.015–0.105 wt %	Four-ball	~35%	~64%	[207]
17	Surface functionalization of rGO with PEG 200	rGO-PEG	PEG-200	0.02–1.0 mg. mL^{-1}	Ball-on-disk	78%	50%	[208]
18	Commercially procured graphene modified with Nitrogen and ammonia plasma	Gr-N_2, Gr-NH_3	Polyolester oil	0.05 wt%	Cylinder-on-plate	–	94% counter body; 62% specimen	[209]
19	Superhigh-exfoliation reduced graphene oxide prepared by thermal reduction of GO with the activation of KOH	SRGO	Base oil	0.1–1.5 wt%	Ball-on-disk	70%	60% wear volume	[210]

of acrylamide with functionalized of GO showed excellent dispersibility in water, and substantially improved the antiwear properties (37%) and decreased the friction (55%) [237].

The composite of GO with carboxylic-functionalized carbon nanotube (GO/MWCNTs–COOH), as an aqueous-based additive improved the lubrication performance between the steel tribopair [246]. As demonstrated in Fig. 22, the GO lamellas could easily delaminate because of shear force between the mating surfaces and transferred to contact interfaces. The deposited GO nanosheets prevent the direct contact between the steel balls and bear the load to reduce the friction. Besides, the MWCNTs–COOH in composite material functions as micro-bearing to convert sliding friction into rolling friction between the mating bodies. The synergistic effects extended by GO/MWCNTs–COOH composite under the tribo-stress promises its potential not only for aqueous-based lubrication but also open new directions for designing of novel hybrid materials and composites for tribological applications. The ZnO-decorated rGO/MoS_2 (Gr-MS-Zn) hybrid as an additive to engine oil improved the tribological performance by significant reduction of wear volume (87%) and the friction (37%). The enhanced lubrication performance was attributed to low shear strength, arising from weak interfacial interaction between the incommensurately stacked graphene and MoS_2 and their uninterrupted supply to tribo-interfaces because of stable dispersion [247].

6. Summary and outlook

Remarkable mechanical, electronic, optical, and structural properties of graphene has propelled enormous interest for fundamental studies to a diversified range of applications. The weak van der Waals interaction between atomic-thick lamellae of graphene, excellent mechanical strength, remarkable thermal conductivity, and high surface area make graphene a potential candidate for tribological applications to reduce the friction and wear of engineering surfaces. Over the recent past, the use of graphene, chemically-functionalized graphene, and

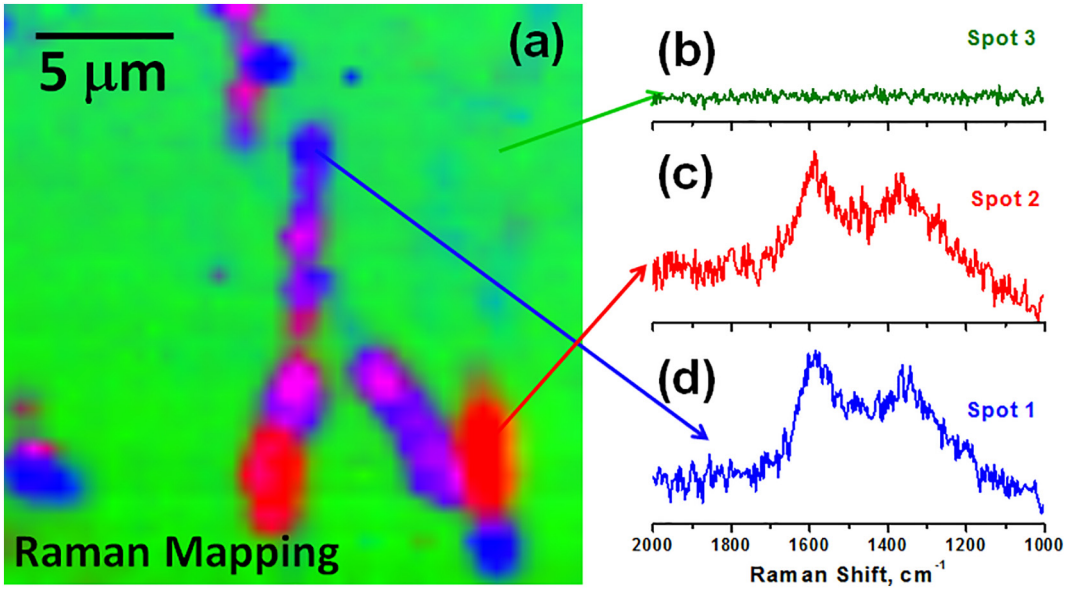

Fig. 19. (a) Raman mapping of the worn scar on the steel ball after the lubrication test using chemically-functionalized graphene blended in the SN-150 mineral lube base oil. The Raman spectra corresponding to different colour pixels in the Raman map revealed the heterogeneity of graphene-based thin film deposition on the worn scar. (b) Raman spectrum shows no signature of D and G bands. (c–d) The red and blue patches exhibit D and G bands, signifying the deposition of graphene. Reproduced with permission [126]. (For interpretation of the references to colour in this figure legend, the reader is referred to the web version of this article.)

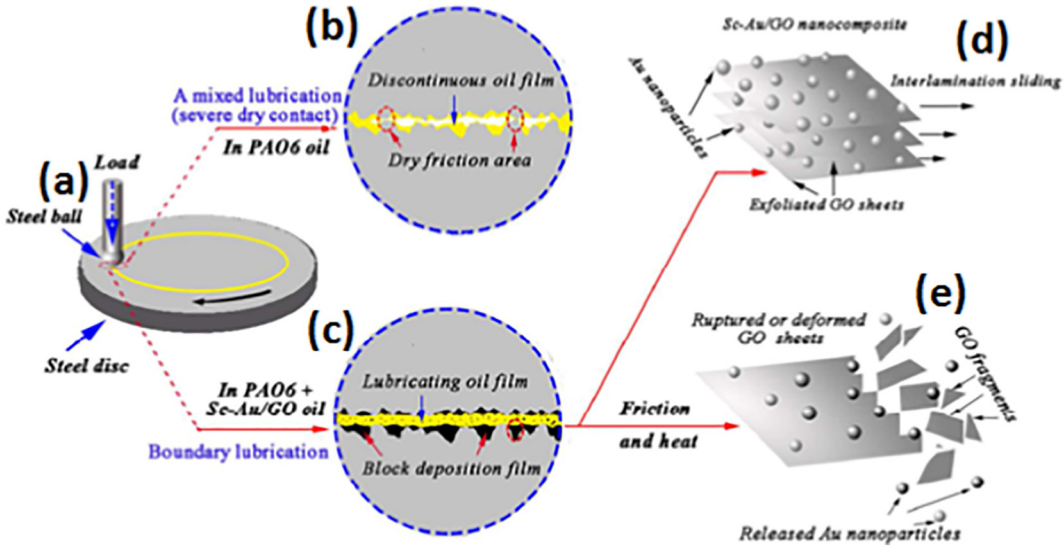

Fig. 20. Schematic demonstration of (a) sliding contact geometry and plausible lubrication model using (b) PAO6 oil and (c) Sc-Au/GO nanocomposite in PAO6 lubricating oil. (d) The interplanar sliding by Sc-Au/GO nanocomposite under the tribo-stress improved tribological properties between the mating surfaces. (e) Some of the GO sheets may ruptured by friction force and the Au nanoparticles are exposed and released. Reproduced with permission [217].

graphene-based composites as additives to variable lubricating medium has increased exponentially. Although graphene-based materials furnish significantly improved tribological properties of variable lubricants, however, their long-term dispersibility has been an important challenge for applications in the mainstream of industrial lubricants. Herein, a thorough and critical review on preparation, structural models, and dispersibility of graphene, GO, rGO, chemically-functionalized graphene, and graphene-based composites are presented. The functionalization and stabilization of GO, rGO, and graphene by variable chemical and physical approaches are discussed for enhancement of their dispersion in water, organic solvents, and variable lube oils. The dispersion of graphene-based materials in aqueous, organic solvents and lubricating oils are found to be governed by variable interactive forces viz. the van der Waals interaction, π-π interaction, charge induced interaction, Coulombic interaction, and so on.

The graphene, GO, rGO, chemically-functionalized graphene, and graphene-based composites as additive to lubricating media including water and industrial lube oils furnish significantly improved tribological properties by reducing the friction, protecting the contact interfaces against the undesirable events of wear, dissipating the heat from tribo-interfaces, and mitigating the corrosion by forming the protecting thin film. The weak van der Waals interaction between graphene lamellae provide low-resistance to shear and facilitate the sliding events, consequently lowering of the

Table 7
Lubrication enhancement by graphene-based nanocomposites as additives to various lubricating media. The contact geometry, dosage, and lubricating media are presented to understand their roles for enhancement of tribological properties.

No.	Preparation method/brief description	Additive	Lube medium	Additive dosage	Contact geometry	Friction reduction	Wear reduction	Reference
1	Supercritical CO_2-assisted deposition of Au nanoparticles on GO nanosheets	Sc-Au/GO	PAO6	0.1 wt%	Ball-on-disk	33.6%	72.8% wear rate	[217]
2	Supercritical CO_2-assisted deposition of Ni nanoparticles on GO nanosheets	Sc-Ni/GO	Paraffin oil	0.08 wt%	Four-ball	32%	42% wear scar diameter	[218]
3	Supercritical CO_2-assisted deposition of Cu nanoparticles on GO nanosheets	Sc-Cu/GO	Paraffin oil	0.05 wt%	Four-ball	27%	52.7% wear scar diameter	[219]
4	rGO-Cu nanocomposite prepared by chemical reduction of $CuSO_4$ and GO dispersion	rGO-Cu	Liquid paraffin	0.5 wt%	Ball-plate	~56%	78% wear scar diameter	[222]
5	Oleic acid capped Cu/rGO composite prepared by single-step chemical reduction of $CuSO_4$ and GO using hydrazine hydrate	Cu/rGO	PAO	0.5 wt%	Four-ball	45%	53% wear scar diameter	[223]
6	Decoration of α-Fe_2O_3 nanorods on GO nanosheets by a facile hydrolysis route	α-Fe_2O_3/GO composites	Paraffin oil	0.5 wt%	Ball-plate	~64%	~76% wear scar diameter	[224]
7	Cubic fluorite ceria decorated graphene prepared by hydrothermal reduction of GO and $Ce(NO_3)_3$	CeO_2/Gr	Paraffin oil	0.06 wt%	Ball-disc	47.6%	98.5% wear rate	[225]
8	LaF_3 nanoparticles-decorated GO prepared by a solution-processed chemical approach using ammonium fluoride and lanthanum nitrate in GO dispersion	LaF_3-GO	Water	1.5 wt%	Four-ball	24%	19% wear scar diameter	[226]
9	rGO/ZrO_2 nanocomposite prepared by hydrothermal reduction of $ZrOCl_2$ and GO using hydrazine hydrate reducing agent	rGO/ZrO_2	Paraffin oil	0.06 wt%	Ball-disc	56%	88% wear rate	[227]
10	Boehmite/GO nano-hybrid prepared by covalent coupling between GO and 3-glycidoxypropyl-trimethoxysilane functionalized boehmite	GO-GPTS-AlOOH	VHVI8 Lube oil	0.03 mg. mL^{-1}	Ball-disk Four-ball	14% (Ball-disk)	28% wear scar diameter	[228]
11	Cu impregnated multi-layer graphene prepared by ultrasound-assisted processing of ammonicaldispersion of GO with $[Cu(NH_3)_4]SO_4$; followed by calcination of resultant product at 400 °C	MLG-Cu	Engine oil	0.5–2.0 wt%	Block-ring	43%	63%, wear scar volume	[229]
12	Calcium borate/GO composites synthesized by hydrothermal processing of borax, calcium nitrate, and graphene oxide	CB/GO	PAO	0.5–2.0 wt%	Four-ball	48%	52% wear scar diameter	[230]
13	Nanocomposite of chemically functionalized GO with MoS_2	FrGO-MoS_2	Group II 500 N oil	0.8 wt%	Four-ball	15.8%	29% wear scar diameter	[231]
14	Hydrothermal synthesis of $MoSe_2$ nanoflowers on rGO	$MoSe_2$/rGO	Paraffin oil	0.2–5.0 wt%	Ball-plate	~40%	75% wear width	[232]
15	Nanosized MoS_2 deposited graphene prepared by chemical processing of $(NH_4)_2MoS_4$ and graphene dispersion followed by annealing at 800 °C	MoS_2/Gr	PAG	0.1–0.5 wt%	Ball-disk	30%	94% wear volume	[233]
16	FeS_2(pyrite)/rGO prepared by hydrothermal method using the solution-processed product of $FeCl_2$, NaOH, polyvinylpyrrolidone, and sulfur powder in GO dispersion	FeS_2/rGO	Paraffin oil	7.0 wt%	Ball-disk	~67%	–	[234]
17	Phosphorus–graphene hybrid prepared by ball-milling of graphene and red phosphorus	P-Gr	PAG	1.0 wt%	Ball-disc	12%	98% wear volume	[235]
18	TiO_2-reinforced boron and nitrogen co-doped microwave-induced reduced graphene oxide	TiO_2-B-N-MRG	Paraffin oil	0.15%*w*/*v*	Four-ball	25.4%	50.9% wear scar diameter	[236]
19	Polyacrylamide-grafted-functionalized GO prepared by microwave-assisted surface-initiated redox polymerization of acrylamide with functionalized GO	FGO-PAM	Water	0.8 wt%	Four-ball	55%	37% wear scar diameter	[237]
20	GO-poly(C_n-acrylate) nanocomposites prepared by surface-initiated atom transfer radical polymerization	GOPA18	Polyol	0.04 mg. mL^{-1}	Four-ball	42%	34% wear scar diameter	[238]
21	PANI–GO hybrid prepared by pressure-assisted processing of chemical processing of aniline and GO	PANI-GO	Paraffin oil	0.012 wt%	Four-ball	44%	18% wear scar diameter	[239]
22	ZnO@graphene core-shell prepared by coating of graphene on ZnO nanoparticle via amine linker	ZnO@graphene	SparkM 40 Base oil	0.25–2 wt%	Four-ball	35%	40% wear scar diameter	[240]
23	Ag/graphene nanocomposite prepared by one-step laser irradiation strategy	L-Ag/rGO	Liquid paraffin	0.1 wt%	Four-ball	40%	36% wear spot diameter	[241]
24	Trihexyltetradecylphosphonium bis(2-ethylhexyl) phosphate modified graphene gel prepared by a simple mechanical grinding method	[P66614] [DEHP]-G	150 N Base oil	0.25–0.75 wt %	Ball-plate	–	85% wear volume	[242]
25	Ultrasound-assisted blending of 2D *h*-BN particles and the 3D graphene nanoflakes	2D *h*-BN/3D graphene	PAO4 oil	0.01–3 wt%	Ball-Sheet	32%	63% wear rate	[243]

friction. The microscopic and spectroscopic analyses of lubricated surfaces and worn scars revealed the formation of a graphene-based protective thin film on the contact interfaces under the tribo-stress, which minimizes the wear. The formation of graphene-based tribo thin-film governs by several factors viz. affinity of graphene with tribo-interfaces, applied load, the dosage of graphene in the lubricating fluid, dispersion stability, effect of

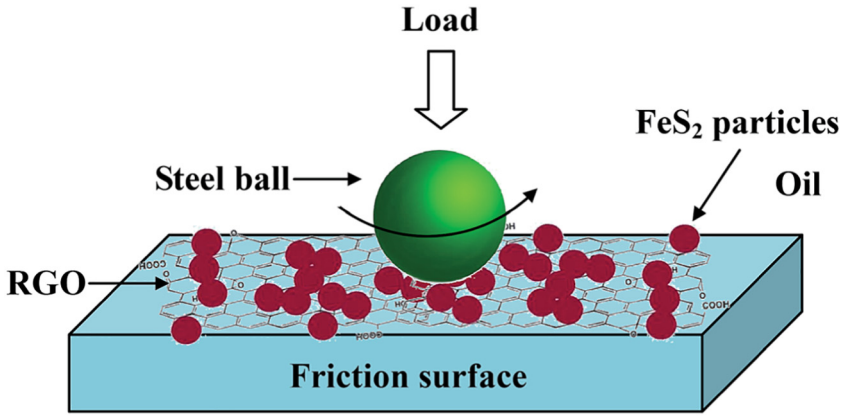

Fig. 21. Lubrication mechanism demonstrating the role of FeS_2/rGO heterojunction under the tribo-stress for a reduction in friction and wear. Reproduced with permission [234].

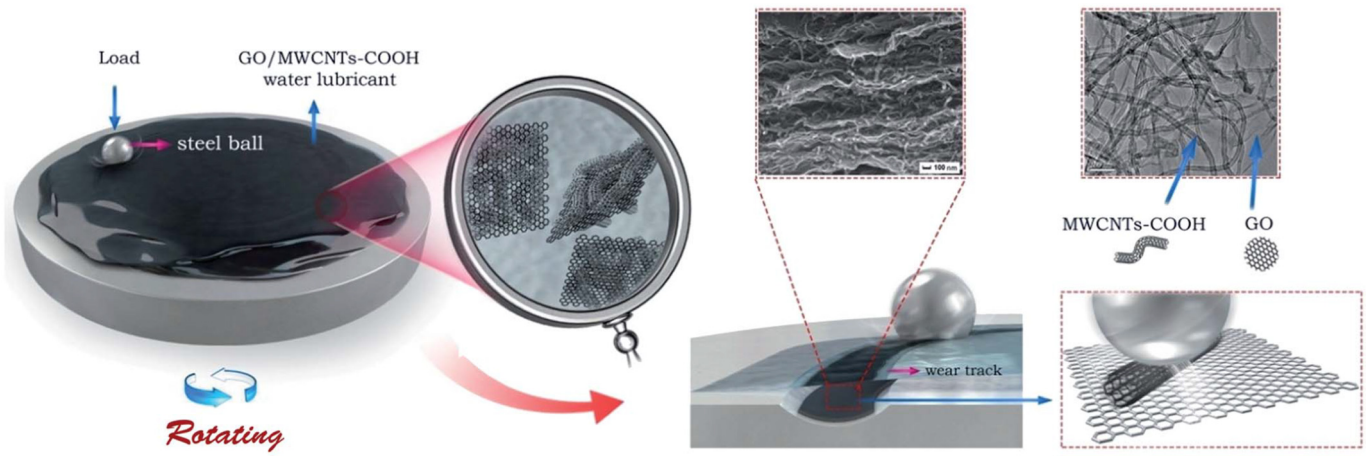

Fig. 22. Lubrication mechanism of GO/MWCNTs–COOH hybrid as an additive to water under the sliding contact between the steel tribopair. Reproduced with permission [246].

other surface-active additives in the lube, structure and chemical composition of graphene, and so on.

The fundamental and laboratory-scale experiments promise the potential of graphene-based materials as new generation additive for enhancement of tribological properties of industrial lubricants such as engine oils, cutting fluids, metal-finishing, and hydraulic oils. Nonetheless, it carries several challenges before graphene-based additives can be used for mainstream industrial lubricants. Over the last decade, several efforts have been directed for functionalization and stabilization of graphene-based materials to achieve long-term stable dispersion in the lubricating media. However, the poor dispersibility of graphene-based materials, particularly, under the high temperature and pressure (unavoidable under tribo-experiments) promotes the agglomeration and compromises the tribo-performance. The role of graphene in the formation of the tribo-thin film under variable tribo-stress and the lubrication mechanism including the interaction of graphene with variable tribo-interfaces are yet to be understood precisely, which is very important to design the contact interfaces and dosage of graphene in industrial lubes. The findings to these major challenges through scientific interventions can make graphene-based materials as novel additives for industrial lubricants.

Declaration of Competing Interest

The authors declare that they have no known competing financial interests or personal relationships that could have appeared to influence the work reported in this paper.

Acknowledgement

Authors are thankful to CSIR, Govt. of India for financial support (CSC-118). AC is grateful to UGC, Govt. of India for the fellowship support.

References

[1] Geim AK, Novoselov KS. The rise of graphene. Nat Mater 2007;6:183–91.
[2] Geim AK. Graphene: status and prospects. Science 2009;324:1530–4.
[3] Stoller MD, Park S, Zhu Y, An J, Ruoff RS. Graphene-based ultracapacitors. Nano Lett 2008;8:3498–502.
[4] Lee C, Wei X, Kysar JW, Hone J. Measurement of the elastic properties and intrinsic strength of monolayer graphene. Science 2012;321:385–8.
[5] Balandin AA, Ghosh S, Bao W, Calizo I, Teweldebrhan D, Miao F, et al. Superior thermal conductivity of single-layer graphene. Nano Lett 2008;8:902–7.
[6] Lee C, Li Q, Kalb W, Liu XZ, Berger H, Carpick RW, et al. Frictional characteristics of atomically thin sheets. Science 2010;328:76–80.
[7] Egberts P, Han GH, Liu XZ, Johnson ATC, Carpick RW. Frictional behavior of atomically thin Islands grown on copper by chemical vapor deposition. ACS Nano 2014;8:5010–21.
[8] Li S, Li Q, Robert W. The evolving quality of frictional contact with graphene. Nature 2016;539:541.
[9] Berman D, Erdemir A, Sumant AV. Graphene: a new emerging lubricant. Mater Today 2014;17:31–42.
[10] Choudhary S, Mungse HP, Khatri OP. Dispersion of alkylated graphene in organic solvents and its potential for lubrication applications. J Mater Chem 2012;22:21032–9.
[11] Kim KS, Lee HJ, Lee C, Lee SK, Jang H, Ahn JH, et al. Chemical vapor deposition-grown graphene: the thinnest solid lubricant. ACS Nano 2011;5:5107–14.

[12] Berman D, Deshmukh SA, Sankaranarayanan SKRS, Erdemir A, Sumant AV. Extraordinary macroscale wear resistance of one atom thick graphene layer. Adv Funct Mater 2014;24:6640–6.
[13] Bunch JS, Verbridge SS, Alden JS, Van Der Zande AM, Parpia JM, Craighead HG, et al. Impermeable atomic membranes from graphene sheets. Nano Lett 2008;8:2458–62.
[14] Paul G, Hirani H, Kuila T, Murmu NC. Nanolubricants dispersed with graphene and its derivatives: an assessment and review of the tribological performance. Nanoscale 2019;11:3458–83.
[15] Rasheed AK, Khalid M, Rashmi W, Gupta TCSM, Chan A. Graphene based nanofluids and nanolubricants – review of recent developments. Renew Sustain Energy Rev 2016;63:346–62.
[16] Fontaras G, Samaras Z. On the way to 130 g CO 2/km — estimating the future characteristics of the average European passenger car. Energy Policy 2010;38:1826–33.
[17] Ryan L, Ferreira S, Convery F. The impact of fiscal and other measures on new passenger car sales and CO 2 emissions intensity: evidence from Europe. Energy Econ 2009;31:365–74.
[18] Holmberg K, Andersson P, Erdemir A. Global energy consumption due to friction in passenger cars. Tribol Int 2012;47:221–34.
[19] Holmberg K, Erdemir A. Global impact of friction on energy consumption, economy and environment. FME Trans 2015;43:181–5.
[20] Rudnick LR. Lubricant additives: chemistry and applications. . 2nd ed.CRC Press; 2009.
[21] Cisson CM, Rausina GA, Stonebraker MP. Human health and environmental hazard characterisation of lubricating oil additives. Lubr Sci 1996;8:145–77.
[22] Rokosz MJ, Chen AE, Lowe-Ma CK, Kucherov AV, Benson D, Paputa Peck MC, et al. Characterization of phosphorus-poisoned automotive exhaust catalysts. Appl Catal Environ 2001;33:205–15.
[23] Rapoport L, Fleischer N, Tenne R. Fullerene-like WS2 nanoparticles: superior lubricants for harsh conditions. Adv Mater 2003;15:651–5.
[24] Bertolazzi S, Brivio J, Kis A. Stretching and breaking of ultrathin MoS2. ACS Nano 2011;5:9703–9.
[25] Liu K, Yan Q, Chen M, Fan W, Sun Y, Suh J, et al. Elastic properties of chemical-vapor-deposited monolayer MoS2, WS2, and their bilayer heterostructures. Nano Lett 2014;14:5097–103.
[26] Falin A, Cai Q, Santos EJG, Scullion D, Qian D, Zhang R, et al. Mechanical properties of atomically thin boron nitride and the role of interlayer interactions. Nat Commun 2017;8:1–9.
[27] Cai Q, Scullion D, Gan W, Falin A, Zhang S, Watanabe K, et al. High thermal conductivity of high-quality monolayer boron nitride and its thermal expansion. Sci Adv 2019;5:1–9.
[28] Drummond C, Alcantar N, Israelachvili J, Tenne R, Golan Y. Microtribology and friction-induced material transfer in WS2 nanoparticle additives. Adv Funct Mater 2001;11:348–54.
[29] Zhao Y, Luo X, Li H, Zhang J, Araujo PT, Gan CK, et al. Interlayer breathing and shear modes in few-trilayer MoS2 and WSe2. Nano Lett 2013;13:1007–15.
[30] Kumari S, Sharma OP, Gusain R, Mungse HP, Kukrety A, Kumar N, et al. Alkyl-chain-grafted hexagonal boron nitride nanoplatelets as oil-dispersible additives for friction and wear reduction. ACS Aplied Mater Interfaces 2015;7:3708–16.
[31] Kumari S, Mungse HP, Gusain R, Kumar N, Sugimura H, Khatri OP. Octadecanethiol-grafted molybdenum disulfide nanosheets as oil-dispersible additive for reduction of friction and wear. FlatChem 2017;3:16–25.
[32] Georgakilas V, Tiwari JN, Kemp KC, Perman JA, Bourlinos AB, Kim KS, et al. Noncovalent functionalization of graphene and graphene oxide for energy materials, biosensing, catalytic, and biomedical applications. Chem Rev 2016;116:5464–519.
[33] Gong X, Liu G, Li Y, Yu DYW, Teoh WY. Functionalized-graphene composites: fabrication and applications in sustainable energy and environment. Chem Mater 2016;28:8082–118.
[34] Sun Z, James DK, Tour JM. Graphene chemistry: synthesis and manipulation. J Phys Chem Lett 2011;2:2425–32.
[35] Szabo T, Berkesi O, Forgo P, Josepovits K, Sanakis Y, Petridis D, et al. Evolution of surface functional groups in a series of progressively oxidized graphite oxides. Chem Mater 2006;18:2740–9.
[36] Cai W, Piner RD, Stadermann FJ, Park S, Shaibat MA, Ishii Y, et al. Synthesis and solid-state NMR structural characterization of 13C-labeled graphite oxide. Science 2008;321:1815–7.
[37] Choudhary S, Mungse HP, Khatri OP. Hydrothermal deoxygenation of graphene oxide: chemical and structural evolution. Chem An Asian J 2013;8:2070–8.
[38] Brodie BC. On the atomic weight of graphite. Philos Trans R Soc Lond A 1859;149:249–59.
[39] Staudenmaier L. Verfahren zur darstellung der graphitsäure. Ber Der Dtsch Chem Ges 1898;31:1481–7.
[40] Hummers Jr William S, Offeman RE. Preparation of graphitic oxide. J Am Chem Soc 1958;80:1339.
[41] Marcano DC, Kosynkin DV, Berlin JM, Sinitskii A, Sun Z, Slesarev A, et al. Improved synthesis of graphene oxide. ACS Nano 2010;4:4806–14.
[42] Park S, Ruoff RS. Chemical methods for the production of graphenes. Nat Nanotechnol 2009;4:217.
[43] Dreyer DR, Park S, Bielawski W, Ruoff RS. The chemistry of graphene oxide. Chem Soc Rev 2010;39:228–40.
[44] Hofmann U, Holst R. Uber die saurenatur und die methylierung von graphitoxyd. Ber Der Dtsch Chem Ges 1939;72:754–71.
[45] Von Ruess G. Uber das graphitoxyhydroxyd (graphitoxyd). Monatsh Für Chem Verwandte Teile Anderer Wissenschaften 1947;76:381–417.
[46] Scholz VW, Boeh HP. Untersuchungen am graphitoxid. VI. Betrachtungen zur struktur des graphitoxids. Z Für Anorg Allg Chem 1969;236:327–40.
[47] Nakajima T, Mabuchi A, Hagiwara R. A new structure model of graphite oxide. Carbon 1988;26:357–61.
[48] Lerf A, He H, Forster M, Klinowski J. Structure of graphite oxide revisited. J Phys Chem B 1998;102:4477–82.
[49] Erickson BK, Erni R, Lee Z, Alem N, Gannett W, Zettl A. Determination of the local chemical structure of graphene oxide and reduced graphene oxide. Adv Mater 2010;22:4467–72.
[50] Boukhvalov DW, Katsnelson MI. Modeling of graphite oxide. J Am Chem Soc 2008;130:10697–701.
[51] Gao W, Alemany LB, Ci L, Ajayan PM. New insights into the structure and reduction of graphite oxide. Nat Chem 2009;1:403.
[52] Paredes JI, Marti A, Tasco JMD, Martı A. Graphene oxide dispersions in organic solvents. Langmuir 2008;24:10560–4.
[53] Yi M, Shen Z. A review on mechanical exfoliation for scalable production of graphene. J Mater Chem A 2015;3:11700–15.
[54] Kosynkin DV, Higginbotham AL, Sinitskii A, Lomeda JR, Dimiev A, Price BK, et al. Longitudinal unzipping of carbon nanotubes to form graphene nanoribbons. Nature 2009;458:872.
[55] Novoselov KS, Geim AK, Morozov SV, Jiang D, Zhang Y, Dubonos SV, et al. Electric field effect in atomically thin carbon films. Science 2004;306:666–9.
[56] Sutter P. Epitaxial graphene: how silicon leaves the scene. Nat Mater 2009;8:171.
[57] Sutter PW, Flege J, Sutter EA. Epitaxial graphene on ruthenium. Sci Mater 2008;7:406.
[58] Edwards RS, Coleman KS. Graphene film growth on polycrystalline metals. Acc Chem Res 2012;46:23–30.
[59] Ciesielski A, Samorì P. Graphene via sonication assisted liquid-phase exfoliation. Chem Soc Rev 2014;43:381–98.
[60] Hernandez Y, Nicolosi V, Lotya M, Blighe FM, Sun Z, De S, et al. High-yield production of graphene by liquid-phase exfoliation of graphite. Nat Nanotechnol 2008;3:563.
[61] Mungse HP, Sharma OP, Sugimura H, Khatri OP. Hydrothermal deoxygenation of graphene oxide in sub- and supercritical water. RSC Adv 2014;4:22589–95.
[62] Stankovich S, Dikin DA, Piner RD, Kohlhaas KA, Kleinhammes A, Jia Y, et al. Synthesis of graphene-based nanosheets via chemical reduction of exfoliated graphite oxide. Carbon 2007;45:1558–65.
[63] Pei S, Cheng HM. The reduction of graphene oxide. Carbon 2012;50:3210–28.
[64] Chua CK, Pumera M. Chemical reduction of graphene oxide: a synthetic chemistry viewpoint. Chem Soc Rev 2014;43:291–312.
[65] Zhang J, Yang H, Shen G, Cheng P. Reduction of graphene oxide via L -ascorbic acid. Chem Commun 2010;46:1112–4.
[66] Chen D, Li L, Guo L. An environment-friendly preparation of reduced graphene oxide nanosheets via amino acid. Nanotechnology 2011;22:325601.
[67] Wang Y, Shi ZX, Yin J. Facile synthesis of soluble graphene via a green reduction of graphene oxide in tea solution and its biocomposites. ACS Appl Mater Interfaces 2011;3:1127–33.
[68] Kuila T, Bose S, Khanra P, Kumar A. A green approach for the reduction of graphene oxide by wild carrot root. Carbon 2012;50:914–21.
[69] Abdelsayed V, Moussa S, Hassan HM, Aluri HS, Collinson MM, El-shall MS. Photothermal deoxygenation of graphite oxide with laser excitation in solution and graphene-aided increase in water temperature. J Phys Chem Lett 2010;1:2804–9.
[70] Larciprete R, Fabris S, Sun T, Lacovig P, Baraldi A, Lizzit S. Dual path mechanism in the thermal reduction of graphene oxide. J Am Chem Soc 2011;133:17315–21.
[71] Guo H, Wang X, Qian Q, Wang F, Xia X. A green approach to the synthesis of graphene nanosheets. ACS Nano 2009;3:2653–9.
[72] Bianco A, Cheng HM, Enoki T, Gogotsi Y, Hurt RH, Koratkar N, et al. All in the graphene family – a recommended nomenclature for two-dimensional carbon materials. Carbon 2013;65:1–6.
[73] Gadgil B, Damlin P, Kvarnström C. Graphene vs. reduced graphene oxide: a comparative study of graphene-based nanoplatforms on electrochromic switching kinetics. Carbon 2016;96:377–81.
[74] Elias DC, Nair RR, Mohiuddin TMG, Morozov SV, Blake P, Halsall MP, et al. Control of graphene's properties by reversible hydrogenation: evidence for graphane. Science 2009;323:610–3.
[75] Fu Q, Bao X. Surface chemistry and catalysis confined under two-dimensional materials. Chem Soc Rev 2017;46:1842–74.
[76] Machado BF, Serp P, Machado BF. Graphene-based materials for catalysis. Cat Sci Technol 2012;2:54–75.
[77] Mungse HP, Verma S, Kumar N, Sain B, Khatri OP. Grafting of oxo-vanadium Schiff base on graphene nanosheets and its catalytic activity for the oxidation of alcohols. J Mater Chem 2012;22:5427–33.
[78] Verma S, Mungse HP, Kumar N, Choudhary S, Jain SL, Sain B, et al. Graphene oxide: an efficient and reusable carbocatalyst for Aza-Michael addition of amines to activated alkenes. Chem Commun 2011;47:12673–5.
[79] Zhang N, Zhang Y, Xu Y. Recent progress on graphene-based photocatalysts: current status and future perspectives. Nanoscale 2012;4:5792–813.
[80] Xiang Q, Yu J, Jaroniec M. Graphene-based semiconductor photocatalysts. Chem Soc Rev 2012;41:782–96.
[81] Kong X-K, Chen C-L, Chen Q-W. Doped graphene for metal-free catalysis. Chem Soc Rev 2014;43:2841–57.
[82] Xia BY, Yan Y, Wang X, Wen X, Lou D. Recent progress on graphene-based hybrid electrocatalysts. Mater Horizons 2014;1:379–99.
[83] Kumar P, Boukherroub R, Shankar K. Sunlight-driven water-splitting using two dimensional carbon based semiconductors. J Mater Chem A 2018;6:12876–931.

[84] Guo D, Shibuya R, Akiba C, Saji S, Kondo T, Nakamura J. Active sites of nitrogen-doped carbon materials for oxygen reduction reaction clarified using model catalysts. Science 2016;351:361–6.
[85] Kumar P, Mungse HP, Khatri OP, Jain SL. Nitrogen-doped graphene-supported copper complex: a novel photocatalyst for CO2 reduction under visible light irradiation. RSC Adv 2015;5:54929–35.
[86] Zhao G, Li X, Huang M, Zhen Z, Zhong Y, Chen Q, et al. The physics and chemistry of graphene-on-surfaces. Chem Soc Rev 2017;46:4417–49.
[87] Loh KP, Bao Q, Ang PK, Yang J. The chemistry of graphene. J Mater Chem 2010;20: 2277–89.
[88] Wang J-N, Zhang Y-L, Liu Y, Zheng W, Leeb LP, Suna H-B. Recent developments in superhydrophobic graphene and graphene-related materials: from preparation to potential applications. Nanoscale 2015;7:7101–14.
[89] Paredes JI, Villar-Rodil S, Martınez-Alonso A, Tascon JMD. Graphene oxide dispersions in organic solvents. Langmuir 2008;24:10560–4.
[90] Konios D, Stylianakis MM, Stratakis E, Kymakis E. Dispersion behaviour of graphene oxide and reduced graphene oxide. J Colloid Interface Sci 2014;430:108–12.
[91] Park S, An J, Jung I, Piner RD, An SJ, Li X, et al. Colloidal suspensions of highly reduced graphene oxide in a wide variety of organic solvents. Nano Lett 2009;9: 1593–7.
[92] Hamilton CE, Lomeda JR, Sun Z, Tour JM, Barron AR. High-yield organic dispersions of unfunctionalized graphene. Nano Lett 2009;9:3460–2.
[93] Khan U, Porwal H, O'Neill A, Nawaz K, May P, Coleman JN. Solvent-exfoliated graphene at extremely high concentration. Langmuir 2011;27:9077–82.
[94] O'Neill A, Khan U, Nirmalraj PN, Boland J, Coleman JN. Graphene dispersion and exfoliation in low boiling point solvents. J Phys Chem C 2011;115:5422–8.
[95] Wang H, Lu S, Zhang Y, Lan F, Lu X, Xiang Y. Pristine graphene dispersion in solvents and its application as a catalyst support: a combined theoretical and experimental study. J Mater Chem A 2015;3:6282–5.
[96] Villar-Rodil S, Paredes JI, Martínez-Alonso A, Tascón JMD. Preparation of graphene dispersions and graphene-polymer composites in organic media. J Mater Chem 2009;19:3591–3.
[97] Zhou D, Cheng QY, Han BH. Solvothermal synthesis of homogeneous graphene dispersion with high concentration. Carbon 2011;49:3920–7.
[98] Xu L, McGraw JW, Gao F, Grundy M, Ye Z, Gu Z, et al. Production of high-concentration graphene dispersions in low-boiling-point organic solvents by liquid-phase noncovalent exfoliation of graphite with a hyperbranched polyethylene and formation of graphene/ethylene copolymer composites. J Phys Chem C 2013;117:10730–42.
[99] Pu NW, Wang CA, Liu YM, Sung Y, Wang DS, Der Ger M. Dispersion of graphene in aqueous solutions with different types of surfactants and the production of graphene films by spray or drop coating. J Taiwan Inst Chem Eng 2012;43:140–6.
[100] Liang Y, Wu D, Feng X, Müllen K. Dispersion of graphene sheets in organic solvent supported by ionic interactions. Adv Mater 2009;21:1679–83.
[101] Zhang L, Zhang Z, He C, Dai L, Liu J, Wang L. Rationally designed surfactants for few-layered graphene exfoliation: ionic groups attached to electron-deficient π-conjugated unit through alkyl spacers. ACS Nano 2014;8:6663–70.
[102] Zhang X, Li X, Zhang S, Li Y, Wang D, Li H, et al. Cation-π-induced exfoliation of graphite by a zwitterionic polymeric dispersant for congo red adsorption. ACS Appl Nano Mater 2018;1:3878–85.
[103] Wang S, Wang C, Ji X, Lin M. Surfactant- and sonication- free exfoliation approach to aqueous graphene dispersion. Mater Lett 2018;217:67–70.
[104] Du H, Pang SD. Dispersion and stability of graphene nanoplatelet in water and its influence on cement composites. Construct Build Mater 2018;167:403–13.
[105] Samoilov VM, Danilov EA, Nikolaeva AV, Yerpuleva GA, Trofimova NN, Abramchuk SS, et al. Formation of graphene aqueous suspensions using fluorinated surfactant-assisted ultrasonication of pristine graphite. Carbon 2015;84:38–46.
[106] Ramalingam P, Pusuluri ST, Periasamy S, Veerabahu R, Kulandaivel J. Role of deoxy group on the high concentration of graphene in surfactant/water media. RSC Adv 2013;3:2369–78.
[107] Lotya M, King PJ, Khan U, De S, Coleman JN. High-concentration, surfactant-stabilized graphene dispersions. ACS Nano 2010;4:3155–62. https://doi.org/10.1021/nn1005304.
[108] Sun Z, Masa J, Liu Z, Schuhmann W, Muhler M. Highly concentrated aqueous dispersions of graphene exfoliated by sodium taurodeoxycholate: dispersion behavior and potential application as a catalyst support for the oxygen-reduction reaction. Chem A Eur J 2012;18:6972–8.
[109] Liu G, Komatsu N. Efficient and scalable production of 2D material dispersions using hexahydroxytriphenylene as a versatile exfoliant and dispersant. ChemPhysChem 2016;17:1557–67.
[110] Cui J, Song Z, Xin L, Zhao S, Yan Y, Liu G. Exfoliation of graphite to few-layer graphene in aqueous media with vinylimidazole-based polymer as high-performance stabilizer. Carbon 2016;99:249–60.
[111] Lotya M, Hernandez Y, King PJ, Smith RJ, Nicolosi V, Karlsson LS, et al. Liquid phase production of graphene by exfoliation of graphite in surfactant/water solutions. J Am Chem Soc 2009;131:3611–20.
[112] Nuvoli D, Valentini L, Alzari V, Scognamillo S, Bon SB, Piccinini M, et al. High concentration few-layer graphene sheets obtained by liquid phase exfoliation of graphite in ionic liquid. J Mater Chem 2011;21:3428–31.
[113] Wang X, Fulvio PF, Baker GA, Veith GM, Unocic RR, Mahurin SM, et al. Direct exfoliation of natural graphite into micrometre size few layers graphene sheets using ionic liquids. Chem Commun 2010;46:4487–9.
[114] Pamies R, Avilés MD, Arias-Pardilla J, Espinosa T, Carrión FJ, Sanes J, et al. Antiwear performance of ionic liquid+graphene dispersions with anomalous viscosity-temperature behavior. Tribol Int 2018;122:200–9.
[115] Zhou X, Wu T, Ding K, Hu B, Hou M, Han B. Dispersion of graphene sheets in ionic liquid [bmim][PF6] stabilized by an ionic liquid polymer. Chem Commun 2010;46: 386–8.
[116] Sharma M, Mondal D, Singh N, Prasad K. Biomass derived solvents for the scalable production of single layered graphene from graphite. ChemComm 2016;52: 9074–7.
[117] Kim DW, Kim D, Min BH, Lee H, Jung HT. Sonication-free dispersion of large-area graphene oxide sheets using internal pressure from release of intercalated carbon dioxide. Carbon 2015;88:126–32.
[118] Si Y, Samulski E. Synthesis of water soluble graphene. Nano Lett 2008;8:1679–82.
[119] Zhao Y, Hu Z. Graphene in ionic liquids: collective van der waals interaction and hindrance of self-assembly pathway. J Phys Chem B 2013;117:10540–7.
[120] Gao H, Zhang S, Lu F, Jia H, Zheng L. Aqueous dispersion of graphene sheets stabilized by ionic liquid-based polyether. Colloid Polym Sci 2012;290:1785–91.
[121] Pham VH, Cuong TV, Hur SH, Oh E, Kim EJ, Shin EW, et al. Chemical functionalization of graphene sheets by solvothermal reduction of a graphene oxide suspension in N-methyl-2-pyrrolidone. J Mater Chem 2011;21:3371–7.
[122] Dubin S, Gilje S, Wang K, Tung VC, Cha K, Hall AS, et al. A one-step, solvothermal reduction method for producing reduced graphene oxide dispersions in organic solvents. ACS Nano 2010;4:3845–52.
[123] Georgakilas V, Bourlinos AB, Zboril R, Steriotis TA, Dallas P, Stubos AK, et al. Organic functionalisation of graphenes. Chem Commun 2010;46:1766–8.
[124] Tung VC, Allen MJ, Yang Y, Kaner RB. High-throughput solution processing of large-scale graphene. Nat Nanotechnol 2009;4:25–9.
[125] Hou S, Su S, Kasner ML, Shah P, Patel K, Madarang CJ. Formation of highly stable dispersions of silane-functionalized reduced graphene oxide. Chem Phys Lett 2010;501:68–74.
[126] Chouhan A, Mungse HP, Sharma OP, Singh RK, Khatri OP. Chemically functionalized graphene for lubricant applications: microscopic and spectroscopic studies of contact interfaces to probe the role of graphene for enhanced tribo-performance. J Colloid Interface Sci 2018;513:666–76.
[127] Fan K, Chen X, Wang X, Liu X, Liu Y, Lai W, et al. Towards excellent tribological performance as oil-based lubricant additive: particular tribological behavior of fluorinated graphene. ACS Appl Mater Interfaces 2018;10:28828–38.
[128] Xu S, Yu W, Yao X, Zhang Q, Fu Q. Nanocellulose-assisted dispersion of graphene to fabricate poly(vinyl alcohol)/graphene nanocomposite for humidity sensing. Compos Sci Technol 2016;131:67–76.
[129] Che J, Shena L, Xiao Y. A new approach to fabricate graphene nanosheets in organic medium: combination of reduction and dispersion. J Mater Chem 2010;20:1722–7.
[130] Gravagnuolo AM, Morales-narváez E, Longobardi S, Silva ET, Giardina P, Merkoçi A. In situ production of biofunctionalized few-layer defect-free microsheets of graphene. Adv Funct Mater 2015;25:2771–9.
[131] Yoon S, In I. Role of poly(N-vinyl-2-pyrrolidone) as stabilizer for dispersion of graphene via hydrophobic interaction. J Mater Sci 2011;46:1316–21.
[132] Zhang W, He W, Jing X. Preparation of a stable graphene dispersion with high concentration by ultrasound. J Phys Chem B 2010;114:10368–73.
[133] Zhuo H, Zhang X, Wang L, Lu Q, Kaplan DL. Sonication exfoliation of defect-free graphene in aqueous silk nanofiber solutions. ACS Sustain Chem Eng 2018;6: 12261–7.
[134] Bak JM, Il Lee H. pH-tunable aqueous dispersion of graphene nanocomposites functionalized with poly(acrylic acid) brushes. Polym (U K) 2012;53:4955–60.
[135] Cui J, Zhou S. High-concentration self-cross-linkable graphene dispersion. Chem Mater 2018;30:4935–42.
[136] Jo K, Lee T, Choi HJ, Park JH, Lee DJ, Lee DW, et al. Stable aqueous dispersion of reduced graphene nanosheets via non-covalent functionalization with conducting polymers and application in transparent electrodes. Langmuir 2011;27:2014–8.
[137] Li D, Müller MB, Gilje S, Kaner RB, Wallace GG. Processable aqueous dispersions of graphene nanosheets. Nat Nanotechnol 2008;3:101–5.
[138] Luo J, Jiang S, Wu Y, Chen M, Liu X. Synthesis of stable aqueous dispersion of graphene/polyaniline composite mediated by polystyrene sulfonic acid. J Polym Sci Part A Polym Chem 2012;50:4888–94.
[139] Park S, An J, Piner RD, Jung I, Velamakanni A, Nguyen ST, et al. Aqueous suspension and characterization of chemically modified graphene sheets. Chem Mater 2008; 20:6592–4.
[140] Ge Y, Wang J, Shi Z, Yin J. Gelatin-assisted fabrication of water-dispersible graphene and its inorganic analogues. J Mater Chem 2012;22:17619–24.
[141] Zu S-Z, Han B-H. Aqueous dispersion of graphene sheets stabilized by pluronic copolymers: formation of supramolecular hydrogel. J Phys Chem C 2009;113: 13651–7.
[142] Zhang Y, Ma HL, Zhang Q, Peng J, Li J, Zhai M, et al. Facile synthesis of well-dispersed graphene by γ-ray induced reduction of graphene oxide. J Mater Chem 2012;22:13064–9.
[143] Gupta B, Kumar N, Panda K, Melvin AA, Joshi S, Dash S, et al. Effective noncovalent functionalization of poly(ethylene glycol) to reduced graphene oxide nanosheets through γ-radiolysis for enhanced lubrication. J Phys Chem C 2016;120:2139–48.
[144] Mungse HP, Khatri OP. Chemically functionalized reduced graphene oxide as a novel material for reduction of friction and wear. J Phys Chem C 2014;118: 14394–402.
[145] Mungse HP, Gupta K, Singh R, Sharma OP, Sugimura H, Khatri OP. Alkylated graphene oxide and reduced graphene oxide: grafting density, dispersion stability to enhancement of lubrication properties. J Colloid Interface Sci 2019;541:150–62.
[146] Fan X, Wang L. High-performance lubricant additives based on modified graphene oxide by ionic liquids. J Colloid Interface Sci 2015;452:98–108.
[147] Gusain R, Mungse HP, Kumar N, Ravindran TR, Pandian R, Sugimura H, et al. Covalently attached graphene-ionic liquid hybrid nanomaterials: synthesis, characterization and tribological application. J Mater Chem A 2016;4:926–37.

[148] Samuel J, Rafiee J, Dhiman P, Yu Z-Z, Koratkar N. Graphene colloidal suspensions as high performance semi-synthetic metal-working fluids. J Phys Chem C 2011;115: 3410–5.
[149] Yu W, Xie H, Wang X, Wang X. Significant thermal conductivity enhancement for nanofluids containing graphene nanosheets. Phys Lett Sect A Gen At Solid State Phys 2011;375:1323–8.
[150] Yu A, Ramesh P, Itkis ME, Bekyarova E, Haddon RC. Graphite nanoplatelet-epoxy composite thermal interface materials. J Phys Chem C 2007;111:7565–9.
[151] Kinoshita H, Nishina Y, Alias AA, Fujii M. Tribological properties of monolayer graphene oxide sheets as water-based lubricant additives. Carbon 2014;66:720–3.
[152] Elomaa O, Singh VK, Iyer A, Hakala TJ, Koskinen J. Graphene oxide in water lubrication on diamond-like carbon vs. stainless steel high-load contacts. Diamond Relat Mater 2015;52:43–8.
[153] He A, Huang S, Yun JH, Jiang Z, Stokes J, Jiao S, et al. The pH-dependent structural and tribological behaviour of aqueous graphene oxide suspensions. Tribol Int 2017;116:460–9.
[154] Li X, Lu H, Guo J, Tong Z, Dong G. Synergistic water lubrication effect of self-assembled nanofilm and graphene oxide additive. Appl Surf Sci 2018;455:1070–7.
[155] Fan K, Liu J, Wang X, Liu Y, Lai W, Gao S, et al. Towards enhanced tribological performance as water-based lubricant additive: selective fluorination of graphene oxide at mild temperature. J Colloid Interface Sci 2018;531:138–47.
[156] Alloy M, Contacts S, Xie H, Jiang B, Dai J, Peng C, et al. Tribological behaviors of graphene and graphene oxide as water-based lubricant additives for magnesium alloy/steel contacts. Mater (Basel) 2018;11:206.
[157] Kinoshita H, Nishina Y, Alias AA, Fujii M. Tribological properties of monolayer graphene oxide sheets as water-based lubricant additives. Carbon 2014;66:720–3.
[158] Elomaa O, Singh VK, Iyer A, Hakala TJ, Koskinen J. Graphene oxide in water lubrication on diamond-like carbon vs. stainless steel high-load contacts. Diamond Relat Mater 2015;52:43–8.
[159] Song HJ, Li N. Frictional behavior of oxide graphene nanosheets as water-base lubricant additive. Appl Phys A Mater Sci Proc 2011;105:827–32.
[160] Liang S, Shen Z, Yi M, Liu L, Zhang X, Ma S. In-situ exfoliated graphene for high-performance water-based lubricants. Carbon 2016;96:1181–90.
[161] Ge X, Li J, Wang H, Zhang C, Liu Y, Luo J. Macroscale superlubricity under extreme pressure enabled by the combination of graphene-oxide nanosheets with ionic liquid. Carbon 2019;151:76–83.
[162] Ge X, Li J, Luo R, Zhang C, Luo J. Macroscale superlubricity enabled by the synergy effect of graphene-oxide nanoflakes and ethanediol. ACS Appl Mater Interfaces 2018;10:40863–70.
[163] Liu Y, Li J, Ge X, Yi S, Wang H, Liu Y, et al. Macroscale superlubricity achieved on the hydrophobic graphene coating with glycerol. ACS Appl Mater Interfaces 2020;12: 18859–69.
[164] Su F, Chen G, Huang P. Lubricating performances of graphene oxide and onion-like carbon as water-based lubricant additives for smooth and sand-blasted steel discs. Friction 2020;8:47–57.
[165] Xie H, Dang S, Jiang B, Xiang L, Zhou S, Sheng H, et al. Tribological performances of SiO 2 /graphene combinations as water-based lubricant additives for magnesium alloy rolling. Appl Surf Sci 2019;475:847–56.
[166] Wu L, Xie Z, Gu L, Song B, Wang L. Investigation of the tribological behavior of graphene oxide nanoplates as lubricant additives for ceramic/steel contact. Tribol Int 2018;128:113–20.
[167] Sarno M, Senatore A, Cirillo C, Petrone V, Ciambelli P. Oil lubricant tribological behaviour improvement through dispersion of few layer graphene oxide. J Nanosci Nanotechnol 2014;14:4960–8.
[168] Berman D, Erdemir A, Sumant AV. Few layer graphene to reduce wear and friction on sliding steel surfaces. Carbon 2013;54:454–9.
[169] Zheng D, bing Cai Z, xue Shen M, yang Li Z, hao Zhu M. Investigation of the tribology behaviour of the graphene nanosheets as oil additives on textured alloy cast iron surface. Appl Surf Sci 2016;387:66–75.
[170] Dou X, Koltonow AR, He X, Jang HD, Wang Q, Chung Y-W, et al. Self-dispersed crumpled graphene balls in oil for friction and wear reduction. Proc Natl Acad Sci 2016;113:1528–33.
[171] Hou K, Gong P, Wang J, Yang Z, Wang Z, Yang S. Structural and tribological characterization of fluorinated graphene with various fluorine contents prepared by liquid-phase exfoliation. RSC Adv 2014;4:56543–51.
[172] Fan X, Li W, Fu H, Zhu M, Wang L, Cai Z, et al. Probing the function of solid nanoparticle structure under boundary lubrication. ACS Sustain Chem Eng 2017;5: 4223–33.
[173] Zin V, Barison S, Agresti F, Colla L, Pagura C, Fabrizio M. Improved tribological and thermal properties of lubricants by graphene based nano-additives. RSC Adv 2016; 6:59477–86.
[174] Xu Y, Peng Y, Dearn KD, Zheng X, Yao L, Hu X. Synergistic lubricating behaviors of graphene and MoS2dispersed in esterified bio-oil for steel/steel contact. Wear 2015;342:297–309.
[175] Eswaraiah V, Sankaranarayanan V, Ramaprabhu S. Graphene-based engine oil nanofluids for tribological applications. ACS Appl Mater Interfaces 2011;3:4221–7.
[176] Zhao J, Li Y, Mao J, He Y, Luo J. Synthesis of thermally reduced graphite oxide in sulfuric acid and its application as an efficient lubrication additive. Tribol Int 2017; 116:303–9.
[177] Li Y, Zhao J, Tang C, He Y, Wang Y, Chen J, et al. Highly exfoliated reduced graphite oxide powders as efficient lubricant oil additives. Adv Mater Interfaces 2016; 3:1600700.
[178] Mao J, Zhao J, Wang W, He Y, Luo J. Influence of the micromorphology of reduced graphene oxide sheets on lubrication properties as a lubrication additive. Tribol Int 2018;119:614–21.
[179] Esquivel-Gaon M, Nguyen NHA, Sgroi MF, Pullini D, Gili F, Mangherini D, et al. In vitro and environmental toxicity of reduced graphene oxide as an additive in automotive lubricants. Nanoscale 2018;10:6539–48.
[180] Zhao J, Mao J, Li Y, He Y, Luo J. Friction-induced nano-structural evolution of graphene as a lubrication additive. Appl Surf Sci 2018;434:21–7.
[181] Zhao J, Li Y, Wang Y, Mao J. Mild thermal reduction of graphene oxide as a lubrication additive for friction and wear reduction. RSC Adv 2017;7:1766–70.
[182] Dienwiebel M, Verhoeven GS, Pradeep N, Frenken JWM, Heimberg JA, Zandbergen HW. Superlubricity of graphite. Phys Rev Lett 2004;92:126101.
[183] Berman D, Deshmukh SA, Sankaranarayanan SKRS, Erdemir A, Sumant AV. Macroscale superlubricity enabled by graphene nanoscroll formation. Science 2015;348: 1118–22.
[184] Feng X, Kwon S, Park JY, Salmeron M. Superlubric sliding of graphene nano flakes on graphene. ACS Nano 2013;7:1718–24.
[185] Sinclair RC, Suter JL, Coveney PV. Graphene–graphene interactions: friction, superlubricity, and exfoliation. Adv Mater 2018;30:1705791.
[186] Compton OC, Nguyen ST. Graphene oxide, highly reduced graphene oxide, and graphene: versatile building blocks for carbon-based materials. Small 2010;6: 711–23.
[187] Akbar B, Cecilia M, Acik M, Chabal YJ, Chhowalla M, Shenoy VB. Structural evolution during the reduction of chemically derived graphene oxide. Nat Chem 2010;2:581.
[188] Georgakilas V, Otyepka M, Bourlinos AB, Chandra V, Kim N, Kemp KC, et al. Functionalization of graphene: covalent and non-covalent approaches, derivatives and applications. Chem Rev 2012;112:6156–214.
[189] Chen D, Feng H, Li J. Graphene oxide: preparation, functionalization, and electrochemical applications. Chem Rev 2012;112:6027–53.
[190] Kuila T, Bose S, Mishra AK, Khanra P, Kim NH, Lee JH. Chemical functionalization of graphene and its applications. Prog Mater Sci 2012;57:1061–105.
[191] Suk JW, Piner RD, An J, Ruoff RS. Mechanical properties of monolayer graphene oxide. ACS Nano 2010;4:6557–64.
[192] Samanta S, Singh S, Sahoo RR. Simultaneous chemical reduction and surface functionalization of graphene oxide for efficient lubrication of steel-steel contact. RSC Adv 2015;5:61888–99.
[193] Li W, Tang X, Zhang H, Jiang Z, Yu Z. Simultaneous surface functionalization and reduction of graphene oxide with octadecylamine for electrically conductive polystyrene composites. Carbon 2011;49:4724–30.
[194] Mungse HP, Singh R, Sugimura H, Kumar N, Khatri OP. Molecular pillar supported graphene oxide framework: conformational heterogeneity and tunable d-spacing. Phys Chem Chem Phys 2015;17:20822–9.
[195] Mungse HP, Kumar N, Khatri OP. Synthesis, dispersion and lubrication potential of basal plane functionalized alkylated graphene nanosheets. RSC Adv 2015;5: 25565–71.
[196] Cheng Z, Li W, Wu P, Liu Z. A strategy for preparing Modi fi ed graphene oxide with good dispersibility and transparency in oil. Ind Eng Chem Res 2017;56:5527–34.
[197] Ismail NA, Bagheri S. Highly oil-dispersed functionalized reduced graphene oxide nanosheets as lube oil friction modifier. Mater Sci Eng B 2017;222:34–42.
[198] Hu Y, Wang Y, Zeng Z, Zhao H, Ge X, Wang K, et al. PEGlated graphene as nanoadditive for enhancing the tribological properties of water-based lubricant. Carbon 2018;137:41–8.
[199] Yang J, Xia Y, Song H, Chen B, Zhang Z. Synthesis of the liquid-like graphene with excellent tribological properties. Tribiol Int 2017;105:118–24.
[200] Zhou F, Liang Y, Liu W. Ionic liquid lubricants: designed chemistry for engineering applications. Chem Soc Rev 2009;38:2590–9.
[201] Zhou Y, Qu J. Ionic liquids as lubricant additives: a review. ACS Appl Mater Interfaces 2017;9:3209–22.
[202] Gusain R, Gupta P, Saran S, Khatri OP. Halogen-free Bis(imidazolium)/Bis(ammonium)- Di[bis(salicylato)borate] ionic liquids as energy-E ffi cient and environmentally friendly lubricant additives. ACS Aplied Mater Interfaces 2014;6:15318–28.
[203] Gusain R, Khatri OP. Fatty acid ionic liquids as environmentally friendly lubricants for low friction and wear. RSC Adv 2016;6:3462–9.
[204] Khare V, Pham MQ, Kumari N, Yoon HS, Kim CS, Il Park J, et al. Graphene-ionic liquid based hybrid nanomaterials as novel lubricant for low friction and wear. ACS Appl Mater Interfaces 2013;5:4063–75.
[205] Sanes J, Avilés MD, Saurín N, Espinosa T, Carrión FJ, Bermúdez MD. Synergy between graphene and ionic liquid lubricant additives. Tribol Int 2017;116:371–82.
[206] Zhang W, Zhou M, Zhu H, Tian Y, Wang K, Wei J, et al. Tribological properties of oleic acid-modified graphene as lubricant oil additives. J Phys D Appl Phys 2011; 44:205303.
[207] Lin J, Wang L, Chen G. Modification of graphene platelets and their tribological properties as a lubricant additive. Tribol Lett 2011;41:209–15.
[208] Gupta B, Kumar N, Panda K, Dash S, Tyagi AK. Energy efficient reduced graphene oxide additives: mechanism of effective lubrication and antiwear properties. Sci Rep 2016;6:18372.
[209] Bordignon R, Salvaro D, Binder C, Klein AN, Drago V, de Mello JDB. Tribological behaviour of plasma-functionalized graphene as low-viscosity oil additive. Tribol Lett 2018;66:114.
[210] Zhao J, Huang Y, Li Y, Gao T, Dou Z, Mao J, et al. Superhigh-exfoliation graphene with a unique two-dimensional (2D) microstructure for lubrication application. Appl Surf Sci 2020;513:145608.
[211] Xiao H, Liu S. 2D nanomaterials as lubricant additive: a review. Mater Des 2017; 135:319–32.
[212] Gong Z, Shi J, Zhang B, Zhang J. Graphene nano scrolls responding to superlow friction of amorphous carbon. Carbon 2017;116:310–7.
[213] Lee C, Li Q, Kalb W, Liu X, Berger H, Carpick RW, et al. Frictional characteristics of atomically thin sheets. Science 2010;328:76–80.

[214] Cho DH, Wang L, Kim JS, Lee GH, Kim ES, Lee S, et al. Effect of surface morphology on friction of graphene on various substrates. Nanoscale 2013;5:3063–9.
[215] Klemenz A, Pastewka L, Balakrishna SG, Caron A, Bennewitz R, Moseler M. Atomic scale mechanisms of friction reduction and wear protection by graphene. Nano Lett 2014;14:7145–52.
[216] Praveena M, Bain CD, Jayarama V, Biswas SK. Total internal reflection (TIR) Raman tribometer: a new tool for in situ study of friction-induced material transfer. RSC Adv 2013;3:5401–11.
[217] Meng Y, Su F, Chen Y. Au/graphene oxide nanocomposite synthesized in supercritical CO2 fluid as energy efficient lubricant additive. ACS Appl Mater Interfaces 2017;9:39549–59.
[218] Meng Y, Su F, Chen Y. A novel nanomaterial of graphene oxide dotted with Ni nanoparticles produced by supercritical CO2-assisted deposition for reducing friction and wear. ACS Appl Mater Interfaces 2015;7:11604–12.
[219] Meng Y, Su F, Chen Y. Synthesis of nano-Cu/graphene oxide composites by supercritical CO2-assisted deposition as a novel material for reducing friction and wear. Chem Eng J 2015;281:11–9.
[220] Dong Y, Jia ZÆ, Yan S, Gui ÆL. Effect of nano-Cu lubrication additive on the contact fatigue behavior of steel. Tribol Lett 2010;37:203–7.
[221] Gusain R, Khatri OP. Ultrasound assisted shape regulation of CuO nanorods in ionic liquids and their use as energy efficient lubricant additives. J Mater Chem A 2013;1:5612–9.
[222] Zhang Y, Tang H, Ji X, Li C, Chen L, Zhang D, et al. Synthesis of reduced graphene oxide/Cu nanoparticle composites and their tribological properties. RSC Adv 2013;3:26086–93.
[223] Jia Z, Chen T, Wang J, Ni J, Li H, Shao X. Synthesis, characterization and tribological properties of Cu/reduced graphene oxide composites. Tribol Int 2015;88:17–24.
[224] Song H-J, Jia X-H, Li N, Yang X-F, Tang H. Synthesis of α-Fe_2O_3 nanorod/graphene oxide composites and their tribological properties. J Mater Chem 2012;22:895–902.
[225] Bai G, Wang J, Yang Z, Wang H, Wang Z, Yang S. Preparation of a highly effective lubricating oil additive – ceria/graphene composite. RSC Adv 2014;4:47096–105.
[226] Hou X, Yang C, He J, Li Z, Zhang Z. Preparation and tribological properties of lanthanum trifluoride nanoparticles-decorated graphene oxide nanosheets. Ind Eng Chem Res 2015;54:4773–80.
[227] Zhou Q, Huang J, Wang J, Yang Z, Liu S, Wang Z, et al. Preparation of a reduced graphene oxide/zirconia nanocomposite and its application as a novel lubricant oil additive. RSC Adv 2015;5:91802–12.
[228] Zhang L, He Y, Feng S, Zheng L, Jiao Z, Zhan Y, et al. Preparation and tribological properties of novel boehmite/graphene oxide nano-hybrid. Ceram Int 2016;42:6178–86.
[229] Ramón-Raygoza ED, Rivera-Solorio CI, Giménez-Torres E, Maldonado-Cortés D, Cardenas-Alemán E, Cué-Sampedro R. Development of nanolubricant based on impregnated multilayer graphene for automotive applications: analysis of tribological properties. Powder Technol 2016;302:363–71.
[230] Jia Z, Pang X, Li H, Ni J, Shao X. Synthesis and wear behavior of oleic acid capped calcium borate/graphene oxide composites. Tribol Int 2015;90:240–7.
[231] Farsadi M, Bagheri S, Ismail NA. Nanocomposite of functionalized graphene and molybdenum disulfide as friction modifier additive for lubricant. J Mol Liq 2017;244:304–8.
[232] Li H, Chen L, Zhang Y, Ji X, Chen S, Song H, et al. Synthesis of MoSe2/reduced graphene oxide composites with improved tribological properties for oil-based additives. Cryst Res Technol 2014;49:204–11.
[233] Gong K, Wu X, Zhao G, Wang X. Nanosized MoS2 deposited on graphene as lubricant additive in polyalkylene glycol for steel/steel contact at elevated temperature. Tribol Int 2017;110:1–7.
[234] Zhang M, Chen B, Tang H, Tang G, Li C, Chen L, et al. Hydrothermal synthesis and tribological properties of FeS2 (pyrite)/reduced graphene oxide heterojunction. RSC Adv 2015;5:1417–23.
[235] Wu X, Gong K, Zhao G, Lou W, Wang X, Liu W. Mechanical synthesis of chemically bonded phosphorus-graphene hybrid as high-temperature lubricating oil additive. RSC Adv 2018;8:4595–603.
[236] Jaiswal V, Kalyani Umrao S, Rastogi RB, Kumar R, Srivastava A. Synthesis, characterization, and tribological evaluation of TiO2-reinforced boron and nitrogen co-doped reduced graphene oxide based hybrid nanomaterials as efficient antiwear lubricant additives. ACS Appl Mater Interfaces 2016;8:11698–710.
[237] Kumar A, Behera B, Ray SS. Microwave-assisted surface-initiated redox polymerization of acrylamide with functionalized graphene oxide for aqueous lubricant additive. RSC Adv 2015;5:39474–81.
[238] Kumar A, Behera B, Thakre GD, Ray SS. Covalently grafted Graphene oxide/poly(Cn-acrylate) nanocomposites by surface-initiated ATRP: an efficient antifriction, antiwear, and pour-point-depressant lubricating additive in oil media. Ind Eng Chem Res 2016;55:8491–500.
[239] Liu L, Zhou W, Chen Y, Jiao S, Huang P. Pressure-assisted synthesis of a polyaniline–graphite oxide (PANI–GO) hybrid and its friction reducing behavior in liquid paraffin (LP). New J Chem 2018;42:936–42.
[240] Ren B, Gao L, BotaoXie Li M, Zhang S, Zu G, et al. Tribological properties and antiwear mechanism of ZnO@graphene core-shell nanoparticles as lubricant additives. Tribol Int 2020;144:106114.
[241] Wang L, Gong P, Li W, Luo T, Cao B. Mono-dispersed Ag/graphene nanocomposite as lubricant additive to reduce friction and wear. Tribol Int 2020;146:106228.
[242] Gan C, Liang T, Chen D, Li W, Fan X, Tang G, et al. Phosphonium-organophosphate modified graphene gel towards lubrication applications. Tribol Int 2020;145:106180.
[243] Qi S, Geng Z, Lu Z, Zhang G, Wu Z. Synergistic lubricating behaviors of 3D graphene and 2D hexagonal boron nitride dispersed in PAO4 for steel/steel contact. Adv Mater Interfaces 2020;7:1901893.
[244] Martin JM, Donnet C, Le Mogne T. Superlubricity of molybdenum disulphide. Phys Rev B 1993;48:10583.
[245] Kumari S, Chouhan A, Sharma OP, Kuriakose S, Tawfik SA, Jeanette M, et al. Structural-defect-mediated grafting of alkylamine on few-layer MoS_2 and its potential for enhancement of tribological properties. ACS Aplied Mater Interfaces 2020;12:30720–30.
[246] Min C, Zhang Q, Shen C, Liu D, Shen X, Song H, et al. Graphene oxide/carboxyl-functionalized multi-walled carbon nanotube hybrids: powerful additives for water-based lubrication. RSC Adv 2017;7:32574–80.
[247] Chouhan A, Sarkar TK, Kumari S, Vemuluri S, Khatri OP. Synergistic lubrication performance by incommensurately stacked ZnO-decorated reduced graphene oxide/MoS_2 heterostructure. Journal of Colloid and Interface Science 2020;580:730–9.

Advances in Colloid and Interface Science 283 (2020) 102215

Contents lists available at ScienceDirect

Advances in Colloid and Interface Science

journal homepage: www.elsevier.com/locate/cis

Historical Perspective

Surface chemistry of graphene and graphene oxide: A versatile route for their dispersion and tribological applications

Ajay Chouhan [a,b,1], Harshal P. Mungse [a,1,2], Om P. Khatri [a,b,*]

[a] Chemical and Material Sciences Division, CSIR-Indian Institute of Petroleum, Dehradun 248005, India
[b] Academy of Scientific and Innovative Research, Ghaziabad 201002, India

ARTICLE INFO

Article history:
15 June 2020
Available online 30 July 2020

Keywords:
Graphene
Materials chemistry
Surfaces and interfaces
Dispersion
Lubrication

ABSTRACT

Graphene, the most promising material of the decade, has attracted immense interest in a diversified range of applications. The weak van der Waals interaction between adjacent atomic-thick lamellae, excellent mechanical strength, remarkable thermal conductivity, and high surface area, make graphene a potential candidate for tribological applications. However, the use of graphene as an additive to liquid lubricants has been a major challenge because of poor dispersibility. Herein, a thorough review is presented on preparation, structural models, chemical functionalization, and dispersibility of graphene, graphene oxide, chemically-functionalized graphene, and graphene-derived nanocomposites. The graphene-based materials as additives to water and lubricating oils improved the lubrication properties by reducing the friction, protecting the contact interfaces against the wear, dissipating the heat from tribo-interfaces, and mitigating the corrosion by forming the protecting thin film. The dispersion stability, structural features, and dosage of graphene-based dispersoids, along with contact geometry, play important roles and govern the tribological properties. The chemistry of lubricated surfaces is critically reviewed by emphasizing the graphene-based thin film formation under the tribo-stress, which minimizes the wear. The comprehensive review provides variable approaches for the development of high-performance lubricant systems and accentuates the lubrication mechanisms by highlighting the role of graphene-based materials for enhancement of tribological properties.

Contents

* Corresponding author at: Chemical and Material Sciences Division, CSIR-Indian Institute of Petroleum, Dehradun 248005, India.
E-mail address: opkhatri@iip.res.in (O.P. Khatri).
[1]Equally contributed.
[2]Present address: Department of Chemistry, Adarsha Science, J. B. Arts & Birla Commerce College, Dhamangaon - 444709, India.

https://doi.org/10.1016/j.cis.2020.102215
0001-8686/

ISSN 2277 - 5730
AN INTERNATIONAL MULTIDISCIPLINARY
QUARTERLY RESEARCH JOURNAL

AJANTA

Volume - IX Issue - II APRIL - JUNE - 2020

MARATHI PART - II / HINDI

Peer Reviewed Referred
and UGC Listed Journal

Journal No. 40776

ज्ञान-विज्ञान विमुक्तये

IMPACT FACTOR / INDEXING
2019 - 6.399
www.sjifactor.com

❖ EDITOR ❖
Asst. Prof. Vinay Shankarrao Hatole
M.Sc (Maths), M.B.A. (Mktg.), M.B.A. (H.R.),
M.Drama (Acting), M.Drama (Prod. & Dir.), M.Ed.

❖ PUBLISHED BY ❖

Ajanta Prakashan
Aurangabad. (M.S.)

Owner, printer & publisher Vinay S. Hatole has printed this journal at Ajanta Computer and Printers, Jaisingpura, University Gate, Aurangabad, also Published the same at Aurangabad.

Printed by

Ajanta Computer, Near University Gate, Jaisingpura, Aurangabad. (M.S.)

Printed by

Ajanta Computer, Near University Gate, Jaisingpura, Aurangabad. (M.S.)
Cell No. : 9579260877, 9822620877, 7030308239 Ph. No. : (0240) 2400877
E-mail : ajanta5050@gmail.com, www.ajantaprakashan.com

AJANTA - ISSN 2277 - 5730 - Impact Factor - 6.399 **(www.sjifactor.com)**

EDITORIAL BOARD

EDITORIAL BOARD

PUBLISHED BY

Ajanta Prakashan
Aurangabad. (M.S.)

CONTENTS OF MARATHI PART - II

CONTENTS OF HINDI

VOLUME - IX, ISSUE - II - APRIL - JUNE - 2020
AJANTA - ISSN 2277 - 5730 - IMPACT FACTOR - 6.399 (www.sjifactor.com)

८. वैदिक ज्ञान परंपरेतून मानवीय विकासाचे प्राप्त झालेले यथार्थ ज्ञान

Dr. Poonam M. Gahukar
Assistant Professor of Sanskrit, Adarsh Mahavidyalaya Dhamangaon Rly.

प्रस्तावना

भारतीय विचारसरणीनुसार वेद नित्य आहेत, अपौरुषेय आहेत, शाश्वत आहेत आणि म्हणूनच सर्व ज्ञानाचे व धर्माचे उगम स्थान आहेत. भारतीयांची अशी धारणा आहे की सर्व ज्ञान हे वेदापासूनच उत्पन्न झाले – ''सर्वज्ञानमयि हि स:!'' वेद म्हणजे ज्ञान व ज्ञान सर्व शास्र, कला, विज्ञान, संगीत, आयुर्वेद, शिल्प वेदापासूनच उत्पन्न झाले. असे मानणे भाग पाडतात. म्हणूनच जिज्ञासू संशोधनाची बीजे शोधण्यासाठी वैदिक साहित्याचा अभ्यास करतात व प्रमाण शोधतात. वैद्यक, गणित, साहित्य, ज्योतिष्य, फार काय तर स्थापत्य कला, पदार्थ विज्ञान, रसायन इत्यादी भौतिक शास्त्रे आपली परारंभिक अवस्था वेदा मध्ये निहित आहे असे सांगतात.

''विदन्ति जानन्ति विद्यन्ते भवन्ति विचारयति सर्वे मनुष्या: सत्य विद्याम यै वा तथा विद्वांसश्च भवंति ते वेदा:!'' – अर्थात ज्याच्या द्वारे संपूर्ण सत्य विद्या ग्राह्य व पराप्त केली जाते व ज्यामुळे विद्वानांना ज्ञान प्राप्त होते त्याला वेद असे म्हणतात. वैदिक साहित्याचा सर्व प्रथम वेद होय, वेदाचा अर्थ आहे – 'ज्ञान !' भारतीय संस्कृतीमध्ये याचे महत्वाचे व गौरव पूर्ण स्थान आहे. वेद शब्द विद धातुला घञ प्रत्यय जोडून बनलेला आहे.

''विद्यन्ते ज्ञायन्ते लभ्यन्ते वा धर्मादि पुरुषार्था एभिरिति वेदा:!'' – अर्थात ज्याच्या द्वारे धर्म-अर्थ-काम-मोक्ष पुरुषार्थ जाणणे व प्राप्त करणे हे यथार्थ ज्ञान सांगणारे 'वेद' होय.

वेदाचे महत्त्व

सृष्टी उत्पत्तीच्या वेळी धार्मिक, नैतिक व आध्यात्मिक ज्ञानासाठी याचा प्रादुर्भाव झाला. हे मानव जातीचे प्चीनतू धर्मग्रंथ होय म्हणूनच वेद त्याकाळातील संस्कृती, सभ्यता, धार्मिक मान्यता व परंपरा इत्यादींना जाणण्याचे एकमात्र स्रोत होय. वेद धर्माचे आधार स्तंभ आहे.

इहलौकिक व पारलौकिक दोन्ही प्रकारचे सुखप्राप्तीचे स्थान वेद आहे. हे उचित व अनुचित याचे निर्देशक आहे, कर्तव्याचे उद्बोधक आहे. सुख शांतीचे साधन आहे. ज्ञान लोका चे व निराशेचे विनाशक वेदच आहे. भारतीय संस्कृती प्रमाणे वेद निंदकाला 'नास्तिक' म्हणतो अर्थात 'नास्तिको वेद निंदक: !'

वेद साहित्य दृष्टींनीसुद्धा अत्यंत महत्त्वपूर्ण आहे. महाकाव्य, गीतिकाव्य, गद्यकाव्य, नाटक, आख्यान, साहित्य इ. काव्याच्या सर्व विधा उत्पत्तित वेदाचे सक्रिय योगदान राहिले आहे.

वनस्पती विज्ञान असोवा सृष्टीविषयक वार्ता असो वा किंवा नौका निर्माण संबंधी कथा असो. सर्वांचे अंकुर वेदामध्ये विद्यमान आहे.

भाषा विज्ञानाच्या दृष्टींनी सुद्धा वेद अत्यंत महत्त्वपूर्ण आहे. वैदिक भाषाविना युरोपीय भाषांचे अध्ययन संभव नाही. वेदांचे उपदेश सार्वकालिन व सार्वभौमिक आहे.

मनुष्याच्या उन्नतीचे सर्वात्तम साधन आहे ते भारतीयांचे आधारस्तंभ आहे.

वैदिक परंपरा व मानवीय विकास

वैदिक आख्यान संदर्भात आजही विश्वातलील प्राचीन धरोहर सुरक्षित आहे. एक विशाल यांचे स्मरण किंवा आर्य संस्कृतली व प्राचीन, ऐतिहासिक, धार्मिक व लौकिक रूप ऋग्वेदातील विविध दैवत कथा प्राप्त होतात. आपली राष्ट्रीय एकता, अखंडता व नैतिक मूल्य यासाठी आकज सुद्धा ह्या देवकथा प्रासंगिक आहे. वैदिक दैवतकथा अनंतरकालीन, अवतारकथा आहे. त्या आजही प्रभावशाली आहेत. वैदिक व लौकिक परंपरा या देवांचे नाव व त्यांची कार्यशैली आपल्याला जरी भिन्न परतीत होत असेल परंतु उद्देश केवळ एकच लोककल्याण, देवत्व शक्ती मनुष्यासाठी उपादेय तत्त्व आहे.

''यदा यदा हि धर्मस्य ग्लानिर्भवति भारत ।
अभ्युत्थानमधर्मस्य तदात्मान सृजाम्यहं ।।''

या गीता वाचनानुसार हे देव भविष्यात सुद्धा युग युगात जन्म घेतीलच. ज्यांच्या विचाराने संपूर्ण विश्व संस्कृती पुष्ट होईल व सर्वांची आत्मा शुभ संस्कारांनी संपन्न होत राहील कारण संस्कारांच्या अभावी संस्कृती नाही. संस्कृती हि राष्ट्रचाराची आत्मा होय.

आपल्या प्राचीन परंपरेत वेदाला 'अ-पौरुषेय' मानले आहे. वेद हे मनुष्यकृत रचना नाही ते अलौकिक आहे. कारण ब्राम्हालच्या चार मुखातून चार वेद निघाले हे एक पौराणिक धारणेचे रूप आहे. परंतु वेदाच्या अ-पौरूषेयत्व ची सिद्धी मीमांसा शास्त्रात तर्क या आधारावर केली आहे – एक तथ्य असे कि महाभारत रामायण इण ग्रंथाचा कर्ता याचे स्मरण किंवा उल्लेख केला जाऊ शकतो. त्याच परमाणे वेदाचा कर्ता कुणीच नाही.

कोणत्याही सत्य वाक्याला 'वेदवाक्य' म्हणतात. उदाहरणार्थ लौकिक ग्रंथ जसे रामायण, महाभारत इ. मध्ये पाठभेद मिळतात. परंतु वेदामध्ये अतिप्राचिनता असूनही पाठभेद आढळत नाही हे एक महत्वपूर्ण तथ्य आहे की शिक्षा, व्याकरणा सारखे षड़ वेदांगानी वेदाला विकृत होण्यापासून वाचविले आहे व सम्यक ज्ञान लोकांपर्यंत पोहचविले. यास्काचार्यांनी आवश्यकतेनुसार विचार व व्याख्याच्या दृष्टीने वैदिक संप्रदाय साय्यर केले ते अशा प्रकारचे आहेत.

१. नैरुक्ता:

२. याज्ञिका:

३. वैयाकरणा:

४. जोतिष्का:

५. भाषाविद:

६. संप्रदायविद:

७. अध्यात्मावाद:

८. ऐतिहासिका:

या संप्रदायांच्या माध्यमांनी वेदार्थ जाणण्याचा पर्यत्न वेदोत्तर काळात झाला.

वैदिक सूक्तांचे वेगवेगळे देव व ऋषी आहेत यातून स्पष्ट होते कि देवता स्तुत्य आहे. प्रार्थनीय आहे. आपले कल्याण करणारे शक्ती स्वरूप आहे आणि स्तुती करता ऋषी त्या मंत्राचे दृष्टा होते. रचयिता नव्हे. काही ठिकाणी असे मंत्र उच्चरित आहे कि ऋषी म्हणतात हहे आमचे मंत्र नाही. पूर्वी पासून चालत आलेले परंपरागत मंत्राचा आम्ही केवळ पाठ किंवा उच्चरण करीत आहोत.

वैदिक परंपरा व 'श्रुति' हेच वेद आहेत जे परंपरेनी गुरुमुखातून श्रुत आहेत. सर्वात आश्चर्य हे कि विश्वातील विद्वानांना असे वाटते की वेद मंत्र उच्चारण व शब्ध विधान वैज्ञानिक प्रतिशाख्य नियमांनी त्यास अक्षुन्य बनवून ठेवणे यासाठी ऋषीमुनींना भाषा शात्रीय नियम बनविण्याची आवशक्यता भासली. हे नियम पौरुषीय आहेत. ज्यांनी वेदांचे रक्षण केले आहेत. देवतांच्या चरित्रावर आधारित वैदिक आख्यान सुद्धा लोकत्वांनी युक्त आहे. इंद्रादी देवतांची स्तुती भौतिक वस्तुच्या प्राप्ती साठी वैदिक ऋषींननी त्यांची प्रार्थना केली. ऋग्वेदातील प्राचीन लोकविश्वास, परंपरा व नैतिक विचारांचे दर्शन होतात. भगवद्गीतेमध्ये भगवान श्रीकृष्ण म्हणतात –

''परित्राणाय साधूनां विनाशाय च दुष्कृताम् ।'' इंद्रांनी सुद्धा सज्जन लोकांच्या हितासाठी कार्य केले आणि लोकांना पीडा देणारे असुरांचा वृत्र रुपी शस्त्राने संहार केला. त्यामुळे स्पष्ट होते की लोक मंगलकारी देवतांचे चरित्र हे समाजातील लोकांसाठी आदर्श भूत चरित्र आहेत ते मग वैदिक काळाचे असो किंवा पौराणिक काळचे.

'एकेन विज्ञातेन सर्वम विज्ञातं भवति' हे वेद वचन किती सार्थ आहे याचा अनुभव प्राचीन, अर्वाचीन शास्त्र निर्मात्यांना ध्यानावस्थेत एकाग्रतेत येतो. भारतीय शास्त्रकारांनी ती अवस्था प्रत्नपूर्वक प्राप्त करून घेतली म्हणूनच अगोचर असलेले जगत्कारण हेच सर्व शास्त्रांचे मूळ आहे व हे वेद रुपी ज्ञान अपौरुषेय आहे हे ऋषी मुनी जाणतात. हे अनुभूतीने जाणलेले भंडार जरी अनंत असले तरी त्यातून ग्राह्य विषय संकल्पाने पूर्ण होतो आणि

एकेक विषयाचे एक शास्त्र निर्माण होते, नवे नवे शोध लागतात आणि मानवीय ज्ञान क्षेत्रे विस्तारू लागतात. जगतकारणाततून प्राप्त झालेले ज्ञान म्हणून सर्व ज्ञान शाखा परस्पर विरोधी वाटलं तरी त्यांची मूळ समानता शोधावयास पाहिजे त्यातून विविध ज्ञान, विज्ञान शाखांचा विस्तार होतो. शमानतेतून एकरूपता जाणवते व विरोध नाहीसा होतो.

विदर्भ संत प्रज्ञा चक्षु श्री, गुलाबराव महाराजांनी शाश्वत वैदिक संस्कृती व परंपरा हि जगाच्या पाठीवरील सर्वप्रथम अस्तित्वात आलेली समृद्ध बहरलेली संस्कृती असून तीच जगभर पसरलेली होती असे साधार विषय मांडले व आर्यांच्या इतिहासावर नवीन प्रकाश टाकला आहे. त्यांच्यानुसार वैदिक संस्कृति हि वैश्विक संस्कृती आहे. ह्या संस्कृतीचे पुनरुत्थान होऊन विश्वाला व्यापिल असे महाराजांचे ठाम मत आहे.

संदर्भग्रंथ

१. वैदिक आख्यान – प्रभाकर नारायण कवठेकर, राष्ट्रिय संस्कृत संस्थानं.

२. ब्रह्म वेदान्तसूत्रं – भावेश नाथ पाठक, Eastern Book Linkers, Delhi

३. ऋग्वेद भाष्य भूमिका – दयानंद सरस्वती

४. अलौकिक व्याख्यानमाला श्री संत गुलाबराव महाराज सर्वोदय ट्रस्ट आळंदी, पुणे

5. Studies in Rugveda and Modern Sanskrit Literature – S. Ranganath, Eastern Book Linker, Delhi.

J Mater Sci: Mater Electron

Enhanced thermoluminescence properties of $CaSrAl_2SiO_7$:Ce^{3+},Tb^{3+} phosphor

Shweta S. Sharma[1,*], Nameeta Brahme[2], D. P. Bisen[2], Pradeep Dewangan[3], Ishwar Prasad Sahu[4], Suresh G. Onkar[1], Vijay S. Thool[1], Shilpa G. Vidhale[1], and Girish S. Mendhe[1]

[1] Department of Physics, Adarsha Science, J. B. Arts and Birla Commerce College, Dhamangaon, Maharashtra 444709, India
[2] School of Studies in Physics and Astrophysics, Pt. Ravishankar Shukla University, Raipur, Chhattisgarh 492010, India
[3] Department of Physics, Faculty of Science, Shri Rawatpura Sarkar University, Raipur, Chhattisgarh 492010, India
[4] Department of Physics, Indira Gandhi National Tribal University, Amarkantak, Madhya Pradesh 484887, India

Received: 15 April 2021
Accepted: 10 October 2021

ABSTRACT

The application of thermoluminescence technique in radiation dosimetry spans field of health physics, biological and geological sciences and personnel monitoring; this led to the search for new compositions with desirable dosimetric properties. In the present work, $CaSrAl_2SiO_7$:Tb^{3+} and $CaSrAl_2SiO_7$:Ce^{3+},Tb^{3+} phosphors were prepared by solid-state reaction method and their TL properties were studied in detail. The comparison of their TL results showed that co-doping of Ce^{3+} ions enhanced TL response of $CaSrAl_2SiO_7$:Tb^{3+} phosphors; this was also verified from measurement of TL emission spectra of the samples. Optimized glow curves were analysed and TL parameters were extracted from Chen's method. Co-doped $CaSrAl_2SiO_7$:Ce^{3+},Tb^{3+} phosphor is found to be useful in dosimetric application.

1 Introduction

When an insulating or a superconducting material is exposed to any kind of ionizing radiation, deposited energy is stored in the defect sites and colour centres of the crystal lattice. Due to action of heat energy, a fraction of this stored energy released and emitted as visible light which is called thermoluminescence [1, 2]. Nowadays application of various radiations such as ultraviolet, X-rays, β-rays, γ-rays in the different fields like medical, industrial, agriculture, etc., is increasing [3]. Thermoluminescence (TL) is one of the techniques used in radiation dosimetry [4]. Thermoluminescent materials are more investigated in on-going researches, because they found to have increasing application in thermoluminescence dosimeters. Thermoluminescent dosimeters necessarily have linearity of TL response with exposed radiation dose.

$CaSrAl_2SiO_7$ is one of the members of melilite group; these melilites that are basically silicate-based materials showed their use in TL dosimetry. In this work, thermoluminescence properties of $CaSrAl_2SiO_7$:Tb^{3+} phosphor are investigated and also

Address correspondence to E-mail: sharma.shweta2812@gmail.com

https://doi.org/10.1007/s10854-021-07260-z
Published online: 25 October 2021

observed that co-doping of Ce^{3+} ions enhanced TL of $CaSrAl_2SiO_7$:Tb^{3+} phosphor. The effect of different Tb^{3+} concentration in both single and co-doped samples on the TL glow curves has been recorded and glow curve is analysed by computerized glow curve deconvolution method. To the best of our knowledge, there is no earlier report on thermoluminescence investigation on $CaSrAl_2SiO_7$:Tb^{3+} and $CaSrAl_2SiO_7$: Ce^{3+},Tb^{3+} phosphors.

2 Synthesis and experimental

Phosphors for the study were prepared by solid-state reaction method at high temperature using analytical reagent (AR) grade raw chemicals with more than 99% accuracy. Calcium carbonate, strontium carbonate, aluminium oxide, silicon di-oxide, ceric oxide and terbium oxide were the starting materials. The amounts of the raw chemicals were calculated according to stoichiometric ratio in $CaSrAl_2SiO_7$:Ce^{3+} (0.5 mol%),Tb^{3+} (y mol%), where y = 1.0, 3.0, 5.0, 7.0, 10.0 mol%. Required quantities of raw materials were mixed homogeneously using agate mortar and pestle for 3 h. The resultant mixtures were fired at high temperature 1300 °C for 5 h. It was then slowly cooled to room temperature inside the closed furnace. The powders so formed were collected by crushing the prepared samples. Now the samples were ready for all other characterization studies.

Phase of synthesized phosphor was confirmed by X-ray diffraction (XRD) technique using Cu-Kα radiation with the help of D2 phaser Bruker diffractometer. Thermoluminescence investigation of phosphor was performed by TLD reader, Nucleonix TL 1009I with constant heating rate of 5 °C/s. As sample must be exposed to any kind of radiation before measurement of TL, UV cabinet is used, where the samples were exposed to UV radiation of 254 nm. Band pass filters of different wavelengths have been used to record TL emission spectrum. To record TL emission spectrum, the processes used in recording TL glow curves were repeated; here the sample that is placed in canthal strip was covered with band pass filter. The band pass filter allows the signals of selected range of wavelengths; hence in TL emission spectrum, characteristic emission peaks were observed.

3 Results and discussion

3.1 XRD investigation

To verify the preparation of phosphors, they were analysed by XRD tool that reveals the phase composition. Figure 1 shows the XRD patterns of Tb^{3+} singly doped and Ce^{3+},Tb^{3+} co-doped $CaSrAl_2SiO_7$ phosphors along with JCPDS file. It is clear that phosphors have good crystallization with no any impurity phase, as experimental diffraction patterns well matched with JCPDS file 26-0327 of $CaSrAl_2SiO_7$. Hence, the as-prepared phosphors have tetragonal crystallographic structure whose space group is $P\bar{4}2_1$ m [5].

3.2 Thermoluminescence investigation

Thermoluminescence (TL) is light emission due to moderate heating of a solid, previously exposed to ionizing radiation. The absorption of the ionizing radiation (UV, X-, β- or γ-rays, high-energy particles) creates traps, and fills them (or those already exist) with electrons and/or holes even at low temperatures. The subsequent heating migrates the electrons

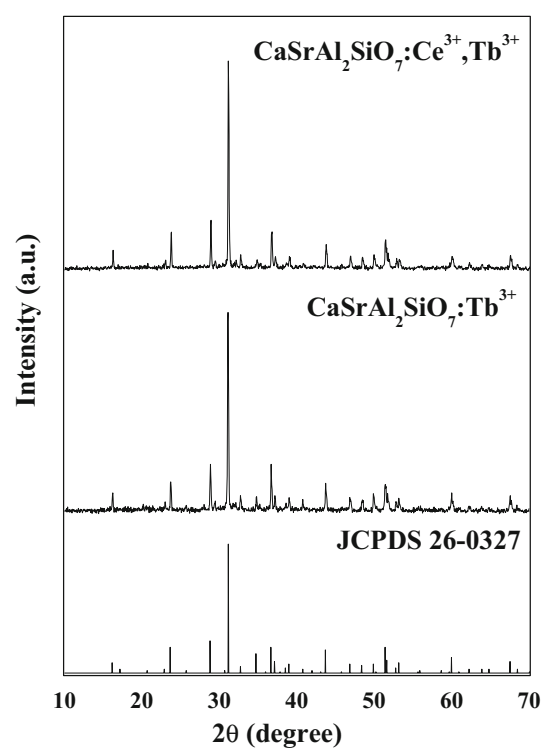

Fig. 1 Diffraction patterns of $CaSrAl_2SiO_7$:Tb^{3+} and $CaSrAl_2SiO_7$:Ce^{3+},Tb^{3+} phosphors

and/or holes in the lattice, until they fall into other traps (or recombine) with a consequent photon emission [6]. Thermoluminescent emission from TL materials is very sensitive to the amount and nature of dopant element and radiation effect. So in the present research work, we used Ce^{3+} and Tb^{3+} as single and co-dopant ions with their various concentrations; after that TL measurement was performed for each sample with optimized dopant and co-dopant concentration with various ultraviolet (UV) exposure time and then TL kinetic parameters were extracted from the Chen's peak shape method.

3.2.1 *Thermoluminescence of $CaSrAl_2SiO_7$:Ce^{3+}*

Let us first focus on the investigated thermoluminescence properties of $CaSrAl_2SiO_7$:Ce^{3+} phosphor; this was already discussed in our previous work in which Ce^{3+} concentration was varied as 0.1, 0.3, 0.5, 1.0, 2.0, 3.0 and 4.0 mol% [7]. The optimized glow curve was obtained for 0.5 mol% Ce^{3+}-doped $CaSrAl_2SiO_7$ phosphor. This optimized phosphor showed an increment in TL intensity up to 35 min of UV irradiation time. As we further increased UV exposure time, saturation in TL intensity was found.

3.2.2 *Thermoluminescence of $CaSrAl_2SiO_7$:Tb^{3+}*

At the second attempt, TL properties of $CaSrAl_2SiO_7$:Tb^{3+} phosphor was seen and this report is dealing here for the first time. Figure 2 represents a series of Tb^{3+} concentration (1.0, 3.0, 5.0, 7.0, 10.0 mol%)-dependent TL glow curves of $CaSrAl_2SiO_7$:Tb^{3+} samples. TL peak position is independent of the concentration of Tb^{3+} element and exhibits no shift with change in doping concentration. The only variation obtained in the TL peak intensity while increasing Tb^{3+} concentration. It can be understood from the inset of Fig. 2 that TL intensity of sample first increased with rise in Tb^{3+} concentration, attained a highest value at 5.0 mol% of Tb^{3+} ions and then decreased with further increase in Tb^{3+} concentration; this behaviour arises from concentration quenching process after a particular Tb^{3+} concentration. As we increase impurity concentration, there is an increase in the number of defects/traps which in turn implies a growth in the density of charge carriers being trapped upon irradiation. Therefore the initial rise in the TL peak intensity or area of the glow curves. Furthermore, on being thermally stimulated,

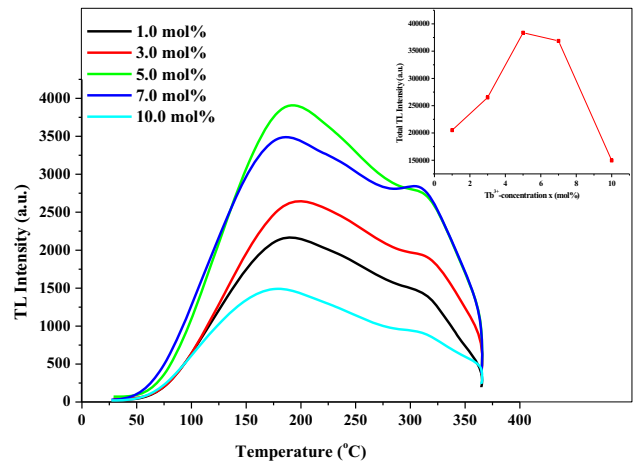

Fig. 2 Concentration-dependent TL glow curves of $CaSrAl_2SiO_7$:yTb^{3+} phosphors with 10-min UV exposure time

these charge carriers release from traps which in turn recombine with their counterparts at the recombination centre and yield diverse TL glow peaks with elevated height [8].

As thermoluminescence properties are greatly affected by exposure time, TL property of $CaSrAl_2SiO_7$:Tb^{3+} (5.0 mol%) phosphor was measured with different UV exposure time. For variable UV exposure time, some of the selected TL glow curves of $CaSrAl_2SiO_7$:Tb^{3+} (5.0 mol%) are represented in Fig. 3. Spectral behaviour was same with increase in length of UV exposure time but peak TL intensity or glow curve area altered with increase in exposure time. The growth in TL response was observed as exposure time was boosted and after 60 min of UV exposure TL response diminished with more added exposure time. With increasing irradiation dose more and more trapping centres or luminescent centres responsible for the TL glow peaks are getting filled. Upon thermal stimulation, these traps liberate their charge carriers and they get recombine with their counterparts, giving rise to different glow peaks. When all the trapping centres that are subjected to desired TL emission get filled, the saturation or decrease in the TL intensity starts appearing [8–10].

3.2.3 *Thermoluminescence of $CaSrAl_2SiO_7$:Ce^{3+},Tb^{3+}*

Thermoluminescence experiments were performed on the series of $CaSrAl_2SiO_7$:xCe^{3+} and $CaSrAl_2SiO_7$:yTb^{3+} phosphors that the results point out optimal concentration of Ce^{3+} as x = 0.5 mol% and of Tb^{3+} as y = 5.0 mol%. In the present work, co-doping

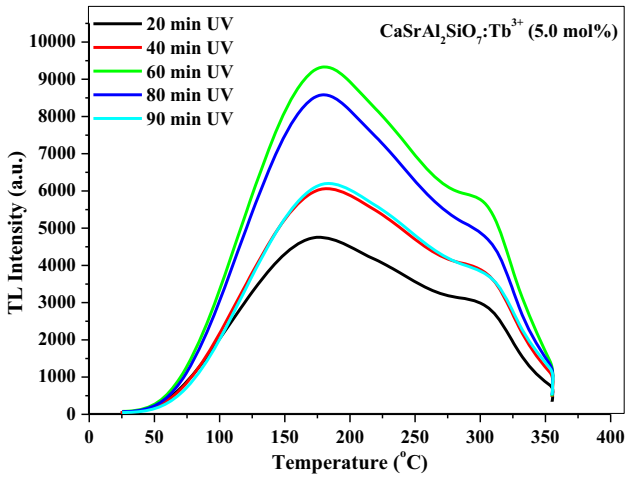

Fig. 3 Effect of UV exposure time on the TL glow curve of $CaSrAl_2SiO_7$:Tb^{3+} (5.0 mol%) phosphor

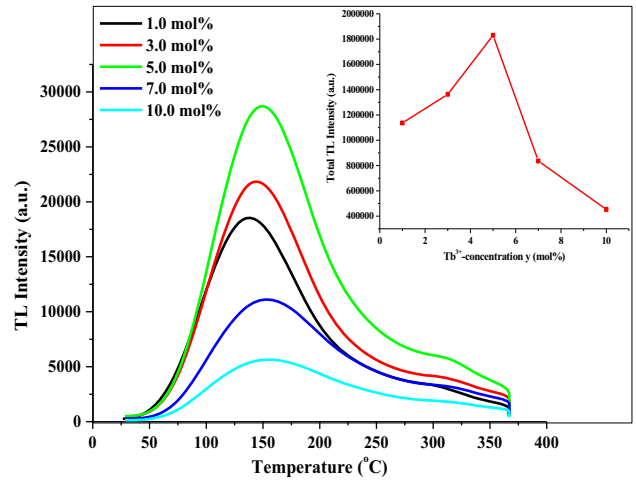

Fig. 4 Tb^{3+} concentration-dependent TL glow curves of $CaSrAl_2SiO_7$:Ce^{3+},Tb^{3+} phosphor with 30-min UV exposure time

of Ce^{3+} and Tb^{3+} was also performed in $CaSrAl_2SiO_7$ host and TL properties of this co-doped sample were also investigated and compared with TL of singly doped samples. Co-doping was performed with fixed concentration of Ce^{3+} (x = 0.5 mol%) and variable concentration of Tb^{3+} (y = 1.0, 3.0, 5.0, 7.0, 10.0 mol%).

Figure 4 shows TL glow curves of $CaSrAl_2SiO_7$:Ce^{3+} (x = 0.5 mol%), Tb^{3+} (y = 1.0, 3.0, 5.0, 7.0, 10.0 mol%) phosphors with fixed UV irradiation time. Glow curves for all samples had similar shape but with change in glow curve area. Concentration quenching occurred at 5.0 mol% of Tb^{3+} ions (see inset of Fig. 4). Like Ce^{3+} and Tb^{3+} singly doped samples, impact of various UV irradiation time on the TL glow curve of optimized co-doped $CaSrAl_2SiO_7$:Ce^{3+} (0.5 mol%),Tb^{3+} (5.0 mol%) sample was seen and this result is depicted in Fig. 5. It can be clearly seen from Fig. 5 that TL intensity of optimized co-doped phosphor increased up to 100 min of UV exposure and then decreased.

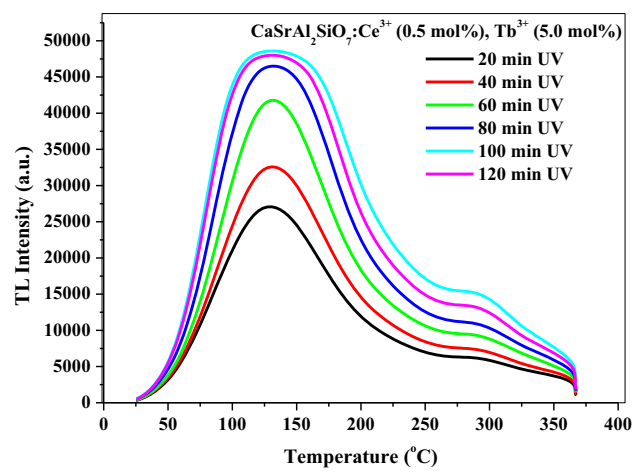

Fig. 5 Effect of UV exposure time on the TL glow curve of $CaSrAl_2SiO_7$:Ce^{3+},Tb^{3+} phosphor

3.2.4 *Evaluation of TL parameters*

To determine TL parameters, broad glow curves of 60-min UV exposed $CaSrAl_2SiO_7$:Tb^{3+} (5.0 mol%) and 100-min UV exposed $CaSrAl_2SiO_7$:Ce^{3+} (0.5 mol%),Tb^{3+} (5.0 mol%) samples were first applied to computerized glow curve deconvolution (CGCD) method. Both samples were found to have four overlapping peaks in their parent glow curves. The position of constituent peaks is shown in Fig. 6. TL parameters like geometrical shape factor (μ_g), order of kinetics (b), frequency factor (S) and activation energy (E) were extracted using Chen's peak shape method. The calculated TL parameters of Tb^{3+}-doped and Ce^{3+},Tb^{3+} co-doped $CaSrAl_2SiO_7$ phosphors are listed in Table 1.

3.2.5 *TL emission spectra*

Figure 7 represents comparison of TL emission spectra of $CaSrAl_2SiO_7$:Ce^{3+}, $CaSrAl_2SiO_7$:Tb^{3+} and $CaSrAl_2SiO_7$:Ce^{3+},Tb^{3+} phosphors. Emission spectra were recorded using interference band pass filters of various wavelengths from 400 to 700 nm. Emission spectra of Ce^{3+}-doped sample was already discussed in our previous article [7], here it is shown for comparison only. The three samples have characteristic

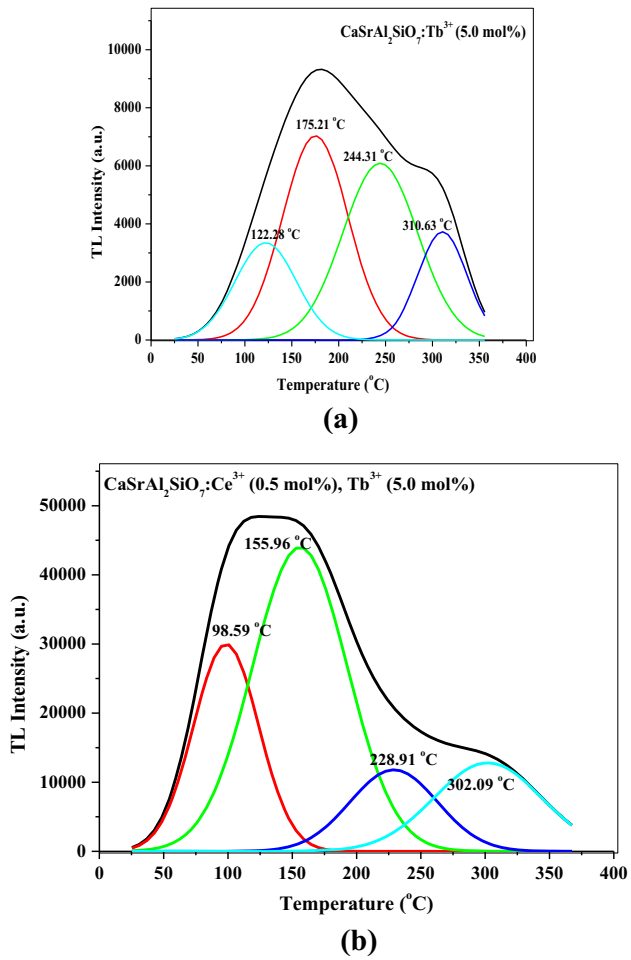

Fig. 6 Representation of peak deconvolution on parent glow curve of **a** $CaSrAl_2SiO_7$:Tb^{3+} and **b** $CaSrAl_2SiO_7$: Ce^{3+},Tb^{3+} phosphors

emission peaks of respective dopant and co-dopant ions. $CaSrAl_2SiO_7$:Tb^{3+} sample has emission peaks at around 480, 545 and 590 nm these are due to characteristic transition $^5D_4 \rightarrow {}^7F_6$, $^5D_4 \rightarrow {}^7F_5$ and $^5D_4 \rightarrow {}^7F_4$ of Tb^{3+} ions [11]. $CaSrAl_2SiO_7$:Ce^{3+},Tb^{3+} sample has characteristic peak of Ce^{3+} ions at around 420 nm, due to 5d ($^5D_{3/2}$) → 4f ($^2F_{5/2}$) [12, 13]and

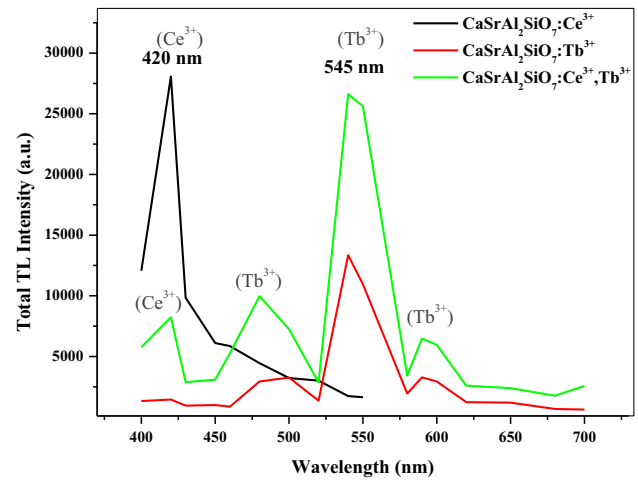

Fig. 7 TL Emission spectra of $CaSrAl_2SiO_7$:Ce^{3+}, $CaSrAl_2SiO_7$:Tb^{3+} and $CaSrAl_2SiO_7$:Ce^{3+},Tb^{3+} phosphors

characteristic peaks of Tb^{3+} ions situated at around 480, 545 and 600 nm; these are due to above-mentioned transitions of Tb^{3+} ions.

Figure 8 shows the comparative TL glow curves of the three optimized phosphors. Ce^{3+},Tb^{3+} co-doped phosphor has most intense TL properties among all three. Also from Fig. 7 it is clearly visible that TL emission of cerium ions is decreased, while TL emission of terbium ions is increased in co-doped sample; hence co-doping of small amount of Ce^{3+} ions, i.e., 0.5 mol%, may enhance TL emission of Tb^{3+} ions in $CaSrAl_2SiO_7$ host.

Present study concludes that among the three, Ce^{3+},Tb^{3+} co-doped $CaSrAl_2SiO_7$ phosphor has almost linear increment in total TL intensity with respect to UV exposure time up to 100 min, which is very large range as compared to other UV irradiated silicate, aluminate and aluminosilicate-based phosphors such as $Ca_2Al_2SiO_7$:Ce^{3+},Tb^{3+} [14]; $Ca_2Al_2SiO_7$:Ce^{3+}[15]; $BaMgAl_{10}O_{17}$:Ce^{3+} [16]. Hence

Table 1 Calculated TL parameters

Phosphor	T_m (°C)	μ_g	b	E (eV)	S (s^{-1})
$CaSrAl_2SiO_7$:Tb^{3+} (5.0 mol%)	122.28	0.48	1	0.46	8.07×10^6
	175.21	0.48	1	0.57	2.45×10^7
	244.31	0.49	1	0.75	1.82×10^8
	310.63	0.70	2	1.41	2.12×10^{13}
$CaSrAl_2SiO_7$:Ce^{3+} (0.5 mol%),Tb^{3+} (5.0 mol%)	98.59	0.49	1	0.54	2.35×10^8
	155.96	0.5	2	0.53	1.4×10^7
	228.91	0.49	1	0.78	7.45×10^8
	302.09	0.49	1	0.82	1.37×10^8

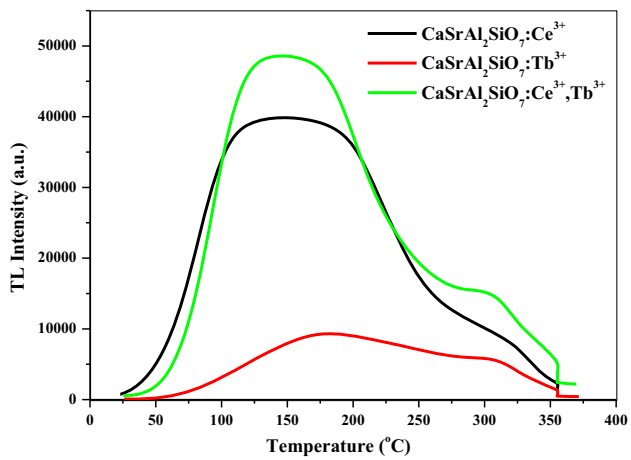

Fig. 8 Comparative TL glow curves of $CaSrAl_2SiO_7:Ce^{3+}$, $CaSrAl_2SiO_7:Tb^{3+}$ and $CaSrAl_2SiO_7:Ce^{3+},Tb^{3+}$ phosphors

$CaSrAl_2SiO_7:Ce^{3+},Tb^{3+}$ phosphor may be most appropriately useful for UV dosimeter application.

4 Conclusions

$CaSrAl_2SiO_7:yTb^{3+}$ and $CaSrAl_2SiO_7:Ce^{3+},yTb^{3+}$ phosphors were prepared by solid-state reaction method. Detail comparative TL study of singly doped and co-doped samples was investigated. Concentration-dependent TL glow curves of $CaSrAl_2SiO_7:yTb^{3+}$ phosphor and $CaSrAl_2SiO_7:Ce^{3+},yTb^{3+}$ phosphors were measured and found that 5.0 mol % is optimized concentration of Tb^{3+} ions in both samples. Tb^{3+} singly doped sample showed linear increment in TL intensity up to 60 min, while Ce^{3+},Tb^{3+} co-doped sample showed this linearity up to 100 min, also TL properties of co-doped sample got enhanced with inclusion of 0.5 mol% of Ce^{3+} ions, this was also verified from TL emission spectra. Hence the optimized $CaSrAl_2SiO_7:Ce^{3+}$(0.5 mol%),Tb^{3+}(5.0 mol%) phosphor may be a potential candidate for UV dosimeter application.

References

1. B.C. Bhatta, M.S. Kulkarni, Thermoluminescent phosphors for radiation dosimetry. Defect Diffus. Forum **347**, 179–227 (2014). https://doi.org/10.4028/www.scientific.net/DDF.347.179
2. T.H. Van, S.N. Manh, Q.V. Xuan, S. Bounyavong, Photoluminescence and thermoluminescence characteristics of $Sr_3B_2O_6:Eu^{2+}$ yellow phosphor. J. Lumin. **31**, 1103–1108 (2016)
3. N.A. Razak, S. Hashim, M.H.A. Mhareba, N. Tamchek, Photoluminescence and thermoluminescence properties of Li_2O-Na_2O-B_2O_3 glass. J. Lumin. **31**, 754–759 (2016)
4. C. Furetta, F. Santopietro, C. Sanipoli, G. Kitis, Thermoluminescent (TL) properties of the perovskite $KMgF_3$ activated by Ce and Er impurities. Appl. Radiat. Isot. **55**, 533–542 (2001)
5. S. Sharma, N. Brahme, D.P. Bisen, P. Dewangan, Luminescence properties of near-UV excitable yellow-orange light emitting warm $CaSrAl_2SiO_7:Sm^{3+}$ phosphors. J. Rare Earths **37**, 365–373 (2019)
6. R. Capelletti, Luminescence, in *Reference Module in Materials Science and Materials Engineering* (2017). https://doi.org/10.1016/B978-0-12-803581-8.012047-9
7. S. Sharma, N. Brahme, D.P. Bisen, P. Dewangan, S. Tigga, G. Tiwari, A. Khare, Study on photoluminescence and thermoluminescence properties of UV-irradiated $CaSrAl_2SiO_7:Ce^{3+}$ phosphors. J. Mater. Sci. **29**, 1412–1419 (2018)
8. K. Sharma, S. Bahl, B. Singh, P. Kumar, S.P. Lochab, A. Pandey, $BaSO_4$: Eu as an energy independent thermoluminescent radiation dosimeter for gamma rays and ^{C6}+ ion beam. Radiat. Phys. Chem. **145**, 64–73 (2018)
9. D. Joseph Daniel, O. Annalakshmi, U. Madhusoodanan, P. Ramasamy, Thermoluminescence characteristics and dosimetric aspects of fluoroperovskites (NaMgF3:Eu2+, Ce3+). J. Rare Earths **32**(6), 496 (2014)
10. N. Kaur, M. Singh, L. Singh, S.P. Lochab, Investigation of thermoluminescence characteristics of gamma irradiated phlogopite mica. Radiat. Phys. Chem. **87**, 26–30 (2013)
11. D. Deng, R. Chen, W. Feng, H. Guan, Terbium single-doped or terbium and sodium codoped barium zinc phosphate: a novel green phosphor for near ultraviolet-pumped white light emitting diodes. Spectrosc. Lett. **50**(8), 451–455 (2017)
12. S. Sharma, N. Brahme, D.P. Bisen, P. Dewangan, R. Gupta, Generation of cold white light by using energy transfer process in single phase Ce^{3+}/Tb^{3+} co-doped $CaSrAl_2SiO_7$ phosphor. Opt. Laser Technol. **135**, 106682 (2021)
13. P. Parasuraman, J. Rajeev Gandhi, M. Rathnakumari, P. Sureshkumar, Photoluminescence in cerium doped barium aluminium borate difluoride—$BaAlBO_3F_2$ glass ceramics. Optik **127**, 8956–8962 (2016)
14. G. Tiwari, N. Brahme, D.P. Bisen, S.K. Sao, R. Sharma, Thermoluminescence and mechanoluminescence properties of UV-irradiated $Ca_2Al_2SiO_7:Ce^{3+}$, Tb^{3+} phosphor. Phys. Procedia **76**, 53–58 (2015)
15. G. Tiwari, N. Brahme, R. Sharma, D.P. Bisen, S.K. Sao, M. Singh, Fracto-mechanoluminescence and thermoluminescence properties of UV and γ-irradiated $Ca_2Al_2SiO_7:Ce^{3+}$ phosphor. J. Biol. Chem. Lumin. **31**(3), 793–801 (2016)

16. S. Tigga, N. Brahme, D.P. Bisen, Investigations on luminescence behaviour of Ce-activated $BaMgAl_{10}O_{17}$ phosphor. J. Biol. Chem. Lumin. **31**(7), 1306–1312 (2016)

Journal of Materials Science: Materials in Electronics

The Journal of Materials Science: Materials in Electronics is an established refereed companion to the Journal of Materials Science. It publishes papers on materials and their applications in modern electronics, covering the ground between fundamental science, such as semiconductor physics, and work concerned specifically with applications. It explores the growth and preparation of new materials, as well as their processing, fabrication, bonding and encapsulation, together with the reliability, failure analysis, quality assurance and characterization related to the whole range of applications in electronics. The Journal presents papers in newly developing fields such as low dimensional structures and devices, optoelectronics including III-V compounds, glasses and linear/non-linear crystal materials and lasers, high Tc superconductors, conducting polymers, thick film materials and new contact technologies, as well as the established electronics device and circuit materials. —

show all

Editor-in-Chief

Safa O. Kasap

Publishing model

Hybrid (Transformative Journal). How to publish with us, including Open Access

2.478 (2020)

Impact factor

2.171 (2020)

Five year impact factor

Filters

Clear All

- *Web of Science* Coverage
- Open Access
- Category
- Country / Region
- Language
- Frequency
- Journal Citation Reports

efine Your Search Results

J Mater Sci: Mater Electron

Search

rt By: Relevancy

earch Results

ound 2,488 results (Page 1)

Share These Results

id you mean this journal?

JOURNAL OF MATERIALS SCIENCE-MATERIALS IN ELECTRONICS

Publisher: SPRINGER , VAN GODEWIJCKSTRAAT 30, DORDRECHT, NETHERLANDS, 3311 GZ

ISSN / eISSN: 0957-4522 / 1573-482X

Web of Science Core Collection: Science Citation Index Expanded

Additional *Web of Science* Indexes: Current Contents Electronics & Telecommunications Collection | Current Contents Engineering, Computing & Technology | Current Contents Physical, Chemical & Earth Sciences | Essential Science Indicators

Share This Journal

View profile page

** Requires free login.*

ther Possible Matches

JOURNAL OF MATERIALS SCIENCE & TECHNOLOGY

Optics & Laser Technology 135 (2021) 106682

Contents lists available at ScienceDirect

Optics and Laser Technology

journal homepage: www.elsevier.com/locate/optlastec

Full length article

Generation of cold white light by using energy transfer process in single phase Ce^{3+}/Tb^{3+} co-doped $CaSrAl_2SiO_7$ phosphor

Shweta Sharma [a,*], Nameeta Brahme [b], D.P. Bisen [b], Pradeep Dewangan [b,c], Ritu Gupta [d]

[a] Department of Physics, Adarsha Science, J. B. Arts and Birla Commerce College, Dhamangaon (Rly), Maharashtra 444607, India
[b] School of Studies in Physics and Astrophysics, Pt. Ravishankar Shukla University, Raipur, Chhattisgarh 492010, India
[c] Department of Physics, Faculty of Science, Shri Rawatpura Sarkar University, Raipur, Chhattisgarh 492010, India
[d] Department of Physics, National Institute of Technology, Raipur 492010, India

ARTICLE INFO

Keywords:
Photoluminescence
White light emitting phosphor
Cerium terbium co-doped phosphor
Energy transfer process
Sensitizer and activator

ABSTRACT

Single phased $CaSrAl_2SiO_7$ phosphor singly doped with different concentrations of trivalent cerium and terbium; and co-doped with varying Tb^{3+} concentration were prepared by standard solid state reaction (SSR) method. The crystallinity and particle morphology of the product samples were analysed by using XRD and TEM characterizations. Photoluminescence characterizations of singly doped and co-doped samples were studied in detail. $CaSrAl_2SiO_7$:Ce^{3+},Tb^{3+} phosphor exhibit a broad blue emission band at 410 nm and some sharp emission bands in blue green and yellow regions, which originate from Ce^{3+} and Tb^{3+} ions, respectively. By increasing the concentration of Tb^{3+} ions while fixing Ce^{3+} concentration in the host lattice energy transfer takes place from Ce^{3+} to Tb^{3+} ions which create luminescence emission in white region. $CaSrAl_2SiO_7$:Ce^{3+},Tb^{3+} phosphors are proved to be promising candidates for white lighting for outdoor illumination.

1. Introduction

Phosphors that are the luminescent materials are widely utilized in our daily life; some of the best applications of phosphors are color television screen, fluorescent lamps, scintillators, dosimeters, X-ray storage, screen intensifying phosphors, sensors, LEDs, watch dials, laser materials etc. [1]. The white light sources based on light emitting diode have so many valuable advantages as compare to conventional incandescent lamps. White LEDs have longer lifetime, better reliability, environmentally characteristics and higher efficiency which provide significant contractions in power consumption and pollution from fossil fuel power plants [2]. In recent years, researchers have been concentrating on investigation of single composition white-light-emitting phosphors that are excited by UV-LED to prevent some difficulties like the cross-color, instability of color temperature, and expensive cost problems [3]. The process of co-doping of sensitizer and activator into one host matrix is one of the best ways to fabricate a single–phased white-light-emitting material by utilising the principle of energy transfer from sensitizer to activator. Now a days the white light can be obtained from co-doping of divalent and trivalent rare earth elements in a single phase host, white light emission was investigated in Eu^{2+}, Mn^{2+} co-doped $Ca_8MgY(PO_4)_7$ [4], Ce^{3+}, Tb^{3+} co-doped $Ba_2Ln(BO_3)_2Cl$ (Ln = Gd and Y) [5], Ce^{3+}, Dy^{3+} co-doped $Ca_3(P_{1-x}B_xO_4)_2$ [6] and Dy^{3+}, Sm^{3+} co-doped $Lu_3Ga_5O_{12}$ [7]systems [8]. Due to predominant $^5D_4 \rightarrow {}^7F_5$ transition (545 nm) of Tb^{3+} ion it is the best candidate for green luminescence among all rare earth ions. However, within the 4*f* configurations of the Tb^{3+} ion, the electric dipole transitions is both spin and parity forbidden, which results in the weak absorption intensity in the near UV region and the narrow width. Therefore a suitable sensitizer is must for the Tb^{3+} activated phosphors. From the very beginning to recent years, Ce^{3+} ion is proven to be an excellent sensitizer for Tb^{3+} ion. Ce^{3+} ion transfer a fraction of its energy to Tb^{3+} ion depending up on its lowest 5d electronic state and broad absorption and emission bands associated with 4f → 5d transitions [9,10,11].

In the present work we synthesized a novel single phase $CaSrAl_2SiO_7$:Ce^{3+},Tb^{3+} phosphor by solid state reaction (SSR) method for generation of cool white-light emission. Photoluminescence (PL) behaviour shows that the present co-doped phosphor covers the entire range of visible region which can create cool white emission which was resulted from the energy transfer from Ce^{3+} to Tb^{3+} ions. To the best of our knowledge, luminescence properties and energy transfer between Ce^{3+} and Tb^{3+} in $CaSrAl_2SiO_7$ host lattice have not been reported so far. PL spectrum of Ce^{3+},Tb^{3+} co-doped sample was compared with PL spectra Ce^{3+} and Tb^{3+} single doped sample. Preparation of powder samples was

* Corresponding author.
E-mail address: sharma.shweta2812@gmail.com (S. Sharma).

https://doi.org/10.1016/j.optlastec.2020.106682
Received 18 May 2020; Received in revised form 19 September 2020; Accepted 11 October 2020

confirmed by X-ray diffraction (XRD) analysis and average particle size was estimated from transmission electron microscopy (TEM).

2. Synthesis and experimental

In the present investigation powder samples $CaSrAl_2SiO_7:Ce^{3+}$, $CaSrAl_2SiO_7:Tb^{3+}$ and $CaSrAl_2SiO_7:Ce^{3+},Tb^{3+}$ were synthesized by SSR method at 1300 °C. The preferred raw materials were calcium carbonate ($CaCO_3$, analytical pure 99.90%), strontium carbonate ($SrCO_3$, analytical pure 99.90%), aluminium oxide (Al_2O_3, analytical pure = 98%), silicon di-oxide (SiO_2, analytical pure 99.99%), ceric oxide (CeO_2, analytical pure 99.99%) and terbium oxide (Tb_2O_3, analytical pure 99.99%). The synthesis route can be understood from the flow chart as shown in Fig. 1.

The luminescent properties of prepared phosphors were analysed by using a RF-5301PC Shimadzu spectrofluorophotometer equipped with a xenon lamp (150 W) as an excitation source. XRD data was obtained with Cu-Kα radiation using a D2 phaser Bruker diffractometer. Average particle size was determined by a JEOL/JEM 2100 transmission electron microscope using LaB_6 as electron source which is available at SAIF Kochi, India.

3. Results and discussion

3.1. XRD analysis

The phase composition and purity of the synthesized samples were measured by XRD method. The XRD patterns of Ce^{3+}/Tb^{3+} single- or co-doped $CaSrAl_2SiO_7$ samples are depicted in Fig. 2. All the reflections of as-prepared samples are in good agreement with the $CaSrAl_2SiO_7$ host and can be indexed to the JCPDS card (No. 26–0327). XRD result of $CaSrAl_2SiO_7:Ce^{3+}$ (1.0 mol%), $CaSrAl_2SiO_7:Tb^{3+}$ (5.0 mol%) and $CaSrAl_2SiO_7:Ce^{3+}$ (1.0 mol%),Tb^{3+} (5.0 mol%) phosphors indicates formation of single phase as no additional peaks from other phases were observed, which shows that the doping of small amount of Ce^{3+}/Tb^{3+} ions does not cause any significant influence on the crystal structure of $CaSrAl_2SiO_7$ host. $CaSrAl_2SiO_7$ has a tetragonal crystal structure with a space group of $P\bar{4}2_1m$.

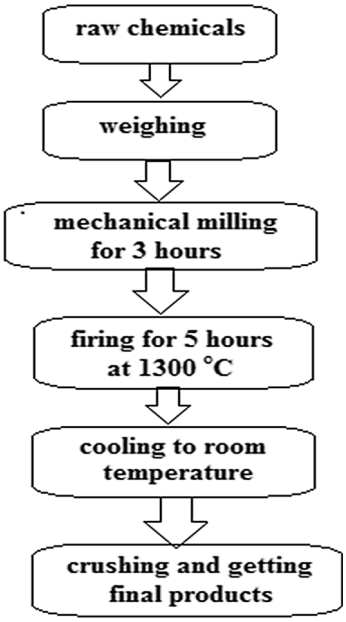

Fig. 1. Synthesis route of $CaSrAl_2SiO_7:Ce^{3+}/Tb^{3+}$ phosphors by SSR method.

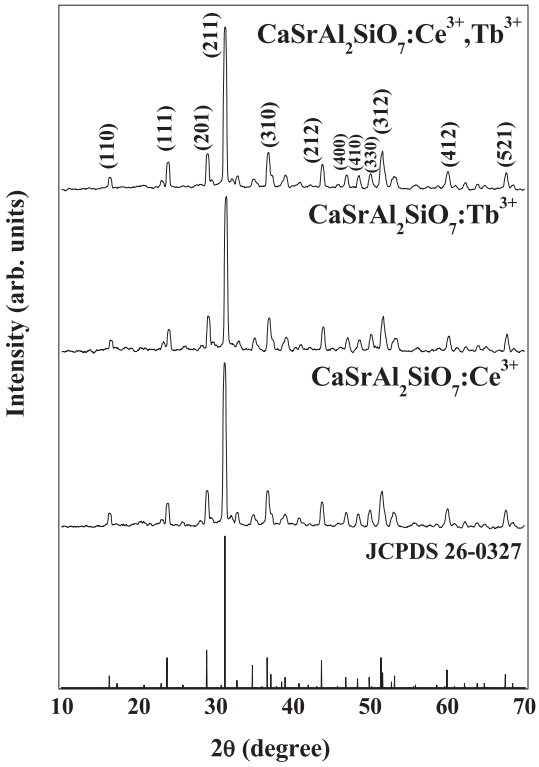

Fig. 2. XRD patterns of $CaSrAl_2SiO_7:Ce^{3+}/Tb^{3+}$ phosphors.

3.2. TEM analysis

A TEM utilizes energetic electrons to provide topographical, morphological, compositional and crystallographic information on samples. The TEM images allow observers to view samples on a molecular level, making possibility to analyse structure and texture. The TEM images of $CaSrAl_2SiO_7:Ce^{3+}$(1.0 mol%), $CaSrAl_2SiO_7:Tb^{3+}$(5.0 mol %) and $CaSrAl_2SiO_7:Ce^{3+}$(1.0 mol%),Tb^{3+}(5.0 mol%) phosphors at the magnifications 100 nm are shown in Fig. 3 (a), 3 (b) and 3 (c), respectively along with their Selected Area Electron Diffraction (SAED) patterns. The agglomeration of powder particles was observed in TEM images this was because of high temperature treatment. The average particle size of entire phosphors is found in nanometre range between 40 and 100 nm. The main diffraction rings in SAED patterns are associated with the diffraction planes in XRD pattern.

3.3. Photoluminescence (PL) spectroscopy

3.3.1. PL of $CaSrAl_2SiO_7:Ce^{3+}$ phosphor

Trivalent Cerium (Ce^{3+}) and terbium (Tb^{3+}) doped phosphors are attractive materials for a broad range of applications. Cerium ions can act as sensitizer in most of luminescent materials. Influence of cerium and terbium concentration on photoluminescence of singly doped $CaSrAl_2SiO_7$ phosphor was first seen. Figs. 4a and 4b exhibit PL excitation (PLE) and PL emission spectra of $CaSrAl_2SiO_7:xCe^{3+}$ phosphor for various concentrations of Ce^{3+} ions, i.e., $x = 0.1, 0.3, 0.5, 1.0, 2.0, 3.0$ and 4.0 mol%, respectively. Optimum luminescence was observed for 1.0 mol% of Ce^{3+} ions and then quenching of emission arises. Three excitation peaks were observed with 415 nm emission for entire series; the excitation peaks were due to 4f → 5d transitions and situated at 250, 290 and 345 nm as shown in inset of Fig. 4a. The strongest excitation at 345 nm was particularly selected to record emission spectra of $CaSrAl_2SiO_7:Ce^{3+}$ phosphors. Concentration dependent PL emission spectra of $CaSrAl_2SiO_7:Ce^{3+}$ sample is displayed in Fig. 4b. There was no change in position of PL emission peaks for various concentrations of Ce^{3+} ions.

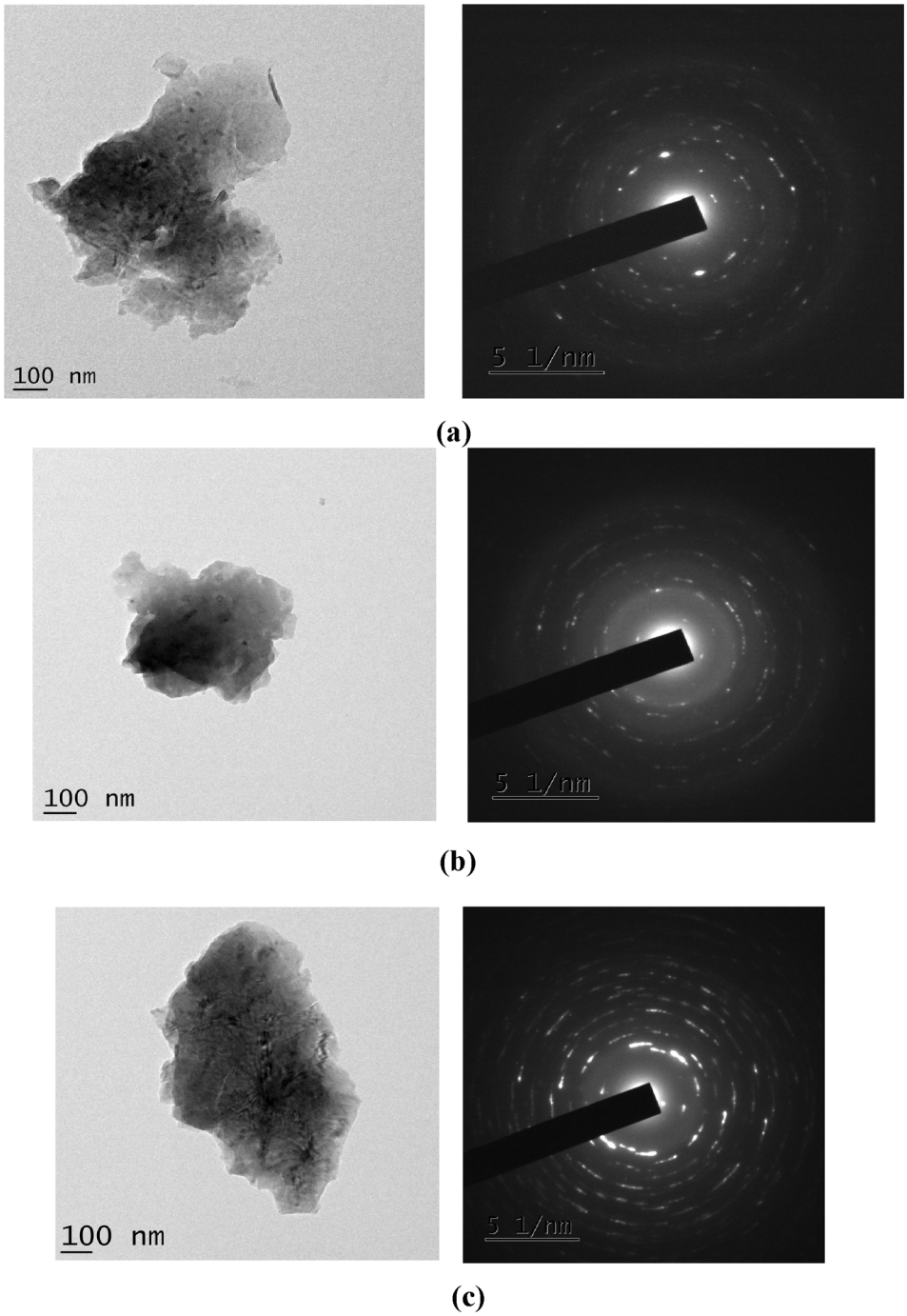

Fig. 3. TEM images of **(a)** $CaSrAl_2SiO_7:Ce^{3+}$, **(b)** $CaSrAl_2SiO_7:Tb^{3+}$ and **(c)** $CaSrAl_2SiO_7:Ce^{3+},Tb^{3+}$ phosphors.

As-prepared $CaSrAl_2SiO_7:xCe^{3+}$ phosphors show a broad emission peak in the blue wavelength region located at around 415 nm which is ascribed to 5d ($^5D_{3/2}$) → 4f ($^2F_{5/2}$) transition of Ce^{3+}. A graph between Ce^{3+}-concentration and luminescence intensity is shown in the inset of Fig. 4b, which shows PL emission intensity increases with rise in Ce^{3+}-concentration and maximum intensity is observed at 1.0 mol% of Ce^{3+} after that quenching in luminescence emission occurs.

3.3.2. PL of $CaSrAl_2SiO_7:Tb^{3+}$ phosphor

Fig. 5a displays PLE spectra of $CaSrAl_2SiO_7:Tb^{3+}$ phosphor doped with various Tb^{3+}-concentrations such as 1.0, 3.0, 5.0, 7.0 and 10.0 mol %. Optimum excitation spectrum was monitored for $CaSrAl_2SiO_7:Tb^{3+}$ (5.0 mol%) phosphor that is represented in the inset of Fig. 5a. PLE spectra for entire series (monitored with 545 nm emission wavelength) have similar fashion consisting a broad absorption band in 220–280 nm region, centred at around 240 nm and with three small excitation peaks at around 351 nm, 375 nm and 483 nm that are due to $^7F_6 \rightarrow {}^5D_2$, $^7F_6 \rightarrow {}^5L_{10}$ and $^7F_6 \rightarrow {}^5D_4$ transitions, respectively [12]. The absorption band at 240 nm is assigned to $4f^8$ ($^7F_5$) → $4f^7 5d^1$ transition of Tb^{3+} ions in the $CaSrAl_2SiO_7$ host composition, which is a spin-allowed transition in accordance with Laporte's rule. Tb^{3+}-doped materials necessarily have strong absorption band in the 200–300 nm range due to 4f – 5d transition. Emission spectra of $CaSrAl_2SiO_7$ doped with × mol% of Tb^{3+} (where × equals to 1.0 – 10.0 mol%) are shown in Fig. 5b. A series of characteristics luminescence signals of Tb^{3+} was appeared in the emission spectra within the range 350–600 nm when samples were excited at

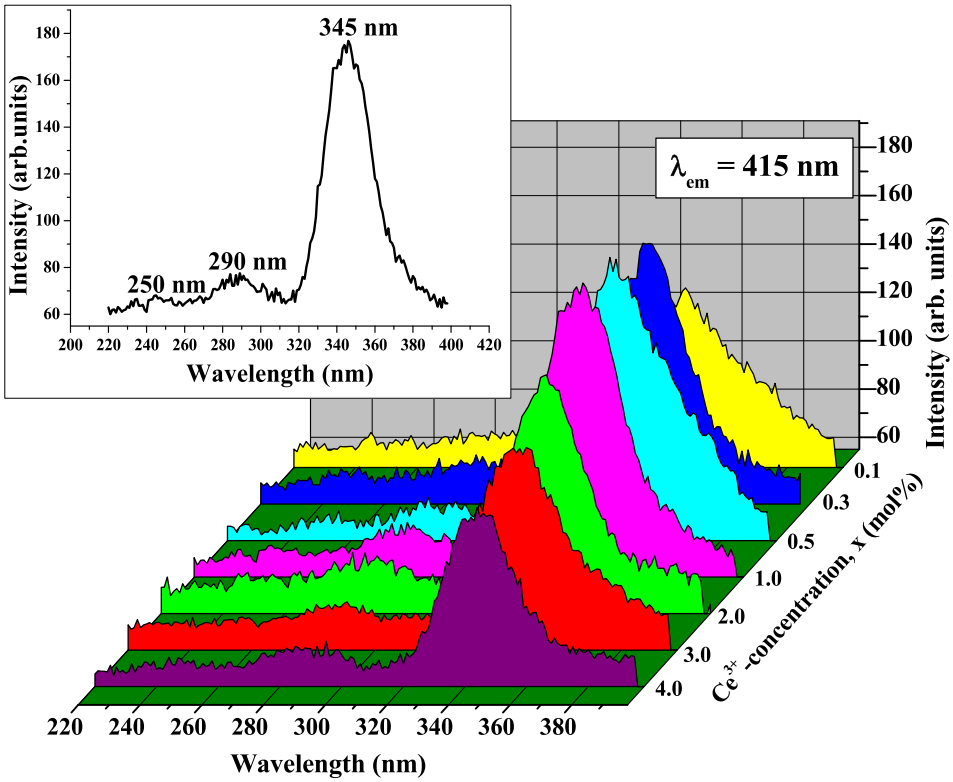

Fig. 4a. PL excitation spectra of $CaSrAl_2SiO_7:Ce^{3+}$ phosphor at different mol% concentration of Ce^{3+} ions. Inset shows PL excitation spectrum of $CaSrAl_2SiO_7:Ce^{3+}$ (1.0 mol%) phosphor.

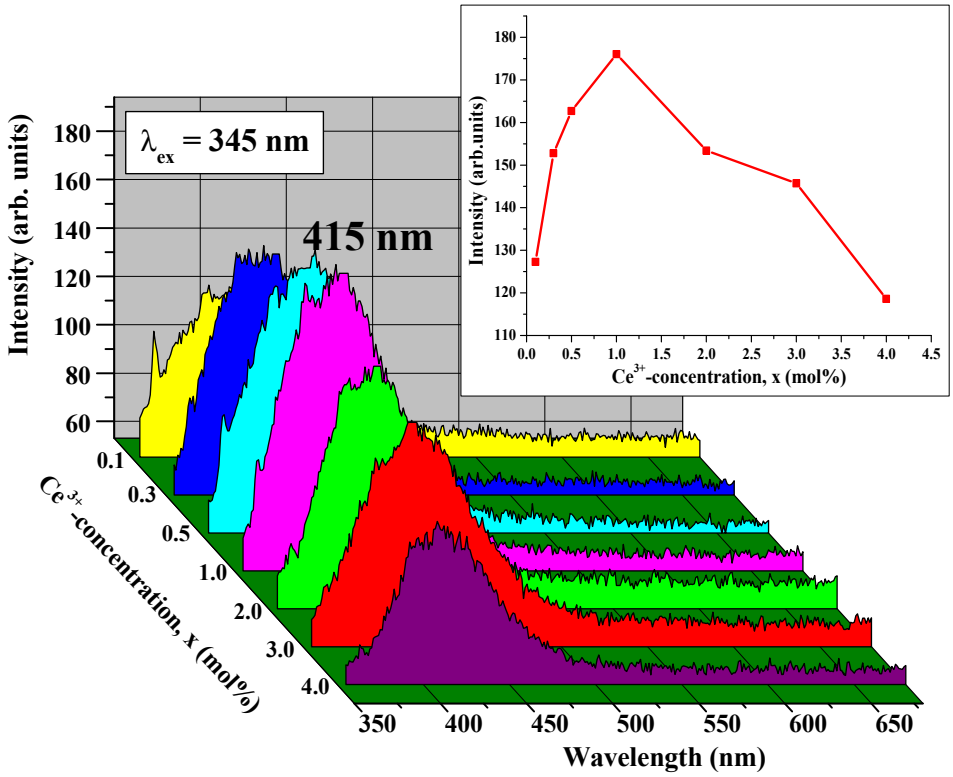

Fig. 4b. PL emission spectra of $CaSrAl_2SiO_7:Ce^{3+}$ phosphor at different mol% concentration of Ce^{3+} ions. Inset shows emission intensity as a function of Ce^{3+}-concentration *x*.

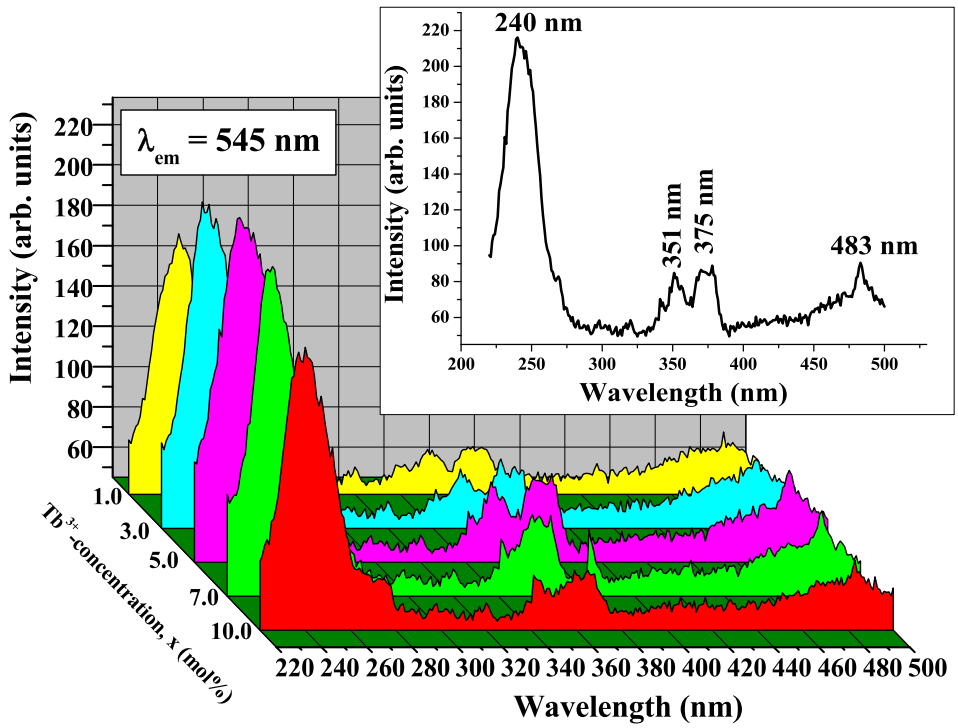

Fig. 5a. PL excitation spectra of $CaSrAl_2SiO_7$:Tb^{3+} phosphor at different mol% concentration of Tb^{3+} ions. Inset shows PL excitation spectrum of $CaSrAl_2SiO_7$:Tb^{3+} (5.0 mol%) phosphor.

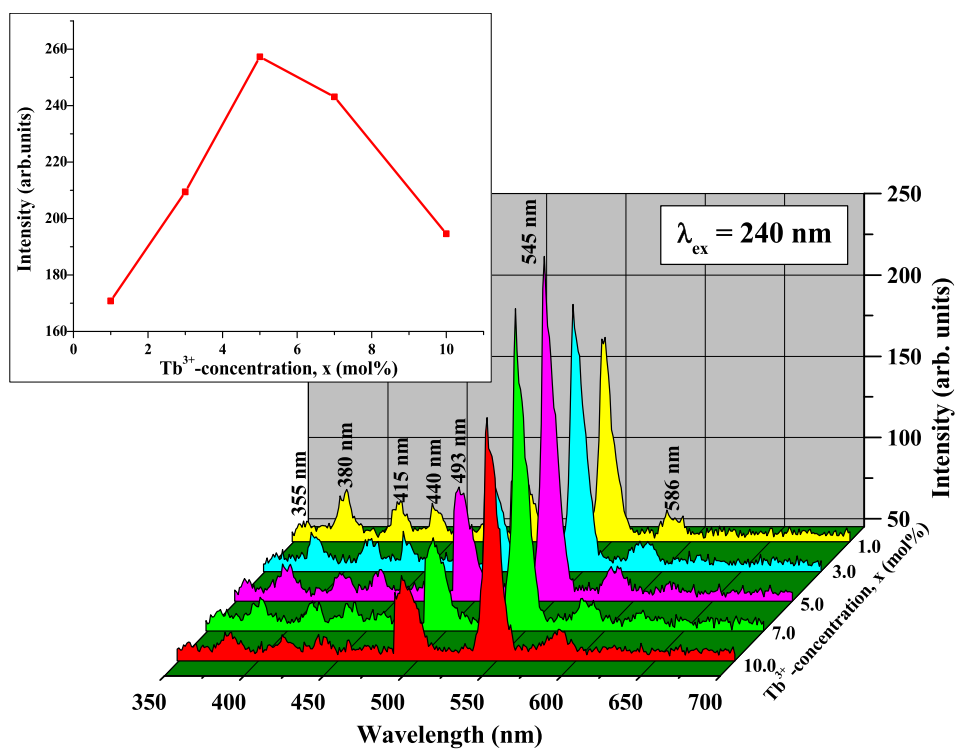

Fig. 5b. PL emission spectra of $CaSrAl_2SiO_7$:Tb^{3+} phosphor at different mol% concentration of Tb^{3+} ions. Inset shows emission intensity (545 nm) as a function of Tb^{3+}-concentration *x*.

240 nm. The emission spectra showed few sharp emission bands that correspond to the $^5D_4 \rightarrow {}^7F_J$ intraconfigurational transitions of Tb^{3+} ions (Tb green luminescence) [13]. The emission spectrum of the Tb^{3+} activator normally presents two typical sets of intense line systems from the $^5D_4 \rightarrow {}^7F_J$ (J = 3 – 6, 620 – 465 nm) and $^5D_3 \rightarrow {}^7F_J$ (J = 3 – 6; 465 – 375 nm) transitions, which result in green and blue emissions, respectively. The dominant set usually corresponds to $^5D_4 \rightarrow {}^7F_J$ transitions (green set), whereas the $^5D_3 \rightarrow {}^7F_J$ transitions (blue set) are difficult to obtain as a primary emission because of the depopulation of the $^5D_3$ state [14] The emission of $^5D_3 \rightarrow {}^7F_J$ transitions are obtained in the

present case, although their intensity was weak but that could be identified. An examination of luminescence spectra of $CaSrAl_2SiO_7$:Tb^{3+} phosphor notifies that it comprises of two UV emission bands (at 355 and 380 nm), three blue emission bands (at 415, 440 and 493 nm) and one green emission band (at 545 nm) and one yellow band (at 586 nm). The sharp emission peaks originated from 4f to 4f transition of Tb^{3+} ions. The emission at 355 nm is due to host emission. The emission band at 380 nm and blue set of emitting peaks monitored at 415/440 nm are because of $^5D_3 \rightarrow {}^7F_{6,5,4}$ transitions; emission band at 493 nm (blue), 545 nm (green) and 586 nm (yellow) represents the transitions $^5D_4 \rightarrow {}^7F_{6,5,4}$, respectively [15]. The transition $^5D_4 \rightarrow {}^7F_6$ (493 nm) is an allowed electric dipole transition since $\Delta J = 2$ while $^5D_4 \rightarrow {}^7F_5$ (545 nm) is allowed magnetic dipole transition as $\Delta J = 1$. Most intense peak was situated 545 nm which is responsible for green luminescence under UV (240 nm) excitation. Inset in Fig. 5b indicates that PL emission intensity enhanced with increase in Tb^{3+}-concentration and reached an optimum value at a Tb^{3+}-concentration of 5.0 mol%. For inclusion exceeds 5.0 mol%, the luminescence was diminished, this behaviour comes from concentration quenching phenomenon. Concentration quenching originates from non-radiative energy transfer between dopant ions. This behaviour implies that the Tb^{3+} aggregates may be formed at high concentration of Tb^{3+}, these aggregates act as the trapping centers and dissipate absorbed energy non-radiatively and reduces PL emission [16]. The increase in concentration of Tb^{3+} ion enhances the interaction between them. The cross relaxation processes are likely to occur in $^5D_3 \rightarrow {}^5D_4$ and $^7F_6 \rightarrow {}^7F_0$ or $^7F_6 \rightarrow {}^5D_4$ and $^5D_3 \rightarrow {}^7F_0$, and then the luminescent emission is quenched [17].

3.3.3. PL of $CaSrAl_2SiO_7$:Ce^{3+},Tb^{3+} phosphor

A series of $CaSrAl_2SiO_7$:Ce^{3+},Tb^{3+} phosphor was prepared by conventional SSR method by fixing Ce^{3+}-concentration × at 1.0 mol% and changing Tb^{3+}-concentration y (y = 1.0, 3.0, 5.0, 7.0 and 10.0 mol%). Fig. 6a shows comparative PLE spectra of $CaSrAl_2SiO_7$:Ce^{3+}(1.0 mol%), Tb^{3+}(y mol%) with varying Tb^{3+}-concentration. Excitation spectra were measured with constant 545 nm emission of Tb^{3+} ions. Inset in the same figure shows excitation spectrum of the optimized Ce^{3+},Tb^{3+} co-doped phosphor, i.e., $CaSrAl_2SiO_7$:Ce^{3+}(1.0 mol%),Tb^{3+}(5.0 mol%). This co-doped phosphor has first excitation peak at 235 nm, second and the most intense peak at around 345 nm and third very weak peak at 482 nm; the third peak could not be observed for low Tb^{3+}-concentration that means for y = 1.0 and 3.0 mol%. The presence of weak blue peak at 482 nm signifies that $CaSrAl_2SiO_7$:Ce^{3+}(1.0 mol%),Tb^{3+}(y mol%) phosphors with $y \geq 5.0$ mol% can weakly excited by blue light. Excitation bands at around 345 nm is the characteristic of 4f → 5d transition of Ce^{3+} and a peak around 235 nm and 482 nm were seen for Tb^{3+} singly doped sample (see Fig. 5a). The absorption band at 235 and 482 nm are due to $4f^8$ ($^7F_5$) – $4f^75d^1$ [9,18] and $^7F_6 \rightarrow {}^5D_4$ [19] transition of Tb^{3+} ions. It is to be noted that spectral distribution of excitation spectra of Ce^{3+},Tb^{3+} co-doped $CaSrAl_2SiO_7$ phosphors was unchanged while changing Tb^{3+}-concentration y.

Illustration of PL emission spectra of $CaSrAl_2SiO_7$:Ce^{3+}(1.0 mol%), $y$$Tb^{3+}$($y$ = 1.0, 3.0, 5.0, 7.0 and 10.0 mol%) phosphors is shown in Fig. 6b. Upon excitation of Ce^{3+} band at 345 nm, the PL spectra of $CaSrAl_2SiO_7$:Ce^{3+}(1.0 mol%),$y$$Tb^{3+}$ consist of the 5d ($^5D_{3/2}$) → 4f ($^2F_{5/2}$) blue emission broad band centred at 410 nm assigned to Ce^{3+} ions while the blue emissions at 484 and 494 nm ($^5D_4 \rightarrow {}^7F_6$); and green and yellow emissions situated at 545 and 589 nm ($^5D_4 \rightarrow {}^7F_{5,4}$) corresponding to Tb^{3+} ions. Inset in Fig. 6b shows the variation of the emission intensities of Ce^{3+} and Tb^{3+} ions in co-doped sample, versus Tb^{3+} concentration. Although the amount of the Ce^{3+} ions is fixed, their emission intensity gradually decreases along with the increase of the concentration of the Tb^{3+} ions. The cerium emission intensity decreases with increasing Tb^{3+} concentration while the terbium emission intensities increases firstly and then reaches a maximum at the Tb^{3+} concentration of 5.0 mol% and decreased gradually with a further increase of Tb^{3+} concentration. It is clear that the addition of Tb^{3+} ions in the 1.0 mol% Ce^{3+} activated $CaSrAl_2SiO_7$ sample results a decrease of the overall Ce^{3+} emission [9]. The result indicates that a lot of Tb^{3+} ions as acceptors accelerate energy diffusion of donors (Ce^{3+}) before they can fluoresce, which speeds up the average transfer rate of $Ce^{3+} \rightarrow Tb^{3+}$ [10,20]. According to Dexter's energy transfer theory, the calculation of efficiency principally based on the spectral overlap between the emission spectra of the sensitizers and the absorption spectra of the activators [21]. Co-doped phosphor possesses two types of energy transfer pathways: nonradiative and

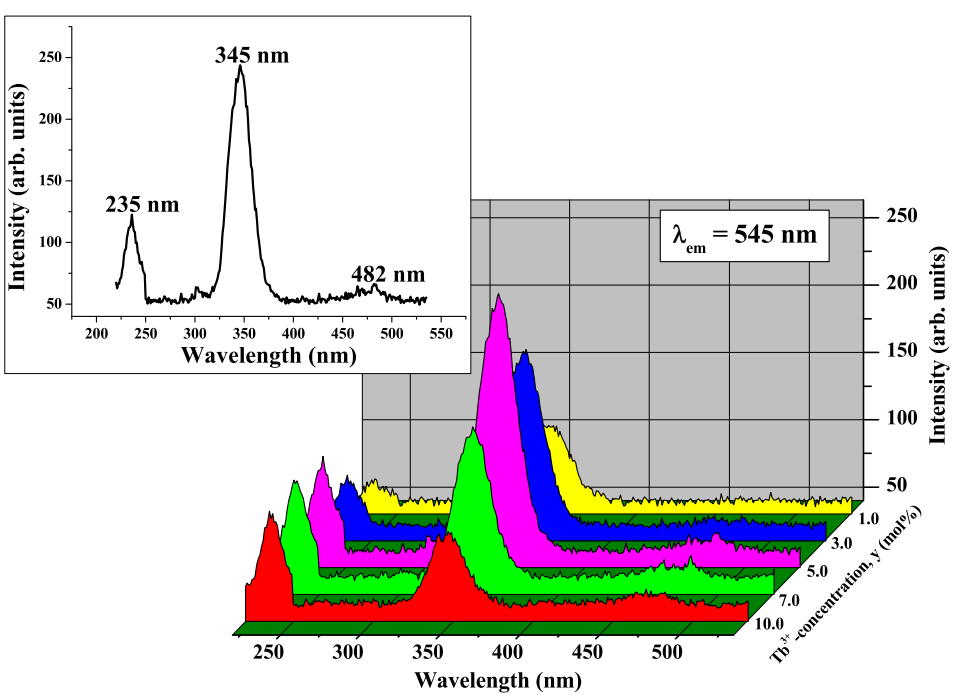

Fig. 6a. PL excitation spectra of $CaSrAl_2SiO_7$:Ce^{3+}(1.0 mol%),Tb^{3+} phosphor at different mol% concentration of Tb^{3+} ions. Inset shows PL excitation spectrum of $CaSrAl_2SiO_7$:Ce^{3+}(1.0 mol%),Tb^{3+}(5.0 mol%) phosphor.

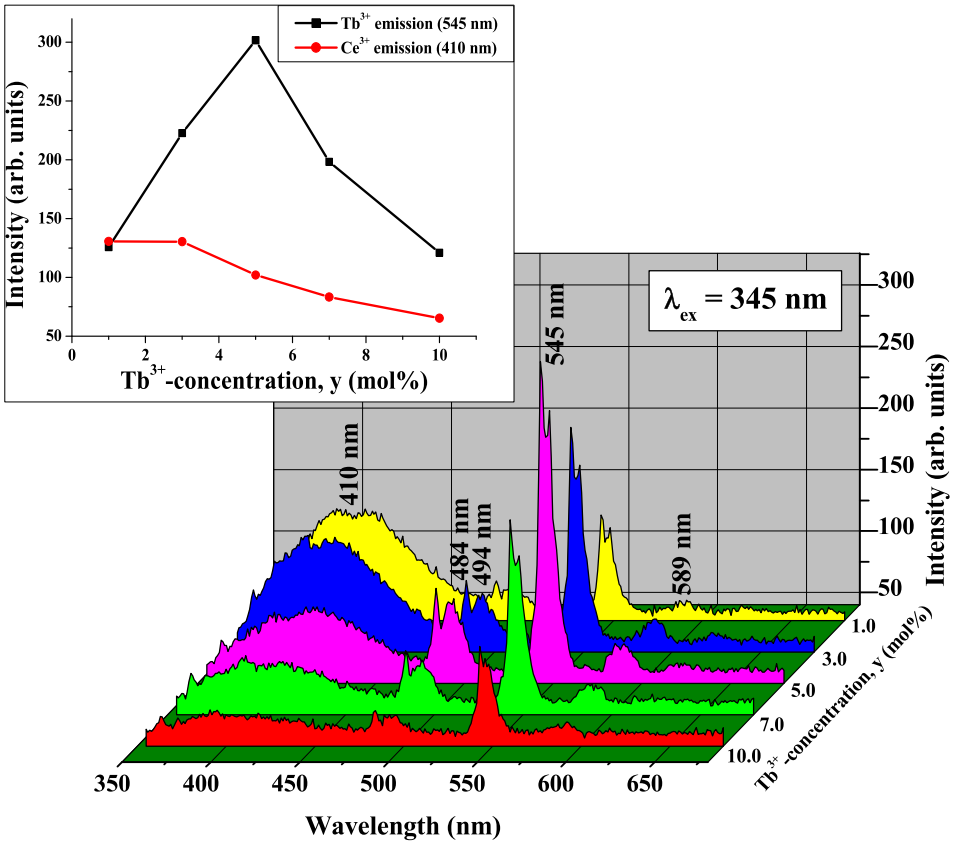

Fig. 6b. PL emission spectra of $CaSrAl_2SiO_7$:Ce^{3+}(1.0 mol%),Tb^{3+} phosphor at different mol% concentration of Tb^{3+} ions. Inset shows emission intensity (410 nm and 545 nm) as a function of Tb^{3+}-concentration *y*.

radiative. The nonradiative transfer mechanism is complex because of the unknown multipolar interaction and exchange interaction [22]. Furthermore, in the radiative energy transfer process, the broad emission (5d → 4f) of the sensitizers, which is allowed by the Laporte parity selection rules, is affected greatly by the crystal field and the covalency of many inorganic hosts [23]. Therefore the sensitized

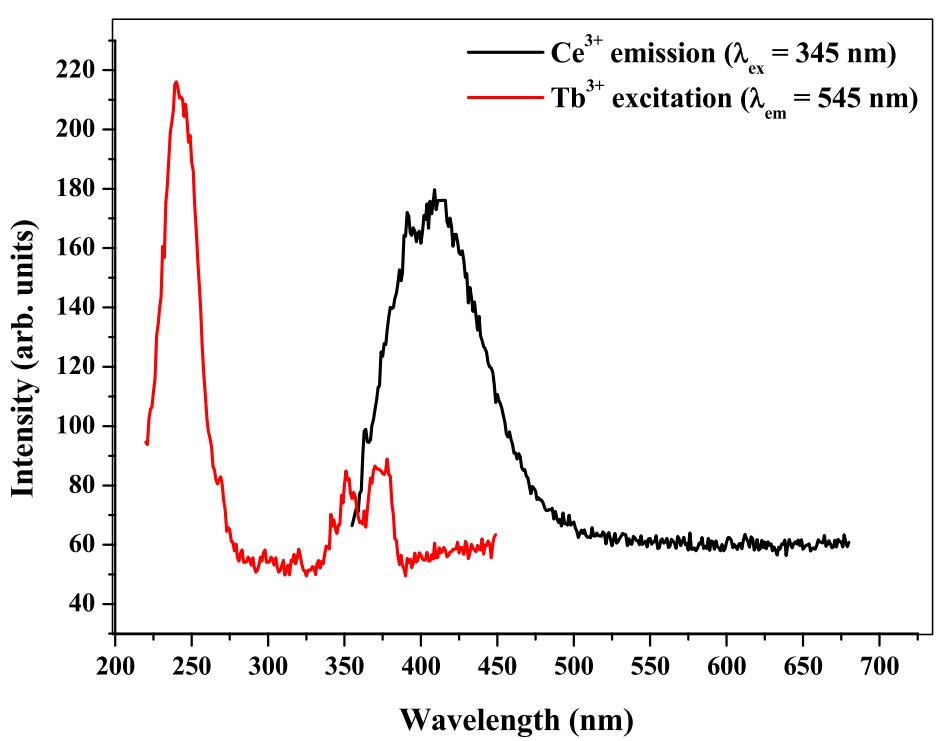

Fig. 7. Overlapping between luminescence spectrum of Ce^{3+} and absorption spectrum of Tb^{3+} in $CaSrAl_2SiO_7$ phosphor.

luminescence of the Tb^{3+} ions by the Ce^{3+} ions can be verified from the Fig. 7, where it was noted that emission spectrum of Ce^{3+} ion overlaps with absorption spectra of Tb^{3+} ion.

The origin of energy transfer process from Ce^{3+} to Tb^{3+} was determined, by using the method based on Dexter's energy transfer formula of multipolar interaction and Reisfeld's approximation:

$$\frac{I_0}{I} = (C)^{\frac{n}{3}}$$

where I_0 and I are the emission intensities of the Ce^{3+} ions without and with the presence of Tb^{3+}, respectively and C is the total dopant concentration of Ce^{3+} and Tb^{3+} ions. The plots of I_0/I versus $C^{n/3}$ for Ce^{3+}:Tb^{3+} (1.0 : 1.0, 3.0, 5.0, 7.0, 10.0 mol%) co-doped $CaSrAl_2SiO_7$ samples, excited at 345 nm with the luminescence monitored at 410 nm, are shown in Fig. 8. The best linear fitting was seen for n = 6 (R^2 = 0.9800), indicating that the energy transfer from Ce^{3+} to Tb^{3+} ions occurs via electric dipole–dipole interaction [24]. Fig. 9 represents the schematic of the energy level system describing energy transfer in the case of $CaSrAl_2SiO_7$:Ce^{3+},Tb^{3+} phosphor.

A comparison beween PL emission of Ce^{3+}/Tb^{3+} singly doped and co-doped samples is shown in Fig. 10, from which it can be seen that in the co-doped sample cerium emission intensity is decreased while terbium emission intensity is enhanced. This result suggested that co-doping of small amount (1.0 mol%) of Ce^{3+} ions in $CaSrAl_2SiO_7$:Tb^{3+} enhanced luminescence emission of Tb^{3+} ions. Thus the energy transfer took place from Ce^{3+} → Tb^{3+} in $CaSrAl_2SiO_7$:Ce^{3+},Tb^{3+} phosphor. Hence Ce^{3+} acted as sensitizer and Tb^{3+} acted as activator.

The color of luminescence emitted from $CaSrAl_2SiO_7$:Ce^{3+} (1.0 mol %), $CaSrAl_2SiO_7$:Tb^{3+} (5.0 mol%) and $CaSrAl_2SiO_7$:Ce^{3+} (1.0 mol%), Tb^{3+} (5.0 mol%) phosphors was determined by Commission International de I'Eclairage (CIE) chromaticity diagram as shown in Fig. 11. CIE chromaticity co-ordinates, calculated correlated color temperature (CCT) value and color purity for three phosphors are examined and represented in table 1. CIE co-ordinates of Tb^{3+} doped and Ce^{3+},Tb^{3+} co-doped samples are very close to equal energy point (0.3333, 0.3333) and highlight emission in near white region, calculated CCT value of these phosphors suggested that these phosphors is considered as cool in appearance. The low value of the color purity indicates the purity for white-light emission [25]. As Ce^{3+},Tb^{3+} co-doped phosphor has low value of color purity as compare to Tb^{3+} doped phosphor, hence co-doping of Ce^{3+} ion sensitises the terbium emission and lowers the value of color purity of Tb^{3+} doped $CaSrAl_2SiO_7$ sample. Thus co-doped sample may be more appropriately useful for white light generation.

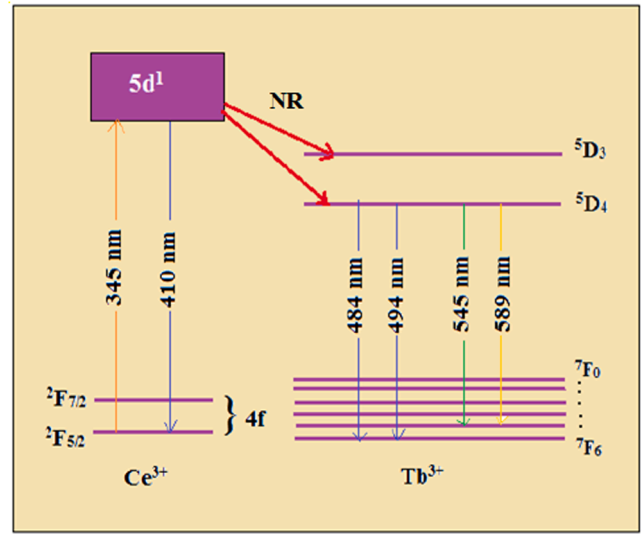

Fig. 9. Scheme of energy-level and energy-transfer pathways in $CaSrAl_2SiO_7$:Ce^{3+},Tb^{3+} phosphor.

4. Conclusions

Tetragonal phase $CaSrAl_2SiO_7$:Ce^{3+}/Tb^{3+} white-light emitting phosphors were successfully prepared by using the solid-state reaction method. The crystallinity and purity of the phase of as-prepared phosphors were measured by XRD technique. $CaSrAl_2SiO_7$:Ce^{3+},Tb^{3+} phosphor showed characteristic luminescence bands of Ce^{3+} (410 nm) and Tb^{3+} (most intense band is at 545 nm) ions. The combination of these emission bands give rise to white-light emission and the chromaticity coordinates for Ce^{3+},Tb^{3+} co-doped phosphor are (x = 0.3007, y = 0.3500) with color purity 9.19×10^{-2} and a CCT value of 6954 K, which are close to the standard cool white region. Although $CaSrAl_2SiO_7$:Tb^{3+} phosphor also emitted near white ligh whose CIE chromaticity co-

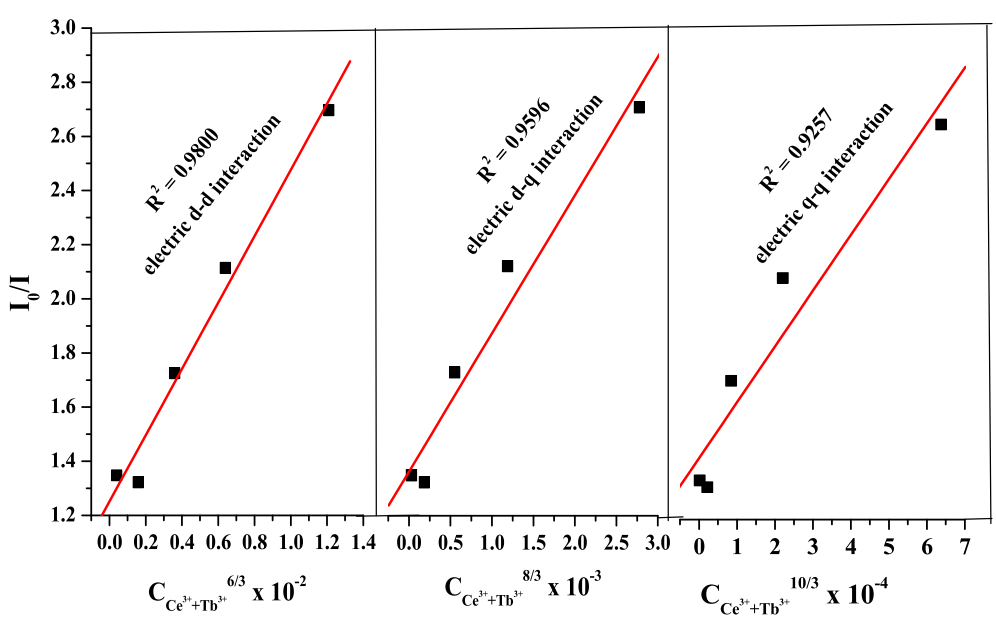

Fig. 8. Plots of I_0/I versus $C_{Ce^{3+}+Tb^{3+}}{}^{n}$ (n = 6, 8 and 10) for Ce^{3+}, Tb^{3+} co-doped $CaSrAl_2SiO_7$ samples excited at 345 nm and with the luminescence monitored at 410 nm.

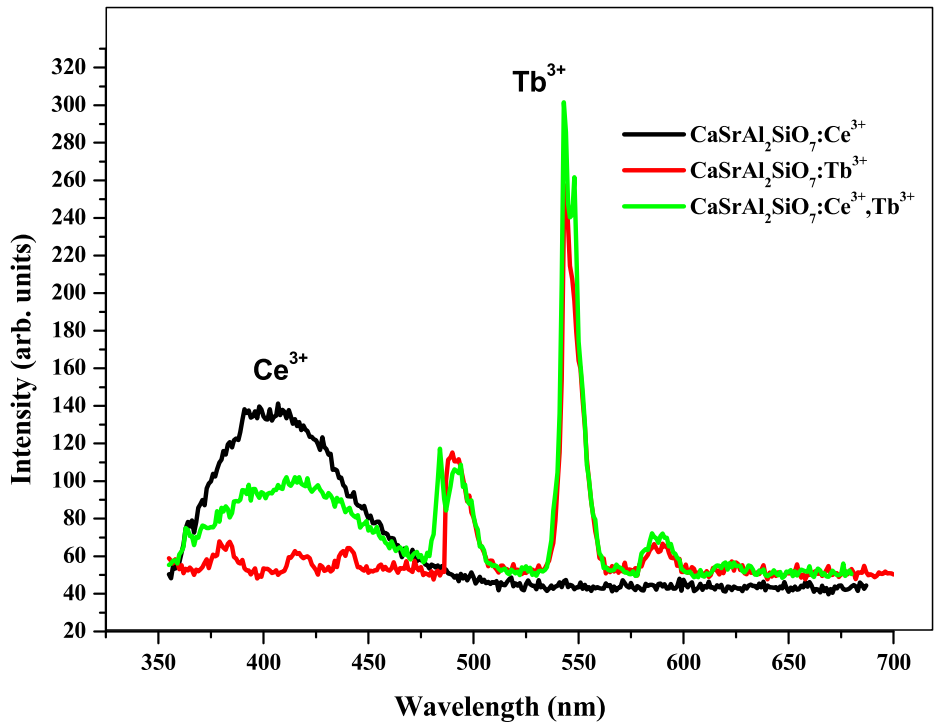

Fig. 10. Comparison beween PL emission spectra of Ce^{3+}/Tb^{3+} singly doped and co-doped $CaSrAl_2SiO_7$ phosphors.

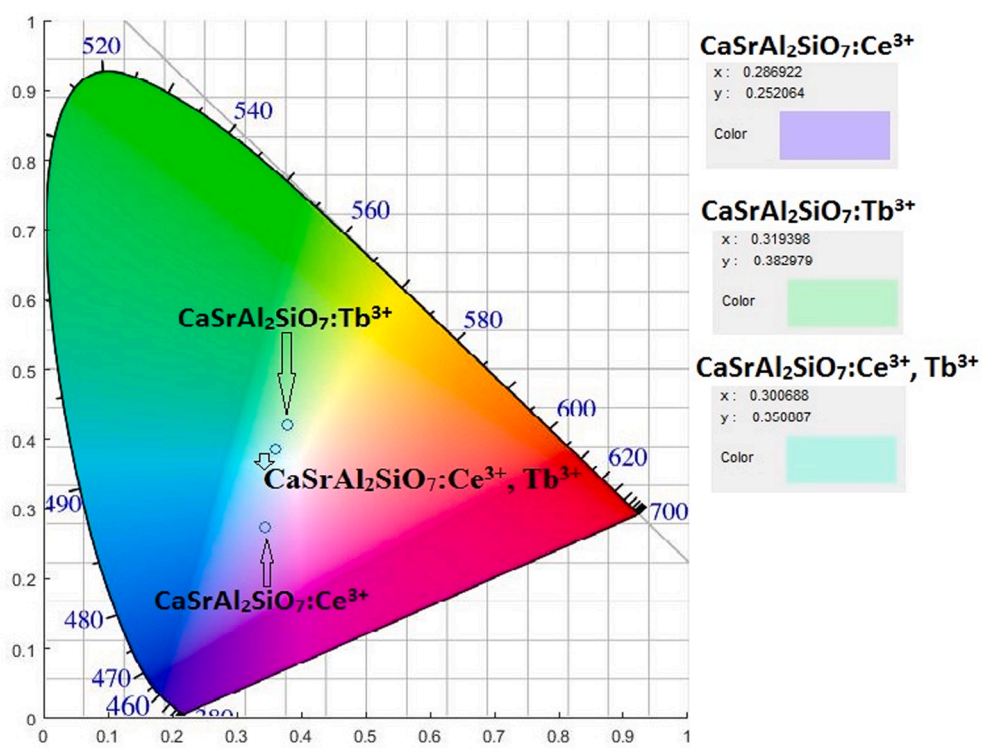

Fig. 11. CIE chromaticity of Ce^{3+}/Tb^{3+} singly doped and co-doped $CaSrAl_2SiO_7$ phosphors.

Table 1
CIE, CCT and color purity values of opimized phosphors.

Phosphor	CIE co-ordinates	CCT	Color purity
$CaSrAl_2SiO_7:Ce^{3+}$	(0.2869, 0.2521)	11959 K	25.47×10^{-2}
$CaSrAl_2SiO_7:Tb^{3+}$	(0.3194, 0.3830)	5972 K	13.05×10^{-2}
$CaSrAl_2SiO_7:Ce^{3+},Tb^{3+}$	(0.3007, 0.3500)	6954 K	9.19×10^{-2}

ordinates are (0.3194, 0.3830), color purity is 13.05×10^{-2}. As the low value of the color purity indicates the purity for white-light emission, hence we can say that inclusion of small amount (1.0 mol%) of Ce^{3+} ions enhanced the purity for white luminescence of Tb^{3+} doped $CaSrAl_2SiO_7$ phosphor. Therefore $CaSrAl_2SiO_7:Ce^{3+},Tb^{3+}$ phosphor can be considered as a potential candidate for fabrication of white LEDs for outdoor illuminations.

5. Compliance with ethical standards

Authors have no conflict of interest.

Declaration of Competing Interest

The authors declared that there is no conflict of interest.

References

[1] A.J. Peter, I.B. Shameem Banu, Synthesis and Luminescent Properties of Tb^{3+} Activated $Li_3Ba_2Gd_{3-x}(MoO_4)_8$ Based Efficient Green Emitting Phosphors, J. Appl. Sci. Eng. 19 (4) (2016) 409–412.

[2] R.-S. Liu, Y.-H. Liu, N.C. Bagkar, Enhanced luminescence of $SrSi_2O_2N_2$:Eu^{2+} phosphors by codoping with Ce^{3+}, Mn^{2+} and Dy^{3+} ions, Appl. Phys. Lett. 91 (2007), 061119.

[3] Chun Che Lin, Yun-Ping Liu, Zhi Ren Xiao, Yin-Kuo Wang, Bing-Ming Cheng and Ru-Shi Liu, All-In-One Light-Tunable Borated Phosphors with Chemical and Luminescence Dynamical Control Resolution, Appl. Mater. Interfaces 6 (2014) 9160–9172.

[4] D. Wen, Z. Dong, J. Shi, M. Gong, W.u. Mingmei, Standard White-Emitting $Ca_8MgY(PO_4)_7$:Eu^{2+}, Mn^{2+} Phosphor for White-Light-Emitting LEDs, ECS Journal of Solid State Science and Technology 2 (9) (2013) R178–R185.

[5] N. Zhang, C. Guo, Heng Jing and Jung Hyun Jeong, Color tunable emission in Ce^{3+} and Tb^{3+} co-doped $Ba_2Ln(BO_3)_2Cl$ (Ln = Gd and Y) phosphors for white light-emitting diodes, Author links open overlay panel, Spectrochimica Acta Part A: Molecular and Biomolecular Spectroscopy 116 (2013) 556–561.

[6] L.u. Meng, C. Zhu, Z. Chen, M. Shi, X. Meng, Ce^{3+} and Dy^{3+} doped $Ca_3(P_{1-x}B_xO_4)_2$ phosphors for white light-emitting applications, Author links open overlay panel, J. Alloy. Compd. 775 (2019) 1044–1051.

[7] Haritha Pamuluri, Mamilla Rathaiah, Kadathala Linganna, Chalicheemalapalli Kulala Jayasankar, Victor Lavın and Vemula Venkatramu, Role of Dy3+ - Sm3+ energy transfer in the tuning of warm to cold white light emission in Dy3+/Sm3+ co-doped Lu3Ga5O12 nano-garnets, New J. Chem., DOI: 10.1039/c7nj04034b.

[8] G.-Y. Lee, W.B. Im, A. Kirakosyan, S.H. Cheong, Ji Yeon Han and Duk Young Jeon, Tunable emission from blue to white light in single-phase $Na_{0.34}Ca_{(0.66-x-y)}Al_{1.66}Si_{2.34}O_8$:x$Eu^{2+}$, y$Mn^{2+}$ (x = 0.07) phosphor for white-light UV LEDs, Opt. Express 21 (3) (2013) 3287–3297.

[9] J.u. Guifang, H.u. Yihua, L.i. Chen, Y. Jin, Z. Yang, T. Wang, Photoluminescence properties of Ce^{3+} and Tb^{3+}-activated $Ba_2Mg(PO_4)_2$, Optical Materials Express 5 (1) (2014) 1–10, https://doi.org/10.1364/OME.5.000001.

[10] Zhen Jia and Mingjun Xia, Blue-green tunable color of Ce3+/Tb3+ coactivated NaBa3La3Si6O20 phosphor via energy transfer, Scientific Reports, 2016, 6, 33283 | DOI: 10.1038/srep33283.

[11] A. Nag, T.R.N. Kutty, Photoluminescence due to efficient energy transfer from Ce^{3+} to Tb^{3+} and Mn^{2+} in (Sr_3AlSiO_{20})-Si-10, Mater. Chem. Phys. 91 (2005) 524–531.

[12] K. Anil Kumar, S. Babu, V. Reddy Prasad, S. Damodaraiah, Y.C. Ratnakaram, Optical response and luminescence characteristics of Sm3+ and Tb3+/sm3+ co-doped potassium-fluoro-phosphate glasses for reddish-orange lighting applications, Mater. Res. Bull. 90 (2017) 31–40.

[13] E. Zych, J. Trojan-Piegza, D. Hreniak, W. Strek, Properties of Tb-doped vacuum-sintered storage phosphor, J. Appl. Phys. 94 (3) (2003) 1318–1324.

[14] Chun Che Lin, Wei-Ting Chen, Cheng-I Chu, Kuan-Wei Huang, Chiao-Wen Yeh, Bing-Ming Cheng and Ru-Shi Liu, UV/VUV switch-driven color-reversal effect for Tb-activated phosphors, Light: Science & Applications 5 (2016) 16066, https://doi.org/10.1038/lsa.2016.66.

[15] X. Xue, T. Cheng, T. Suzuki, Y. Ohishi, Upconversion emissions from high energy levels of Tb^{3+} under near-infrared laser excitation at 976 nm, Optical Materials Express 5 (12) (2015) 2768–2776.

[16] T.u. Dong, Y. Liang, R. Liu, D. Li, Eu/Tb ions co-doped white light luminescence Y_2O_3 phosphors, J. Lumin. 131 (2011) 2569–2573.

[17] D. Deng, R. Chen, W. Feng, H. Guan, Terbium single-doped or terbium and sodium codoped barium zinc phosphate: A novel green phosphor for near ultraviolet-pumped white light emitting diodes, Spectrosc. Lett. 50 (8) (2017) 451–455.

[18] M. Jiao, W. Lì, B. Shao, L. Zhao, H. You, Synthesis, Structure, and Photoluminescence Properties of Novel KBaSc2(PO4)3:Ce3+/Eu2+/Tb3+ Phosphors for White-Light-Emitting Diodes, ChemPhysChem 16 (2015) 2663–2669.

[19] C. Parthasaradhi Reddy, V. Naresh, R. Ramaraghavulu, B.H. Rudramadevi, K. T. Ramakrishna Reddy, S. Buddhudu, Energy transfer based emission analysis of (Tb^{3+}, Sm^{3+}): Lithium zinc phosphate glasses, Spectrochimica Acta Part A: Molecular and Biomolecular Spectroscopy 144 (5) (2015) 68–75.

[20] L. Wang, X.u. Mengjiao, H. Zhao, D. Jia, Luminescence, energy transfer and tunable color of Ce^{3+}, D^{y3}+/T^{b3}+ doped $BaZ_n2(P_O4_)2$ phosphors, New J. Chem. 40 (2016) 3086–3093.

[21] D.L. Dexter, A Theory of sensitized luminescence in solids, J. Chem. Phys. 21 (1953), 836–1−15.

[22] G. Blasse, B.C. Grabmaier, Luminescent materials, Berlin, Springer- Verlag, 1994.

[23] S. Ye, Z.S. Liu, J.G. Wang, X.P. Jing, Luminescent properties of $Sr_2P_2O_7$:Eu, Mn phosphor under Near UV excitation, Mater. Res. Bull. 43 (2008) 1057–1065.

[24] N. Rakov, G.S. Maciel, An efficient energy transfer process in Nd^{3+}:Yb^{3+} co-doped SrF_2 powders containing Al^{3+} and prepared by the combustion synthesis technique, J. Mater. Chem. C 4 (2016) 5442–5447.

[25] A.K. Vishwakarma, M. Kaushal Jha, B.S. Jayasimhadri, B. Gahtoria, D. Haranath, Emerging cool white light emission from Dy^{3+} doped single phase alkaline earth niobate phosphors for indoor lighting applications, Dalton Trans. 44 (2015) 17166.

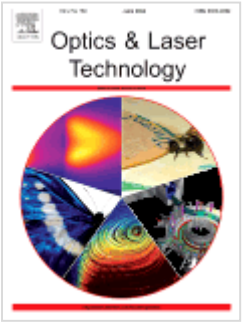

ISSN: 0030-3992

Optics & Laser Technology

> Elsevier in Optics homepage

> Elsevier Physics homepage

Publishing options: OA Open Access ↗ S Subscription ↗

↗ Guide for authors Track your paper ↗ Order journal

Editor-in-Chief > Editorial board

M. Schmidt

Optics & Laser Technology aims to provide a vehicle for the publication of a broad range of high quality research and review papers in those fields of scientific and engineering

Read full aims & scope

Submit your paper

The Impact Factor of this journal is 3.867, ranking it 21 out of 99 in *Optics*

With this journal indexed in 8 international databases, your published article can be read and cited by researchers worldwide

Filters

Clear All

- *Web of Science* Coverage
- Open Access
- Category
- Country / Region
- Language
- Frequency
- Journal Citation Reports

efine Your Search Results

Optics and Laser Technology

Search

rt By: Relevancy

earch Results

ound 3,232 results (Page 1)

Share These Results

xact Match Found

OPTICS AND LASER TECHNOLOGY

Publisher: ELSEVIER SCI LTD , THE BOULEVARD, LANGFORD LANE, KIDLINGTON, OXFORD, ENGLAND, OXON, OX5 1GB

ISSN / eISSN: 0030-3992 / 1879-2545

Web of Science Core Collection: Science Citation Index Expanded

Additional *Web of Science* Indexes: Current Contents Electronics & Telecommunications Collection | Current Contents Engineering, Computing & Technology | Current Contents Physical, Chemical & Earth Sciences | Essential Science Indicators

Share This Journal

View profile page

** Requires free login.*

ther Possible Matches

OPTICS AND LASERS IN ENGINEERING

Optical and Quantum Electronics (2020) 52:441
https://doi.org/10.1007/s11082-020-02554-8

Investigation of structural and thermal response of Sm^{3+} doped $Sr_3MgSi_2O_8$ phosphors

Pradeep Dewangan[1,2] · D. P. Bisen[1] · Nameeta Brahme[1] · Shweta Sharma[1] · Raunak Kumar Tamrakar[3] · Ishwar Prasad Sahu[4]

Received: 21 March 2020 / Accepted: 15 September 2020

Abstract
Present study deals with the effect of Sm^{3+} doping on crystal and optical behaviour of $Sr_3MgSi_2O_8$. For these studies prepared phosphor was characterized by using X-ray powder diffraction and luminescence spectra by recording excitation and emissions spectra. Emission spectra have emission wave lengths centered at 490 nm and 545 nm. Effect of Sm^{3+} ion concentration shows dipole–dipole interaction was responsible for the quenching shown by phosphor. The thermoluminescence curves were used to define the ability of the trap to trapping the carriers for Sm^{3+} doped $Sr_3MgSi_2O_8$ phosphor.

Keywords $Sr_3MgSi_2O_8$:Sm^{3+} · Solid state reaction method · Luminescence

1 Introduction

Rare earth doped $Sr_3MgSi_2O_8$ phosphors have been broadly contemplated by scientists inferable from their interesting physical and optical properties. These nanomaterials have been used in device fabrication, enthusiasm for examination of their conceivable ease of use in various fields of gadget applications. They may take jobs in part of gadgets, for example, opto-electronics, sensors, identifiers, im-petuses, luminescent and bio-medical gadgets. A few kinds of silicate-based phosphor have been found and examined (Talwar et al. 2009; Klasens et al. 1957; Barry 1968; Blasse et al. 1968; Liu et al. 2014; Pan et al. 2011).

✉ Pradeep Dewangan
pradeep_dewangan15@rediffmail.com

1 SoS in Physics and Astrophysics, Pt. Ravishankar Shukla University, Raipur, Chhattisgarh 492010, India

2 Department of Physics, Faculty of Science, Shri Rawatpura Sarkar University, Raipur, Chhattisgarh 492015, India

3 Department of Applied Physics, Bhilai Institute of Technology (Seth Balkrishan Memorial), Near Bhilai Power House, Durg, Chhattisgarh 49100, India

4 Department of Physics, Indira Gandhi National Tribal University, Amarkantak, Madhya Pradesh 484887, India

Published online: 26 September 2020

In this type of material synthesis temperature play a major role to produce pure phases materials, its luminescent brightness, brilliance and luminescence characteristics. Recently, silicate based materials have been extensively studied as host lattices for rare earth doping, which show un-usual, interesting luminescence properties (Pan et al. 2011; Zhang et al. 2016; Wang et al. 2018; Jung and Seo 2006).

Previously, optical and thermal response was investigations were achieved and reported for $Sr_3MgSi_2O_8$:Sm^{3+} phosphor (Pan et al. 2011). In present study, synthesis, crystal structure, photoluminescence and thermoluminescence properties of Sm^{3+} doped $Sr_3MgSi_2O_8$ phosphor. The phase purity and structure was characterized by XRD, morphology and particle size determination was performed by SEM and TEM respectively. The excitation and emission spectra of title phosphor were measured and the mechanism of CQ was discussed. The thermoluminescence properties were also studied in detail for Sm^{3+} doped $Sr_3MgSi_2O_8$ phosphor. The trapping parameters of glow curves were also calculated by CGCD curve fitting method (Dewangan et al. 2018, 2019a, b).

2 Experimental

The pure and Sm^{3+} doped $Sr_3MgSi_2O_8$ phosphor was prepared by solid state reaction method. The raw materials for pure phosphor were [$SrCO_3$ (99.90%)], [MgO (99.90%)] and [SiO_2 (99.99%)] and the raw materials for Sm^{3+} doped phosphor were same except the addition of small amount of Sm_2O_3 (99.99%)]. All the raw materials are of analytical grade. These raw chemicals were weighted and grinded into a fine powder by agate mortar and pestle for 2 h, then transferred in to a crucible, and calcined at 1250 °C for 5 h. All samples were observed when furnace-cooled to room temperature. Amount of raw ingredients extracted from the following chemical reactions:

$$SrCO_3 + MgO + SiO_2 \xrightarrow[5\ h]{1250\ ^\circ C} Sr_3MgSi_2O_8 + CO_2 \uparrow + O_2 \uparrow$$

$$SrCO_3 + MgO + SiO_2 + Sm_2O_3 \xrightarrow[5\ h]{1250\ ^\circ C} Sr_3MgSi_2O_8 : Sm^{3+} + CO_2 \uparrow + O_2 \uparrow$$

3 Results and discussion

3.1 X-ray diffraction (XRD)

Phase compositions of un-doped and Sm^{3+} doped $Sr_3MgSi_2O_8$ phosphors were examined by XRD and their diffraction patterns obtained (Fig. 1). JCPDS cards of $Sr_3MgSi_2O_8$ (no. 10-0075) is also illustrated in Fig. 1 as a comparison. The diffraction peaks well match with the standard pattern, suggesting that obtained samples have pure monoclinic phase $Sr_3MgSi_2O_8$. By small amounts of Sm^{3+} ions did not made any structural change which confirms proper incorporation of Sm^{3+} ion in crystal lattice, it maintained monoclinic phase (Dewangan et al. 2018, 2019a, b; Chen et al. 2016). The $Sr_3MgSi_2O_8$ phosphor samples exhibit obvious agglomeration and irregular shape without any porous structure. It is noted that the morphology of the samples did not significantly change when the dopant introduced into it.

Table 1. Different Parameter Calculated from XRD of $Sr_3MgSi_2O_8$ and $Sr_3MgSi_2O_8:Sm^{3+}$ phosphors

Sample's	2Θ	FWHM	Particle size	Strain	Dislocation Density
$Sr_3MgSi_2O_8$ Phosphors	22.62	0.12	67.52	0.00261	0.00021
	26.77	0.13	62.82	0.00238	0.00025
	38.91	0.19	44.35	0.00234	0.00050
	46.39	0.18	48.02	0.00183	0.00043
Sm^{3+} Doped $Sr_3MgSi_2O_8$ Phosphors	22.62	0.13	62.33	0.00283	0.00025
	26.77	0.14	58.33	0.00257	0.00029
	38.91	0.17	49.56	0.00209	0.00040
	46.39	0.16	54.02	0.00163	0.00034

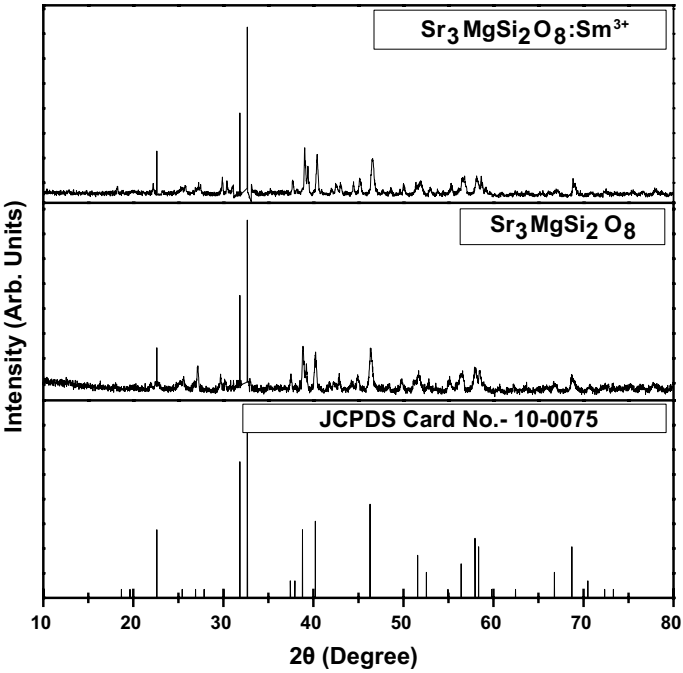

Fig. 1 X-ray diffraction (XRD) patterns of $Sr_3MgSi_2O_8$ and $Sr_3MgSi_2O_8:Sm^{3+}$ phosphors

3.2 Transmission electron microscopy (TEM)

The morphologies of single phase un-doped and Sm^{3+} doped $Sr_3MgSi_2O_8$ phosphors were observed by TEM and micrographs are displayed in Fig. 2 shown that quasi-spherical morphology. SEAD pattern also displayed.

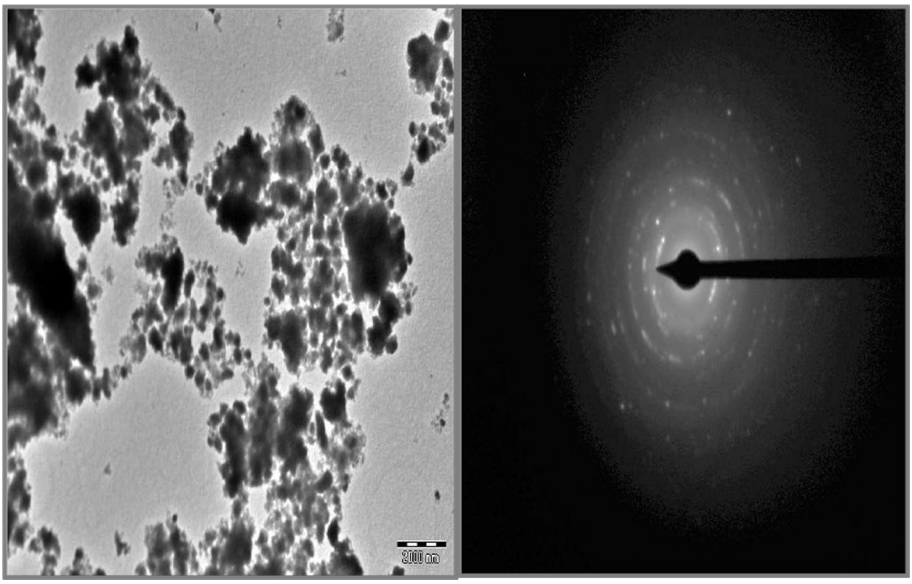

Fig. 2 TEM images of Sm^{3+} doped $Sr_3MgSi_2O_8$ phosphor

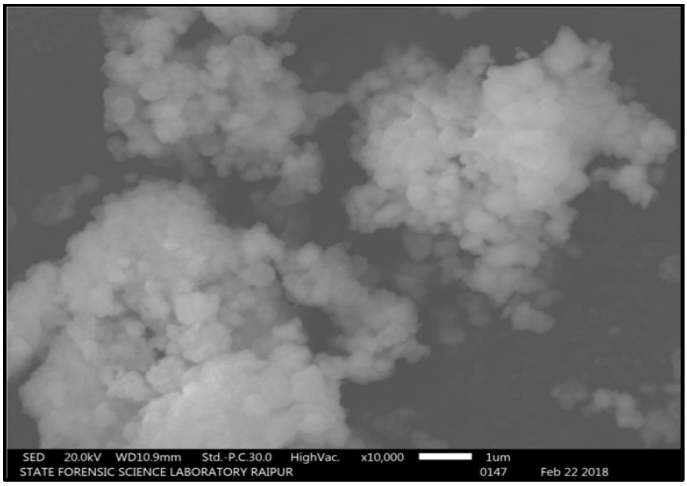

Fig. 3 SEM images of Sm^{3+} doped $Sr_3MgSi_2O_8$ phosphor

3.3 Scanning electron microscopy (SEM)

The grain morphologies of single phase pure and Sm^{3+} rare earth doped $Sr_3MgSi_2O_8$ phosphors were done by field FESEM and the micrographs are displayed in Figs. 3 and 4, respectively.

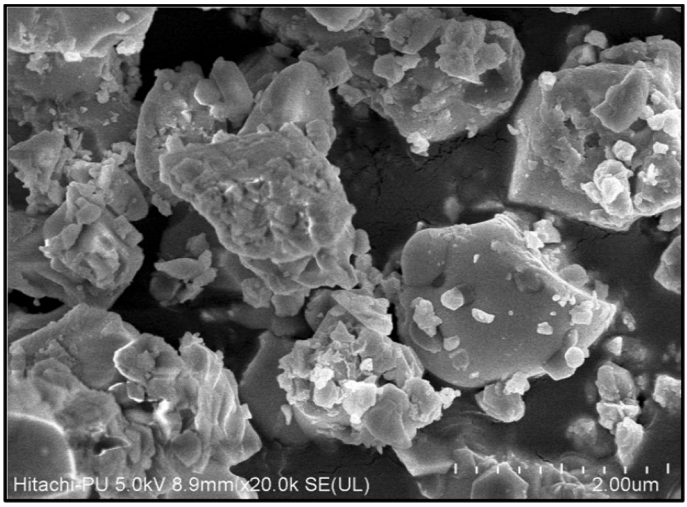

Fig. 4 FESEM images of Sm^{3+} doped $Sr_3MgSi_2O_8$ phosphor

Table 1 Chemical composition of Sm^{3+} doped $Sr_3MgSi_2O_8$ phosphor

S. no.	Element	Weight%	Atomic%
1.	Sr K	38.68	12.77
2.	Mg K	4.29	5.11
3.	Si K	9.20	9.47
4.	O K	39.26	70.99
5.	Sm K	8.57	1.65
Total		100	100

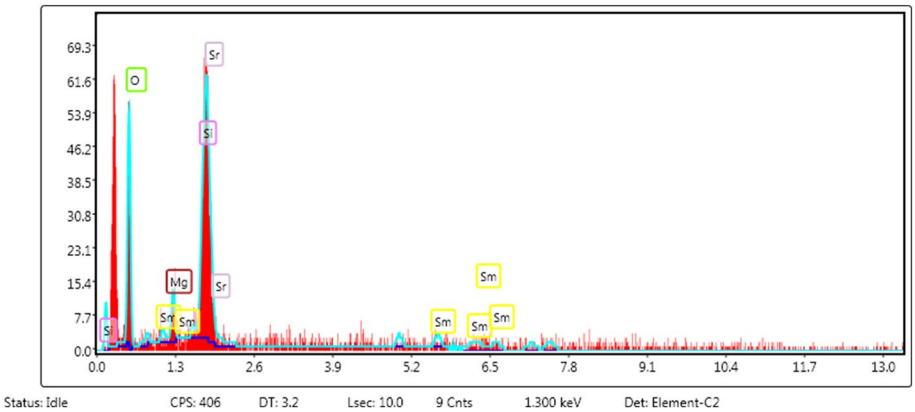

Fig. 5 EDS spectrum of Sm^{3+} doped $Sr_3MgSi_2O_8$ phosphor

3.4 Energy dispersive spectroscopy (EDS)

Elemental compositions of the prepared sample were determined using EDS. There were no emissions of other element in the EDS, other than those from doped Sr, Mg, Si, O, and Sm for Sm^{3+} doped $Sr_3MgSi_2O_8$ phosphors. Table 1 shows the compositional elements of rare earth doped $Sr_3MgSi_2O_8$ phosphors (Fig. 5).

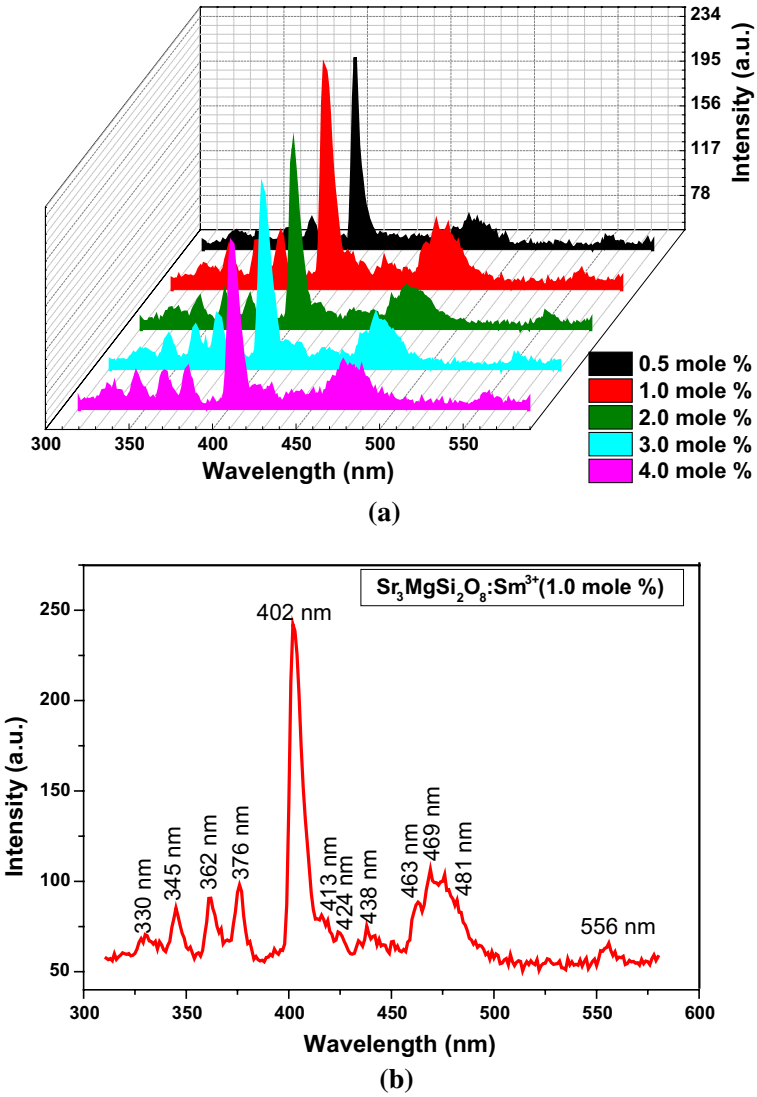

Fig. 6 Photoluminescence excitation (PL) spectra of **a** $Sr_3MgSi_2O_8$: Sm^{3+} phosphors with variable Sm^{3+} concentration **b** $Sr_3MgSi_2O_8$:Sm^{3+} (1.0 mol%) phosphor

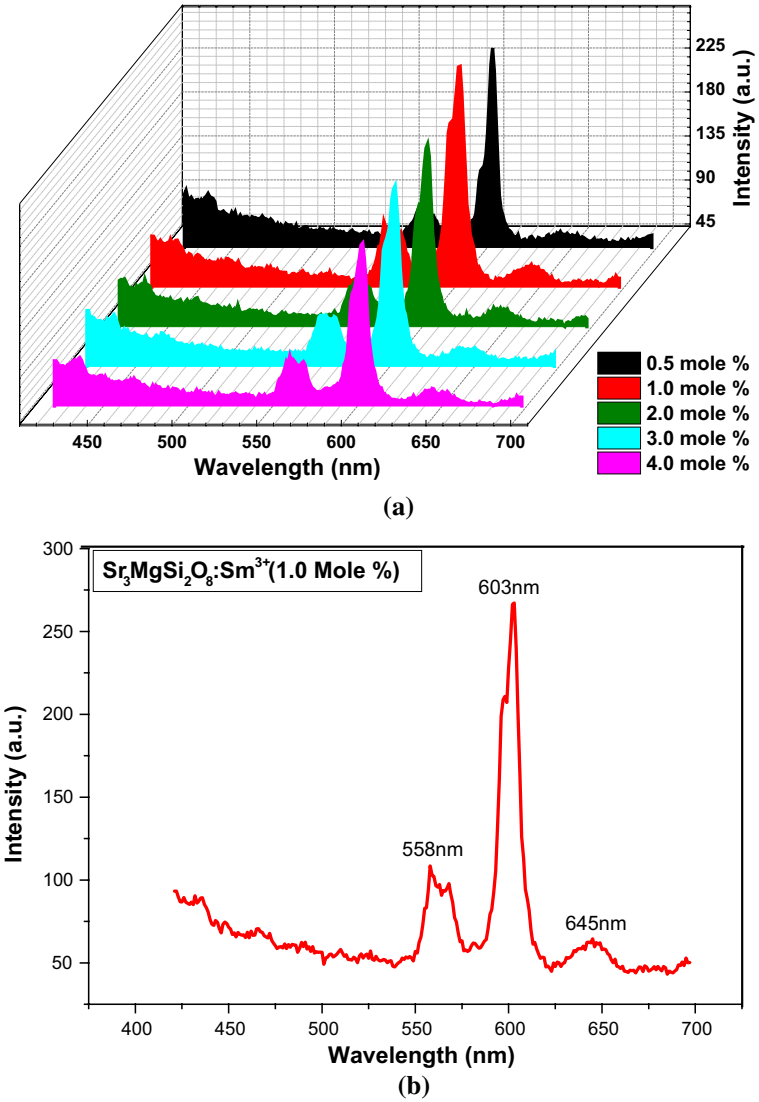

Fig. 7 Photoluminescence emission spectra of **a** $Sr_3MgSi_2O_8$:xSm^{3+} (x = 0.5, 1.0, 2.0, 3.0 and 4.0 mol%) phosphors and **b** $Sr_3MgSi_2O_8$:Sm^{3+} (1.0 mol%) phosphor, under 402 nm excitation

3.5 Photoluminescence (PL)

For PL study of $Sr_3MgSi_2O_8$:Sm^{3+}, its luminescence spectra were recorded (Fig. 6a, b). Under 603 nm wavelength excitation spectra were recorded and shows peak in UV to visible region. Excitation peaks are located at 330 nm ($^6H_{5/2} \rightarrow {}^2L_{15/2}$), 345 nm ($^6H_{5/2} \rightarrow {}^4H_{9/2}$), 362 nm ($^6H_{5/2} \rightarrow {}^4D_{3/2}$), 376 nm ($^6H_{5/2} \rightarrow {}^4D_{1/2}$), 402 nm ($^6H_{5/2} \rightarrow {}^4F_{7/2}$), 413 nm ($^6H_{5/2} \rightarrow {}^4M_{19/2} + ({}^6P, {}^4P)_{5/2}$), 424 nm ($^6H_{5/2} \rightarrow {}^4P_{5/2}$), 438 nm ($^6H_{5/2} \rightarrow {}^4G_{9/2}$), 463 nm ($^6H_{5/2} \rightarrow {}^4I_{13/2}$), 469 nm and 481 nm ($^6H_{5/2} \rightarrow {}^4I_{11/2} + {}^4M_{15/2}$ and 556 nm ($^6H_{5/2} \rightarrow {}^4G_{5/2}$) (Jha

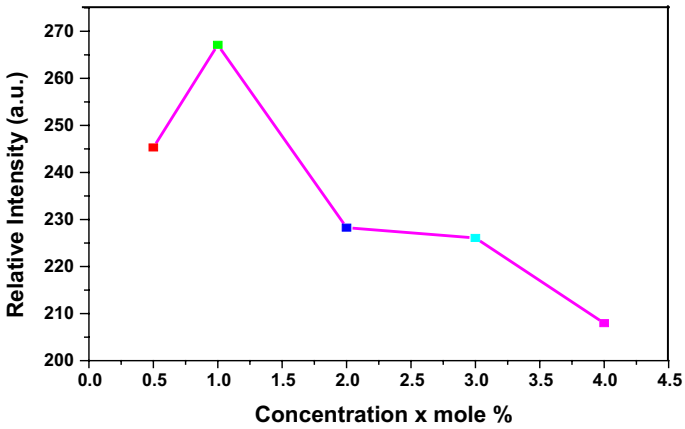

Fig. 8 Dependence of emission intensity of Sm^{3+} concentration for $Sr_3MgSi_2O_8$:Sm^{3+} phosphor

et al. 2017; Sun et al. 2016; Lu et al. 2017). At 402 nm corresponds to $^6H_{5/2} \rightarrow {}^4F_{7/2}$ transition, is the strongest one so used to record emission spectra (Ilkhechi et al. 2015a, b, c; Ilkhechi and Kaleji 2016).

Figure 7a, b shows emission spectra of $Sr_3MgSi_2O_8$:xSm^{3+} (x = 0.5 to 4.0 mol%) phosphors recorded under 402 nm excitation. The emission peaks centred at yellow-orange-red region at 558 nm, 603 nm and 645 nm.

The emission band located at 558 is due to transition $^4G_{5/2} \rightarrow {}^6H_{5/2}$, 603 nm and 645 nm are due to $^4G_{5/2} \rightarrow {}^6H_{7/2}$ and $^4G_{5/2} \rightarrow {}^6H_{9/2}$, respectively (Yu et al. 2012). Unaffected peak positions remains with variation in Sm^{3+} molar percentage but emission intensity alters (Fig. 8).

With increasing Sm^{3+} concentration intensity increase up to 1.0 mol% further increase in concentration results in concentration quenching (CQ) due to non radiative energy transfer between neighbouring Sm^{3+} ions. It is depends on critical distance (R_c) and calculated by using the Blasse equation in Eq. (1) (Blasse 1969; Dewangan et al. 2020): by using critical concentration x_c, number of cations N and volume of unite cell V

$$R_c \approx 2\left(\frac{3V}{4\pi x_c N}\right)^{\frac{1}{3}} \tag{1}$$

For $Sr_3MgSi_2O_8$ N = 4, V = 715.9 Å^3, and x_c = 0.01. R_c was found around 33 Å. For R_c shorted than 5 Å quenching is due to exchange above this multipolar interaction. Therefore, energy transfer mechanism in $Sr_3MgSi_2O_8$:Sm^{3+} phosphor has multipolar interaction.

Here emission intensity per doped ion is followed by the Eq. (2):

$$\log\frac{I}{x} = -Q/3\log x + \log K - \log\beta \tag{2}$$

It is a straight line equation. From slope of log (I/x) Vs log (x) plot we find out Q value (Fig. 9). The Q value is 3.336 which is closer to 4 as compare to 8. Hence energy transfers mechanism between Sm^{3+} ions in $Sr_3MgSi_2O_8$:Sm^{3+} phosphor follows the dipole–dipole interaction. Corresponding energy level diagram for luminescence emission

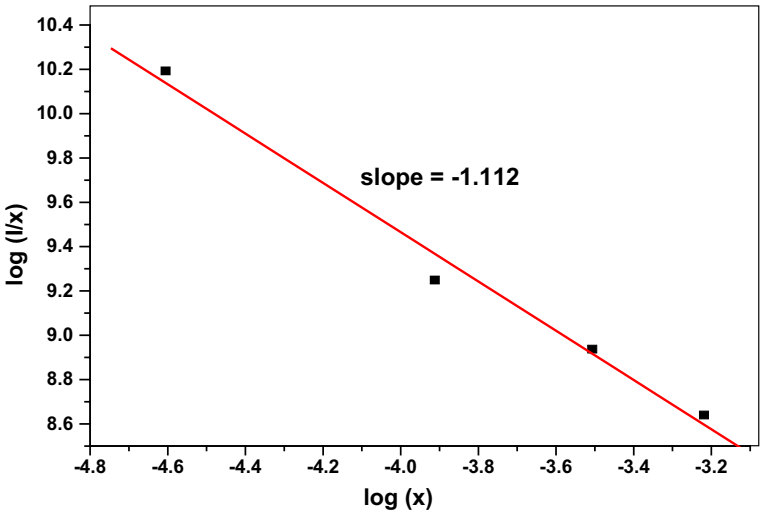

Fig. 9 Plot between log (*I*/*x*) and log (*x*) for $Sr_3MgSi_2O_8$:Sm^{3+} phosphor

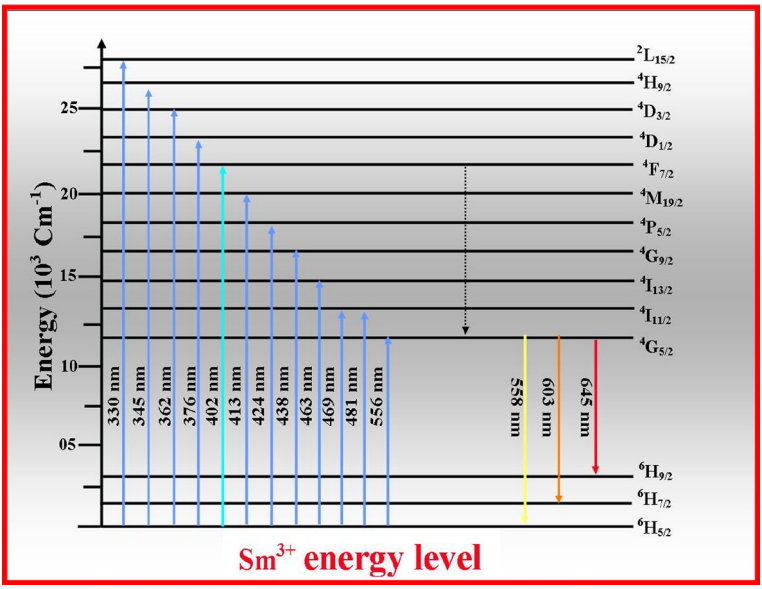

Fig. 10 Energy level diagram of Sm^{3+} ions

from $Sr_3MgSi_2O_8$:Sm^{3+} phosphor is represented in Fig. 10 (Dexter and Schulman 1954; Uitert 1967).

The luminescence color of Sm^{3+} doped $Sr_3MgSi_2O_8$ phosphor is identified by using CIE coordinates placed at X = 0.417 and Y = 0.420 that very close to the orange light emission in the chromaticity diagram (Fig. 11) (CIE, International Commission on Illumination. Publication CIE, no. 15 1931).

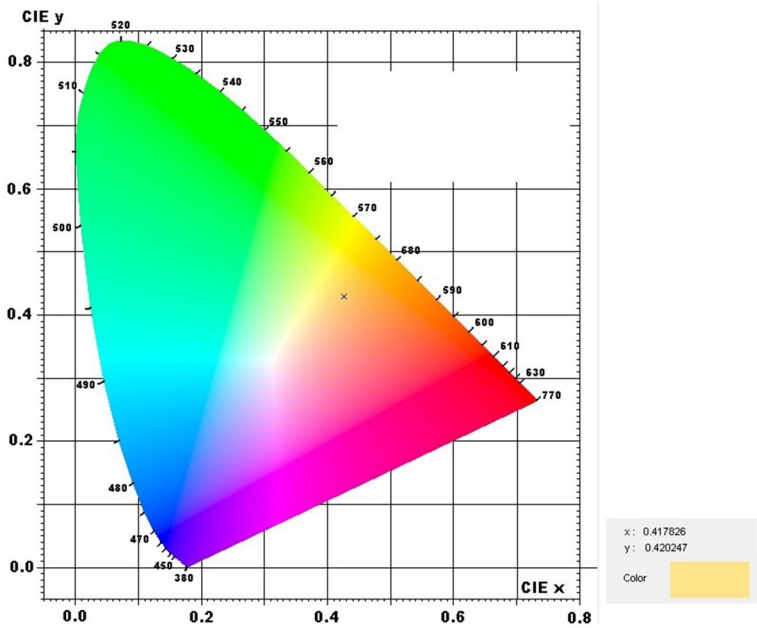

Fig. 11 CIE chromaticity diagram for $Sr_3MgSi_2O_8$:Sm^{3+} (1.0 mol%) phosphor excited at 402 nm

3.6 Thermoluminescence (TL)

Thermally stimulated luminescence glow curves were recorded at room temperature on a thermoluminescent dosimetric material reader TL1009I supplied by Nucleonix Systems Pvt. Ltd. Hyderabad. The phosphor obtained under thermoluminescent examination was given ultraviolet (UV) radiation from a 365 nm source.

TL of prepared phosphors was recorded by giving 365 nm UV source irradiation for different time. Every time 0.5 mg weighed powdered phosphor was taken for TL measurement. The heating rate used for TL measurements was 3° C s^{-1}, 4° C s^{-1}, 5° C s^{-1}, 6° C s^{-1}, 7° C s^{-1} and 8° C s^{-1} (Chen and Kirsh 1981).

TL glow curve of the Sm^{3+} doped sample was obtained and it was observed that the glow curve has two peaks at 132 °C and 233 °C. To optimize the heating rate TL glow curve was recorded with different heating rate from 3 to 8 °C s^{-1}. A slight variation in peak position along with intensity was observed. Optimization of heating rate is necessary to overcome the effect of thermal quenching. Maximum intense peak was obtained for 5 °C s^{-1} heating rate therefore it was used as optimal heating rate for the further study (Fig. 12).

Concentration was optimized by recording the TL glow peak for different concentration of Sm^{3+}. The intensity of both the glow peak increases with increasing Sm^{3+} intensity up to 2.0 mol % after that the glow peak intensity starts to fall due to the CQ (Fig. 13). Another factor such as the optimization of UV exposure time was further determined. As shown in Figs. 14 and 15 the glow peak intensity increases up to 70 min of UV exposure time after its decrease due to destroy of the traps. The corresponding activation energy (E) values were calculated by the use of formulas modified by Chen

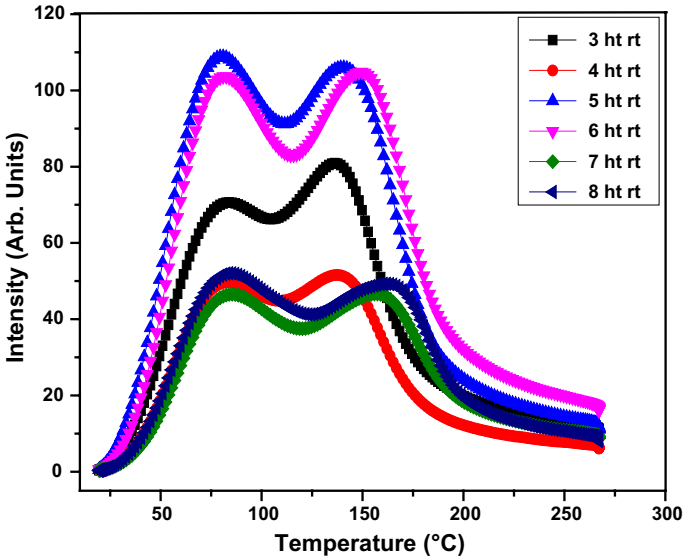

Fig. 12 TL glow curves of $Sr_3MgSi_2O_8$:Sm^{3+} (2.0 mol%) for different heating rates

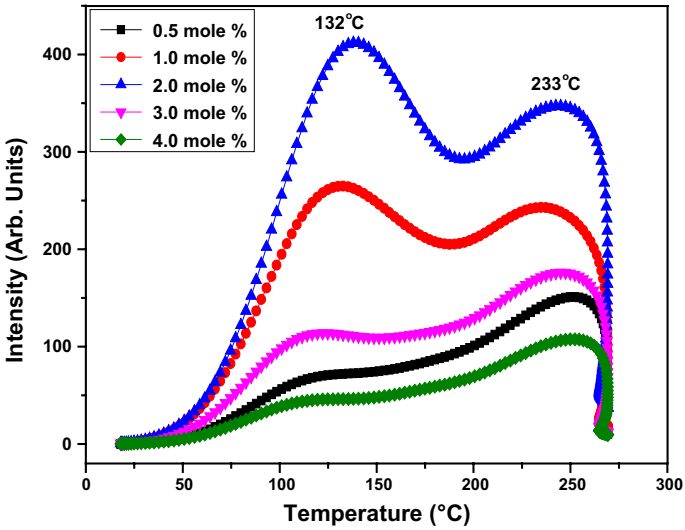

Fig. 13 Sm^{3+} concentration dependent TL glow curves of $Sr_3MgSi_2O_8$:Sm^{3+} phosphor for 70 min UV exposure time

and others (Chen and Kirsh 1981; Chen and Mc Keever 1997; Chen and Pagonis 2011; Chen 1969a).

TL glow peak of the sample was deconvoluted by using computerized glow curve deconvolution process. The sample shows two deconvolution peaks as shown in Fig. 16. Peak shape method were used to calculated TL parameters (Dewangan et al. 2018;

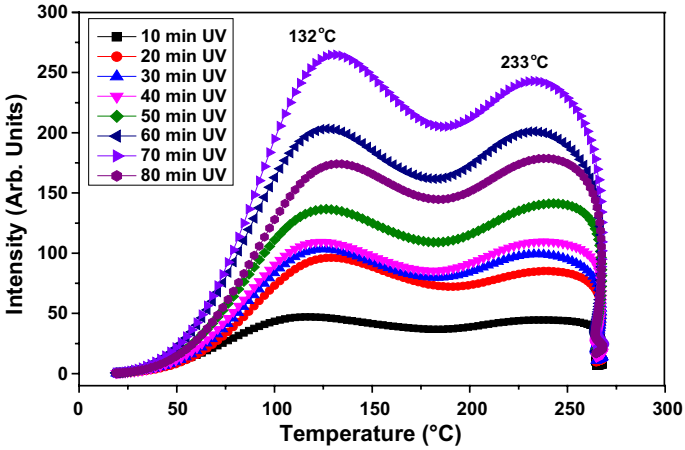

Fig. 14 TL glow curves of $Sr_3MgSi_2O_8:Sm^{3+}$ (2.0 mol%) phosphor for different UV exposure time

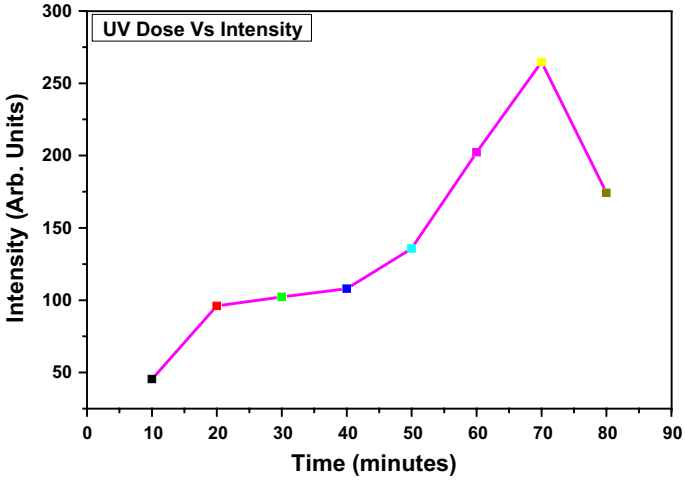

Fig. 15 TL intensity V/S UV exposure time for $Sr_3MgSi_2O_8:Sm^{3+}$ (2.0 mol%) phosphor

Pagonis et al. 2006; Tamrakar and Upadhyay 2017). The relationship between the frequency factor's' and the activation energy 'E' is given by the Eq. (3)

$$\frac{\beta E}{kT_m^2} = s\left[1 + (b-1)\frac{2kT_m}{E}\right]\exp(E/KT_m) \tag{3}$$

where, k = Boltzmann constant, E = activation energy, b = order of kinetics, T_m = temperature of higher peak position and b = order of kinetics.

In the present work β 5 °C/s. For Trap depth calculation for 2nd order kinetics is using the Eq. (4) (Chen 1969b).

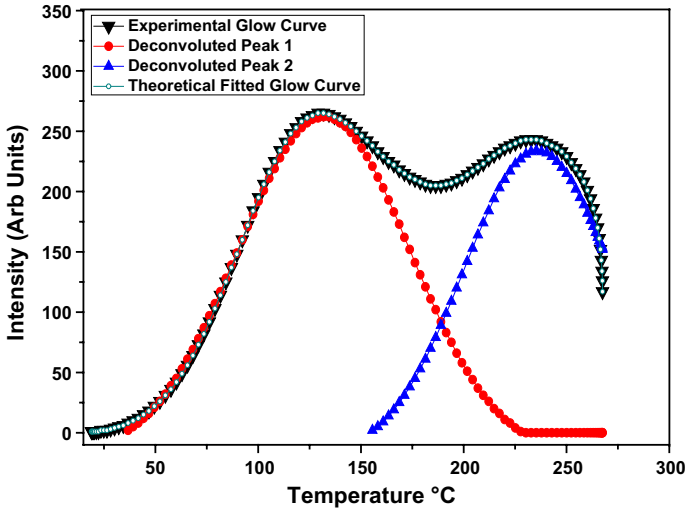

Fig. 16 Peak deconvolution of TL glow curve of 70 min UV exposed $Sr_3MgSi_2O_8$:Sm^{3+} (2.0 mol%) phosphor

$$E = 2kT_m\left(1.76\frac{T_m}{\omega} - 1\right) \tag{4}$$

The calculated kinetic parameters of $Sr_3MgSi_2O_8$:Sm^{3+} phosphor by the peak shape method is given in Table 2. In our case, the value of shape factor has been calculated to be ≈ 0.51 for both the peak, which indicates that it is a case of second order kinetics. The activation energies for the prepared $Sr_3MgSi_2O_8$:Sm^{3+} phosphor were estimated to be 0.49 and 1.53 eV for 1st and 2nd peak respectively (Dewangan et al. 2019a; Tamrakar et al. 2017, 2019; Tamrakar and Upadhyay 2016; Tamrakar 2013; Tamrakar and Bisen 2015).

4 Conclusion

The Sm^{3+} doped phosphor was obtained by solid state reaction method. Phosphor have crystallizes in a monoclinic phase confirmed by XRD analysis. The XRD patterns confirmed single phase, monoclinic structure of the sample. The particle size is in nano range confirmed by TEM. All the component elements in the desired samples have been detected by employing the EDS spectrum. FESEM results confirmed agglomerated morphology of the sample.

Under 402 nm excitation, characteristic photoluminescence (PL) peaks recorded. The emission peaks centred at yellow-orange-red region at 558 nm, 603 nm and 645 nm for Sm^{3+} doped phosphor. Further, the phosphor showed excellent CIE chromaticity coordinates (X,Y) in white region and CCT observed in orange light emission as a result. The mechanism of CQ was discussed well which due to dipole–dipole interactions. The phosphor emits in yellow-orange-red region.

Table 2 Analysis of glow curves by CGCD curve fitting and trapping parameters of $Sr_3MgSi_2O_8:Sm^{3+}$ (2.0 mol%) phosphor

Phosphor name	Peaks	T_1 (°C)	T_2 (°C)	T_m (°C)	τ (°C)	δ (°C)	ω (°C)	$\mu_g = \delta/\omega$	E (eV)	S (s^{-1})
$Sr_3MgSi_2O_8:Sm^{3+}$	Peak 1	89.64	173.74	131.79	42.15	41.95	84.10	0.50	0.49	9.9×10^6
	Peak 2	212.16	260.16	235.33	23.17	24.83	48.00	0.51	1.53	3.2×10^{16}

The TL curve was recorded under UV exposure. The glow peak has two peaks that may be due to formation of two different trap centres. The optimized factors for TL glow curve were obtained as 5 °C s^{-1} heating rate, 2.0 mol % of Sm^{3+} concentration and 70 min UV exposure time. The computerized glow curve deconvolution study showed the presence of two traps having activation energies of 0.49 eV and 1.53 eV for the lower temperature and higher temperature peaks respectively which confirms the presence of shallow traps and deep traps respectively.

References

Barry, T.L.: Equilibria and Eu^{2+} luminescence of subsolidus phases bounded by $Ba_3MgSi_2O_8$, $Sr_3MgSi_2O_8$, and $Ca_3MgSi_2O_8$. J. Electrochem. Soc. **115**, 733 (1968)

Blasse, G.: Energy transfer in oxidic phosphors. Philips J. Res. **24**, 131–144 (1969)

Blasse, G., Wanmaker, W.L., Vrugt, J.W., Bril, A.: Fluorescence of Eu^{2+} activated silicates. Philips J. Res. **23**, 189–200 (1968)

Chen, R.: Thermally stimulated current curves with non-constant recombination lifetime. Br. J. Appl. Phys. **2**, 371–375 (1969a)

Chen, R.: Glow curves with general order kinetics. J. Electrochem. Soc. **116**, 1254 (1969b)

Chen, R., Kirsh, Y.: The analysis of thermally stimulated processes, p. 361. Pergamon Press, Oxford (1981)

Chen, R., Mc Keever, S.W.S.: Theory of thermoluminescence and related phenomena, p. 576. World Scientific Publications, London (1997)

Chen, R., Pagonis, V.: Thermally and optically stimulated luminescence: a simulation approach, p. 434. Wiley, Chichester (2011)

Chen, Y., Zhou, B., Sun, Q., Wang, Y., Yan, B.: Synthesis and luminescence properties of $Sr_3MgSi_2O_8$:Ce^{3+}, Tb^{3+} for application in near ultraviolet excitable white light-emitting-diodes. J. Superlattices Microstruct. **100**, 158–167 (2016)

CIE, International Commission on Illumination. Publication CIE, no. 15 (1931)

Dewangan, P., Bisen, D.P., Brahme, N., Tamrakar, R.K., Upadhyay, K., Sharma, S., Sahu, I.P.: Studies on thermoluminescence properties of alkaline earth silicate phosphors. J. Alloys. Compd. **735**, 1383–1388 (2018)

Dewangan, P., Bisen, D.P., Brahme, N., Sharma, S., Tamrakar, R.K., Sahu, I.P.: Thermoluminescence glow curve for UV induced $Sr_3MgSi_2O_8$ phosphor with its structural characterization. J. Mater. Sci. Mater. Electron. **30**, 771–777 (2019a)

Dewangan, P., Bisen, D.P., Brahme, N., Tamrakar, R.K.: Growth and synthesis of $Sr_3MgSi_2O_8$:Dy^{3+} nanorod arrays by a solid state reaction method. J. Opt. Quantum Electron. **50**(10), 367 (2019b)

Dewangan, P., Bisen, D.P., Brahme, N., Sharma, S., Tamrakar, R.K., Sahu, I.P.: Influence of Dy^{3+} concentration on spectroscopic behaviour of $Sr_3MgSi_2O_8$:Dy^{3+} phosphors. J. Alloys. Compd. **816**, 152590 (2020)

Dexter, D.L., Schulman, J.H.: Theory of concentration quenching in inorganic phosphors. J. Chem. Phys. **22**, 1063–1070 (1954)

Ilkhechi, N.N., Kaleji, B.K.: Effect of Cu^{2+}, Si^{4+} and Zr^{4+} dopant on structural, optical and photocatalytic properties of titania nanopowders. J. Opt. Quantum Electron. **48**, 347 (2016)

Ilkhechi, N.N., Kaleji, B.K., Salahi, E.: Effect of heating rate on structural and optical properties of Si and Mg co-doped ZrO_2 nanopowders. J. Opt. Quantum Electron. **47**, 1187–1195 (2015a)

Ilkhechi, N.N., Ahmadi, A., Kale, B.K.: Optical and structural properties of nanocrystalline anatase powders doped by Zr, Si and Cu at high temperature. J. Opt. Quantum Electron. **47**, 2423–2434 (2015b)

Ilkhechi, N.N., Kaleji, B.K., Salahi, E., Hosseinabadi, N.: Comparison of optical and structural properties of Cu doped and Cu/Zr co doped TiO_2 nanopowders calcined at various temperatures. J. Sol–Gel. Sci. Technol. **74**, 765–773 (2015c)

Jha, K., Vishwakarma, A.K., Jayasimhadri, M., Haranath, D.: Multicolor and white light emitting Tb^{3+}/Sm^{3+} co-doped zinc phosphate barium titanate glasses via energy transfer for optoelectronic device applications. J. Alloys. Compd. **719**, 116–124 (2017)

Jung, H.K., Seo, K.S.: Luminescent properties of Eu^{2+} activated (Ba, Sr)$_3MgSi_2O_8$ phosphor under VUV irradiation. J. Opt. Mater. **28**, 602–605 (2006)

Klasens, H.A., Hoekstra, A.H., Cox, A.P.M.: Modern materials: advances in development and applications. J. Electrochem. Soc. **104**, 93 (1957)

Liu, Q., Liu, Y., Ding, Y., Peng, Z., Tian, X., Yu, Q., Dong, G.: A White light emitting luminescent material $Ba_3Y(PO_4)_3:Dy^{3+}$. Ceram. Int. **40**(2014), 10125–10129 (2014)

Lu, G., Qiu, K., Li, J., Zhang, W., Yuan, X.: Synthesis and photoluminescence characteristics of Sm^{3+}-doped $Bi_4Si_3O_{12}$ red-emitting phosphor. J. Lumin. **32**, 93–99 (2017)

Pagonis, V., Kiti, G., Furetta, C.: Numerical and practical exercises in thermoluminescence. Springer, New York (2006)

Pan, W., Wang, N., Wang, Z., Li, G., Ning, G.: Enhanced L-minescent properties of $Sr_3MgSi_2O_8:Eu^{2+}$ spherical blue phosphor via modified sol–gel approach. SID Symp. Dig. Tech. Pap. **41**, 1561–1564 (2011)

Sun, J., Ding, D., Sun, J.: Synthesis and photoluminescence properties of a novel reddish orange-emitting Sm^{3+}-doped strontium borosilicate phosphor. J. Opt. Mater. **58**, 188–195 (2016)

Talwar, G.J., Joshi, C.P., Moharil, S.V., Dhopte, S.M., Muthal, P.L., Kondawar, V.K.: Combustion synthesis of $Sr_3MgSi_2O_8:Eu^{2+}$ and $Sr_2MgSi_2O_7:Eu^{2+}$ phosphors. J. Lumin. **129**, 1239–1241 (2009)

Tamrakar, R.K.: Thermoluminescence studies of copper-doped cadmium sulphide nanoparticles with trap depth parameters. J. Res. Chem. Intermed. **39**(9), 4239–4245 (2013)

Tamrakar, R.K., Bisen, D.P.: Thermoluminescence studies of ultraviolet and gamma irradiated erbium(III)- and ytterbium(III)-doped gadolinium oxide phosphors. J. Mater. Sci. Semicond. Process. **33**, 169–188 (2015)

Tamrakar, R.K., Upadhyay, K.: Studies of thermoluminescence glow curve of $GdAlO_3$ phosphors synthesized by solid-state reaction methods. J. Disp. Technol. **12**(6), 599–604 (2016)

Tamrakar, R.K., Upadhyay, K.: Thermoluminescence behaviour of $Gd_2O_3:Er^{3+}$ phosphor prepared by combustion synthesis method. J. Mater. Sci. Mater. Electron. **28**(5), 4267–4278 (2017)

Tamrakar, R.K., Upadhyay, K., Bisen, D.P.: 3T1R model and tuning of thermoluminescence intensity by optimization of dopant concentration in monoclinic $Gd_2O_3:Er^{3+};Yb^{3+}$ co-doped phosphor. J. Phys. Chem. Chem. Phys. **19**(22), 14680–14694 (2017)

Tamrakar, R.K., Bisen, D.P., Upadhyay, K., Sahu, I.P., Sahu, M.: The effect of annealing and irradiation dose on the thermoluminescence glow peak of a monoclinic $Gd_2O_3:Yb^{3+}$ phosphor. J. RSC Adv. **6**(84), 80797–80807 (2019)

Uitert, I.G.V.: Characterization of energy transfer interactions between rare earth ions. J. Electrochem. Soc. **114**, 1048–1053 (1967)

Wang, B., Liu, Y., Huang, Z., Fang, M.: Photoluminescence properties of a Ce^{3+} doped $Sr_3MgSi_2O_8$ phosphor with good thermal stability. J. RSC Adv. **8**, 15587–15594 (2018)

Yu, H., Zi, W., Lan, S., Gan, S., Zou, H., Xu, X.: Green light emission by Ce^{3+} and Tb^{3+} co-doped $Sr_3MgSi_2O_8$ phosphors for potential application in ultraviolet white light-emitting diodes. J. Opt. Laser Technol. **44**, 2306–2311 (2012)

Zhang, P., Chen, X.L., Zhang, Z., Fei, M., Chen, L.: Synthesis and photoluminescence of the blue phosphor $Sr_3MgSi_2O_8:Eu^{2+}$ optimized with the Taguchi method for application in near ultraviolet excitable white light-emitting diodes. J. Lumin. **169**, 733–738 (2016)

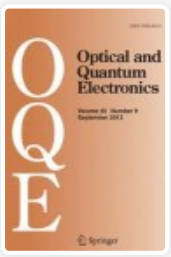

Optical and Quantum Electronics

Optical and Quantum Electronics provides an international forum for the publication of original research papers, tutorial reviews and letters in such fields as optical physics, optical engineering and optoelectronics. Special issues are published on topics of current interest. — show all

Publishing model
Hybrid (Transformative Journal). How to publish with us, including Open Access

2.084 (2020)
Impact factor

1.625 (2020)
Five year impact factor

59 days
Submission to first decision (Median)

296,230 (2021)
Downloads

Filters
Clear All

- *Web of Science* Coverage
- Open Access
- Category
- Country / Region
- Language
- Frequency
- Journal Citation Reports

efine Your Search Results

Optical and Quantum Electronics
Search

rt By: Relevancy

earch Results

ound 873 results (Page 1)
Share These Results

xact Match Found

OPTICAL AND QUANTUM ELECTRONICS

Publisher: SPRINGER , VAN GODEWIJCKSTRAAT 30, DORDRECHT, NETHERLANDS, 3311 GZ
ISSN / eISSN: 0306-8919 / 1572-817X
Web of Science Core Collection: Science Citation Index Expanded
Additional *Web of Science* Indexes: Current Contents Electronics & Telecommunications Collection | Current Contents Engineering, Computing & Technology | Essential Science Indicators

Share This Journal
View profile page
* *Requires free login.*

ther Possible Matches

IEEE JOURNAL OF QUANTUM ELECTRONICS

Publisher: IEEE-INST ELECTRICAL ELECTRONICS ENGINEERS

Biotechnological Communication

BBRC Bioscience Biotechnology Research Communications

Biosc.Biotech.Res.Comm. Vol 13 (2) April-May-June 2020 Pp-842-847

Adaptation of an Indigenous Insect Cell Line DZNU-Bm-1 to Mitsuhashi and Maramorosch (MM) Culture Medium Supplemented With 3% Foetal Bovine Serum

Syed Obaid Qureshi

Department of Zoology, Adarsha Science, J. B. Arts and Birla Commerce College, Dhamangaon Railway, Amravati, Maharashtra. 444709 India

ABSTRACT

Although utility of insect cell lines for production of proteins of human interest has been scaled up from experiment-level to industrial production level, use of vertebrate sera is discouraged during industrial production of therapeutics. DZNU-Bm-1, a larval ovarian cell line is highly susceptible to BmNPV in MGM-448 medium supplemented with 10% Foetal Bovine Serum and can be used as IC-BEVS platform for foreign gene expression. The high cost of this medium is a serious bottleneck for use of DZNU-Bm-1 in production of therapeutics. This study reports reduction in serum dependence of this cell line and its successful adaptation to a low-cost Mitsuhashi and Maramorosch (MM) medium supplemented with 3% FBS to bring down the cost of maintaining the cell line. Adaptation of MM medium was achieved by decreasing the volume of original medium by 20% and increasing the volume of the new medium -to which the cell line was being adapted- by 20% at each passage. The initial cell density, final cell density, number of days taken to attain final cell density and population doubling time were noted at each passage. The cell line was slow to reach sufficient cell density during initial steps but showed reduced population doubling time during subsequent passages

KEY WORDS: DZNU-Bm-1; INSECT CELL LINE; ADAPTATION; POPULATION DOUBLING TIME.

INTRODUCTION

Insect cell lines have found application in a wide array of fields including cell biology, genetics, virology and agriculture. Insect cells have many advantages over mammalian cells in culture, being able to tolerate a broad range of environmental conditions, to proliferate and maintain physiological function in variable pH, temperature, and oxygen conditions (Akiyama et al., 2013). Their ability to grow without carbon dioxide supplementation has further simplified culture systems and has made them an economically viable alternative to mammalian cells (Irons et al., 2018). Insect cells exhibit many additional desirable characteristics like easy adaptation to suspension and serum-free culture as well as low media requirements. These qualities point to possibility of their large-scale culture (Neermann and Wagner, 1996; Donaldson and Shuler, 1998; Lynn, 2001; Ikonomou et al., 2003; Mitsuhashi and Goodwin, 2018).

ARTICLE INFORMATION

*Corresponding Author: drsoqureshi@gmail.com
Received 9th May 2020 Accepted after revision 20th June 2020
Print ISSN: 0974-6455 Online ISSN: 2321-4007 CODEN: BBRCBA

Thomson Reuters ISI Web of Science Clarivate Analytics USA and Crossref Indexed Journal

NAAS Journal Score 2020 (4.31) SJIF: 2020 (7.728)
A Society of Science and Nature Publication,

Online Contents Available at: http//www.bbrc.in/
DOI: 10.21786/bbrc/13.2/69

Recently, Rubio et al. (2019) have suggested that pursuing development of insect cell-based foods may lead to new sustainable food products thereby accelerating the field of cellular agriculture. Trager's (1935) success in using inorganic salts, maltose, digested egg albumin and *B. mori* haemolymph to maintain ovarian tissues of *B. mori* spawned a wave of experiments to formulate growth media for culture of insect cells. Mitsuhashi (1982, 1984) successfully modified Grace's medium several times for cultivation of different cell lines. Supplementation with vertebrate sera like foetal bovine serum (FBS) or other proteinaceous materials has been successfully used to get high growth rate (Weiss and Vaughn, 1986). Gradually with increase in interest of researchers in insect cell culture, many serum-free media have been developed (Hink, 1991; Donaldson et al., 1998). Caron et al. (1990) reported high growth rate by increasing total Pluronic F-68 concentration to 0.3% with IPL/41 serum-free medium. Lepidopteran cell lines are now being viewed as an attractive alternative to mammalian cell lines for biomanufacturing of proteins of human interest, biopesticides and vaccines (Kost et al., 2005; Drugmand et al., 2012; Airenne et al., 2013; Van Oers et al., 2015).

Over the years the utility of insect cell lines for production of proteins of human interest has been scaled up from experiment-level to industrial production level (Elias, 2007). Use of vertebrate sera is discouraged during industrial production of therapeutics because of inherent potential risk for transmission of infectious agents as well as the heterogeneity and lack of reliability (Grillberger et al., 2009). Insect cell lines that have high susceptibility to a baculovirus can be used to develop efficient Insect Cell-Baculovirus Expression Vector Systems (IC-BEVS) (Agathos, 2010). An efficient IC-BEVS production platform can be used for foreign gene expression, production of therapeutic compounds and vaccines. DZNU-Bm-1, a larval ovarian cell line has been shown to be highly susceptible to BmNPV in MGM-448 medium (Khurad et al., 2006) and can be used as IC-BEVS platform for foreign gene expression (Khurad et al., 2013).

However, the high cost of MGM-448 medium with supplementation of 10% Foetal Bovine Serum (FBS) is a serious bottleneck for its use in production of therapeutics or other proteins of interest. The present study describes successful reduction in the serum dependence of the cell line DZNU-Bm-1 by first adapting it to MGM 448 growth medium supplemented with 3% FBS and then to a low-cost Mitsuhashi and Maramorosch (MM) medium supplemented with 3% FBS to reduce the cost of maintaining this cell line.

MATERIAL AND METHODS

Culture Media: Modified Grace's medium MGM-448 (Mitsuhashi, 1984) and Mitsuhashi and Maramorosch medium (Mitsuhashi and Maramorosch, 1964) were prepared in laboratory. Modified Grace's Medium (MGM-448): MGM-448 is a complex medium composed of six salts, twenty amino acids, three sugars, four organic acids, ten vitamins and four additives, inosine, cytochrome-c, fetuin and bovine plasma albumin fraction-V. Five stock solutions viz. MGM O.S.A., GMA-salt-mix-A, GMA-salt-mix-B, GMA-Vita-mix-IA, GMA-Vita-mix-IIB were prepared as described by Mitsuhashi (1984).

In order to prepare 250 ml of complete MGM-448 medium, required quantities of respective stock solutions were mixed and the double distilled water was added to make up the volume. To this solution bovine plasma albumin fraction-V, fetuin, cytochrome- c, inosine were added. The medium was supplemented with required quantity (3% or 10%) of FBS. The pH was adjusted to 6.37-6.40 with saturated KOH. The medium was sterilized by passing through 0.2 µm pore size Millipore membrane filter using negative pressure through Sartorius filter unit. No antibiotics were added to the medium.

Mitsuhashi and Maramorosch medium (MM Medium): It is among the simplest insect tissue culture media. It is a mixture of salts used in Carlson's Balanced Salt Solution (CBSS), lactalbumin hydrolysate, TC-yeastolate and glucose supplemented with 3% Foetal Bovine Serum (FBS). For preparation of this medium, stock solution A and stock solution B of CBSS were prepared. 25 ml of each stock solution was mixed. The additives were added and the volume was made up to 250 ml by adding double distilled water. The medium was supplemented with 3% FBS. Sterilization was carried out by passing through 0.2 µm pore size Millipore membrane filters using negative pressure through Sartorius filter unit. No antibiotics were added to the medium.

Maintenance of cell line and subculturing: DZNU-Bm-1 a larval ovarian cell line from B. mori was kindly provided by Dr. A. M. Khurad. The cell line was being cultured in MGM-448 medium supplemented with 10% FBS. The cell line was maintained in the laboratory in glass tissue culture flasks, incubated at 25± 1^0C and passaged regularly. After some time, the cell line could be subcultured regularly by splitting the cultures in a ratio of 1:2 at an interval of 4-5 days.

Adaptation to MGM-448 medium supplemented with 3% FBS: The cell line was first adapted to MGM-448 supplemented with 3% FBS to reduce its serum dependence as described by Mitsuhashi and Grace (1969) through passaging of the cells. This was done by decreasing the volume of original medium (MGM-448 supplemented with 10% FBS) by 20% and increasing the volume of MGM-448 medium supplemented with 3% FBS by 20% at each passage. The initial cell density, final cell density, number of days taken to attain final cell density and population doubling time were noted at each passage.

Adaptation to MM medium supplemented with 3% FBS: The cell line was subsequently adapted to MM medium supplemented with 3% FBS. The volume of MGM-448 supplemented with 3% FBS was reduced while the volume of MM medium supplemented with 3% FBS

was increased through regular passaging. During each passage, the volume of original medium was reduced by 20% while the volume of MM medium supplemented with 3% FBS was increased by 20%. The process was repeated till MGM-448 supplemented with 3% FBS was completely replaced with MM medium supplemented with 3% FBS. The initial cell density, final cell density, number of days taken to attain final cell density and population doubling time were noted at each passage.

Population Doubling Time: Cell suspension was sampled from culture flasks at the time of seeding the culture and on attainment of final cell density. The cell suspension was allowed to flow in the chambers of Neaubauer haemocytometer chamber and cells were counted in four large corner squares each of which is divided into 16 small squares. The volume of one large square is 0.1 mm^3. Therefore, average cell count was multiplied by 104 to give number of cells per ml. The cell number was determined as an average of readings from two culture flasks. The population doubling time (PDT) was calculated using the exponential formula given by Hayflick (1973).

$$r = 3.32 (\text{Log } x_2/x_1)/t_2-t_1$$

where,
r = Multiplication rate,
x_1 = Initial cell number at selected time t_1,
x_2 = Final cell number at selected time t_2,

Generation time (g) = 1/r

Cell Morphology: The cell cultures were observed under MAGNUS INVI inverted phase contrast microscope and photographed regularly after they were adapted to MM medium supplemented with 3% FBS. Cell population comprised of different cell types. The cell size of each type was determined by ocular micrometer in the population taking about 50-100 readings. The relative percentage of each type in population was determined by counting different cell types in optical fields under the inverted microscope.

Karyotype Analysis: Karyotypic studies were carried out in healthy cell cultures during exponential cell growth phase after their successful adaptation to MM medium supplemented with 3% FBS. Demicolcine (Sigma) having a concentration of 50 µg/ml was added to culture flasks to arrest the cell division at metaphase. Final concentration of demicolcine in the culture flask was 1 µg/ml of medium. The cultures were allowed to stand at 25°C for 24-72 hours. The cells were harvested by centrifugation and the supernatant was removed. The pellet was resuspended in hypotonic solution (0.6% KCl) for 15-20 minutes. The cells were again centrifuged and the cell pellet was fixed in 50% glacial acetic acid for 10-15 minutes. The fixed cells were spread on glass slides and allowed to air dry. The slides were washed in distilled water, transferred to Acetorcein stain for 20 minutes, washed briefly in running tap water, air-dried for 12 hours, cleared in two changes of xylene and mounted in DPX. About 50 chromosome spreads were counted and spreads were photographed to determine the range of chromosomes.

Table 1. Population Doubling Time of DZNU-Bm-1 during adaptation from MGM-448 medium supplemented with 10% FBS (A) to MGM-448 medium supplemented with 3% FBS (B).

No. of Days after Seeding of Cultures	Step	Medium Composition	Population Doubling Time in Hours
06	a	80% A + 20% B	52
07	b	60% A + 40% B	68
09	c	40% A + 60% B	83
09	d	20% A + 80% B	81
08	e	100% B	70

(A)= MGM-448 medium supplemented with 10% FBS
(B)= MGM-448 medium supplemented with 3% FBS

Figure 1. Graph showing adaptation of DZNU-Bm-1 from MGM-448 medium supplemented with 10% FBS (A) to MGM-448 medium supplemented with 3% FBS (B). a– 80% A + 20% B; b- 60% A + 40% B; c- 40% A + 60% B; d– 20% A + 80% B; e– 100% B

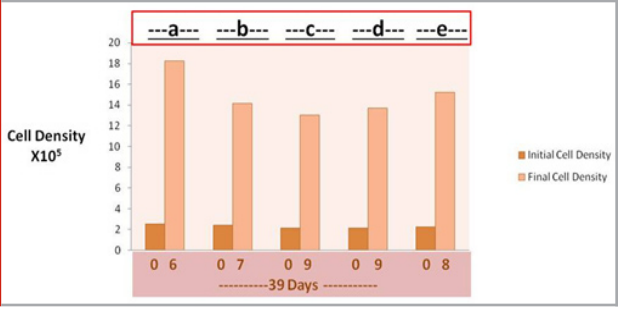

RESULTS AND DISCUSSION

In the first stage of experiment, DZNU-Bm-1 cell line originally cultured in MGM-448 medium supplemented with 10% FBS was successfully adapted to MGM-448 medium supplemented with 3% FBS through several passages. The cell line took about 39 days for adaptation (Fig.1). DZNU-Bm-1 has been reported to take more than 10 months for adaptation to haemolymph-free MGM-448 (Bahekar, 2018). The cells remained freely suspended in culture medium. Cell clumping reported in earlier studies (Bahekar and Qureshi, 2013) was not observed. During step b of adaptation the cells showed reduced growth (Fig. 1). The growth of cells during step c and step d was slowest (Fig. 1). During each of these steps cells required 9 days to reach sufficient cell density for subculturing. The population doubling time was also highest during these steps showing a peak value of about 83 hours (Table 1). Belloncik et al. (1990) have reported slow

growth rate and other difficulties during adaptation. In the present study, by step e the population doubling time was reduced to about 70 hours. After further passages in the same medium population doubling time was reduced to about 49 hours.

The cell line was later adapted to more cost-effective MM culture medium supplemented with 3% FBS. The cell line was easily adapted to MM medium taking about 32 days for adaptation (Fig. 2). Growth of cells was slow during step b and c requiring about 7 days each for attaining sufficient cell density for subculture. Population doubling time was maximum (about 81 hours) during step b (Table 2). During next subcultures the cell line could be passaged by day 6 with population doubling time being reduced to about 54 hours. There was no significant change in cell morphology after adaptation to MM medium supplemented with 3% FBS. The population of DZNU-Bm-1 cell line is heterogeneous and can be differentiated into four cell types- large round, small round, giant cells and spindle shape - on the basis of their shape and size.

Table 2. Population Doubling Time of DZNU-Bm-1 during adaptation from MGM-448 medium supplemented with 3% FBS to MM medium supplemented with 3% FBS (B)

No. of Days after Seeding of cultures	Step designation	Medium composition	Population Doubling time in Hours
06	a	80% A + 20% B	48
07	b	60% A + 40% B	81
07	c	40% A + 60% B	70
06	d	20% A + 80% B	53
06	e	100% B	54

(A)= MGM-448 medium supplemented with 3% FBS
(B)= MM medium supplemented with 3% FBS

Figure 2: Graph showing adaptation of DZNU-Bm-1 from MGM-448 medium supplemented with 3% FBS (A) to MM medium supplemented with 3% FBS (B). a– 80% A + 20% B; b- 60% A + 40% B; c- 40% A + 60% B; d– 20% A + 80% B; e– 100% B

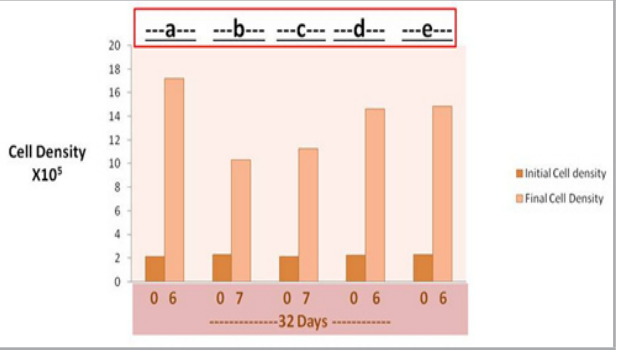

Figure 3: Chromosomes of DZNU-Bm-1 cell line grown in MM culture medium supplemented with 3% FBS. Bar= 30 µm

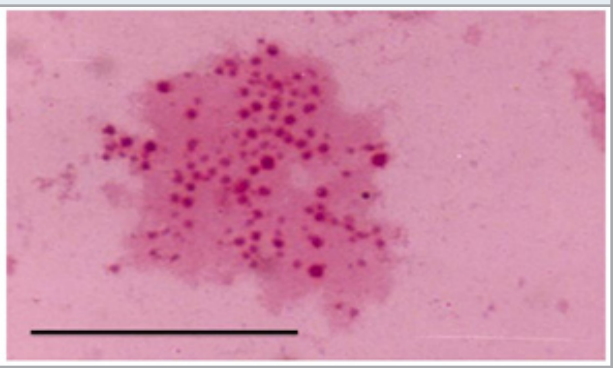

Large round cells: They are round, measuring about 31 ± 0.62 µm in diameter. Their relative percentage in the population is about 30.2%. Initially, they showed partial attachment to the surface of culture flask immediately after subculture.

Small round cells: The small round cells measure about 13.74 ± 0.16 µm. They form 53.4% of the total cell population.

Figure 4: Graph showing distribution of chromosome number in DZNU-Bm-1 cells.

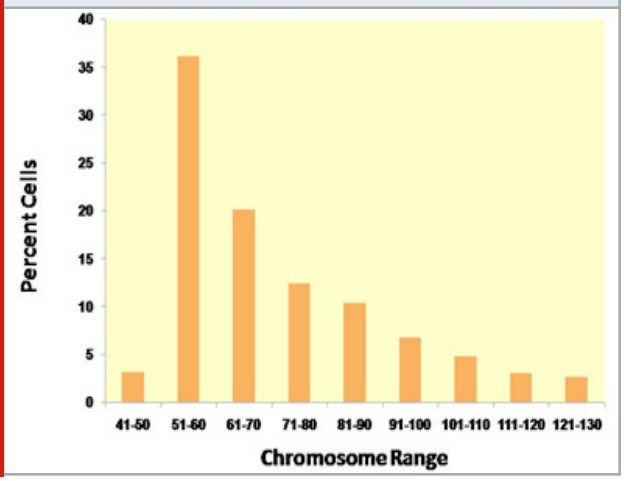

Giant cells: These are very large round cells having a diameter of about 69 ± 3.22 µm. They form 4.7% of the total cell population.

Spindle-shape cells: These cells have protoplasmic processes on the sides giving them appearance of a spindle. Their size is about 51 ± 3.42 µm × 11 ± 0.51 µm. Their percentage in cell population is 11.7%.

The chromosome spreads of cells exhibited numerous microchromosomes that resembled the chromosomes of DZNU-Bm-12 cell line (Khurad et al., 2009). The chromosomes appeared as numerous dot-like, darkly stained bodies (Fig. 3). The diploid number of *B. mori* chromosomes has been known to be 56. The chromosome

number in the cell line ranged from 45 to 126 with a mode towards diploidy. A few cells also possessed more than 100 chromosomes indicating the presence of polyploid cells (Fig. 4). Grace (1967) has reported more than 100 chromosomes in the cells of B. mori ovarian cell line. Chromosome range of 35 to 150 in larval ovarian cell line and 60 to 180 in the pupal ovarian cell line of *B. mori* have also been reported (Sudeep et al., 2002).

CONCLUSION

In the present study DZNU-Bm-1 cell line being cultured in MGM-448 medium supplemented with 10% FBS was first adapted to MGM-448 medium supplemented with 3% FBS. The cell line was slow to reach sufficient cell density during initial steps but showed reduced population doubling time during subsequent passages. The cell line was then successfully adapted to cost effective MM medium supplemented with 3% FBS. The morphological and cultural characteristics as well as the chromosome range of the cells did not exhibit any significant change from those cultured in MGM-448 (10% FBS). DZNU-Bm-1 has earlier been shown to be able to produce foreign proteins. The current study establishes its reduced serum dependence and ability to grow in low-cost culture media raising hopes of adapting it to other serum-free media.

ACKNOWLEDGMENTS

Author is thankful to Professor Dr. A.M. Khurad, Former Head, P.G.T.D. Zoology, RTM, Nagpur University Campus, Nagpur for providing cell line and insightful guidance for this study.

REFERENCES

Agathos, S., 2010. Insect cell culture. In: Baltz, R., Demaine, A., Davies, J., Bull, A., Junker, B., Katz, L., Lynd, L., Masurekar, P., Reeves, C., Zhao, H. (Eds.), Manual of Industrial Microbiology and Biotechnology, 3rd edn. ASM Press, Washington DC, pp. 212-222.

Akiyama, Y., Sakuma, T., Funakoshi, K., Hoshino, T., Iwabuchi, K., and Morishima, K., 2013. Atmospheric-operable bioactuator powered by insect muscle packaged with medium. Lab Chip 13, 4870–4880.

Airenne, K.J., Hu, Y.C., Kost, T.A., Smith, R.H., Kotin, R.M., Ono, C., Matsuura, Y, Wang, S., Seppo, Y., 2013. Baculovirus: An insect-derived vector for diverse gene transfer applications. Molecular Therapy 21(4), 739–749.

Bahekar, R.S., 2018. Growth kinetics and baculovirus productivity of indigenously developed cell line DZNU-Bm-1 of *Bombyx mori* (L) in different medium. Research Directions 6(5), 67-76.

Bahekar, R.S., Qureshi, S. O., 2013. Study of some morphological and chromosomal parameters for the characterization of three indigenously developed ovarian cell lines of *Bombyx mori* (L). Bioscience Biotechnology Research Communications 6(1), 28-31.

Belloncik, S., Allard, C., Rouleau, D., 1991. Adaptation of a *Bombyx mori* cell line to serum-free media. In: Proceedings of the 8th International Conference on Invertebrate and Fish Tissue Culture, Anaheim, CA, USA, 178-180.

Caron, A.W., Archambault, J. and Massie B., 1990. High level recombinant protein production in bioreactors using the baculovirus-insect cell expression system. Biotechnol. Bioeng. 36, 1133-1140.

Donaldson, M.S., Shuler, M.L., 1998. Low serum-free medium for the BTI-Tn5B1-4 insect cell line. Biotechnol. Prog. 14, 573-579.

Drugmand, J.C., Schneider, Y.J., Agathos, S.N., 2012. Insect cells as factories for biomanufacturing. Biotechnol. Adv. 30(5), 1140–1157.

Elias, C.B., Jardin, B., Kamen, A., 2007. Recombinant protein production in large-scale agitated bioreactors using the baculovirus expression system. In: Murhammer D.W. (Ed.) Methods in molecular biology series. Baculovirus and insect cell expression protocols. Springer, New York, pp. 225-245.

Grace, T.D.C., 1967. Establishment of a cell line from the silkworm, *Bombyx mori*. Nature 216, 613.

Grillberger, L., Kreil, T.R., Nasr, S., Reiter, M., 2009. Emerging trends in plasma-free manufacturing of recombinant protein therapeutics expressed in mammalian cells. Biotechnol. J. 4, 186–201.

Hayflick, L., 1973. Subculturing human diploid fibroblast cultures. In: Kurse, P.F, Patterson, M. K. Jr. (Eds.), Methods and Applications. Academic Press, New York, pp. 220-223.

Hink, W.F., 1991. A serum free medium for the subculture of insect cells and production of recombinant proteins. In Vitro Cell. Dev. Biol. 27 A (5), 397-401.

Ikonomou, L., Schneider, Y.-J., and Agathos, S. N., 2003. Insect cell culture for industrial production of recombinant proteins. Appl. Microbiol. Biotechnol. 62, 1–20.

Irons, S.L., Chambers, A.C., Lissina, O., King, L.A., and Possee, R.D., 2018. Protein production using the baculovirus expression system. Curr. Protoc. Protein Sci. 91, 5.5.1–5.5.22.

Khurad, A.M., Kanginakudru, S., Qureshi, S.O., Rathod, M.K., Rai, M. M., Nagaraju, J., 2006. A new *Bombyx mori* larval ovarian cell line highly susceptible to nucleopolyhedrovirus. Journal of Invertebrate Pathology 92, 59-65.

Khurad, A.M., Zhang, M.J., Deshmukh, C.G., Bahekar, R.S., Tiple, A.D., Zhang, C.X., 2013. A new continuous cell line from larval ovaries of silkworm, *Bombyx mori*. In Vitr. Cell. Dev. Biol. Anim. 45, 414–419.

Khurad, A.M., Bahekar, R.S., Zhang, M.J., Tiple, A.D., Lee, J. M., Zhang, C.X., Kusakabe, T., 2013. Development and characterization of a new *Bombyx mori* cell line for protein expression. Journal of Asia-Pacific Entomology 16, 17–22.

Kost, T.A., Condreay, J.P. and Jarvis, D.L., 2005. Baculovirus as versatile vectors for protein expression

in insect and mammalian cells. Nat Biotechnol. 23, 567-575.

Lynn, D. E., 2001. Novel techniques to establish new insect cell lines. In Vitr. Cell. Dev. Biol. Anim. 37, 319–321.

Mitsuhashi, J., 1982. Media for insect cell cultures. In: Maramorosch, K. (Ed.), Advances in Cell Culture. Academic Press, New York, Vol. 2. pp. 133-196.

Mitsuhashi, J., 1984. Isolation of a continuous cell line from larval fat bodies of an Arctiid moth, *Spilarctia seriatopunctata* (Insecta, Lepidoptera, Arctiidae). Zool. Sci. 1, 415-419.

Mitsuhashi, J., Maramorosch, K., 1964. Leafhopper tissue culture: embryonic, nymphal and imaginal tissues from aseptic insects. Contrib. Boyce Thompson Inst. 22, 435-460.

Mitsuhashi, J. and Grace, T.D.C., 1969. Adaptation of established cell lines to a different medium. Appl. Ent. Zool. 4(3), 122-125.

Mitsuhashi, J., and Goodwin, R. H., 2018. The Serum-Free Culture of Insect Cells In Vitro. In: Mitsuhashi, J. (Ed.), Invertebrate Cell System Applications, CRC Press, Boca Raton, Florida, pp. 31–43.

Neermann, J., and Wagner, R., 1996. Comparative analysis of glucose and glutamine metabolism in transformed mammalian cell lines, insect and primary liver cells. J. Cell. Physiol. 166, 152–169.

Rubio, N.R., Fish, K.D., Trimmer, B.A., Kaplan D.L., 2019. Possibilities for Engineered Insect Tissue as a Food Source. Front. Sustain. Food Syst. 3, 1-13.

Sudeep, A.B., Mishra, A.C., Shouche, Y.S., Pant, U., Mourya, D.T., 2002. Establishment of two new cell lines from *Bombyx mori* (L.) (Lepidoptera: Bombycidae) and their susceptibility to baculoviruses. Indian J. Med. Res. 115, 189-193.

Trager, W., 1935. Cultivation of the virus of grasserie in silkworm tissue culture. J. Exp. Med. 61, 501-513.

Van Oers, M.M., Pijlman, G.P., Vlak, J.M., 2015. Thirty years of baculovirus-insect cell protein expression: From dark horse to mainstream technology. J Gen Virol. 96(Pt 1), 6-23.

Weiss, S.A., Vaughn, J.L., 1986. Cell culture methods for large-scale production of baculoviruses. In: Granados, R.R. and Federici, B.A. (Eds.), The Biology of baculoviruses, CRC Press, Boca Raton, Florida, pp. 63-87.

ISSN 2277 - 5730
AN INTERNATIONAL MULTIDISCIPLINARY
QUARTERLY RESEARCH JOURNAL

AJANTA

Volume - IX Issue - II APRIL - JUNE - 2020

ENGLISH / MARATHI / HINDI PART - I

Peer Reviewed Referred
and UGC Listed Journal

Journal No. 40776

ज्ञान-विज्ञान विमुक्तये

IMPACT FACTOR / INDEXING
2019 - 6.399
www.sjifactor.com

❖ EDITOR ❖
Asst. Prof. Vinay Shankarrao Hatole
M.Sc (Maths), M.B.A. (Mktg.), M.B.A. (H.R.),
M.Drama (Acting), M.Drama (Prod. & Dir.), M.Ed.

❖ PUBLISHED BY ❖

Ajanta Prakashan
Aurangabad. (M.S.)

VOLUME - IX, ISSUE - II - APRIL - JUNE - 2020
AJANTA - ISSN 2277 - 5730 - IMPACT FACTOR - 6.399 (www.sjifactor.com)

CONTENTS OF ENGLISH PART - I

VOLUME - IX, ISSUE - II - APRIL - JUNE - 2020
AJANTA - ISSN 2277 - 5730 - IMPACT FACTOR - 6.399 (www.sjifactor.com)

CONTENTS OF MARATHI PART - I

VOLUME - IX, ISSUE - II - APRIL - JUNE - 2020
AJANTA - ISSN 2277 - 5730 - IMPACT FACTOR - 6.399 (www.sjifactor.com)

३. जागतिकीकरणात भारतातील दारिद्रय : एक अभ्यास

प्रा. डॉ. दिपक शृगांरे
अर्थशास्त्र विभाग प्रमुख, आदर्श महाविद्यालय, धामणगाव रेल्वे, जि. अमरावती.

प्रस्तावना

भारत हा एक श्रीमंत देश आहे. पण भारतातील लोक मात्र गरीब आहे याचा अर्थ असा की भारतात नैसर्गिक साधन संपत्ती विपुल प्रमाणात आहे. परंतु या साधनांचा पुरेपूर वापर होत नसल्यामुळे भारत हा गरीब राहिला आहे. आर्थिक नियोजनाचा स्वीकार करून जवळपास 60 वर्ष पूर्ण होत आहे. अजूनही 29.8% लोक दारिद्रयरेषेखालील जीवन जगत आहेत. जगातील एकूण दारिद्रय रेषेखालील जीवन जगणाऱ्या लोकसंख्येच्या एक तृतीयांश लोकसंख्या भारतातील आहे. भारतीय अर्थव्यवस्था लोकसंख्येच्या दृष्टीने दुसऱ्या क्रमांकाची अर्थव्यवस्था म्हणून ओळखली जाते.

1991 ला भारतात आर्थिक सुधारणांचे पर्व सुरू झाले आणि 2020 ला 18 वर्ष पूर्ण झाले. या काळात भारताला दारिद्रय आणि विषमता यावर मात करणे शक्य झाले आहे काय? विकास सर्वसमावेशक असेल तर देशाचा जसाजसा विकास होत जातो तसे तसे दारिद्रयाचे प्रमाण कमी कमी होत जाते. अर्थशास्त्रात दारिद्रय आणि विषमता याबाबत अर्मत्य सेन यांचे योगदान महत्त्वाचे आहे. त्यांनी उत्पन्नातील विषमतेचे विवेचन केले. ॲडम स्मिथ यांनी आपल्या ग्रंथात जेव्हा समाजातील बहुतांशी लोक दुःखी आणि गरीब असतात तेव्हा कोणताही समाज सुखी किंवा समृद्ध असूच शकत नाही असे म्हटले आहे. जीवनावश्यक अशा मूलभूत गरजांची पूर्तता करण्याची क्षमता नसणे म्हणजे दारिद्रय होय. आर्थिक विकासाचा उद्देश्य दारिद्रय, बेरोजगारी, विषमता निर्मूलन तसेच मूलभूत गरजाची पूर्णतः समान न्याय आणि सर्वात महत्वाची बाब म्हणजे "मानवाचा सर्वांगिन विकास" हा असायला पाहिजे.

शोधनिबंधाची उद्दिष्टे

१) भारतातील दारिद्रयाच्या प्रश्नाची तीव्रता अभ्यासणे.

२) भारतातील दारिद्रयाच्या कारणांचा अभ्यास करणे.

३) दारिद्रय निर्मुलनासाठी विविध संभाव्य उपायाचे अध्ययन करणे.

अभ्यास पध्दती

प्रस्तुत शोधनिबंधातून भारतातील दारिद्रयाचा अभ्यास करण्याचा प्रयत्न करण्यात आला आहे. दारिद्रयाच्या संदर्भात संदर्भ ग्रंथ, पाक्षिक, मासिके, नियतकालिके, भारताची आर्थिक पाहणी इत्यादी मधून माहिती संकलित केली आहे. भारतातील दारिद्रयाची संकल्पना, दारिद्रयाचे प्रकार, दारिद्रयाचे मोजमाप, वाढीची कारणे त्यामुळे निर्माण होणाऱ्या समस्या व दारिद्रय निर्मुलनाचे उपाय सुचविणे हा लेखनामागचा उद्देश असून याकरिता दुय्यम माहितीचा आधार घेण्यात आला आहे.

शोधनिबंधाची गृहिते

१) भारतातील दारिद्रयाचे प्रमाण जास्त आहे.

२) भारतातील दारिद्रय वाढीसाठी सरकारी धोरणे कारणीभूत आहेत.

३) भारतातील दारिद्रय निर्मुलनासाठी करण्यात येणारी उपाययोजना पर्याप्त आहे.

दारिद्रयाची संकल्पना

"भानसी दर दिवशी एक डॉलरपेक्षा कमी उत्पन्न मिळणाऱ्या व्यक्ती म्हणजे दारिद्रय रेषेखालील व्यक्ती होय".

– जागतिक बँक

"एखाद्या व्यक्तीला त्याने जोपासलेल्या मूल्याप्रमाणे जगता न येणे म्हणजे दारिद्रय होय".

– प्रा. अमर्त्य सेन

"दारिद्रय म्हणजे संधी व निवड यांचा परित्याग व मानवी प्रतिष्ठेची पायमल्ली होय. दारिद्रय म्हणजे समाजात प्रभावीपणे सहभाग घेण्याची संधी न मिळणे. अन्न व कपडे पुरेसे नसणे, दारिद्रय म्हणजे असे कुटुंब जे शाळेत किंवा दवाखान्यात जाऊ शकत नाही भूमिहीन आणि बेरोजगार आहे, तसेच असुरक्षितता व दुर्बलता होय".

– संयुक्त राष्ट्र संघ

"दारिद्रय म्हणजे स्वतःवर अवलंबून असणाऱ्या व्यक्तीचे पालन–पोषण करण्यासाठी तसेच निरोगी, उत्साही राहण्यासाठी लागणाऱ्या जरुरीच्या वस्तूंचा अपुरा पुरवठा होय".

– गोडार्ड

दारिद्रय ही संकल्पना व्यापक असून ती देशपरत्वे व कालपरत्वे बदलणारी आहे. दारिद्रयाचा सर्वसमावेश अर्थ असा होतो की, "किमान निर्वाह पातळी किंवा चांगल्या जिवनमानाची कल्पना हाच आहे.

निरपेक्ष दारिद्रय

निरपेक्ष दारिद्रयाचा संबंध किमान निर्वाह पातळीशी जोडला जातो. ज्या व्यक्तीस आपल्या प्राप्त उत्पन्नातून किमान गरजा भागविणे शक्य नसते त्यास निरपेक्ष दारिद्रय असे म्हणतात.

सापेक्ष दारिद्रय

एकाच देशातील 5% ते 10% अति उच्च उत्पन्न असणारा गट आणि 5% ते 10% न्यून उत्पन्न असणारा गट या दोहोंच्या उत्पन्नाची, उपभोगाची आणि राहणीमानाची तुलना केल्यास न्यून उत्पन्न असणाऱ्या गटाचा उपयोग आणि उत्पन्न खूप कमी असते. उपभोग आणि उत्पन्नात जे अंतर प्रतिबिंबित होते त्याला सापेक्ष दारिद्रय असे म्हणतात.

भारतातील दारिद्रयाचे मोजमाप

भारतीय नियोजन मंडळाने स्थापन केलेल्या विविध समित्या आणि अर्थतज्ञांकडून दारिद्रयाचे मोजमाप केले जाते. भारतातील दारिद्रयाचा अभ्यास करून निष्कर्ष काढले जातात. 1997 पासून नियोजन आयोगामार्फत दारिद्रय रेषा व दारिद्रयाचे प्रमाण मोजण्यासाठी नवीन पद्धतीचा वापर केला जात आहे. यामध्ये सर्व उपभोग्य वस्तूचा 30 दिवसाच्या उपभोग आकडेवारीचा समावेश केला जातो.

मिन्हास, जैन व टेंडूलकर

यांच्या समितीने केलेल्या दारिद्रयाच्या अभ्यासानुसार 1987–88 मध्ये भारतातील एकूण दारिद्रयाचे प्रमाण 42.7% होते. त्यापैकी ग्रामीण भागातील दारिद्रयाचे प्रमाण 44.8% तर शहरी भागातील दारिद्रयाचे प्रमाण 36.5% असल्याचे आढळून आले.

सुरेश तेंडुलकर समिती

या समितीने 8 डिसेंबर 2009 मध्ये आपला अहवाल सादर केला. 2009–10 साठी ग्रामीण भागाकरिता 673 रुपये शहरी भागाकरिता 860 रुपये दरडोई मासिक खर्च ठरवून दारिद्रयरेषा निश्चित केली. त्यानुसार समितीला देशात एकूण दारिद्रयाचे प्रमाण 29.8% आढळले. ग्रामीण भागात ते 33.8% तर शहरी भागात ते 20.9% आढळून आले.

दारिद्रयरेषा

दारिद्रयात जीवन जगणाऱ्या लोकांच्या प्रमाणाचे मोजमाप व योग्य आकलन होण्यासाठी दारिद्रयरेषा निश्चित केली जाते. लॉर्ड बॉयड यांनी इ.स. 1945 ला सर्वप्रथम Hunger Line ही संकल्पना मांडली. जगण्यासाठी प्रत्येक व्यक्तीला शहरी भागात 2100 ते ग्रामीण भागात 2400 कॅलरीजयुक्त आहार दररोज उपलब्ध न होणाऱ्या व्यक्ती दारिद्रयरेषेखाली आहे असे मानले जाते. नियोजन आयोगाने जून 2014 ला प्रसिद्ध केलेल्या अहवालानुसार इ.स. 2011–12 च्या किंमतीवर आधारित प्रतिव्यक्ती प्रतिमाह ग्रामीण भागाकरिता रुपये 972 व शहरी भागाकरिता रुपये 1407 किमान उपभोग खर्च दारीद्र रेषा म्हणून निश्चित केली. जागतिक बँकेने आंतरराष्ट्रीय दारिद्रयरेषेच्या निकषानुसार 2012 च्या किंमतीवर आधारित जागतिक लोकसंख्येच्या 12.7% लोक व भारतातील 21.3% लोक आंतरराष्ट्रीय दारिद्रयरेषेखाली जीवन जगत असल्याचे दिसून आले.

भारतातील दारिद्रयाची कारणे

अतिरिक्त लोकसंख्या

भारतातील वाढती लोकसंख्या हे एक दारिद्रयाचे कारण आहे. 1951 मध्ये भारताची लोकसंख्या 36.10 कोटी तर 2001 मध्ये ती 102.72 कोटी झाली. 2011 मध्ये वाढून 121.02 कोटी झाली. भारतात लोकसंख्या वाढीच्या वाढत्या दरामुळे उत्पन्नातील वाढ कमी दिसून येते त्यामुळे दारिद्रय टिकून आहे.

शेतीची न्यून उत्पादकता

भारतीय शेतीत वापरण्यात येणारी जुनाट यंत्र, तंत्र, सिंचनाचा अभाव, अयोग्य खते, कीटकनाशके, बियाण्याचा वापर याचा परिणाम शेतीच्या उत्पादकतेवर होतो. भारताची अर्थव्यवस्था कृषिप्रधान असल्यामुळे बहुतांश लोक शेतीवर अवलंबून आहे. शेतीची उत्पादकता कमी असल्यामुळे उत्पादन कमी होते म्हणून उत्पन्न कमी होऊन दारिद्रय निर्माण होते.

वाढती बेकारी

लोकसंख्या जास्त असल्यामुळे रोजगार उपलब्ध होत नाही. त्यामुळे लोकांना आपल्या किमान गरजा पूर्ण करण्याकरिता आवश्यक उत्पन्न कमी पडत असल्यामुळे दारिद्रयाची निर्मिती होते व ते टिकून राहते. दारिद्रय व

बेरोजगारी हा एकाच नाण्याच्या दोन बाजू आहेत. रोजगाराच्या संधी नसल्यामुळे बेरोजगार लोकांमध्ये मोठ्या प्रमाणात दारिद्रय आढळून येते.

परकीय सत्ता

1947 ला भारताला स्वातंत्र्य मिळाले. तत्पूर्वी भारतावर 150 वर्ष ब्रिटिशांनी राज्य केले. तसेच पोर्तुगाल, ग्रीक, मोगल, डच अशा अनेक देशांनी व राजांनी आक्रमण करून भारतातील सोने, चांदी अनेक अमूल्य वस्तूंची लूट केली आणि भारताच्या विकासाकडे फारसे लक्ष दिले नाही.

उत्पन्न विषमता

भारतात गरीब आणि श्रीमंत यामध्ये मोठी तफावत दिसून येते. राष्ट्रीय उत्पन्नाच्या असमान वाटपामुळे आर्थिक विषमता आढळून येते. महालनोबिस समिती नुसार उच्च उत्पन्न गटातल्या 20% लोकांना पूर्ण राष्ट्रीय उत्पन्नातील 53% हिस्सा मिळतो. तर 20% गरीब लोकांना फक्त 5% हिस्सा मिळतो. त्यामुळे या लोकांना मूलभूत गरजा पासून वंचित राहावे लागते व ते दारिद्रयात जीवन जगण्यास प्रवृत्त होतात.

भांडवल निर्मितीचा दर कमी

भांडवल ही विकासाची किल्ली असते. भांडवल निर्मितीचा दर बचत दरावर अवलंबून असतो. गुंतवणुकीसाठी भांडवल आवश्यक आहे. देशात विविध क्षेत्रात भांडवलाच्या अभावी गुंतवणूक केली जात नाही. त्यामुळे रोजगार निर्माण न होता देशातील लोकांना बेकार राहावे लागते त्यामुळे ते गरीब राहतात.

दोषपूर्ण शिक्षणव्यवस्था

2011 च्या जनगणनेनुसार भारतातील साक्षरतेचे प्रमाण 75% जवळपास आहे. महाविद्यालय स्तरापर्यंत दिलेले शिक्षण व्यवसाय दृष्टिकोनातून नसल्यामुळे नोकरी न मिळाल्यास स्वयंरोजगार किंवा स्वतःचा व्यवसाय करू शकत नाही. त्यामुळे त्यांना बेकार राहावे लागते. म्हणून देशात दारिद्रयाचे प्रमाण वाढत जाते.

अल्प वितरण प्रभाव

दारिद्रय निर्मूलन करण्यासाठी शासनामार्फत अनेक कल्याणकारी योजना राबविल्या जातात. परंतु योजनेची अंमलबजावणी प्रभावीपणे न झाल्यामुळे व याचा लाभ गरीब लोकांना न मिळाल्यामुळे त्याच्या उत्पन्नात वाढ झाली नाही. अनेक शासनकर्ते, अधिकारी, कर्मचारी अशा योजनेचे पूर्ण लाभ गरजू लोकांपर्यंत पोहोचू देत नाही. त्यामुळे त्यांच्या दारिद्रयात सुधारणा होत नाही.

दारिद्रय निर्मूलन उपाय

आर्थिक विकासात वाढ

आर्थिक विकासाचा अल्प दर हे दारिद्रय वाढीचे मुख्य कारण आहे. आर्थिक विकासामुळे अनेक क्षेत्रात गुंतवणूक, रोजगार, उत्पादन व उत्पन्न वाढण्यास मदत होते. त्यामुळे लोकांची क्रयशक्ती वाढून त्याच्या मूलभूत गरजा पूर्ण होऊन दारिद्रयाचे प्रमाण कमी होण्यास मदत होते.

लोकसंख्या नियंत्रण

लोकसंख्या वाढीचा दर जास्त असल्याने दरडोई उत्पन्न कमी होते. भारतात लोकसंख्या नियंत्रण धोरण कडक आणि प्रभावीपणे राबविण्याची आवश्यकता आहे. यामुळे लोकसंख्या वाढीवर नियंत्रण बसून लोकसंख्या वाढीचा वेग कमी होईल. त्यामुळे दारिद्रय कमी होण्यास मदत होईल.

ग्रामीण भागाचा विकास

भारतातील 70% लोकसंख्या ग्रामीण भागात वास्तव्य करते. त्यांचा उदरनिर्वाहाचा मुख्य आधार शेती आहे. ती हंगामी स्वरूपाची असल्याने अर्धवेळ लोकांना बेकार राहावे लागते. ग्रामीण भागात शेती व शेतीवर आधारित उद्योग, व्यवसायाला प्रोत्साहन दिल्यास ग्रामीण भागातील लोकांच्या जीवनमानात सुधारणा होईल.

औद्योगिकीकरणाचा जलद गतीने विकास

लघु, मध्यम व कुटीर उद्योगात श्रम प्रधान तंत्राचा वापर अधिक प्रमाणात केला जातो. त्यामुळे यात रोजगार निर्मितीची संधी जास्त असतात. असे उद्योग प्रामुख्याने ग्रामीण भागात स्थापित झालेले असतात. अशा उद्योगाच्या विकासासाठी योग्य धोरण आखल्यास रोजगार निर्मिती होईल.

शिक्षण पद्धतीत सुधारणा

भारतात शिक्षित बेकारीचे प्रमाण अधिक आहे. शिक्षण पद्धतीत सुधारणा करून व्यावसायिक शिक्षण दिल्यास त्यांच्या कौशल्यात व ज्ञानात वाढ होऊन जर नोकरीच्या संधी नसतील तर असे लोक स्वतःचे उद्योग व्यवसाय निर्माण करतील त्यातून त्यांची आर्थिक प्रगती होईल दारिद्रयाचे प्रमाण कमी होईल.

सामाजिक सुधारणा

भारतीय लोक सामाजिक, धार्मिक आणि सांस्कृतिक रूढी परंपरा जसे लग्न, बारसे, श्राध्द, सण, उत्सव इत्यादी प्रथेचे काटेकोरपणे पालन करून अनावश्यक खर्च करतात. बरेचदा अशा रूढी कर्ज काढून साजरा केल्या जातात. त्यामुळे कर्जबाजारीपणा वाढतो तसेच दैववाद, अंधश्रद्धा, अज्ञान, निरसता इत्यादी कारणामुळे ते दारिद्रयाच्या दृष्टचक्रात अडकतात. यासाठी त्यांच्यात वैज्ञानिक दृष्टिकोनाची जागृती करणे आवश्यक आहे.

पायाभूत सुविधेत वाढ

देशाच्या जलद आर्थिक विकास करण्यासाठी पायाभूत सुविधा असणे आवश्यक आहे. विज, पाणी, वित्तपुरवठा, रस्ते, पूल, रेल्वे विभाग व्यवस्था, शिक्षण, आरोग्य व्यवस्था इत्यादीचा मोठ्या प्रमाणातं निर्माण करण्यासाठी रोजगार निर्मिती होईल. तसेच या सुविधेमुळे कृषी उद्योग–व्यापार क्षेत्राचा विकास होऊन अनेक लोकांना यात रोजगार मिळून त्यांचे दारिद्रय दूर होईल.

राष्ट्रीय ग्रामीण जीवन्नोती अभियान

18 जुलै 2011 ला राष्ट्रीय ग्रामीण जीवन्नोती अभियान सुरू करण्यात आले. परंतु त्यात अनेक उणिवा केंद्रशासनाच्या निदर्शनास आल्या हया योजना देशातील सर्व गरीब कुटुंबापर्यंत पोहोचून त्यांना कायमस्वरूपी उपजीविकेच्या संधी उपलब्ध करणे व गरिबी रेषेच्यावर येईपर्यंत त्यांना मदतीचा हात देऊन त्यांचे जीवनमान उंचावण्यासाठी मदत करणे हा अभियानाचा उद्देश असणे अभिप्राय आहे.

ग्रामीण भागातील गरीब लोकांतील विधवा, अपंग, अनुसूचित जाती, जमाती, अल्पसंख्यांक, वयोवृद्ध, आदिवासी इत्यादीसाठी स्वयंरोजगाराचे उन्नतीकरण, मागणी आधारित योजना, अनुदान, अर्थसहाय्य देऊन अनेक योजनांचे एकत्रीकरण करून या लोकांच्या कौशल्यात वाढ करण्यात विशेष प्रशिक्षण कार्यक्रम आयोजित करणे आवश्यक आहे. सक्षम दारिद्रय व्यक्तीच्या हाताला काम, रोजगार संधी, सुविधा, आरोग्य, शिक्षण सुविधा पुरवून दुर्बल वर्गासाठी योजना राबविणे हा दारिद्रय निर्मूलनासाठी एक उपाय आहे.

निष्कर्ष

भारत देशाला येत्या काही वर्षात जगातील महाशक्ती म्हणून पाहिले जाईल. भारत देशातील होणाऱ्या विकासाचा फायदा समाजातील शेवटच्या घटकापर्यंत पोहोचला पाहिजे. सदर शोधनिबंध अध्ययनातून असे दिसून येते की, भारतातील दारिद्रयाचे प्रमाण जास्त आहे. लोकसंख्या नियंत्रण आणि सरकारची चुकीची धोरणे यामुळे दारिद्रय वाढीचा दर कमी करण्यात अपयश आलेले आहे. शासकीय धोरणानुसार आवास, स्वयंरोजगार, सिंचन, आरोग्य, कौशल्य विकास, ग्रामसुधार इत्यादी संबंधी विविध योजनांची अंमलबजावणी केली जाते. या योजनेची योग्य अंमलबजावणी करण्यासाठी कुशल, कार्यक्षम, शासनकर्ते व अधिकारी वर्ग यांच्यामार्फत दारिद्रयाचे न्यायपूर्ण मोजमाप होण्यासाठी व दारिद्रय निर्मूलनासाठी एकत्रित येऊन सर्वकष प्रयत्न करून प्रभावीपणे राबविल्यास दारिद्रयाची समस्या दूर होण्यास मदत होईल. आज भारत जगात सर्वाधिक वेगाने आर्थिक प्रगती करीत आहे. असे असले तरी दारिद्रयाचे निर्मूलन केल्याशिवाय या आर्थिक विकासाला काहीही अर्थ राहणार नाही.

संदर्भ

१) एन.एल. चव्हाण, भारतीय अर्थव्यवस्था, प्रशांत प्रकाशन, जळगाव, मार्च 2015, पृ. क्र. 91.

२) करमसिंग राजपूत, भारतीय अर्थव्यवस्था, साई–ज्योती प्रकाशन, नागपूर, जुलै 2019, पृ. क्र. 157.

३) रवींद्र देशमुख, भारतीय अर्थव्यवस्था, पिंपळापुरे प्रकाशन, नागपूर, जुलै 2019, पृ. क्र. 183.

४) www-shodhganga-intlibnet-ac-in, भारतीय अर्थव्यवस्था आणि दारिद्रय, जाने. 2017 पृ. क्र. 23, 24.

५) अर्थसंवाद ऑक्टो–डीसें 2012 अंक–16, खंड–3, पृ. क्र. 306, 345.

६) अर्थसंवाद ऑक्टो–डीसें 2017 अंक–41, खंड–3, पृ. क्र. 225.

String Source in Cosmological Model for Theory of Gravitation

S. N. Bayaskar[1], U. T. Arbat[2]
Adarsh Science, Jairamdas Bhagchand Arts & Birala Commerce Mahavidyalaya, Dhamangaon Rly, Dist.-Amravati 444709
E-mail: snbayaskar@rediffmail.com

DES College of Engineering and Technology, Dhamangaon Rly, Dist.-Amravati 444709
E-mail: umesharbat1201@gmail.com

Abstract: *We have investigated the cosmological model in presence of cosmic string source, for solving field equations in Brans-Dicke theory of gravitation for plane symmetric space time. It is observed that cosmological model exist. Some interesting physical and geometrical properties of the model are also discussed.*

Keywords**:** *Plane symmetric cosmological model, Cosmic string, Brans- Dicke theory, Tension density*

1. Introduction

In the theory of gravitation, the plane symmetric model plays an important role. A space time that admits the three parameters groups of motion of the Euclidean plane is said to posses' plane symmetry called plane symmetric space time. Einstein theory of gravitation serves as a basic for the construction of mathematical model of the universe. Cosmological model play an important role in understanding some essential feature of the universe such as the formation of galaxies during early stage of evolution. Brans-Dicke (1961) formulated a scalar tensor theory of gravitation in which gravity is mediated by a scalar field ϕ in addition to the usual metric tensor field g_{ij} present in the Einstein theory. In this theory the long range scalar field ϕ is generated by the whole of matter in the universe according to Mach's principle (Dicke 1964) and has the dimension of the universe of the gravitational constant G. The field equations in Brans- Dicke theory are

$$G_{ij} = -8\pi\varphi^{-1}T_{ij} - \omega\varphi^{-2}\left(\varphi,_i \varphi,_j - \frac{1}{2} g_{ij}\varphi,_k \varphi^{'k}\right) - \varphi^{-1}\left(\varphi_{i;j} - g_{ij}\Box\varphi\right) \tag{1}$$

and $\Box\varphi = \varphi^{'k}_{;k} = 8\pi\varphi^{-1}T\left(3+2\omega\right)^{-1}$ (2)

Where $G_{ij} = R_{ij} - \frac{1}{2} g_{ij}R$ is the Einstein tensor, T_{ij} is the stress energy of the matter, ω is the coupling constant, comma and semi comma denotes partial and covariant differentiation respectively.

The equation of motion

$$T^{ij}_{;j} = 0 \tag{3}$$

are consequences of the field equation (1) and (2).

Some researcher there has been a lot of interest in cosmic strings and the cosmological models. Cosmic strings are one dimensional topological defects associated with spontaneous symmetry breaking, whose plausible production site is cosmological phase transmittions in the year universe (Kibble ,1976 and Vilenkin 1985), Latelier (1983), Vilenkin (1981), Krori et al. (1990,1994) are some of the authors who have initiated the study of string cosmological models. Pimental (1996) (1997) studied inhomogeneous cosmological models in Brans Dicke scalar tensor theory and obtained exact solution which is conformally related to the non singular model recently found in general relativity. Raheman et al. (2001, 2002, 2003) have studied several aspects of cosmic string in Brans Dicke (1961), Saez-Ballester (1985) scalar tensor theories of gravitation and Lyra (1951) geometry.

2. Metric and Field Equations

We consider the plane symmetric space time

$$ds^2 = dt^2 - A^2\left(dx^2 + dy^2\right) - B^2 dz^2 \tag{4}$$

Where A and B are the functions of time t only.

The energy momentum tensor for the cosmic string is

$$T_{ij} = \rho u_i u_j - \lambda x_i x_j \tag{5}$$

Where ρ is the rest energy density of cloud of string with particles attached to them.

λ is the tension density of string

u^i is the cloud four velocity and

x^i is the direction of anisotropy

We have

$$u^i u_i = -x^i x_i = 1 \text{ and } u^i x_i = 0 \tag{6}$$

We consider

$$\rho = \rho_p + \lambda$$

Where ρ_p is the rest energy density of particle and x^i to be along z axis, so that

$$x^i = \left(0,0,A^{-1},0\right) \tag{7}$$

$$u^i = \left(0,0,0,1\right) \tag{8}$$

The field equation (1), (2) and metric (4) for equation (5) with the help of equation (6),(7) and (8) can be written as

$$\frac{\ddot{A}}{A}+\frac{\ddot{B}}{B}+\frac{\dot{A}\dot{B}}{AB}=-\frac{\omega}{2}\left(\frac{\dot{\phi}}{\phi}\right)^2-\frac{\ddot{\phi}}{\phi}-\left(\frac{\dot{A}}{A}+\frac{\dot{B}}{B}\right)\frac{\dot{\phi}}{\phi}$$

$$2\left(\frac{\ddot{A}}{A}\right)+2\left(\frac{\dot{A}}{A}\right)^2=8\pi\phi^{-1}\lambda-\frac{\omega}{2}\left(\frac{\dot{\phi}}{\phi}\right)^2-\frac{\ddot{\phi}}{\phi}-2\frac{\dot{A}}{A}\frac{\dot{\phi}}{\phi}$$

$$2\frac{\dot{A}\dot{B}}{AB}+\left(\frac{\dot{A}}{A}\right)^2=8\pi\phi^{-1}\rho+\frac{\omega}{2}\left(\frac{\dot{\phi}}{\phi}\right)^2-\left(2\frac{\dot{A}}{A}+\frac{\dot{B}}{B}\right)\frac{\dot{\phi}}{\phi} \qquad (9)$$

$$\left(2\frac{\dot{A}}{A}+\frac{\dot{B}}{B}\right)\dot{\phi}+\ddot{\phi}=\frac{8\pi\phi^{-1}}{(3+2\omega)}(\rho+\lambda)$$

$$\dot{\rho}+2\rho\frac{\dot{A}}{A}+(\rho-\lambda)\frac{\dot{B}}{B}=0$$

Where the suffix (.) denotes ordinary differentiation with respect to time

Introducing the transformation,

$$A=e^{\alpha},\quad B=e^{\beta},\quad dt=A^2BdT$$

$$\alpha''-(\alpha')^2+\beta''-2\alpha'\beta'+\frac{\omega}{2}\left(\frac{\phi'}{\phi}\right)^2+\frac{\phi''}{\phi}-\frac{\alpha'\phi'}{\phi}=0$$

$$2\alpha''-(\alpha')^2-2\alpha'\beta'+\frac{\omega}{2}\left(\frac{\phi'}{\phi}\right)^2+\frac{\phi''}{\phi}-\frac{\beta'\phi'}{\phi}=8\pi\phi^{-1}e^{(4\alpha+2\beta)} \qquad (10)$$

$$2\alpha'\beta'+(\alpha')^2-\frac{\omega}{2}\left(\frac{\phi'}{\phi}\right)^2+2\frac{\alpha'\phi'}{\phi}+\frac{\beta'\phi'}{\phi}=8\pi\phi^{-1}\rho e^{(4\alpha+2\beta)}$$

$$\phi''=\frac{8\pi\phi^{-1}}{(3+2\omega)}(\rho+\lambda)e^{(4\alpha+2\beta)}$$

$$\rho'+2\rho\alpha'+(\rho-\lambda)\beta'=0$$

Where the superscript primes indicates differentiation w. r. to T

3. String Cosmological Model

The set of field equation (10) being highly nonlinear, to get the determinate solution, we assume

$$\rho + \lambda = 0 \tag{11}$$

i.e sum of rest energy density and tension density for a cloud of string vanishes.

Using equation (11), the set of equation (10) can be written as

$$2\alpha'' + 2\frac{\alpha'\phi'}{\phi} = 0$$

$$\beta'' + \frac{\beta'\phi'}{\phi} = 8\pi\phi^{-1}\rho e^{(4\alpha+2\beta)}$$

(12)

$$\phi'' = 0$$

$$8\pi\rho e^{(2\alpha+2\beta)} = k_3$$

Which yield an exact solution given by

$$A = e^{\alpha} = (aT+b)^{k_1/a} \tag{13}$$

$$B = e^{\beta} = e^{\left[\frac{k_3}{(2k_1+a)^2}(aT+b)^{(2k_1+a)/a}\right](aT+b)^{k_2/a}}$$

$$\phi = aT + b \tag{14}$$

$$\therefore 8\pi\rho = -8\pi\lambda = k_3 e^{\left[\frac{-2k_3}{(2k_1+a)^2}(aT+b)^{(2k_1+a)/a}\right](aT+b)^{(-2k_1+k_2)/a}} \tag{15}$$

Where constants $a \neq 0$, $b \neq 0$ and k_i, $i = 1,2,3$ satisfy the relation

$$(k_1k_2 + k_2k_3 + k_3k_1) + a(k_1 + k_2 + k_3) - \frac{\omega}{2}a^2 = 0 \tag{16}$$

Using equation (5) and (10), plane symmetric cosmological model for string source corresponding to above solution can be written as

$$ds^2 = e^{\left[\frac{-2k_3}{(2k_1+a)^2}(aT+b)^{(2k_1+a)/a}\right](aT+b)^{2k_2/a}}\left[(aT+b)^{\frac{4k_1}{a}}dT^2 - dz^2\right] - (aT+b)^{\frac{2k_1}{a}}(dx^2 + dy^2)$$

(17)

Where the rest energy density of the cosmic string and scalar field in the model are given by the equation (14), (13) respectively

4. Some physical properties

The plane symmetric string cosmological model in Brans Dicke theory is represented by (16) when the sum of tension density λ and the rest energy density ρ of the cosmic

string vanishes. The model has no initial singularity. The scalar field ϕ given by the equation (14) and the energy density and tension density of the string given by equation (15) in the model (17) are free from initial singularities. The spatial volume of the model is given by

$$V=\sqrt{-g}=(aT+b)^{\frac{4k_1+2k_2}{a}}e^{\left[\frac{2k_3}{(2k_1+a)^2}(aT+b)^{\frac{2k_1+a}{a}}\right]} \tag{18}$$

This shows the anisotropic of the universe (17) with time $k_3 \succ 0$

In order to obtain more clear and simple behavior of the physical kinematical variables with their simple explicit expressions, we choose the constants as

$$k_1=k_2=k_3=1=a=b; \quad a\neq 0, \quad b\neq 0 \tag{19}$$

Therefore the following expressions for the parameters are

Spatial volume $V=e^{\left[\frac{2}{9}(T+1)^3\right](T+1)^6}$ (20)

Expansion scalar $\theta=\frac{1}{3}u^i_{;j}=\left[\frac{1}{T+1}+\frac{(T+1)^2}{9}\right]$ (21)

Shear scalar

$$\sigma=\frac{1}{2}\sigma_{ij}\sigma^{ij}=\frac{1}{2}\left[\frac{1}{9}\left(1-\frac{2}{e^{\frac{2}{9}(T+1)^3(T+1)^6}}+\frac{1}{e^{\frac{4}{9}(T+1)^3(T+1)^{12}}}\right)\right]\left[\frac{1}{3(T+1)}+\frac{(T+1)^2}{27}\right]^2 \tag{22}$$

$$8\pi\rho=-8\pi\lambda=e^{\left[-\frac{2}{9}(T+1)^3\right](T+1)^{-1}} \tag{23}$$

$$8\pi\rho_p=2e^{\left[-\frac{2}{9}(T+1)^3\right](T+1)^{-1}} \tag{24}$$

The scalar field ϕ in the model takes the form

$$\phi=T+1 \tag{25}$$

The energy condition shows that $\rho\succ 0$ and $\rho_p\succ 0$. The rest energy density ρ, sting tension density λ and the particle density ρ_p tends to zero as time T increases indefinitely. The spatial volume tends to infinity and expansion scalar θ and shear scalar σ tends to zero as $T\to\infty$. The model (17) can be considered as an inflationary model of string cosmology in Brans Dicke theory of gravitations. From equation (15), it can be observed that for $k_3=0$, $\rho=\lambda=0$ and the model (17) degenerates into the singularity free plane symmetric vacuum model in Brans Dicke theory.

Conclusion:

We considered the plane symmetric metric and Brans Dicke (1961) field equation of string. While solving the field equation, we have assumed that sum of the energy density and tension density of the massive string is zero. The cosmological model obtained, which represent an inflationary plane symmetric string cosmological model in Brans Dicke theory of gravitation.

REFERENCES:

[1] Brans, C.,Dicke, R.H. :Phy. Rev.124, 925 **(1961).**

[2] Bayaskar S N,Pawar D D, Deshmukh A G : Rom. Journ. Phys., Vol. 54, Nos. 7–8, P. 763–770, Bucharest, (2009)

[3] Dicke, R.H.: Relativity, Group and Topology, Gordan and Breach Science pub., New York **(1964).**

[4] Kibble, T.W.B.: J. Phys. A9, 1387 (1976).

[5] Krori, K. D., Choudhari, T., Mahanta, C. R. : Gen. Relativity Gravitation 22, 123 **(1990)**.

[6] Krori, K. D., Choudhari, T., Mahanta, C. R. : Gen. Relativity Gravitation 26, 265 **(1990)**.

[7] Letelier, P. S. : Phys. Rev. D28,2414 **(1983)**.

[8] Vilenkin, A. : Phys. Rev. D23 ,852 **(1981)**.

[9] Vilenkin, A. : Phys. Rev. 121 ,263 **(1985)**.

[10] Pimentel, L. O. : Physical Review D53, **(1996)**.

[11] Pimentel, L. O. : Morden Physics Letters A. 12, **(1997)**.

[12] Lyra, G. : Maths. Zeitschrift 54, 52 **(1951)**.

[13] Rahaman, F., Chakraborty, S., Hossain, M., Das, S., : Bulg. J. Phys. 28, 217 **(2001)**.

[14] Rahaman, F., Chakraborty, S., Hossain, M., Begum, N., : Bera. J. : Ind. J. Physics, 768, 747 **(2002)**.

[15] Rahaman, F., Chakraborty, S., Hossain, M., Begum, N., : Kalam. M. : Pramana 60, 1153 **(2003)**.

[16] Reddy, D.R.K. : Astrophys. Space Sci. 286, 365 **(2003a)**.

[17] Panigrahi U.K. and Sahu R.C. : Science Letter Vol. 25, No. 11 and 12 **(2002)**.

[18] Panigrahi U.K. and Sahu R.C. : Theoret. Appl. Mech. Vol. 30, No. 3 pp.163-175 Belgiade.